A Study of Doped Ceria Electrolytes

James Michael Ralph

A thesis submitted for the degree of Doctor of Philosophy of the University of London and for the Diploma of Imperial College



Department of Materials,
Imperial College of Science, Technology and Medicine,
Prince Consort Road,
London, SW7 2BP

February 1998

BIBL. LONDON UNIV

Abstract

Solid oxide fuel cells provide a clean and efficient means to produce electricity. The main problem associated with the commercialisation of this kind of fuel cell, is the high operating temperatures required (1000°C), which necessitates the use of expensive materials and materials processing. The high temperatures are needed so that the zirconia electrolyte achieves an adequate conductivity for efficient fuel cell operation. An electrolyte with a higher conductivity is doped ceria. Using this material the operating temperature could be reduced to between 500-700°C, which would greatly lower the total cost of the fuel cell system.

A literature survey of the present day fuel cell technology is provided, including a discussion of the operating principles of the solid oxide fuel cell and designs of the fuel cell stack. The properties required of an electrolyte in a fuel cell are discussed and the current electrolyte materials under research are reviewed. Attention is then focused on the properties of doped ceria electrolytes, with particular emphasis on the electrical conductivity.

The aim of the experimental section is to optimise both the bulk and grain boundary conductivities in air for doped ceria and to minimise the electronic conductivity in reducing atmospheres. A number of experimental techniques have been employed to analyse these materials including, a.c. impedance spectroscopy, d.c. conductivity, transmission electron microscopy, secondary ion mass spectrometry and low energy ion scattering.

Attempts to improve the bulk conductivity were not successful but the grain boundary conductivity was improved, using a number of different doping techniques. The highest total conductivity was achieved for $Ce_{0.94}Sm_{0.03}Y_{0.03}O_{2-X}$. The electronic conductivity is shown to be reduced for calcium doped ceria-gadolinia samples at 500°C. Attempts to trap electrons at dopant ion sites, or lower their mobility by using electron blocking layers at the grain boundaries, have been explored. The conductivity mechanisms present for each doping scenario are fully discussed.

Acknowledgements

I would like to thank my supervisor Prof. John Kilner, for all the help and guidance that he has given during my three years of study, and for the patience he has shown during the proof reading of this thesis. A special thank you must go to Prof. Brian Steele for many important discussions, and my industrial supervisor, Dr. Thierry Seguelong, for making my stay in Paris a very memorable experience.

The past and present members of the ceramic ion conducting membrane and SIMS groups are acknowledged for their help and assistance during this project, in particular: the expertise and knowledge of Mr.Robert Rudkin, Mr.Richard Chater, Dr.David Waller and Dr.Jonathan Lane. Many thanks also go to the other students in the group who have made this study bearable, including, Dr.John Sirman, Mr.Enrique Ruiz-Trejo, Mr.Simon Hogg and Miss Sarah Benson, who, helped me to keep things running smoothly during my stay in Paris.

I am indebted to all the people at Rhône-Poulenc in Paris who made my stay a fantastic experience. Special thanks must go to Mme.Fabienne Pettini for her invaluable help, M.Georges Riglet and M.Daniel Péré for help with the electrical measurements and their miraculous abilities to solve any problem and lastly to M.Yuan Montardi for performing the TEM measurements. I would also like to thank the 'bosses', Dr.Patrick Maestro and Dr.Jean-Claude Gadea.

I would also like to thank the following for their contributions to this work: EPSRC and Rhône-Poulenc for financial support, Mr.Richard Sweeny for help with XRD, DTA and TG, Mr.Michael Haddon for AAS measurements, Mr.James Wright, Prof. Nigel Sammes for the high temperature XRD and Prof. H.H.Brongersma's group in Eindhoven for allowing me to perform the LEIS measurements, in particular Dr.R.G. van Welzenis and Mr.M.W.G.Ponjée.

Finally, I would like to thank my good friend Dr.Jan Pryzdatek for the long hours spent performing TEM analysis, my parents and sister, for their constant support, understanding and encouragement, and Jessica, for proof-reading this thesis and generally making life feel less stressful.

"L'Art est fait pour troubler, la Science rassure."

Georges Braque (1882-1963)

Table of Contents

Abstract 2
Acknowledgements 3
Table of Contents 4
List of Figures 9
List of Tables 13

Section 1: General Introduction and Review of Literature

Chapter 1. Introduction 15
1.1. Outline of the Thesis 16

Chapter 2. The Fuel Cell 18
2.1. Introduction 18
2.2. History 19
2.3 Principles of Operation 21
2.4 Alkaline Fuel Cell 22
2.5 Phosphoric Acid Fuel Cell 23
2.6 Solid Polymer Membrane Fuel Cell 23
2.7 Molten Carbonate Fuel Cell 25
2.8. Solid Oxide Fuel Cell 27

Chapter 3. Solid Oxide Fuel Cells 29
3.1. Introduction 29
3.2. Principles of Operation 30
3.3. Efficiency and Polarisation Losses 31
3.4. Cell Components 35
3.4.1. The Anode 35
3.4.2. The Electrolyte 37
3.4.3. The Cathode 38
3.4.4. The Interconnect or Bipolar Plate 40
3.4.5. Interlayers 43
3.4.6. Balance-of-Plant Materials 43
3.5. SOFC Stack Designs 44
3.5.1. Tubular 44
3.5.2. Planar or Flat Plate 46
3.5.3. Monolithic Design 48

Chapter 4. Associated Electrolyte Applications 53
4.1. Introduction 53
4.2. Air Separation Membranes 53
4.3. Oxygen Sensors/Probes 55
4.4. Oxygen Pumps 56
4.5. Water Electrolysers 56
4.6. Electrochemical Production of Industrial Gases 57

Chapter 5. Electrolytes - Diffusion, Conductivity and Defect Chemistry 59
5.1. Introduction 59
5.2. Defect Types 60
5.3. Diffusion and Conductivity 62
5.4. Fluorite Related Structures 70
5.4.1. CeO_2 Electrolytes 70
5.4.1.1. Brouwer Diagrams 71
5.4.1.2. Deviations from Brouwer Assumptions 75
5.4.2. $Zr(M)O_2$ Electrolytes 75
5.4.3. Bi_2O_3 Based Electrolytes 77
5.4.4. ThO_2 Electrolytes 77
5.4.5. Pyrochlore 78
5.5. Perovskite Related Structures 79
5.5.1. Ionic Conductors (LSGM) 80
5.5.2. Proton Conductors 80
5.5.3. Mixed Ionic and Electronic Conductors 81
5.5.4. Brownmillerite 81

Chapter 6. Doped Ceria Electrolytes 85
6.1. Introduction 85
6.2. Preparation of Pure Ceria 85
6.3. Preparation of Doped Ceria 87
6.3.1. Impurity Effects 90
6.4. Dopant and Impurity Segregation 92
6.5. Dilute Solution Theory 94
6.5.1. Defect Association 95
6.6. Cation Mobility/Grain Boundary Mobility in Doped Ceria 100
6.7. Ionic Transference Number 102
6.8. Conduction Mechanisms 103
6.8.1. Grain Boundary Conductivity 103
6.9. Alkaline Earth Dopants 105
6.9.1. Scandia and Yttria Doped Ceria 107
6.10. Rare Earth Dopants 109
6.11. Multiple Doping in Ceria 113
6.11.1. Other Dopants 114
6.12. Electronic Conductivity 114
6.12.1. Grain Boundary P_{O2} Dependencies 116
6.12.2. P-Type Conductivity in Doped Ceria 117
6.13. Mechanical Stability 117

Chapter 7. Electrolyte Films 123
7.1. Introduction 123
7.2. ZrO_2 and CeO_2 Films 125
7.3. CeO_2 Thin Films and Depostion Techniques 126
7.4. Pulsed Laser Deposition 127

Chapter 8. Glass Additions 130
8.1. Introduction 130
8.2. Liquid Phase Sintering 131
8.3. Conductivity in Glasses 132

8.3.1. Ionically Conducting Glasses 133
8.3.2. Electronically Conducting Glasses 136
8.4. Strontium Gallate Glasses 138

Section 2: Experimental

Chapter 9. Powder Preparation 144
9.1. Introduction 144
9.2. Solid State Technique 144
9.3. Co-Precipitation Technique 145
9.4. Amorphous Citrate Technique 147
9.5. Combustion Synthesis Technique 149
9.6. Powders Prepared at Rhône-Poulenc (RP) 149
9.6.1. Co-Precipitation Route 150
9.6.2. Powder Atomisation 150
9.7. ECN Powder 150
9.8. Sintering 150

Chapter 10. Characterisation Techniques 153
10.1. Introduction 153
10.2. Thermogravimetry of Precursor Material 153
10.3. Composition Analysis 154
10.3.1. Inductively Coupled Plasma 154
10.3.2. Atomic Absorption Analysis 154
10.4. Particle Size Analysis 155
10.4.1. Specific Surface Area Measurements 155
10.4.2. Scanning Electron Microscopy 156
10.5. Dilatometry 156
10.5.1. Sintering Dilatometry 156
10.5.2. Thermal Expansion Coefficients 156
10.6. X-Ray Diffraction 157
10.6.1. High Temperature X-Ray Diffraction 157
10.7. Density Measurements 157
10.8. Grain Size Determination using Optical Microscopy 158
10.9. A.C. Impedance Spectroscopy 159
10.9.1. Introduction 159
10.9.2. Sample Preparation 159
10.10. Four-Point D.C. Resistivity 160
10.11. Electrical Measurements at Rhône-Poulenc 162
10.12. Transmission Electron Microscopy 162
10.12.1. TEM Prepartion 163
10.12.1.1. Preparation Route 1 163
10.12.1.2. Preparation Route 2 164
10.12.1.3. Preparation Route 3 164
10.13. Measurement of Oxygen Diffusion Coefficients 165
10.13.1. Sample Preparation and Oxygen Isotope Exchange 165
10.13.2. Secondary Ion Mass Spectroscopy 166
10.14. Low Energy Ion Scattering 169
10.14.1. Introduction 169
10.14.2. Sample Preparation 170

10.15. Thin Film Analysis 171

Section 3: Results and Discussions

Chapter 11. Sample Preparation 174
11.1. Introduction 174
11.2. Thermogravimetry 174
11.3. Composition Analysis 175
11.3.1. Inductively Coupled Plasma 175
11.3.2. Atomic Absorption Spectroscopy 176
11.4. Particle Size Analysis, Surface Area and Morphology 177
11.5. Dilatometry 179
11.5.1. Sintering Characteristics 179
11.5.2. Thermal Expansion Coefficients 182
11.6. XRD 183
11.6.1. High Temperature XRD 184

Chapter 12. Effects of Doping in Ceria and the Production of CGO Thin Films
12.1. Introduction 186
12.2. A.C. Impedance Spectroscopy 186
12.2.1. Empirical Observations of Impedance Data 189
12.3. Electrical Properties 190
12.3.1. A.C. Impedance Spectroscopy - Bulk Data 190
12.3.2. A.C. Impedance Spectroscopy - Grain Boundary Data 199
12.3.3. A.C. Impedance Spectroscopy - Total Data 203
12.3.4. Silica Additions 205
12.4. Low Energy Ion Scattering (LEIS) 207
12.4.1. XPS 215
12.5. TEM 216
12.6. Conclusions 219
12.7. Thin Films 220

Chapter 13. Double Doping in Ceria 225
13.1. Introduction 225
13.2. Powder Characterisation 225
13.3. Electrical Properties 229
13.3.1. A.C. Impedance Spectroscopy - Bulk Data 229
13.3.2. A.C. Impedance Spectroscopy - G.B. Data 232
13.3.3. A.C. Impedance Spectroscopy - Total Data 234
13.3.4. Comparison Between IC and RP Prepared Powders 236
13.3.5. D.C. Conductivity in Air 237
13.3.6. D.C. Conductivity in Reducing Conditions 239
13.4. SIMS Data 241
13.4.1. Isotope Exchange 241
13.4.2. Diffusion Profile Measurements 242
13.5. TEM 247
13.6. Conclusions 252

Chapter 14. Ca-Codoping and the Reduction of Electronic Conductivity using Glass Additions 254
14.1. Introduction 254
14.2. Ca-Codoping in CGO 254
14.3. Electron Trapping Using Variable Valent Dopants 259
14.4. Effect of Strontium Gallate Additions 264
14.4.1. Preparation 264
14.4.2. Conductivity Measurements 264
14.5. Conclusions 270

Section 4: Conclusions and Future Work

Conclusions 272

Suggestions for Further Work 274

Appendix A 275
A.1. Mechanical and Dielectric Breakdown Relationships 275
A.2. Experimental 281
A.3. Results and Discussion 281
Appendix B Derivation of the Impedance of a Parallel RC Circuit and how this Produces a Semi-Circle on an Impedance Plot 284

References are included at the end of each chapter.

List of Figures

Fig.2.1. The basic components of a fuel cell.
Fig.3.1. Schematic representation of an SOFC stack.
Fig.3.2. Effect of temperature on the efficiencies of heat engines and fuel cells.
Fig.3.3. Typical voltage-current density characteristics for a SOFC.
Fig.3.4. The Westinghouse tubular SOFC.
Fig.3.5. The Westinghouse tubular SOFC Stack.
Fig.3.6. The planar SOFC configuration.
Fig.4.1. Ceramic oxygen separation membranes. a). Pressure driven system ($P_{O2}'>P_{O2}''$). b). Electrically driven system.
Fig.5.1. A). Ideal unit cell of doped ceria. B). Fluorite structure showing anion co-ordination.
Fig.5.2. Brouwer diagram for Gd-doped ceria also showing the variation in conductivity.
Fig.5.3. The ideal perovskite structure.
Fig.6.1. Ideal bulk conductivity graph for doped ceria showing regions I (intrinsic), II (extrinsic, dissociated) and III (extrinsic, associated).
Fig.6.2. Graph showing the experimental and calculated effects of dopant ion size on the association enthalpy in the ceria lattice for trivalent dopants. Ionic radii are obtained from lattice parameters.
Fig.6.3. Lattice parameter map showing host lattices and rare earth oxide dopants.
Fig.6.4. Effect of dopant concentration on the ceria lattice parameter.
Fig.6.5. Schematic representation of the two grain boundary models.
Fig.8.1. Two-dimensional representation of a boron oxide glass.
Fig.8.2. Two dimensional representation of a sodium silicate glass.
Fig.8.3. A comparison of d.c. resistivity in some alkaline earth boroaluminate glasses at 450°C.
Fig.8.4. Activation energies for d.c. conductivity in some alkaline earth boroaluminate glasses.
Fig.9.1. Molecular structure of a citric acid molecule showing the four potential hydroxide substitution sites.
Fig.10.1. Schematic of the a.c. impedance sample holder.
Fig.10.2. Schematic of the bar samples used for electrical resistivity measurements.
Fig.10.3. Schematic of the 4-point d.c. electrical conductivity holder.
Fig.10.4. Schematic representation of a mounted TEM sample.
Fig.10.5. Schematic diagram illustrating the key features of the Atomika 6500 SIMS.
Fig.10.6. Schematic diagram of the SIMS line-scanning technique.
Fig.11.1. Typical thermogravimetric graphs for Gd and Ce nitrate.
Fig.11.2. Typical SEM morphology of a calcined CGO powder ($Ce_{0.94}Gd_{0.06}O_{2-X}$).
Fig.11.3. Dilatometric shrinkage curves for CGO and Ca doped CGO.
Fig.11.4. Typical micrographs for polished and thermally etched samples of $Ce_{0.77}Gd_{0.23}O_X$ and $Ce_{0.9}Gd_{0.09}Ca_{0.01}O_X$. Dark spots indicate closed porosity.
Fig.11.5. Thermal expansion coefficients in a number of doped ceria samples.
Fig.11.6. Typical XRD trace for doped ceria.
Fig.11.7. Variation of lattice parameter with dopant concentration.

Fig.11.8. XRD spectra for $Ce_{0.7}Gd_{0.3}O_{1.85}$ at 1000°C, displaying shoulder peaks from a second phase.
Fig.12.1. Ideal impedance spectra for a polycrystalline electrolyte, showing the equivalent R-C circuit for each process.
Fig.12.2. Impedance spectra for several CGO samples, measured in air at 250°C.
Fig.12.3. Arrhenius graph of the bulk conductivity for a series of CGO samples with increasing Gd concentrations. Ce-26%Gd displays lines obtained by regression analysis, used to calculate the low and high temperature gradients.
Fig.12.4. Comparison of the bulk activation energies for ionic conduction as a function of dopant concentration, in the high and low temperature ranges.
Fig.12.5. Comparison of the high and low temperature bulk pre-exponential terms as a function of dopant concentration for CGO.
Fig.12.6. Relationship between the pre-exponential and activation enthalpy for the bulk component of CGO, both below and above 350°C.
Fig.12.7. Arrhenius graph of the grain boundary conductivity for a series of CGO samples with increasing Gd concentrations.
Fig.12.8. Grain boundary activation enthalpies for ionic conduction as a function of dopant concentration.
Fig.12.9. Grain boundary pre-exponential term as a function of dopant concentration for CGO.
Fig.12.10. Comparison of the measured and corrected grain boundary conductivities for CGO at 300°C.
Fig.12.11. Arrhenius graph of the total conductivity for a series of CGO samples with increasing Gd concentrations.
Fig.12.12. Isothermal conductivity of CGO at 500°C as a function of Gd concentration, showing data for the bulk, grain boundary and total contributions.
Fig.12.13. Comparison between the conductivities of pure ceria and pure gadolinia against a standard Ce-10%Gd sample.
Fig.12.14. Comparison of the bulk and grain boundary conductivities for a normal Ce-10%Gd sample and a silica doped CGO sample.
Fig.12.15. LEIS spectra for as-sintered Ce-6%Gd and Ce-9%Gd-1%Ca showing the initial area scans (3×3mm) using $^3He^+$ beam (3keV, I=1nA).
Fig.12.16. LEIS spectrum for as-sintered Ce-6%Gd using a $^4He^+$ beam, showing the development of the Ce+Gd peak and the presence of a thick surface region (several tens of monolayers thick). Ion beam doses as indicated (3keV, I=2-3nA).
Fig.12.17. LEIS spectra for the as-sintered, sputtered and annealed surface of a Ce-6%Gd pellet. Segregation peaks disappear after sputtering but re-appear after the short anneal (3keV, I=2-4nA).
Fig.12.18. LEIS spectrum obtained from a spot measurement using a Ne^+ beam, showing a Gd shoulder on a Ce peak, for a Ce-26%Gd sample (4.75keV, I=3nA).
Fig.12.19. LEIS spectra showing the development of the Ce+Gd peak for a Ca-doped CGO pellet and a thick surface layer, using $^4He^+$ spot measurements (3keV, I=1-8nA).
Fig.12.20. LEIS spectra to show the comparison between as-sintered and polished and annealed Ca-doped CGO, using a $^4He^+$ area scan (3keV, I=1-3nA). Dose=3×10^{13}ions/cm^2 for both compositions.
Fig.12.21. XPS spectrum for as-sintered Ce-6%Gd using a Mg K_α beam. Inset shows peaks at higher binding energies.
Fig.12.22. Bright field HRTEM image of a $Ce_{0.8}Gd_{0.19}Ca_{0.01}O_{2-X}$ sample with grain boundary aligned parallel to electron beam.
Fig.12.23. Schematic representation of the grain boundary in doped ceria.

Fig.12.24. Typical XRD trace for thin film CGO on a ferritic stainless steel substrate. Measurement courtesy of Dr.D.Waller.
Fig.12.25. AFM image of the surface of a CGO thin film, showing a very flat topography and no pinholes.
Fig.12.26. Impedance Data of all laser ablated CGO thin films at 130°C. Inset shows the poorly resolved bulk semi-circle for the 20%Gd sample.
Fig.12.27. Arrhenius conductivity plots for the laser ablated thin films compared to the conductivity data from pellets of the same composition.
Fig.13.1. SEM micrograph showing the morphology of a double doped ceria powder.
Fig.13.2. Dilatometric shrinkage curves for CGO and double doped ceria materials supplied by Rhône-Poulenc.
Fig.13.3. Typical micrograph for double doped ceria showing the grain structure. Dark spots indicate closed porosity.
Fig.13.4. Variation of lattice parameter with the larger dopant concentration for double doped ceria. Errors in lattice parameter are too small to be displayed.
Fig.13.5. Arrhenius plots of the bulk conductivity, obtained by impedance spectroscopy, for $Ce(Sm,Y)O_2$ and $Ce(La,Yb)O_2$, both showing a reference CGO (see legends).
Fig.13.6. Arrhenius plots of the grain boundary conductivity, obtained by impedance spectroscopy for $Ce(Sm,Y)O_2$ and $Ce(La,Yb)O_2$, both showing a reference CGO (see legends).
Fig.13.7. Arrhenius plots of the total conductivity, obtained by impedance spectroscopy, for $Ce(Sm,Y)O_2$ and $Ce(La,Yb)O_2$, both showing a reference CGO (see legends).
Fig.13.8. Graph of the bulk and grain boundary conductivity, showing a comparison between Ce-3%Sm-3%Y and Ce-5%Sm-5%Y.
Fig.13.9. Comparison of the electrical properties between IC and Rhône-Poulenc prepared powders for 6% Gd.
Fig.13.10. Graph to show the good agreement between ac measurements and dc measurement over the temperature range 150°-900°C, on a Ce-3%Sm-3%Y sample. The straight line pronounces the curvature in data at higher temperatures.
Fig.13.11. Conductivity graph comparing the double doped material from Rhône-Poulenc with the material from IC, in reducing H_2/CO_2 atmospheres at 700°C. The line is used as a guide to show the typical behaviour for doped ceria.
Fig.13.12. Graph showing the P(-) value for a double rare earth doped ceria.
Fig.13.13. Experimental and fitted (dotted line) temperature-time profiles for the $^{18}O/^{16}O$ isotopic exchange of $Ce_{0.94}Gd_{0.06}O_{2-X}$.
Fig.13.14. Experimental diffusion profile for $Ce_{0.94}La_{0.03}Yb_{0.03}O_{2-X}$ and the least squares fit of this data to equation 10.5.
Fig.13.15. Arrhenius plot of the self-diffusion coefficient, D*, and the surface exchange coefficient, k, for several RP materials, compared to a Ce-10%Gd sample (black circles and white squares). The straight lines show trends in the data.
Fig.13.16. Bright field TEM image of a linescanned Ce-6%Gd sample, with the analysed grain boundary indicated by the numbered straight line.
Fig.13.17. Electron diffraction patterns corresponding to the numbered regions in Fig.13.16, showing amorphous rings at the grain boundary.
Fig.13.18. Bright field TEM image of a linescanned Ce-3%La-3%Yb sample, with the analysed grain boundary indicated by the numbered straight line.
Fig.13.19. Electron diffraction patterns corresponding to the numbered regions in Fig.13.18. There are no amorphous rings visible at the grain boundary.

Fig.14.1. Impedance spectrum comparing the Ca doped CGO samples to the standard CGO compositions at 250°C.
Fig.14.2. Arrhenius plots of conductivity comparing Ca doped and undoped CGO. (A) is the bulk conductivity and (B) is the grain boundary conductivity.
Fig.14.3. Arrhenius plot for the total conductivity of Ca doped and undoped CGO.
Fig.14.4. Comparison of the total conductivity data obtained in air from a.c. and d.c. techniques, for Ca doped and undoped CGO.
Fig.14.5. Comparison of the total conductivities for the best conductors in each material group studied.
Fig.14.6. Electrical Behaviour of Ca doped and undoped CGO in reducing conditions at three different temperatures.
Fig.14.7. Arrhenius graph of the electronic conductivity for both Ce-20%Gd and a Ca doped CGO.
Fig.14.8. Arrhenius graph showing the bulk and grain boundary conductivities for a number of codoped CGO samples.
Fig.14.9. Comparison of the total conductivity of several doped ceria samples in reducing conditions at 700°C.
Fig.14.10. Graph showing the P(-) values calculated at 700°C, for the samples analysed in Fig.14.9.
Fig.14.11. Arrhenius graph of the conductivity of glassy and crystalline strontium gallate. The total conductivity of Ce-10%Gd is also shown for comparison.
Fig.14.12. Arrhenius graph of the total conductivity of SGO doped CGO pellets, made by mechanical mixing and powder atomisation (RP samples), compared to an undoped CGO.
Fig.14.13. D.C. conductivity in reducing H_2/CO_2 conditions for CGO with SGO additions, measured at 700°C. IC powder is mechanically mixed and RP powder has been atomised onto CGO.
Fig.A.1. Dielectric breakdown characteristics of $Ce_{0.9}Gd_{0.1}O_{2-X}$ as a function of thickness.
Fig.A.2. Weibull plot of dielectric strength for $Ce_{0.9}Gd_{0.1}O_{2-X}$.
Fig.B.1. A parallel RC circuit.
Fig.B.2. Corresponding impedance semi-circle.

List of Tables

Table 6.1. Synthesis temperatures and densities of some pure ceria powders.
Table 6.2. Synthesis temperatures and densities of some doped ceria powders.
Table 6.3. Typical variation in measured impurity levels in ceria solid solutions.
Table 6.4. Fracture toughness and Young's modulus for CGO.
Table 6.5. Thermal expansion coefficients between 50-1000°C.
Table 7.1. Laser parameters.
Table 11.1. Theoretical and measured weights of water in the nitrate precursors.
Table 11.2. Concentration of elements in doped ceria samples measured by ICP.
Table 11.3. Concentration of Ca in doped ceria samples calculated from AAS.
Table 11.4. Mean particle sizes for CGO powders.
Table 11.5. Density and average grain size of CGO and Ca-doped CGO pellets.
Table 12.1. Calculated association enthalpies for CGO.
Table 12.2. Film thicknesses.
Table 13.1. Particle sizes and surface areas of double doped ceria powders.
Table 13.2. Density and average grain size of CGO and double doped ceria pellets.
Table 13.3. Calculated values for the low and high temperature bulk activation enthalpies, the association enthalpy and the grain boundary activation enthalpy.
Table 13.4. Temperatures and corresponding times for $^{18}O/^{16}O$ anneals for several Rhône-Poulenc materials.
Table 13.5. Tracer diffusion coefficients, D_T, surface exchange coefficients, k, self-diffusion coefficients, D*, conductivity diffusion coefficients, D_σ, Haven ratios, H_R and conductivity correlation factors, f_c, for several RP materials.
Table 14.1. Sintering and cooling characteristics for the production of SGO doped CGO pellets.
Table A.1. Comparison of mechanical properties between YSZ and ceria electrolytes.

Section 1

General Introduction

And

Review of Literature

Chapter 1. Introduction

Ionic conduction was first studied in liquids, where the process known as electrolysis was discovered. Electrolysis involves the conversion of electrical energy into chemical energy in order to form, or breakdown compounds, by oxidation or reduction processes. Electrolysis became important in the isolation of elements and formation of compounds which were difficult to produce using conventional chemistry and started the first serious research into electrolytes. The principles of electrolysis are still important today, especially in the area of corrosion: Oil rig superstructures are cathodically protected using a sacrificial metal that is placed in contact with the structure and corrodes in preference to the rig metal. The sea water acts as the electrolyte to complete the circuit for the conduction of metal ions.

For many decades, the study of liquid electrolytes dominated because of the higher mobilities of ions in liquids compared to those in solids. The invention of the first batteries intensified research into these liquid electrolytes. In these batteries, chemical energy stored in a liquid electrolyte could be converted into useful electrical energy via a chemical reaction. The development of the battery as a mobile power source still continues today, with the majority of the electrolytes remaining in liquid form. A myriad of different electrolytes have now been studied but technology has demanded that only electrolytes with the highest conductivities receive attention for the storage of electricity.

The traditional lead acid batteries, used in automobiles, are now being replaced by the higher energy density battery systems, in which the conducting ions are Li and Na, such as in the Na-S and Li-FeS battery systems. Battery production is now a mature technology, with an ever increasing number of battery systems available, both in the primary and secondary (rechargeable) battery systems.

The study of solid ion conducting electrolytes is, in contrast to the liquid electrolytes, more recent, with early reports of ionic conductivity discovered by Nernst in 1899, for the solid Y_2O_3 stabilised ZrO_2. This material was reported to conduct oxygen ions and at present is still the most widely used oxygen ion conducting solid.

There are an increasing number of applications where solid electrolytes are being used and many more potential applications. Both cation and anion conducting solid electrolytes are being developed. β-alumina ($Na_2O.11Al_2O_3$) and 'nasicon' ($Na_3Zr_2Si_2PO_{12}$), the basis of the Na-S batteries, are examples in which the sodium ion is the conducting species. The lithium ion is also found to have a high mobility in, for example, the compound Li_3N. The silver ion perhaps demonstrates the highest of the ionic conductivities in the solid electrolyte $RbAg_4I_5$. Among the anion conductors is the electrolyte $La_{0.95}Sr_{0.05}F_{2.95}$, which is used in sensors to monitor the concentration of fluorine ions in drinking water. There are also many glass electrolytes and this subject is reviewed in more detail in chapter 8.

Some of the most studied solid electrolytes are the oxygen ion conductors (e.g. yttria stabilised zirconia and gadolinia doped ceria), due to their applicability in a number of potentially high return markets, such as power generation. Comprehensive reviews of oxygen ion conductors can be found in the literature [1, 2, 3, 4] and are considered in more depth in chapter 5.

1.1. Outline of the Thesis

The thesis begins with an introduction to the fuel cell, a highly efficient device for production of electricity, followed by an in-depth look at the most promising of the fuel cells, the solid oxide fuel cell. The emphasis then focuses on the different electrolytes used and, more importantly, the use of doped cerias and the properties of this material. Short chapters on thin films and glass electrolytes are also included to complement the research performed in this thesis. The experimental section encompasses a discussion of the powder preparation techniques and the wide range of experimental equipment that was necessary, in order to elucidate the conduction mechanisms in these electrolytes.

The results and discussion section are then split into four chapters and deal with the preparation of the samples, and the effects of doping and double doping to improve the ionic conductivity, both in the bulk of the material, as well as at the grain boundaries.

The final chapter concentrates on the electronic properties of doped ceria. Methods for improving the performance of ceria electrolytes in reducing atmospheres are explored, including suitable dopants and the use of glass additions. Finally, there are some general conclusions and pathways for new areas of research.

References

1. T.H.Estell and S.N.Flengas. Chem.Rev. **70**, (1970), 339.
2. E.C.Subbarao and H.S.Maiti. Solid State Ionics. **11**, (1984), 317.
3. T.Kudo. The CRC Handbook of Solid State Electrochemistry. Eds. P.J.Gellings and H.J.M.Bouwmeester. CRC Press, Inc. 1997, 195.
4. H.-H.Möbius. J.Solid State Electrochem. **1**, (1997), 2.

Chapter 2. The Fuel Cell

2.1. Introduction

It has been estimated [1] that the world energy demand at present is in the range of $340\text{-}370\times10^{18}$J per year. This energy use is equivalent to 10^{10}tons of coal per year, or 5.5×10^{10}barrels of oil. Per Capita, the world average power usage is about 2000kWh per year, while in Europe it is three times this figure. With the world population set to double in the next 50 years and the expected dramatic growth rate of heavy industry in the developing countries, the energy burdens on our world can only increase. Today, civilisation is such that without electricity the world would cease to function. At present, the conventional fossil fuels (coal, oil and natural gas) have met the world's needs and will do, undoubtedly, for the next 50 years. More recently, the advent of nuclear power has commanded a large share of the market.

It was not until the end of this century that the predictions concerning the future reserves of the world's fossil fuels were released. Calculations showed that fossil fuels, at current and predicted usages, would start to be depleted towards the end of the next century.

The oil crisis in 1973 and more recently the Gulf War, have highlighted to the world the importance that is placed on fossil fuels and the needs for diversification. The nuclear industry and its concepts of unlimited energy were irreversibly affected by the Chernobyl disaster from which the world is still recovering. The search for renewable energy sources thus turned to nature but it was quickly acknowledged that substantial energy from solar power and other smaller renewable sources was unrealistic.

Probably the most significant change, is the increased global awareness of our environment and the damage that is being inflicted upon it. The emission levels of NO_X, SO_X, particulates, CO_2 and many other gases from industry and combustion engines in automobiles, have been shown to pollute our atmosphere. The effects have

been global; from acid rain to the controversial "Green House" effect, causing a gradual warming of the earth. Most inhabitants of large cities experience the effects of pollution with poor air quality and in the extreme, smog. Nuclear power does not produce pollutants to the air but brings a greater unknown threat to the environment, that of the disposal of highly radioactive waste.

With this unprecedented pressure on the world to find new, cleaner and more efficient power sources, it is surprising that one that has existed for over a hundred years has not received more attention. This power source is the *Fuel Cell*.

2.2. History

The fuel cell is an electrochemical device which directly and continuously converts the chemical energy of a fuel and an oxidant into electrical energy. Its operation is analogous to that of a battery, whereby an electrochemical reaction provides a supply of low voltage d.c. electricity. Unlike a battery, however, where the chemical reaction proceeds until the stored substances are fully converted or need recharging, the fuel cell delivers continuous operation, provided the feed of fuel and oxidant are maintained. Fuel cells also differ strongly from batteries both in terms of design and engineering.

The first working fuel cell was demonstrated in 1839 by Sir William Grove [2]. It was based on a dilute sulphuric acid electrolyte with platinum electrodes. The cell fell short of the power output of the more conventional galvanic cells and the research was soon stopped. At the time, coal was an important fuel source and as a consequence, attempts were made to operate fuel cells with coal as fuel. Ludwig Mond and Charles Langer repeated Grove's work but replaced oxygen with air and hydrogen with gas obtained from coal. The cell worked and they coined the term *fuel cell* but research did not continue, because of the high cost for the large amounts of platinum used and severe polarisation. Further research into electrochemical conversion devices was very limited for the rest of the nineteenth century and it was not until the turn of the century that alternative electrolytes were really considered [3]. In 1900, Nernst constructed a

fuel cell based on the solid oxide electrolyte, yttria stabilised zirconia, while J.H.Reid first describes a fuel cell based on an aqueous KOH electrolyte in 1902. The first real attempt to produce a fuel cell, based on a molten carbonate electrolyte, is credited to E.Baur in 1921. It operated at 1000°C but due to a poor understanding of electrode kinetics and the corrosion problems at high temperatures, he too terminated his work in the field.

By 1940, one hundred years after the invention of the fuel cell, the technology was still very much in its infancy and most work was still laboratory based. During this period the introduction of the internal combustion engine was seen, whose theoretical foundation was much better understood than the fuel cell and the relative ease of its fabrication led to its complete dominance. The first real development of fuel cells was led by Francis T. Bacon, who, in 1939, built a pressurised fuel cell, based on KOH, which was later to be scaled up and used in the Apollo space missions [4].

It was the space applications that were to launch the fuel cell as a credible power source and inject the necessary resources for further research opportunities. The Gemini missions saw the introduction of an ion exchange membrane fuel cell, which was also used in the Apollo missions to put the first man on the moon. Fuel cells have since become commonplace in the space shuttle programme but their introduction for terrestrial use has not been so successful. Unfortunately, the high cost of the pure hydrogen and oxygen gases needed, prevented the development of the fuel cell for terrestrial applications and research diminished. After the 1970's oil crisis, the funding into fuel cells began to increase rapidly and a number of different fuel cell programmes are still in existence today. The fuel cell is now developed on a large scale with kilowatt to megawatt units already commercially available as demonstration units. With the heightened environmental awareness and drive for a new power source, it is anticipated that in the next decade, the fuel cell will become fully commercial.

2.3. Principles of Operation

All fuel cells consist of the same basic components, an anode, electrolyte and cathode, which form a single cell (Fig.2.1.). The cells are electronically interconnected by a separator or bipolar plate to form a fuel cell stack. A fuel such as hydrogen or a hydrocarbon is oxidised at the anode, which releases electrons to the external circuit. An oxidant such as oxygen is fed to the cathode, where it is reduced by accepting the electrons from the external circuit. Ions are then conducted through the electrolyte to complete the circuit, producing water and, depending on the fuel, CO_2 at the appropriate electrode. The flow of electrons through the external circuit produces d.c electricity.

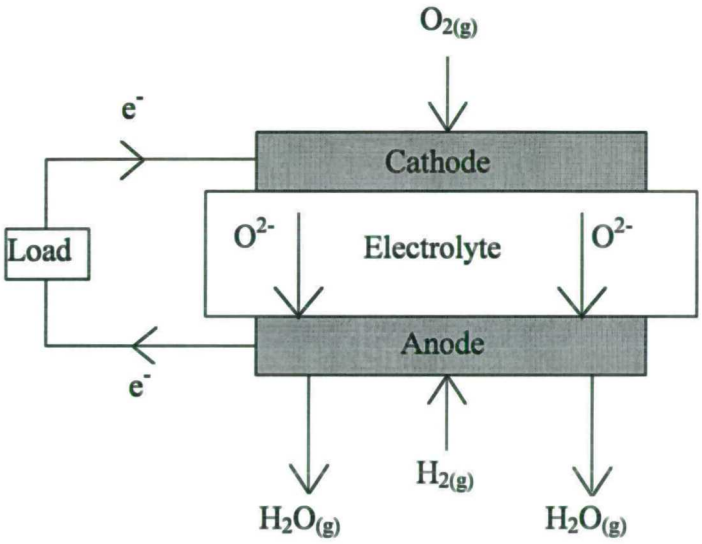


Fig.2.1. The basic components of a fuel cell. (Detailed electrochemistry will be discussed later).

The theoretical efficiencies of a fuel cell are around 95%, there are, however, a number of irreversible losses in a fuel cell which limit the efficiency. These losses will be discussed further in the next chapter. The fuel cell offers many advantages over conventional power sources, of which the most significant may be delocalised power generation, which would enable the replacement of the very inefficient national grid system. This modularity gives the fuel cell a large market to exploit, from individual housing, to large scale industrial systems and cities.

The obvious benefits of higher efficiencies for fossil fuel conversion will extend, in the short term, the life expectancy of the fossil fuels. In the long term, non-fossil fuels such as methanol are expected to be used. The much lower emission levels of fuel cells compared to combustion engines, will drastically reduce the levels of NO_X, SO_X and CO in the atmosphere, and improve environmental conditions. The potential for fuel cell powered automobiles will further improve the environment. Other benefits include low levels of noise pollution and small site requirements, allowing small power stations to be built in the centre of cities. This will result in a reduction in the length of transmission lines and reduce the number of step-up transformers required, achieving a large energy saving. In addition, the high efficiency of power output at part load will allow greater flexibility over conventional systems.

A brief summary of the current fuel cells under development is given below, describing the materials used, the benefits and drawbacks and the development stage of each type.

2.4. Alkaline Fuel Cell (AFC)

Developed in the 1960's as a power source for the Apollo space missions, as discussed in section 2.2, alkaline fuel cells consist of a concentrated potassium hydroxide (KOH) solution as the electrolyte. The electrodes are porous nickel or carbon in PTFE and act as current collectors, supporting a finely divided nickel or platinum catalyst [5]. Hydroxide ions (OH^-) act as the conducting species through the electrolyte, formed by the reaction of oxygen and water at the cathode. The OH^- ions react with hydrogen at the anode, releasing electrons to the external circuit.

The AFC is attractive because of its simplicity, high current density and low operating temperature (60-150°C) but is unlikely to find widespread use due to its necessity to have pure oxygen and hydrogen feed gases. The high purity required results from the reactivity of trace amounts of CO_2 with the electrolyte, producing insoluble potassium carbonate. Removal of CO_2 from the gas feeds is both impractical and expensive and thus terrestrial applications will be limited.

2.5. Phosphoric Acid Fuel Cell (PAFC)

The phosphoric acid fuel cell is the most technologically advanced of all the fuel cells and the closest to full commercialisation. Units of 50, 100, 200kW are now being evaluated commercially and mass production facilities are already in place with over 130 units delivered [4]. Larger scale prototype power stations in the range 0.5-11MW are also being evaluated and considerable efforts are apparent in both Japan and the USA. For a more in-depth look into PAFC development, the reader is referred to reference [6].

The PAFC uses a phosphoric acid (H_3PO_4) electrolyte, which has the advantage over the AFC that it does not react with CO_2, thus allowing atmospheric air to be used as the oxidant and fuel gases produced from the steam reforming of fossil fuels. The phosphoric acid is contained within a matrix of silicon carbide powder bonded to PTFE, while the electrodes consist of a dispersed platinum catalyst on a porous carbon based support. The temperature of operation is required to be ≥200°C, to prevent CO degrading the performance of the platinum based electrocatalysts. Oxidation of the reformed hydrocarbon fuel produces H^+ ions which are conducted through the electrolyte and converted into water on the cathode side on reaction with the air.

Alongside improving the corrosion resistance of cell materials, research into cheaper and greater activity electrocatalysts continues, in an attempt to reduce the commercially prohibitively high cost of the PAFC system, currently around $3000/kW, to between $1800-2000/kW by the year 2000. In addition, external reforming of the hydrocarbon fuels is required, which lowers the total efficiency to around 40% and the unproven reliability of PAFC systems remains a barrier to large scale commercialisation.

2.6. Solid Polymer Membrane Fuel Cell (SPFC)

The polymer membrane fuel cell (SPFC) was first demonstrated around the same time as the alkaline fuel cell was developed for the space missions. The SPFC was

originally designed as the power source for submarine propulsion, but it has now been re-designed and aimed at the automotive market. The leading developers in this fuel cell system are Ballard Power Systems Inc., who in 1995 developed a compact, light weight 25kW stack, capable of powering an automobile [6]. Although the polymer membrane fuel cell is not expected to enter the large scale power market, Ballard have developed a 30kW on-site power plant and are developing a 250kW natural gas fired power plant.

The electrolyte in this case is a specially engineered sulfonated fluorocarbon polymer, such as that produced by Du Pont (Nafion) and the Dow Chemical Company. The polymer on a molecular level, has a tubular structure in which the incorporated functional acid groups (SO_3^{2-}) are on the inner surface of the tubes and are capable of exchanging cations or anions. For fuel cell use the polymer is saturated with water (about 20% by weight) to expand the structure. Hydrogen ions can then be conducted through the membrane which accumulate water molecules and thus water, too, is conducted through the membrane. The electrodes consist of finely divided platinum dispersed onto a porous support and the fuel cell operates at around 80°C.

The high tolerance of the SPFC to vibration, compared to other fuel cells, allows the SPFC to be designed into automobile applications. Corrosion problems are minimised in the SPFC, with low operating temperatures and water as the only liquid present in the system. The SPFC, however, suffers from the high cost of the polymer membrane and the relatively high platinum loadings used to ensure high current densities. The problems of water management are still to be fully resolved, where on the anode side there can be a dehydration effect reducing the ionic conductivity, and at the cathode the water flux must be removed efficiently to prevent flooding of the cathode. In addition, the cells are poisoned by relatively low concentrations of CO, although they are able to recover when gas free from CO is passed. Despite the draw backs there are a number of groups around the world working with polymer membrane powered automobiles, e.g. Daimler-Benz and Ballard have just signed an agreement to invest over $450 million to develop efficient and clean engines for automobiles using Ballard fuel cells. Ballard SPFC's have also featured in 6 commercial buses delivered to Chicago and Vancouver during 1997 and General Motors are also developing a Ballard SPFC

powered vehicle. Similarly, the Toyota Motor Corporation have demonstrated a sports utility vehicle, "RAV4", using an in-house designed SPFC [7, 8].

A small mention must be made here of the direct methanol fuel cell (DMFC). Methanol is the ideal fuel for fuel cell systems, especially for electric vehicles. Methanol is a relatively cheap liquid and can be produced on a large scale from fossil fuels, making it more suitable as a fuel for transportation purposes. Although studies on acid electrolyte based fuel cells have been performed, it is the work on the polymer membrane fuel cells that have recently received much attention. The proton conducting membrane Nafion is normally used, with large amounts of noble metal as catalysts in each electrode. At the anode the methanol oxidation can be written as:

$$CH_3OH + H_2O \rightarrow CO_2 + 6H^+ + 6e^- \qquad 2.1$$

Unfortunately, the Nafion membrane is permeable to methanol which ultimately lowers the efficiency of the fuel cell and the expensive catalysts can be poisoned by methanol and other products resulting from the oxidation. Coupled with the relatively low power densities that are obtained using methanol because of high polarisation losses at the anode, development of the DMFC has remained limited.

2.7. Molten Carbonate Fuel Cell (MCFC)

The molten carbonate fuel cell is one of the two high temperature fuel cells currently under development. It has been intensively studied for the past two decades but has not developed as fast as the PAFC because of some fundamental materials problems. Nonetheless, in 1993 the Energy Research Corporation in the USA tested a 120kW stack successfully and a demonstration 1.8MW power plant has been operated since 1996, using natural gas. The MC Power Corporation, also in the US, is in the process of demonstrating a 250kW stack at Miramar. Similar scaled projects are also on-going in Japan and Europe but it is thought commercialisation will be delayed until the materials problems listed below, can be solved.

The MCFC incorporates a molten salt electrolyte consisting of K_2CO_3-Li_2CO_3, which is immobilised in a porous lithium aluminate ceramic matrix. The electrolyte conducts CO_3^{2-} ions, operating at temperatures of 650°C. This high temperature allows internal reforming of hydrocarbon fuels, which reduce the cost of expensive peripheral equipment and serves to increase the efficiency of the fuel cell. The high temperature also accelerates chemical and physical processes and allows the cheaper nickel electrocatalysts to be used in preference to the noble metals. The MCFC is thus insensitive to CO_2 and CO, which poison the noble metal catalysts, a common feature of the low temperature fuel cells.

The cathode is based on a porous NiO, over which are passed O_2 and CO_2, which combine with electrons from the external circuit to form the carbonate ions. At the anode, the carbonate ions react with the internally reformed fossil fuel to produce water and CO_2. To ensure that the electrolyte composition remains constant, the CO_2 produced at the anode must be recycled back to the cathode, requiring a CO_2 separation device. This adds to the complexity and expense of the system. The anode is based on porous nickel, with small additions of chromium oxide and alumina to control the sintering and dimensional stability.

Working at lower temperatures compared to the solid oxide fuel cell (see section 2.8), the MCFC has lower efficiency losses ($\Delta G/\Delta H$) and can thus achieve higher open circuit voltages. The valuable waste heat can be used for co-generation purposes, or for reforming fuel such as methane. The major disadvantages of the MCFC are the reactions of the cathode and bipolar plate material with the molten electrolyte. The cathode is slowly dissolved in the electrolyte, eventually leading to short circuiting, while the bipolar plate must be manufactured from expensive, corrosion resistant stainless steels. The MCFC is also sensitive to sulphur impurities in the fuel and oxidant gas streams and these must be removed prior to use. Coupled with the problem of recycling the CO_2, the MCFC arguably offers the greatest challenge of all the fuel cells to the materials engineer, to achieve full commercialisation.

2.8. Solid Oxide Fuel Cell (SOFC)

The development of the SOFC is a little behind that of the MCFC but shows great promise for power generation in utility and industrial applications. The SOFC demonstrates many advantages over the existing fuel cells and has consequently received attention from many research groups around the world. Westinghouse Electric Corp. are now the leading company for the commercialisation of the SOFC, with their tubular design (discussed in section 3.5.1.). Currently, 100kW demonstration units are being evaluated both at Westinghouse and in the Netherlands, for on-site power generation using natural gas. Scale-up to megawatt power systems is the next goal, with commercialisation targeted for early next century. SOFC development is also prevalent in Europe, Japan and Australia [9], with the planar design producing durable 10kW prototype stacks and plans to scale up to 100kW and megawatt power systems over the next decade.

The SOFC is an all ceramic electrolyte that operates at temperatures of 800-1000°C. The use of solid electrolytes eliminates corrosion and electrolyte management problems. Similar to the MCFC, the high operating temperatures allow cheaper electrocatalyst materials, with the possibility of co-generation and internal reforming of hydrocarbon fuels. The electrolyte is normally very stable under cell operation with no compositional changes across the electrolyte. The SOFC is tolerant to many fuel gases and impurities, removing any complicating separation systems and there are no problems of flooding or catalyst wetting, which are present in the SPFC.

The main disadvantages of the SOFC at present are the high cost of the ceramic materials, which are required at the high operating temperatures and the problems of sealing and balance of plant equipment, such as pumps and gas piping. A more detailed discussion of the materials used and engineering aspects of the SOFC are included in the next chapter. The discussions in this thesis will be concerned with this class of fuel cell.

References

1. Fuel Cell Systems. Eds. L.J.M.J.Blomen and M.Mugerwa. Plenum Press, New York, 1993.
2. W.R.Grove. Philos.Mag. **14**, (1839), 127.
3. Fuel Cell Handbook. Eds. A.J.Appleby and F.R.Foulkes. Van Nostrand Reinhold, New York, 1989.
4. T.F.Fuller. Interface. **6**, 3, (1997), 26.
5. J.A.Lane. Ph.D. Thesis. University of London, 1995.
6. Fuel Cells and Their Applications. Eds. K.Kordesch and G.Simader. VCH, Weinheim and New York, 1996.
7. Fuel Cells UK Newsletter. Ed. W.Capstick. **4**, (1997), 1.
8. C.E.Borroni-Bird. J.Power Sources. **61**, (1996), 33.
9. S.P.S.Badwal and K.Foger. ISSI Letters. **8**, 1, (1997), 6.

Chapter 3. Solid Oxide Fuel Cells

3.1. Introduction

The SOFC was introduced in chapter 2 as arguably, the most promising fuel cell for the commercial power generation markets. Like all fuel cells, the SOFC is able to produce electricity much more efficiently than conventional heat engines, which directly burn the fuel and are thus limited by the Carnot cycle [1, 2]. By chemically converting the fuel, a fuel cell can theoretically achieve very high efficiencies but in practice the efficiency of an SOFC does not exceed 50-55% because of a number of losses [3]. These losses will be considered in more depth in section 3.3.

At present, all SOFC prototype stacks are based on a stabilised zirconia electrolyte, usually stabilised by additions of yttria (YSZ) [2]. To achieve acceptable ionic conductivity, the operating temperature of the cell is determined by the choice of electrolyte and currently ranges between 800-1000°C, depending upon the thickness of the electrolyte [4, 5]. The high operating temperature of the SOFC creates considerable material selection problems and alternative electrolytes are under consideration, in an attempt to reduce the operating temperature to between 500°C and 700°C [6, 7]. These include gadolinia doped ceria (CGO) and doped lanthanum gallate ($La_{0.8}Sr_{0.2}Ga_{0.9}Mg_{0.1}O_3$). At lower temperatures it will be possible to use cheaper materials for the peripheral components of a SOFC system, such as the bipolar plate and ducting etc. and therefore greatly reduce the cost of the whole system [4, 8, 9].

The rest of this chapter will consider the various aspects of materials and design of the SOFC. It is important to remember that there are many other applications to which this technology can be used and some of the more important ones are discussed in the next chapter. It is believed, however, that the potential income from power generation is so large, that other applications of this technology will remain niche markets. The results presented in this thesis are aimed at improving the electrolyte in a SOFC.

3.2. Principles of Operation

The electrolyte in a SOFC conducts oxygen ions, created at the cathode by the reaction of oxygen in the oxidant gas and electrons from the external circuit. The oxygen ions migrate through the electrolyte to the anode, where they combine with hydrogen ions that have been oxidised from the fuel gas to produce water vapour. Electrons are released from the anode to the external circuit generating the direct current. Each cell is then electrically connected to another by an electronically conducting interconnect or bipolar plate, forming a stack to enable a useful power output. A schematic representation of an SOFC stack is illustrated in Fig.3.1.

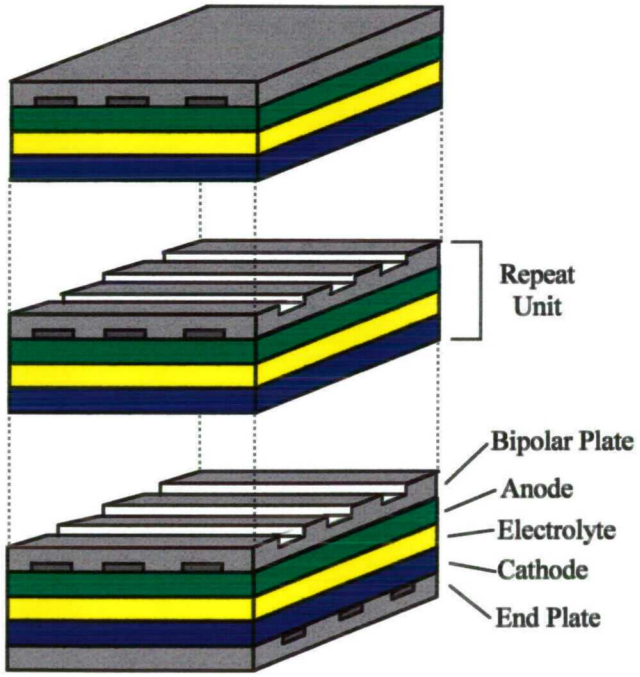


Fig.3.1. Schematic representation of an SOFC stack.

Pure hydrogen and oxygen achieve the highest efficiencies and cell voltages in a SOFC [2, 3], with the reaction at each electrode as follows:

$$\text{Cathode} \qquad \tfrac{1}{2}O_2 + 2e^- \rightarrow O^{2-} \qquad (3.1)$$

$$\text{Anode} \qquad H_2 \rightarrow 2H^+ + 2e^- \qquad (3.2)$$

Combining equations 3.1 and 3.2 the overall reaction for the fuel cell is obtained, which is simply the combination of hydrogen and oxygen to form water (equ.3.3).

$$\text{Overall} \qquad H_2 + \tfrac{1}{2}O_2 \rightarrow H_2O \qquad (3.3)$$

The driving force for the fuel cell is the oxygen partial pressure difference between the fuel and oxidant gas streams. At the cathode the oxygen partial pressure is around 0.2atm, while at the anode it is around 10^{-19}atm [10, 11]. The reversible open circuit voltage (E_{rev}) thus obtainable for the conversion of one mole of oxygen molecules is then given by the Nernst equation shown in equ.3.4.

$$E_{rev} = \frac{RT}{4F} \ln\left[\frac{(pO_2)_{Cathode}}{(pO_2)_{Anode}}\right] \qquad (3.4)$$

This equation gives an open circuit voltage of about 1V, but when a current is delivered the cell voltage decreases with increasing current, due to a number of internal losses which are discussed in the next section.

3.3. Efficiency and Polarisation Losses

The maximum efficiency of a combustion engine is determined by the ratio of the input to output heat as predicted by the Carnot theorem:

$$\text{Efficiency} = \frac{T_1 - T_2}{T_1} \qquad (3.5)$$

Where T_1 is the input heat temperature and T_2 the sink temperature. Clearly, for the highest efficiencies a high input temperature is needed and a low sink temperature. In practice, these temperatures are around 833K and 291K respectively, giving a maximum theoretical efficiency of 65%. In reality, the actual efficiency is around 46% because heat is lost to the surroundings. Even the most modern combined gas and

steam turbine (combined cycle) power stations, that operate at higher temperatures and recover some of the wasted heat, only have rated efficiencies around 55% [2].

To allow a comparison between the efficiency of a heat engine and a fuel cell, the relationship between the change in enthalpy, ΔH (i.e. the heat of combustion of the fuel) and the energy produced by the device, can be used:

$$\text{Efficiency} = \frac{\text{Energy Output}}{\Delta H} \tag{3.6}$$

For the ideal electrochemical cell all the free energy change, ΔG is available as electrical energy and thus the maximum energy conversion efficiency for a fuel cell at a specified temperature is given by equ.3.7.

$$\text{Efficiency} = \frac{\Delta G}{\Delta H} \tag{3.7}$$

By substituting for the common relationship

$$\Delta H = \Delta G + T\Delta S \tag{3.8}$$

where $T\Delta S$ is the reversible heat loss to the surroundings, it becomes clear that the maximum theoretical efficiency is a function of the system entropy loss when the reaction proceeds. These efficiencies are around 95% but vary slightly for different fuels and oxidants. The efficiency of a fuel cell thus decreases as the temperature of operation is increased, which is in contrast to that of a heat engine as demonstrated in Fig.3.2. It should be noted that the perfect heat engine operating at the maximum temperature limit allowed for the combustion of the fuel, would have the same efficiency as that of a perfect isothermal fuel cell using the same fuel and operating at the same sink temperature. The high input temperature needed severely limits the efficiency of the heat engine and in practice a much lower temperature has to be used as a result of material requirements. The fuel cell does not suffer from these limitations.

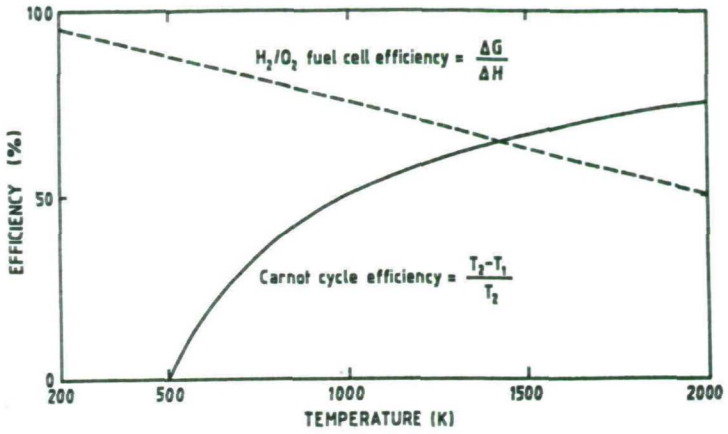


Fig.3.2. Effect of temperature on the efficiencies of heat engines and fuel cells [12].

As mentioned previously, the open circuit voltage of a fuel cell decreases as increasing current is drawn, because of a number of irreversible losses which reduce the working efficiency of a fuel cell. These losses are usually termed polarisation losses and result in heat losses within the cell. Fig.3.3 illustrates the effects of each polarisation, which are divided into ohmic (IR) and non-ohmic (η) polarisation losses and thus the cell voltage becomes

$$E_{cell} = E_{rev} - I(R_{ele} + R_a + R_c) - (\eta_{activation} + \eta_{concentration}) \qquad (3.9)$$

where R_{ele}, R_a and R_c are the electrical resistances of the electrolyte, anode and cathode respectively and E_{rev} is the open circuit voltage for the cell.

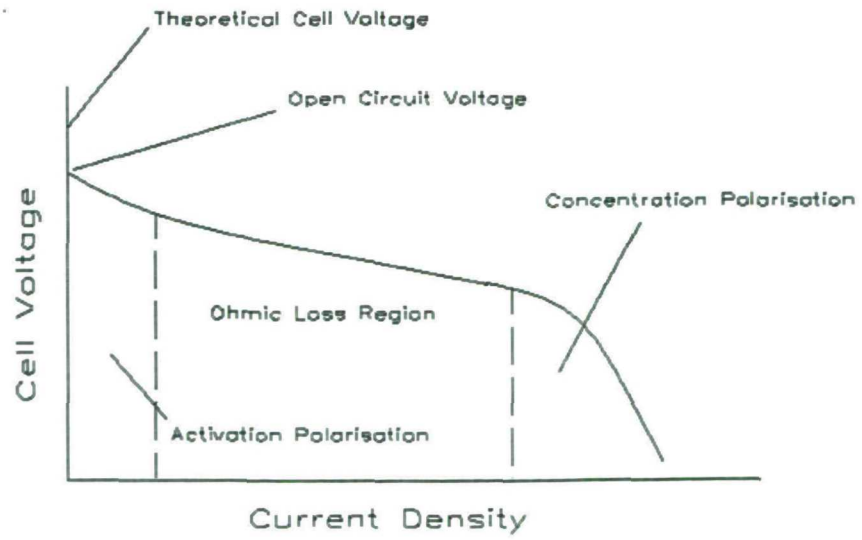


Fig.3.3. Typical voltage-current density characteristics for a SOFC.

The theoretical open circuit voltage (reversible voltage) is not attained even at zero current density in practice, due to a number of competing reaction losses. The exchange current density at the cathode is generally slow, allowing competing anodic reactions to lower the cell voltage by 0.1-0.2V.

The activation polarisation (η_a) is significant at low current densities and is a result of energy losses associated with the activation barriers that must be overcome at the electrodes, for the electrochemical reactions to proceed. Under open circuit conditions, all reactions are at equilibrium but when a current is drawn one reaction rate must dominate to provide the current flow. This requires a driving potential which is lost from the open circuit voltage. Increasing the electrode area or catalytic activity of the electrodes can reduce the activation polarisation.

The ohmic polarisation losses follow Ohm's Law and represent the energy losses due to the resistance of the electrolyte and electrodes to the flow of ions and electrons. Increasing the current increases the energy loss, which is dissipated as heat. By choosing materials with high conductivities the ohmic polarisations can be limited.

Concentration polarisations (η_c) become significant at high current densities when the mass transport of reactants to, or products away from the active sites of the electrodes is slower than the rate required to sustain the electric current. In the extreme, it is possible for the cell to reach a limiting value where no more current can be drawn. In practice, a sufficient supply of fuel and oxidant gases are needed and a potential is required to drive the reactants to the reactive sites, which again lowers the cell voltage. Increasing the reactant surface area by using porous electrodes with a fine particle size can reduce the concentration polarisation. In operational high temperature SOFC's, the polarisation curve is approximately linear and the effects of concentration polarisation can usually be neglected.

Increasing the temperature of operation of a fuel cell lowers the theoretical open circuit voltage but in practice a fuel cell delivers a current which is then affected by the polarisation losses discussed above. As the temperature increases, ions become more mobile and diffusion rates increase and thus the losses due to electrical resistance and

polarisation tend to decrease. The result is a decrease in open circuit voltage but also a decrease in internal resistances as the temperature increases. Hence the maximum power output of a fuel cell tends to increase with increasing temperature.

3.4. Cell Components

The SOFC comprises of four components, the electrolyte, two electrodes (the anode and cathode) and the interconnect or bipolar plate. These form a single unit which is repeated until a stack with the required power output is achieved. All components must be thermally, mechanically and chemically compatible with each other at the high operating temperature and each must perform a different function, as described below.

3.4.1. The Anode

The choice of material for the anode in all practical SOFC's has been restricted to a Ni-YSZ cermet. This material provides adequate properties and a polarisation resistance somewhat less than that of the cathode. For this reason, the transport mechanisms in operation at the anode are much less well understood.

The primary requirements of the anode, are to remain stable in the reducing atmosphere of around 10^{-19}atm that is present on the fuel side and to act as a catalyst for the oxidation and adsorption of the hydrogen molecules, which can then combine with the oxygen ions. The anode must also be an electronic conductor to facilitate the collection and transport of electrons to the external circuit.

Metals have high electronic conductivities and are generally stable in reducing conditions. Metals, therefore, appear to be candidate anode materials, but due to poorly matching thermal expansion coefficients to the zirconia electrolyte, it has been necessary to combine a metal with zirconia to improve the matching of the anode and electrolyte. Zirconia is one of the few oxide ceramics that is stable in a reducing environment. The metal must also act as a catalyst for the electrochemical reaction, which narrows the choice of metal, and so far nickel has been the best option, fulfilling

all of the above criteria at a lower cost to the alternative metals, Pt, Pd, Ru and Co. Nickel can readily adsorb hydrogen, which is then able to migrate across the surface of the nickel particles towards the electrolyte.

The concentration of nickel in the cermet has to be high enough to allow a complete electrical path through the anode but low enough to avoid problems with mechanical stresses from the thermal mismatch with the electrolyte, which can lead to cracking. In practice a 1:1 ratio of metal to ceramic is used. The anode is made porous to allow the hydrogen gas to reach the electrolyte and the nickel is dispersed as fine particles to increase the catalytic surface area. A benefit of the ceramic present is that it prevents the coarsening of the nickel particles at high temperatures and thus maintains the catalytic area. In practice nickel oxide is usually added to YSZ and under the reducing fuel conditions the nickel is reduced to the metal.

A potential problem with the Ni-YSZ anodes is the deposition of carbon during the internal steam reforming of hydrocarbon fuels. It is thought that the use of conducting oxide anodes instead of Ni can reduce the amount of carbon deposition [13].

Alternative anodes are now being researched for use in the lower temperature SOFC systems. Watanabe [5] used samaria doped ceria loaded with a very small quantity of noble metal and achieved a large decrease in polarisation resistance. A Ni-Ce(M)O_2 cermet is being studied for use with ceria electrolytes to allow a good thermal matching [7]. Pure ceria anodes have also been considered for electrochemical production of certain chemicals [14]. Other anodes based on perovskite structured oxides which are both protonic and electronic conductors are also under consideration, e.g. $SrCeO_3$, $BaCeO_3$, $CaZrO_3$, $SrZrO_3$ [15] and $LaYO_3$ [16]. Doping on either the A or B sites can lead to increased ionic conductivity, while doping with variable valence cations (Fe) introduces electronic conductivity. These ceramics suffer from large differences in the thermal expansion coefficient compared to the electrolyte and can lead to cracking. The stability of these ceramics is not certain in reducing atmospheres and thus the use of these alternative anodes may be limited.

3.4.2. The Electrolyte

From a scientific viewpoint, the electrolyte is the key component of all fuel cells. The electrolyte separates the oxygen and the hydrogen from the feed gases and facilitates the migration of one of these species to a chemical reaction at the surface and production of an electric current. From an electrochemical viewpoint, the conduction mechanisms of the current carrying species within the electrolyte are much better understood compared to the interfacial reactions. Consequently, the interfacial reactions within a fuel cell remain the rate limiting steps.

The key requirements for the electrolyte include a high ionic electrical conductivity and a good stability to the reducing environments experienced within a fuel cell. Electronic conductivity in the electrolyte causes short circuiting and a lowering of the fuel cell efficiency. The electrolyte must have a high density to prevent permeation of gases through the electrolyte via pores, which can again lower operating efficiencies, and should demonstrate chemical stability with the anode and cathode during fabrication and operation. All components within a fuel cell must also have closely matched thermal expansion coefficients to prevent cracking and delamination during heating cycles.

Section 3.3 showed that by lowering the operating temperature of a fuel cell, the maximum obtainable OCV increases. This becomes an important factor in the SOFC which currently runs at around 1000°C. The standard electrolyte used in most developed SOFC systems is based on a yttria stabilised zirconia (YSZ). To maintain the same resistance value in YSZ at lower operating temperatures, the thickness of the YSZ layer must be reduced. Steele [4] demonstrates that film thicknesses of 10-15μm are sufficient to operate a SOFC at around 700°C. Film thicknesses of this order are no longer self supporting and can lead to problems during fabrication of the electrolyte on the electrode (discussed in chapter 7). Thinner films are susceptible to gas permeation, which causes a substantial reduction in cell efficiencies.

Current YSZ thin films are operated at temperatures between 800-850°C [17, 18]. Lower temperatures are not possible because of the slower electrode kinetics involved

as the temperature decreases. It is desirable to operate SOFC's at lower temperatures, so that less expensive electrode and interconnect materials can be chosen. Lower temperatures also allow a wider selection of materials and fabrication routes. Combined with the lower cost of balance-of-plant materials (sealants, gas piping etc.), the overall cost and reliability of a SOFC system are considerably improved.

A second method that can be used to reduce the operating temperature of a SOFC is to chose a higher conductivity electrolyte material. Several materials exhibit higher conductivities compared to YSZ, including δ-Bi_2O_3, $Ce(Gd)O_2$ and $La(Sr)Ga(Mg)O_3$. A number of proton conducting electrolytes have also been studied, e.g. $BaCe(Gd)O_3$, but are unlikely to be used in a SOFC due to their mixed conducting nature [15, 19].

Ceria based electrolytes should be operable at temperatures of 500-700°C [11, 20], which would allow the use of relatively cheap ferritic stainless steel for the bipolar plate and thus significantly reduced costs. However, the reducibility of ceria on the fuel side of an SOFC leads to the introduction of electronic carriers, which lower the OCV and thus the efficiency of the SOFC [21]. An additional problem associated with temperatures below 700°C is the significant contribution of grain boundary resistances within the electrolyte and a large part of this thesis is aimed at reducing grain boundary resistances [22]. A more in-depth discussion of the various electrolyte materials can be found in chapters 5 & 6. A further problem at these lower temperatures is reducing the polarisation losses at the electrodes, especially the cathode, but it is hoped that novel electrodes will be found as research is intensified into lower operating temperature SOFC systems.

3.4.3. The Cathode

The polarisation losses at the cathode side of the SOFC are higher than those on the anode side, due to the greater energy barrier for the reduction of oxygen [23]. The most significant improvements in the SOFC can thus be made by improving the cathode kinetics and consequently, a great deal of research has concentrated on the cathode.

The cathode requires a number of functions similar to those of the anode, i.e. similar thermal expansion coefficient to the electrolyte, high electronic conductivity, chemical stability and, of course, moderate cost. The cathode must also be stable in oxidising atmospheres at the high temperatures experienced within the SOFC and show catalytic behaviour for the reduction of oxygen, thus only noble metals such as Pt, Pd, Ag and electronically conducting oxides are suitable. The noble metals are too expensive for use as cathode materials and in the case of silver, its lack of stability at high temperatures is a problem. The electronically conducting oxides have therefore been the only available choice of material, with the perovskite family being the most widely studied. The cathode is made with 30-40% porosity to allow sufficient catalytically active surface area for the reduction of oxygen.

The cathode material used in most SOFC's is a strontium doped lanthanum manganate, La(Sr)MnO_3 [1]. In oxidising atmospheres, an oxygen excess is apparent in the $LaMnO_3$ lattice, which decreases as the temperature increases. The result is the formation of cation vacancies in the lattice. The formation of cation vacancies requires the creation of positive holes to maintain the charge neutrality within the lattice and hence p-type conductivity is exhibited in the oxide. Strontium doping [24] on the A-site enhances the electronic conductivity by creation of more positive holes to compensate for the Sr^{2+} ions in the lattice, according to equation 3.10.

$$SrMnO_3 \xrightarrow{LaMnO_3} Sr'_{La} + Mn^{\times}_{Mn} + 3O^{\times}_{O} + h^{\bullet} \qquad (3.10)$$

The electronic conductivity increases with strontium content but is usually restricted to between 15-30mol% because of an increase in thermal expansion coefficient.

The fabrication temperature of the cathode must be below 1200°C, because of the formation of insulating phases from the reaction of the electrolyte and cathode at high temperatures, forming $SrZrO_3$ [25] and $La_2Zr_2O_7$ [26]. These phases can form due to the high mobility of the Mn ion but can be reduced by preparing lanthanum deficient $LaMnO_3$.

There is still no ideal cathode material for use with YSZ [27], however, the substitution of La with Ca in $LaMnO_3$ has been shown to reduce the thermal expansion coefficient and leads to a closer matching with the YSZ electrolyte. Substitution of Co for Mn on the B-site increases the electronic conductivity but the cobalt is much less stable in oxidising atmospheres and will readily react with the YSZ. At lower operating temperatures, a much greater range of cathode compositions appear stable, especially when using a ceria electrolyte, because phases such as $La_2Ce_2O_7$ are not thermodynamically stable.

Cathodes based on LSM reduce oxygen at locations where the oxygen, electrolyte and cathode are in intimate contact. These positions of intimate contact have been termed as three phase boundaries. It is thought that the ideal cathode material needs both high electronic and ionic conductivity, as it appears easier to inject oxygen ions into the electrolyte compared to the standard cathodes that rely only on three phase boundary contacts. $LaCoO_3$ is such a cathode material because the Co content increases the catalytic activity of the perovskite compared to the manganese doped material [28]. Lanthanum cobaltate has a large thermal expansion coefficient and is unlikely to be used with YSZ electrolytes but it may be used with ceria electrolytes, where its lower chemical stability is less important due to the lower operating temperatures. It has been shown that $LaCoO_3$, doped with Sr and Fe (LSCF) to improve the electronic and ionic conductivities ($La_{0.6}Sr_{0.4}Fe_{0.8}Co_{0.2}O_3$), is stable in contact with ceria and exhibits a very low electrode resistivity ($0.2\Omega cm^2$) at temperatures of 700°C [23]. This material is not suitable for temperatures below 700°C and alternative materials are required. Krumpelt [29] has proposed an Ag-yttria doped Bi_2O_3 cermet, which is reported to have a resistance lower than the CGO electrolyte at 600°C. Research into other cathode materials remains limited due to the high demands imposed on the cathode and much work is now concentrated on the fabrication processes of the existing cathode materials.

3.4.4. The Interconnect or Bipolar Plate

The interconnect or bipolar plate has the most stringent requirements of all the fuel cell components, with its main functions being that of current collector and gas separator.

The interconnect is usually the thickest component in a stack and often provides the mechanical support for each cell. Small grooves in the interconnect are used in some stack designs to provide pathways for the feed gases to flow along, exposing the interconnect to both oxidising (0.2atm) and reducing (10^{-19}atm) atmospheres at the high operating temperatures of the SOFC. A good electronic conductivity is required for current collection and a negligible ionic conductivity is necessary to prevent short circuiting and a reduction in cell efficiency. The interconnect must be sintered to a high density to prevent gas transport through pores to either side of the cell, which will again lower cell efficiencies. Chemical stability with the anode and cathode is needed, as well as closely matching thermal expansion coefficients to prevent cell cracking. In addition, moderate material and processing costs are desirable. A high thermal conductivity is also needed to aid heat flow from the cathode to the anode, where an endothermic reaction occurs, in order to produce an even temperature distribution in the stack. These are some of the greatest demands placed on any material and it is not surprising that there are only a few candidate materials for the interconnect.

The material choice depends on the temperature of operation and for most SOFC systems this is around 1000°C. At this high temperature there is no ideal material but the most commonly used interconnect is based on the perovskite, $LaCrO_3$. Lanthanum chromate is sufficiently stable over the entire range of oxygen partial pressures (0.2 – 10^{-19}atm), and is chemically compatible with the electrode materials [30, 31]. Recent reports concerning oxygen diffusivity, have suggested that the permeation of oxygen through this material is not as low as at first thought [32]. Oxygen leakage currents as high as 0.3A have been calculated under SOFC operating conditions which can lead to serious problems. Kawada [33] studying $La_{0.7}Ca_{0.3}CrO_3$, demonstrated the existence of fast oxygen diffusion pathways along grain boundaries, which would significantly contribute to the increased oxygen fluxes observed. Additionally, $LaCrO_3$ has a small thermal expansion coefficient and undergoes a phase transformation between 240-280°C, which leads to further thermal expansion mismatch [34]. Some of these problems can be solved by the correct choice of dopant, as will be discussed below.

The electronic conductivity in $LaCrO_3$ arises from holes in the 3d band of the chromium ions, producing a p-type conductor. For sufficient conductivity to operate in

a SOFC, doping on either the A or B-sites is necessary. In oxidising atmospheres, charge compensating holes are created when doping with divalent ions (Sr, Ca, Mg). However, in highly reducing atmospheres charge compensation occurs by the creation of oxygen vacancies [35]. This leads to a concentration gradient across the material in a SOFC, however, the total conductivity is still thought to be sufficient for SOFC use.

Mg doping gives the most stable doped material but Mg does not alter the phase transition temperature or the thermal expansion coefficient and as a consequence Ca and Sr doping have been studied recently [36]. Strontium doping lowers the phase transformation temperature, stabilising the rhombohedral phase down to room temperature, and also achieves a higher electronic conductivity compared to Mg doping. Also, as the Sr concentration increases, the thermal expansion coefficient increases and exact matching to the electrolyte can be achieved [30]. Calcium doping attains similar results to that of Sr but the phase transition temperature is increased.

The main problem with $LaCrO_3$ is its poor sinterability. High density is obtained only at temperatures around 1700°C in reducing atmospheres and is attributed to the high volatility of chromium when sintering in air [37]. As the sintering proceeds via an evaporation-condensation method, there is little material diffusion from the bulk of the grains and the highly volatile chromium produces thin films of Cr_2O_3 on the grain surfaces. The resulting material thus densifies very slowly. A number of techniques have been used to lower the sintering temperature of doped $LaCrO_3$, and are reviewed by Minh [1]. Both Sr but more significantly Ca doping in chromium deficient $LaCrO_3$, can allow a certain degree of liquid phase sintering [38, 39], forming a Ca-Cr-O liquid, but it is thought that Ca doped material can degrade in reducing atmospheres and displays poor high temperature mechanical properties. Other methods include: use of highly reactive powders with very high surface areas [40], dopants which introduce vacancies, allowing bulk material transport and liquid phase sintering aids, e.g. MgF_2 [41], although the stability of the liquid phase under SOFC operating conditions is questionable.

Alternative ceramic materials are very limited and only $YCrO_3$ [42] has been studied recently, as it shows greater stability to reduction in the fuel cell environment

compared to $LaCrO_3$. If the temperature of operation is lowered to between 700-850°C, a number of metal alloys can be used, all of which have high Cr contents for corrosion resistance, including Haynes 230 and Inconnel 600. Metals have the advantage of easy fabrication, high thermal conductivity and relatively low cost. At even lower temperatures (500-700°C), the use of ferritic stainless steels is possible, reducing the cost further. The main problems with these alloys are the large thermal expansion mismatch to the cell materials, uncertainty over the corrosion resistance and the formation of oxide scales, which introduce a high contact resistance between the electrodes. It is thought that a protective LSM coating can be used to significantly decrease the contact resistances [43].

3.4.5. Interlayers

The advantage of applying very thin layers between the electrolyte and electrodes to reduce the polarisation resistances has been a recent discovery. The use of 1-2μm layers of YSZ have been employed on CGO electrolytes to prevent reduction of ceria on the anode side of an SOFC [8, 11, 44, 45]. It has since been found that very thin layers (0.2μm) of Ce(Y or Sm)O_2 on both the anode and cathode side of a YSZ electrolyte dramatically improves the conductivity across the cell [9, 46, 47, 48]. Although extra layers require additional processing steps, the advantages that can be gained may out-weigh these additional costs and may become insignificant as cheaper, mass production techniques are adopted. As thinner cell components are possible, it looks likely that these interlayers will play an important role in the success of the lower temperature SOFC's.

3.4.6. Balance-of-Plant Materials

When designing a fuel cell system, the majority of the total cost is made up of the materials which encase the fuel cell stacks and provide the gases to the cells. The exact compositions of sealants and piping etc. are normally proprietary information and thus it is not possible to give a definitive account of the materials used. This section aims at providing a brief account of the balance-of-plant materials needed in a

complete SOFC system and where possible, the class of materials being studied for each component.

At 1000°C the gas piping, manifolds, heat exchangers, pumps and casing material require expensive superalloys or ceramic components. Ceramics are usually difficult to form into complex shapes and thus piping etc. can become expensive. Sealants can also be a major problem in some designs. Glass, ceramic and glass-ceramic seals are all being considered, such as the CaO-Al_2O_3-B_2O_3-SiO_2 system [4]. There are doubts about the reactivity of these materials with the cell components and their long term stability under operating conditions. At lower temperatures these problems are expected to be lessened. The manifolds in some designs are made from a ceramic Al_2O_3-MgO spinel structure [49], while the casing would be lined with an insulator such as Saffil.

At temperatures below 850°C the relatively cheap stainless steels can be used for piping, heat exchanger, pumps etc. Metals are far easier to shape and piping is widely available, providing significant improvements in the overall cost of an SOFC system.

3.5. SOFC Stack Designs

There are three main designs of SOFC stacks, which have various advantages and disadvantages over the others but at present it is not clear which of the designs will eventually be successful on the commercial markets. A brief summary of each design is given below.

3.5.1. Tubular

The tubular SOFC is by far the most technologically advanced of the various designs, helped by large investment from the US government and significant materials processing advances made by Westinghouse Electric Corporation. The Westinghouse tubular SOFC is constructed from a number of tubes between 0.5-1.5m in length, which consist of the cell components (Fig.3.4). The tubes are sealed at one end, which

eliminates the need for sealants and a ceramic heat exchanger reduces the exhaust gas temperature to about 850°C, allowing the use of stainless steel for peripheral equipment. An extrusion sintered porous air electrode (LSM), with an internal diameter between 12-20mm and a wall thickness around 2.5mm, acts as the support for the other components. The only expensive and slow step in the process is the electrochemical vapour deposition (EVD) of a 40μm thick, dense layer of YSZ along the tube, with a 9mm strip masked off along the length of the tube. A strip of magnesium doped lanthanum chromate is then plasma sprayed into the masked area to form a 40μm thick impermeable layer to act as the interconnect. The final step is a slurry deposition and sinter of a porous Ni-YSZ cermet for the anode. Careful masking is used to prevent contact of the anode and interconnect material, to avoid short circuiting in the cell.

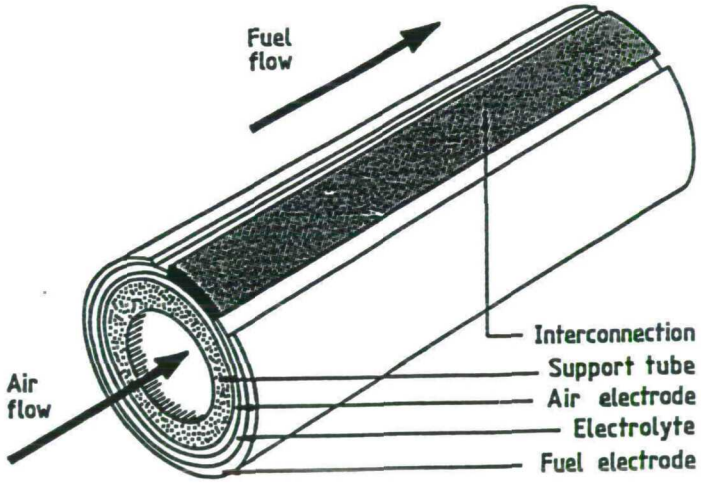


Fig.3.4. The Westinghouse tubular SOFC [3].

Each tube is then connected in series and parallel to other tubes to form a bundle. Nickel felt is used to make the connections, providing a soft compliant contact between tubes, minimising the stresses on the tubes. The connections also allow stack operation even when an individual cell fails. Air is fed inside each tube via injector tubes to the closed end so that it flows back to the open end, while the fuel gas is passed on the outside from the closed end to the open end. The depleted fuel and oxidant gases are combusted at the exhaust and the heat is used to heat the incoming gases.

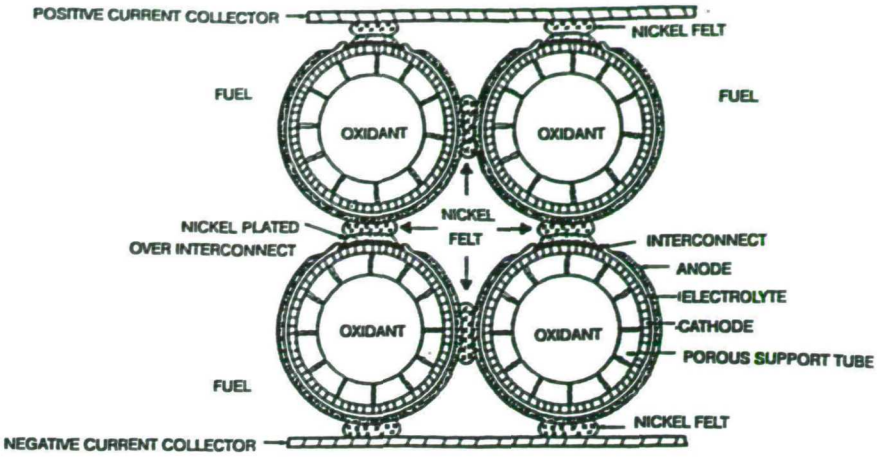


Fig.3.5. The Westinghouse tubular SOFC stack [1].

The main drawbacks of this design are the costly and time consuming electrolyte deposition step, large ohmic resistive losses due to the long current path lengths along the tubes and the lower power density of this design compared to the other designs. This design is closest to commercialisation and solutions to these problems are already being considered [50]. A 100kW power system is now being tested and has a size of 8m×3m×2.5m. Future plans are to combine the SOFC with a gas turbine to improve the efficiency, with a total power output of around 3MW. The SOFC is to be operated in a pressurised container to increase the power density and will have dimensions of 15m×11m×10m.

3.5.2. Planar or Flat Plate

The planar fuel cell components can be produced by tapecasting and other cheap, well established techniques, making it the simplest of the SOFC constructions and the most similar to all other fuel cell types. The power density is higher than that of the tubular design, because the in-plane conduction produces lower internal resistances, as it is independent of the cell area. The fabrication of the plates can be accomplished using simple mass production techniques. The electrolyte is normally 150-250μm thick, such that it is self supporting, and is prepared by tape casting or calendering [7, 51, 52, 53]. The dimensions of this plate can vary between 5cm×5cm to 25cm×25cm but the larger plates tend to suffer from warping, as the electrodes are sintered on top [54].

The YSZ electrolyte can either be sintered and then the electrodes applied and co-sintered, or the electrodes can by laid onto the green density electrolyte and co-sintered in one step [55]. The most common techniques for applying the electrodes (both LSM and Ni-YSZ) include screen printing [56], tape casting [57], slurry coating [58, 59] and plasma spraying [60, 61]. The electrodes are normally made thin to reduce the resistances in the cell.

The interconnect is fabricated separately by hot pressing [41] or tape casting [41, 62] and the stack is built up by placing components on top of one another. This preparation procedure allows each individual component to be inspected before incorporation into the stack. The interconnect is usual grooved on both sides to form gas channels for the fuel and oxidant gases, most commonly in a cross flow configuration. A typical planar SOFC design is shown in Fig.3.6.

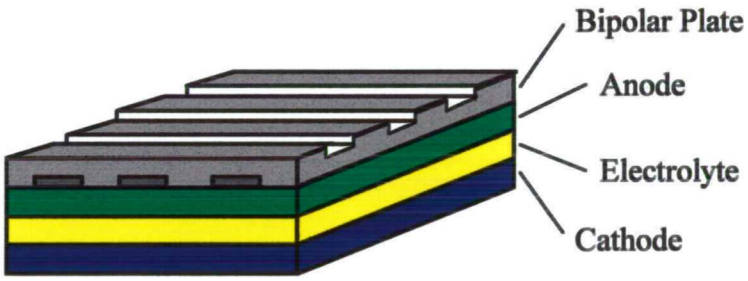


Fig.3.6. The planar SOFC configuration.

The main problem with the planar SOFC is the need for high temperature seals at the edges of the plates, as discussed in section 3.4.6. It is hoped that the operating temperature of the planar cell can be reduced by using thinner electrolyte layers and the better conducting doped ceria electrolytes, such that lower thermal stresses and better corrosion resistances are achieved. The planar design is also less stable to thermal and mechanical stresses compared to the tubular design, which will probably exclude the planar SOFC in automotive applications.

Currently, there are projects with powers ranging from around 1kW-20kW in operation with planar SOFC stacks. Siemens intend to build a 50kW stack and ultimately a

100kW demonstration plant over the next few years [18]. Small kW demonstration stacks are also being evaluated in Japan [63].

3.5.3. Monolithic Design

The monolithic SOFC (MSOFC) produces higher power densities than the other configurations and has been developed by Argonne National Laboratory. The stack consists of alternating layers of flat anode/interconnect/cathode plates and corrugated anode/electrolyte/cathode plates, which reduce the size of each cell. This design is unlikely to reach commercialisation due to problems producing the plates, associated with insufficient matching of thermal expansion during sintering [64].

References

1. N.Q.Minh. J.Am.Ceram.Soc. **76**, 3, (1993), 563.
2. D.H.Scott. IEA Coal Research, London, IEACR/59, 1993.
3. B.C.H. Steele. Encyclopedia of Advanced Materials. Ed. R.J.Brook. Pergamon Press. 1994, 885.
4. B.C.H. Steele. Proc. 1st European Solid Oxide Fuel Cell Forum. Eds. U.Bossel. (1994), 375.
5. M.Watanabe, H.Uchida, M.Shibata, N.Mochizuki, K.Amikura. J.Electrochem.Soc. **141**, 2, (1994), 342.
6. W.Bakker, C.Milliken, J.Hartvigsen, S.Elangovan and A.Khandkar. Proc. of the 5th International Symposium on SOFC's. Eds. U.Stimming, S.C.Singhal, H.Tagawa and W.Lehnert. The Electrochem.Soc. (1997), 254.
7. G.M.Christie and J.P.P.Huijsmans. Proc. of the 5th International Symposium on SOFC's. Eds. U.Stimming, S.C.Singhal, H.Tagawa and W.Lehnert. The Electrochem.Soc. (1997), 718.
8. S.P.S.Badwal. Proc. 1st European Solid Oxide Fuel Cell Forum. Ed. U.Bossel. (1994), 399.
9. S.A.Barnett. Energy. **15**, 1, (1990), 1.

10. J.A.Lane. Ph.D. Thesis. University of London, 1995.
11. H. Yahiro, Y. Baba, K. Eguchi and H. Arai. J.Electrochem. Soc. **135**, 8, (1988), 2077.
12. B.C.H.Steele. Electronic Ceramics. Ed. B.C.H.Steele. Elsevier Science Publishers LTD. 1991, 203.
13. G.M.Christie. Ph.D. Thesis. University of London, 1993.
14. B.C.H.Steele, P.H.Middleton and R.A.Rudkin. Solid State Ionics. **40/41**, (1990), 388.
15. R.A.De Souza. Ph.D. Thesis. University of London, 1996.
16. E.Ruiz-Trejo and J.A.Kilner. Proc. of the 17th Risø International Symposium on Materials Science. Eds. F.W.Poulsen, N.Bonanos, S.Linderoth, M.Mogensen and B.Zachan-Christiansen. (1996), 411.
17. S.De Souza, S.Visco and L.C. De Jonghe. Proc. of the 2nd European SOFC Forum. Ed. B.Thorstensen. (1996), 677.
18. H.J.Beie, L.Blum, W.Drenckhahn, H.Greiner, B.Rudolf and H.Schichl. Proc. of the 5th International Symposium on SOFC's. Eds. U.Stimming, S.C.Singhal, H.Tagawa and W.Lehnert. The Electrochem.Soc. (1997), 51.
19. N.Bonanos, B.Ellis and M.N.Mahmood. Solid State Ionics. **44**, (1991), 305.
20. T.J.Kirk and J.Winnick. J.Electrochem.Soc. **140**, 12, (1993), 3494.
21. P.N.Ross and T.G.Benjamin. J.Power Sources. **1**, (1977), 311.
22. J.M.Ralph and J.A.Kilner. Proc. of the 2nd European SOFC Forum. Ed. B.Thorstensen. (1996), 773.
23. T.Inoue, K.Eguchi, T.Setoguchi and H.Arai. Solid State Ionics. **40-41**, 1, (1990), 407.
24. J.H.Kuo, H.U.Anderson and D.M.Sparlin. J.Solid State Chem. **87**, (1990), 55.
25. O.Yamamoto, Y.Takeda, R.Kanno and M.Noda. Solid State Ionics. **22**, (1987), 241.
26. H.Taimatsu, K.Wada and H.Kaneko. J.Am.Ceram.Soc. **75**, 2, (1992), 401.
27. J.A.Lane, H.Fox, B.C.H.Steele and J.A.Kilner. Electroceramics: Production, Properties and Microstuctures. Eds. W.E.Lee and A.Bell. British Ceramics Proceedings. No.52, 1994.
28. J.Mizusaki, Y.Mima, S.Yamamuchi, K.Fueki and H.Tagawa. J.Solid State Chem. **80**, (1990), 69.

BIBL. LONDIN. UNIV.

29. R.Doshi, V.L.Richards and M.Krumpelt. Proc. of the 5th International Symposium on SOFC's. Eds. U.Stimming, S.C.Singhal, H.Tagawa and W.Lehnert. The Electrochem.Soc. (1997), 379.
30. S.Srilomsak, D.P.Schilling and H.U.Anderson. Proc. 1st International Symposium on SOFC's. Ed. S.C.Singhal. The Electrochem.Soc. (1989), 129.
31. I.Yasuda, K.Ogasawra and N.Hishinuma. Proc. of the 2nd International Symposium on Ionic and Mixed Conducting Ceramics. Eds. T.A.Ramanarayanan, W.L.Worrel and H.L.Tuller. The Electrochem.Soc. (1994), 164.
32. B.A.van Hassel, T.Kawada, N.Sakai, H.Yokokawa and M.Dokiya. Solid State Ionics. **66**, (1993), 41.
33. T.Kawada, T.Horita, N.Sakai, H.Yokokawa and M.Dokiya. Solid State Ionics. **79**, (1995), 201.
34. C.P.Khattak and D.E.Cox. Mat.Res.Bull. **12**, (1977), 463.
35. D.B.Meadowcroft. Brit.J.Appl.Phys. **2**, (1969), 1225.
36. B.K.Flandermeyer, M.M.Nasrallah, A.K.Agarwal and H.U.Anderson. J.Am.Ceram.Soc. **67**, (1984), 195.
37. L.Groupp and H.U.Anderson. J.Am.Ceram.Soc. **59**, (1976), 449.
38. L.A.Chick, J.L.Bates and G.D.Maupin. Proc. of the 2nd International Symposium on SOFC's. Eds. F.Gross, P.Zegers, S.C.Singhal and O.Yamamoto. Commision of the European Communities, (1991), 621.
39. N.Sakai, T.Kawada, H.Yokokawa M.Dokiya. Proc. of the 2nd International Symposium on SOFC's. Eds. F.Gross, P.Zegers, S.C.Singhal and O.Yamamoto. Commision of the European Communities, (1991), 629.
40. L.A.Chick, J.L.Bates, L.R.Pederson and H.E.Kissinger. Proc. of the 1st International Symposium on SOFC's. Ed. S.C.Singhal. The Electrochem.Soc. (1989), 170.
41. C.Milliken and A.Khandkar. Proc. of the 1st International Symposium on SOFC's. Ed. S.C.Singhal. The Electrochem.Soc. (1989), 361.
42. W.J.Weber, C.W.Griffin and J.B.Bates. J.Am.Ceram.Soc. **70**, (1987), 265.
43. B.Bruckner. Proc. of the 3rd International Symposium on SOFC's. Eds. S.C.Singhal and H.Iwahara. The Electrochem.Soc. (1993), 641.
44. T.Inoue, T.Setoguchi, K.Eguchi and H.Arai. Solid State Ionics. **35**, (1989), 285.
45. A.V.Virkar. J.Electrochem.Soc. **138**, 5, (1991), 1481.

46. C.C.Chen, M.M.Nasrallah and H.U.Anderson. J.Electrochem.Soc. **140**, 12, (1993), 3555.

47. P.Soral, U.Pal and W.L.Worrell. Proc. of the 5th International Symposium on SOFC's. Eds. U.Stimming, S.C.Singhal, H.Tagawa and W.Lehnert. The Electrochem.Soc. (1997), 264.

48. T.Tsai and S.A.Barnett. Proc. of the 5th International Symposium on SOFC's. Eds. U.Stimming, S.C.Singhal, H.Tagawa and W.Lehnert. The Electrochem.Soc. (1997), 274.

49. J.Heitzer, R.Späh and K.Zurell. Proc. of the 5th International Symposium on SOFC's. Eds. U.Stimming, S.C.Singhal, H.Tagawa and W.Lehnert. The Electrochem.Soc. (1997), 212.

50. S.C.Singhal. Proc. of the 5th International Symposium on SOFC's. Eds. U.Stimming, S.C.Singhal, H.Tagawa and W.Lehnert. The Electrochem.Soc. (1997), 37.

51. H.Takagi, H.Taira, S.Kobayashi, Y.Sugimoto, S.Sakamoto and K.Tomono. Proc. of the 3rd International Symposium on SOFC's. Eds. S.C.Singhal and H.Iwahara. The Electrochem.Soc. (1993), 738.

52. F.P.F. van Berkel, F.H. van Heuveln and J.J.P.Huijsman. Proc. of the 3rd International Symposium on SOFC's. Eds. S.C.Singhal and H.Iwahara. The Electrochem.Soc. (1993), 744.

53. K.Kendall. Proc. of the 3rd International Symposium on SOFC's. Eds. S.C.Singhal and H.Iwahara. The Electrochem.Soc. (1993), 813.

54. R.W.Steinbrech, A.Caron, G.Blaß and F.Dias. Proc. of the 5th International Symposium on SOFC's. Eds. U.Stimming, S.C.Singhal, H.Tagawa and W.Lehnert. The Electrochem.Soc. (1997), 727.

55. M.Shimotsu, M.Izumi and K.Murata. Proc. of the 3rd International Symposium on SOFC's. Eds. S.C.Singhal and H.Iwahara. The Electrochem.Soc. (1993), 732.

56. T.Hikita, M.Hishinuma, T.Kawashima, I.Yasuda, T.Koyama and Y.Matsuzaki. Proc. of the 3rd International Symposium on SOFC's. Eds. S.C.Singhal and H.Iwahara. The Electrochem.Soc. (1993), 714.

57. N.Christiansen, P.Gordes and H.Topsøe. Proc. of the 2nd International Symposium on SOFC's. Eds. F.Gross, P.Zegers, S.C.Singhal and O.Yamamoto. Commision of the European Communities, (1991), 495.

58. R.Yamaguchi, K.Hashimoto, H.Sakata, H.Kajiwara, K.Watanabe, T.Setoguchi, K.Eguchi and H.Aria. Proc. of the 3rd International Symposium on SOFC's. Eds. S.C.Singhal and H.Iwahara. The Electrochem.Soc. (1993), 704.

59. M.Shimotsu, M.Izumi and K.Murata. Proc. of the 3rd International Symposium on SOFC's. Eds. S.C.Singhal and H.Iwahara. The Electrochem.Soc. (1993), 732.

60. D.Stöver, R.Hecker, H.Jansen and W.Malléner. Proc. of the 3rd International Symposium on SOFC's. Eds. S.C.Singhal and H.Iwahara. The Electrochem.Soc. (1993), 215.

61. E.A.Barringer, D.P.Heitzenrater and M.R.Tharp. Proc. of the 3rd International Symposium on SOFC's. Eds. S.C.Singhal and H.Iwahara. The Electrochem.Soc. (1993), 771.

62. P.A.Lessing, L.W.Tai and K.A.Klemm. Proc. of the 1st International Symposium on SOFC's. Ed. S.C.Singhal. The Electrochem.Soc. (1989), 337.

63. Y.Sakaki, Y.Esaki, M.Hattori, H.Miyamoto, T.Satake, F.Nanjo, T.Matsudaira and K.Takenobu. Proc. of the 5th Int. Symposium on SOFC's. Eds. U.Stimming, S.C.Singhal, H.Tagawa and W.Lehnert. The Electrochem.Soc. (1997), 61.

64. S.Majumdar, T.Claar and B.Flandermeyer. J.Am.Ceram.Soc. **69**, (1986), 628.

Chapter 4. Associated Electrolyte Applications

4.1. Introduction

Although the SOFC is the target application for many research groups, there are a number of alternatives for this technology. These alternative applications are generally more simple in construction and operate under less harsh conditions and it is, therefore, expected that these devices will reach commercialisation before the SOFC. This chapter briefly summarises these alternative applications and the present status of each one's development. Progress in one or all of these devices could lead to improvements in the SOFC because these technologies are all very closely related.

4.2. Air Separation Membranes

The separation of oxygen from air is still an expensive and energy intensive process. Large scale production of oxygen is achieved via a cryogenic process, whereby oxygen is distilled from the rest of the air. There is at present no way of separating oxygen on a small scale without some residual gases remaining, as is the case for the pressure swing absorption method. When a SOFC is operated in the reverse manner, i.e. when a voltage is applied across the cells, oxygen is driven through the electrolyte to produce 100% pure oxygen.

There are two approaches, shown in Fig.4.1, that are under development for the separation of oxygen from air. The first uses a mixed conducting membrane such as the perovskite LSCF [1], whereby an oxygen partial pressure gradient across the membrane drives the oxygen through to the low P_{O_2} side. A simultaneous flow of electrons accompanies the oxygen flow but in the reverse direction, to supply the air side with the electrons for the reduction of the oxygen. The pure oxygen is then continuously removed in order to preserve the low P_{O_2}. This method is hindered by the mechanical stability of the thin film electrolyte under large pressure differentials [2].

A new approach is to produce dual phase materials, with an ionically conducting phase (e.g. YSZ) and an electronically conducting phase (e.g. Ag) intimately mixed [3]. Each phase is stable at the high temperatures and in the pressure gradient present.

The second method involves a purely ionically conducting electrolyte, such as doped zirconia or doped ceria. A d.c. current is driven through the membrane by an applied potential, transporting the oxygen from the air side to the other side of the electrolyte [2, 3]. The applied potential must be high enough to allow a sufficient flux of oxygen ions through the electrolyte but remain low enough to prevent the partial reduction of the electrolyte, which will reduce the efficiency. Mixed conducting electrodes such as LSCF are applied to both sides of the electrolyte to facilitate the supply of the current. The input gases are generally heated by the output gases and therefore a low operating temperature is desirable. Doped ceria is the most suitable material for these applications because it has a better matched thermal expansion coefficient to LSCF compared to that of zirconia.

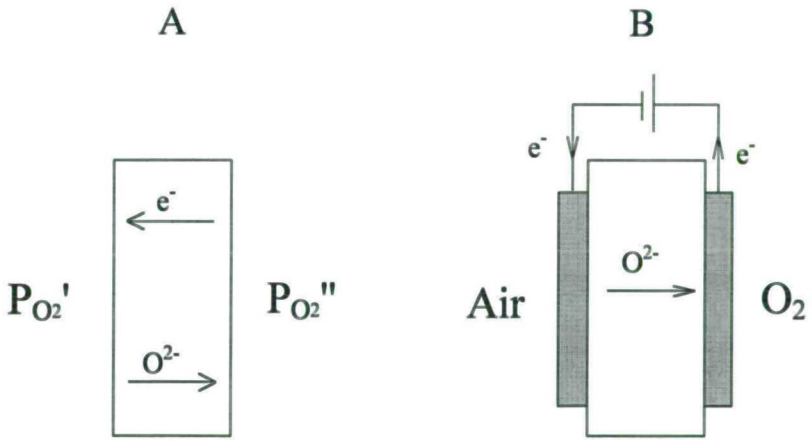


Fig.4.1. Ceramic oxygen separation membranes. a). Pressure driven system ($P_{O_2}'>P_{O_2}''$). b). Electrically driven system.

The electrically driven oxygen separation devices have the advantages of higher oxygen fluxes and smaller size compared to the pressure driven devices. The more complicated device structure, however, leads to some familiar problems such as materials compatibility, both chemically and thermally, at the high operating temperatures. The need for sealants in some designs further complicates the situation. It is thought that air separators are likely to reach the market before SOFC's and it is

hoped that this will stimulate the commercialisation of the low temperature SOFC systems. Industry, military and medical uses already exist for the production of pure oxygen and thus the future of the ceramic oxygen separation membrane already seems assured.

4.3. Oxygen Sensors/Probes

Oxygen sensors based on calcia stabilised zirconia (CSZ) are already used in a number of applications to measure and control the oxygen content in gases [4]. Platinum gauze electrodes are pressed onto the surface of the CSZ before sintering, with platinum wires used to connected the device to a high impedance voltmeter. These sensors are then used with 3-way catalysts to monitor the exhaust gas emissions from an automobile to control the fuel-to-air ratio in the so called lean burn engines [5]. At the correct ratio the engine has a higher efficiency and lower emissions compared to a conventional engine.

The platinum helps to catalyse the dissociation and recombination of oxygen at the electrodes. Air is passed over one side of the device as the reference gas, while the exhaust gas is passed over the opposite side. In this way a potential is developed across the electrolyte, according to equ.4.1.

$$E = \frac{RT}{4F} \ln\left(\frac{P_1}{P_2}\right) \qquad (4.1)$$

where $P_2 = 0.209$atm, P_1 is the unknown oxygen partial pressure, other symbols having their normal meaning.

By using a feedback loop and altering the fuel and air ratio, it is thus possible to keep the e.m.f. constant. The sensor is heated by the exhaust heat of the engine to achieve a conductivity that can be measured on a high impedance analyser. The input impedance of the analyser needs to be 100 times that of the cell for 1% precision [4]. Therefore, sensors with higher conductivities will permit greater precision in determining the lean

burn condition of the engine. Stable ceria electrolytes may then lead to improved engine efficiency compared to zirconia electrolytes.

Oxygen probes based on the same principle as the sensors are also used to monitor the oxygen content in solutions of molten metals, e.g. steels. The main requirement here is a good thermal shock resistance when the probe is immersed into the molten metal, qualities which both zirconia and ceria demonstrate.

4.4. Oxygen Pumps

Oxygen pumps are essentially the same as the electrically driven oxygen separation membranes, except that a potential is applied to the electrolyte to control the P_{O_2} within a closed atmosphere. Oxygen is pumped through the electrolyte to an air atmosphere. The use of oxygen pumps allows accurate control of the P_{O_2} over the entire P_{O_2} range, a feat which is not possible by mixing gases such as H_2 or CO. Some care has to be taken not to apply too high a potential, in order to prevent reduction of the electrolyte material which can lead to incorrect P_{O_2} measurements. Oxygen pumps find application in many laboratory based experiments where accurate control of oxygen partial pressure is required.

4.5. Water Electrolysers

The electrolysis of water (in the gaseous state) to produce pure oxygen and hydrogen is just another of the modified uses of the ceramic electrolyte, again operating in the reverse sense to that of the SOFC. A direct current is used to split the steam into pure oxygen (which diffuses through the electrolyte), and hydrogen/steam. If a ceramic proton conducting electrolyte were used (e.g. $SrCeO_3$), it would be possible to obtain pure hydrogen [6, 7].

4.6. Electrochemical Production of Industrial Gases

An increasingly important industrial use of SOFC like systems is in the production of useful chemicals through oxidation or partial oxidation of hydrocarbons [8]. By applying a potential across a typical SOFC cell, it is possible to convert methane into ethene or ethane via oxidative coupling. The potential controls the flow of the oxygen ions through the membrane to give a highly efficient conversion rate [9]. This technique can also be applied to a number of other situations, such as the oxidation of CO and the reduction of NO_X in automobile exhausts. It is also possible to produce the industrially useful syngas ($CO + H_2$). In all these applications electricity is also produced, which makes the production of industrially useful chemicals using ceramic membranes even more attractive.

It is also possible to use ceramic proton conducting membranes to produce these gases [10]. In this situation, non-oxidative coupling is used to reduce the number of hydrogen ions within the hydrocarbon, which are then transported through the membrane. The degree of electronic conductivity in these materials, however, may lower the efficiency of conversion, suggesting that the oxygen ion conducting membranes are more promising.

References

1. R.M.Thorogood, R.Srinivasan, T.F.Yu and M.P.Drake. U.S. Patent, 5,240,480 (31/8/1993).
2. B.C.H. Steele. Proc. of the 1st European Solid Oxide Fuel Cell Forum. Ed. U.Bossel. (1994), 375.
3. J.A.Kilner, S.J.Benson, J.A.Lane and D.Waller. Chemistry and Industry. Nov., (1997), 907.
4. Electroceramics: Materials, Properties and Applications. Eds. A.J.Moulson and J.M.Herbert. Chapman and Hall, London. 1990.

5. Physical Ceramics. Eds. Y-M.Chiang, D.Birnie and W.D.Kingery. John Wiley & Sons, Inc. 1997, 234.
6. H.Iwahara. Solid State Ionics. **77**, (1995), 289.
7. R.A.De Souza. Ph.D. Thesis. University of London, (1996), 40.
8. B.C.H.Steele, P.H.Middleton and R.A.Rudkin. Solid State Ionics. **40/41**, (1990), 388.
9. Y.Jiang, I.V.Yeutekakis and C.G.Vayenas. Science. **264**, 5165, (1994), 1563.
10. L.G.Tejuca, J.L.G.Fierro and J.M.D.Tascon. Adv. in Catalysis. **36**, (1989), 237.

Chapter 5. Electrolytes - Diffusion, Conductivity and Defect Chemistry

5.1. Introduction

The criteria for a good SOFC electrolyte, including physical and microstructural properties, are listed below:

- High ionic conductivity
- Ionic transference number close to one (t_{ion}=1), i.e. negligible electronic conductivity
- Stability in a range of oxygen partial pressures
- A large ionic domain, i.e. P(-)<10^{-19}atm at the operating temperature
- Chemical stability to electrode and bipolar plate or sealant material
- Suitably matched thermal expansion coefficients to other cell components
- Low protonic conductivity
- Good strength, so that thin supporting films are possible
- Thermal shock resistance during temperature cycling
- Low sintering temperature and ease of fabrication
- Reasonable cost

Materials of interest for SOFC electrolyte applications are based on fluorite (MO_2) or perovskite (ABO_3) related structures. Oxygen ion conduction proceeds through oxygen vacancies, which can be introduced into the structure by aliovalent doping, e.g. YSZ, CGO, LSGM. Alternatively, the structure may incorporate intrinsic oxygen ion conductivity, e.g. δ-Bi_2O_3, $A_2B_2O_7$ (pyrochlore) and $A_2B_2O_5$ (brownmillerite). Each of these structures are briefly reviewed, taking YSZ as the standard electrolyte material for comparison. It should be remembered, that the presence of anion vacancies in a structure can also introduce protonic conductivity, according to the reaction,

$$H_2O + V_O^{\bullet\bullet} \rightarrow O_O^X + 2H_i^{\bullet} \qquad (5.1)$$

The solubility of water in oxides and the subsequent generation of interstitial protons will also be briefly reviewed, concentrating on the perovskite and fluorite structures. The most important criteria for the electrolytes discussed in this chapter, are the mobility of the conducting oxygen ions and the contribution they make to the total conductivity. Therefore, it is necessary to develop an understanding of the defect chemistry present, and how the presence of defects effect the diffusion and conductivity of the oxygen ions, before a comparison can be made of the different electrolyte materials.

5.2. Defect Types

In an ideal crystal structure, ionic conduction is not possible. It is the presence of defects within a crystal that allows ions to move and constitute a current. The discussion below is concerned with only one type of defect, the *point defect*, because it is this type of defect that has a large influence on the mobility of ions in a crystal. There are a number of extended defects which can also be present and may contribute to the electrical and physical properties of a material, but their influence on electroceramics is not well documented. Line defects (one dimensional), such as dislocations, are present in all crystalline materials but they tend to play a more significant role in metals. Planar defects (two dimensional) include crystal surfaces and grain boundaries and can dramatically alter the total conductivity of a material. Planar defects will be discussed in more detail in the next chapter. Volume defects (three dimensional) consist of second phases and pores and are generally deleterious to electrical properties.

Point defects consist of the following types: Vacancies, interstitials, misplaced atoms, impurity/solute atoms and electronic defects. Vacancies describe a site, where an atom is missing from a normally occupied site. Interstitials are sites, where an atom is found on a normally unoccupied site. Misplaced atoms represent sites, where one type of atom is found at the site of another type. Impurity or solute atoms can occupy either interstitial sites or host atom sites, where they are described as substitutional. Electronic defects arise when sites possess a different charge from that present in the

ideal crystal and can result from the defects mentioned above, as well as from the creation of free electrons and electron-holes.

In a pure compound (MO), defects can be introduced into a lattice by two simple intrinsic disorder reactions, which maintain the stoichiometry of the crystal. The first is Schottky disorder, which is normally favoured in perovskite compounds [1],

$$"0" \leftrightarrow V_M^{"} + V_O^{\bullet\bullet} \qquad (5.2)$$

The second type is Frenkel disorder, which involves the formation of interstitial species. In the fluorite oxide structure, the formation of a cation interstitial requires considerably more energy than that of an anion interstitial and thus anti-Frenkel disorder is usually considered [2],

$$O_O^X \leftrightarrow O_i^{"} + V_O^{\bullet\bullet} \qquad (5.3)$$

Both of these reactions are temperature dependant but generally they only produce significantly high levels of defects at temperatures near to the melting point. Consequently, dopants are added to increase the defect concentrations at technologically important temperatures. In the fluorite oxides, density, x-ray diffraction and a number of other techniques have indicated that oxygen vacancies are favoured over oxygen interstitials at temperatures <1500°C [3] and thus aliovalent doping can give rise to two defect reactions. For dopants with an effective 2+ or 3+ charge, the reaction can be written as,

$$MO \xrightarrow{CeO_2} M_{Ce}^{"} + V_O^{\bullet\bullet} + O_O^X \qquad (5.4)$$

OR

$$M_2O_3 \xrightarrow{CeO_2} 2M_{Ce}^{'} + V_O^{\bullet\bullet} + 3O_O^X \qquad (5.5)$$

For dopants with 5+ or higher charge, the defect reaction introduces electronic defects into the lattice,

$$M_2O_5 \xrightarrow{CeO_2} 2M_{Ce}^{\bullet} + 2e' + 4O_O^X + \tfrac{1}{2}O_{2(g)} \qquad (5.6)$$

For electrolyte applications, the reactions in equations 5.4 and 5.5 are required. Defects can also be introduced into the crystal by deviation from stoichiometry at high temperatures, or different oxygen partial pressures. To understand the properties of these materials in different environments, a model must be used to describe the formation and change in concentration of these defect species. Usually, point defects can be treated as chemical species in solution in the crystal, as suggested by Wagner and Schottky [4]. The point defects are then assumed to obey the Law of Mass Action. Any normally occupied lattice position is assumed to have unit activity and the point defect activities are taken as their concentrations (mole fractions). Furthermore, the fugacity of oxygen gas is equal to its partial pressure. It is also assumed that charged defects are fully ionised, a fact that has been confirmed by Tuller [5] for oxygen vacancies in ceria. In describing defect reactions in ionic solids, the defect equations must balance with respect to mass and charge and, in addition, the ratio of the cation and anion sites must be maintained. These concepts are considered in more detail later in this chapter.

5.3. Diffusion and Conductivity

In the study of oxygen ion conducting electrolytes, an understanding of both electrical conductivity and diffusion is necessary, in order to elucidate upon the charge transport properties. Electrical conductivity and diffusion are closely related and can normally be determined by the type of defects present within a crystal and their concentration. When considering the transport of mass or charge, it is necessary to have an understanding of the processes which occur on the atomic scale. For this purpose, it is easier to start with the diffusion process. It is important, at this point, to introduce a term known as the *diffusion coefficient, D*. The diffusion coefficient is a materials parameter, which characterises the rate of the diffusion process for a particular atomic species in a particular phase. The diffusion derivation described below follows that given by Kingery [6].

When two miscible components are brought together, the two components will start to diffuse into each other, until a uniform solid solution is achieved. The speed with which the atoms diffuse is related to the mobility of the atoms, which in turn is determined by the crystal structure, composition and defect structure of the two components. It is standard to use a random walk diffusion process to describe the motion of these atoms, whereby an atom is able to jump to any neighbouring site with equal probability. For this to be true a dilute solution situation must exist, i.e. the diffusing atoms do not come into contact with similar diffusing atoms. Now consider a solution of atoms, *a*, with a concentration n_a, diffusing into a solution, *b*, with a concentration n_b. The *a* atoms will have a characteristic jump frequency, Γ, with which they can exchange with adjacent atoms. In one dimension, the frequency of the *a* atoms jumping in one direction is $1/2n_a\Gamma$, and the frequency of the reverse exchange is $1/2n_b\Gamma$. The net flux of *a* atoms, *J*, is then the difference in jump frequency:

$$J = 1/2(n_a - n_b)\Gamma \qquad (5.7)$$

If the atomic planes are separated by a distance, λ, then the concentration of the plane with *a* atoms, $C_a=n_a/\lambda$ and that of the plane with *b* atoms, $C_b=n_b/\lambda$. The concentration gradient is thus given by,

$$-\frac{dC}{dx} = \frac{(C_a - C_b)}{\lambda} = \frac{(n_a - n_b)}{\lambda^2} \qquad (5.8)$$

Equation 5.7 can then be rewritten as:

$$J = -\left(\frac{1}{2}\lambda^2\Gamma\right)\frac{dC}{dx} \qquad (5.9)$$

This equation is in the form of Fick's first law of diffusion,

$$J = -D\frac{dC}{dx} \qquad (5.10)$$

and thus the diffusion coefficient, *D*, is given by,

$$D = \tfrac{1}{2}\lambda^2\Gamma \qquad (5.11)$$

In a three dimensional solid, the geometric factor, $\gamma=\frac{1}{2}$, changes and becomes dependent on the co-ordination of neighbouring atoms. Generally, the geometric factor can be written as $\gamma = 1/N$, where N is the number of neighbouring sites for the atom to jump into. For a simple cubic structure where atoms can jump in three orthogonal directions, the diffusion coefficient becomes

$$D = 1/6\lambda^2\Gamma \qquad (5.12)$$

The diffusion coefficient can vary enormously between different materials and this is directly related to the variation in jump frequency. The jump frequency depends on factors like the energy for migration, temperature and the defect concentration (availability of jump sites).

Diffusion in most ceramics shows an Arrhenius type behaviour, over at least a limited temperature range, and can therefore be expressed as,

$$D = D_0 \exp\left(\frac{-E_a}{RT}\right) \qquad (5.13)$$

where D_0 is a constant and E_a is the diffusion activation energy. This suggests that diffusion is a thermally activated process, and the jump frequency can now be expressed as:

$$\Gamma = \nu_0 \exp\left(\frac{-\Delta G_m}{kT}\right) = \nu_0 \exp\left(\frac{\Delta S_m}{k}\right)\exp\left(\frac{-\Delta H_m}{kT}\right) \qquad (5.14)$$

where ν_0 is the vibrational or attempt frequency, ΔG_m is the free energy of migration, ΔH_m is the enthalpy of migration and ΔS_m is the entropy associated with the migration process. The diffusion coefficient thus becomes:

$$D = \gamma\lambda^2\Gamma = \gamma\lambda^2\nu_0 \exp\left(\frac{\Delta S_m}{k}\right)\exp\left(\frac{-\Delta H_m}{kT}\right) \qquad (5.15)$$

So far only dilute solutions have been considered but for the electrolytes studied in this chapter, the solid solutions have defect concentrations considerably above the dilute solution limit, where defect interactions affect the diffusion of atoms. The diffusion coefficient is often proportional to the defect concentration, where the defect concentration itself can show a dependence on temperature. Consequently, the diffusion activation energy may contain other energy terms such as the defect formation energy and the defect association energy, as well as the migration enthalpy. The defect diffusion mechanism in these electrolytes is via oxygen vacancies through which the oxygen ions can migrate. In dilute solutions the vacancy diffusion coefficient is independent of the vacancy concentration because there is no interaction of these defects. The diffusion coefficient of the lattice oxygen, however, is strongly dependant on the defect concentration. In the case of an oxygen vacancy mechanism, the oxygen self diffusion coefficient, D^*, is related to the vacancy diffusion coefficient, D_V, according to equation 5.16:

$$D^*\left[O_O^X\right] = D_V\left[V_O^{\bullet\bullet}\right] \qquad (5.16)$$

The oxygen self-diffusion coefficient is therefore dependent on the defect concentration, atmosphere and temperature. Measurement of this value is normally difficult and so the *tracer diffusion coefficient,* D_T, is measured, using an oxygen isotope method. The tracer diffusion coefficient is not exactly the same as the self-diffusion coefficient, because it is thought that atom jumps are not random but that each successive jump is correlated. The tracer diffusion coefficient is then less than the self-diffusion coefficient, by a correlation factor, f_D:

$$D_T = f_D D^* \qquad (5.17)$$

For vacancy diffusion in a dilute simple cubic lattice, f_D has been calculated to be 0.65 [7]. In more concentrated solutions, defect associates are formed and f_D becomes smaller.

By combining equations 5.15-5.17 the measured oxygen tracer diffusion coefficient can be expressed as:

$$D_T = \gamma f_D \left[V_O^{\bullet\bullet}\right] \lambda^2 \nu_O \exp\left(\frac{-\Delta H_m}{kT}\right) \qquad (5.18)$$

where γ is now defined as,

$$\gamma = \frac{z}{6} \exp\left(\frac{\Delta S_m}{k}\right) \qquad (5.19)$$

and z is the co-ordination number of the atom.

Both zirconia and ceria electrolytes show high solubilities for some alkaline earth oxides (CaO, SrO), Y_2O_3 and most rare earth oxides. Acceptor doping with these oxides results in substitutional incorporation of the dopant ions on the cation sublattice, with the formation of oxygen vacancies as charge compensating defects. For the electrolyte material, Gd_2O_3 doped CeO_2, the defect reaction can be expressed in Kröger-Vink notation [8] as:

$$Gd_2O_3 \xrightarrow{CeO_2} 2Gd'_{Ce} + V_O^{\bullet\bullet} + 3O_O^X \qquad (5.20)$$

In dilute solutions, the oxygen vacancies are free and do not interact with each other. As the solution becomes more concentrated, the probability of an oxygen vacancy encountering another oxygen vacancy or a dopant ion increases. When a vacancy and dopant ion meet, Coulombic and elastic forces attract the two defects together to form an associate, i.e.

$$(Gd'_{Ce}V_O^{\bullet\bullet})^{\bullet} \textit{ or } (Gd'_{Ce}V_O^{\bullet\bullet}Gd'_{Ce})^X \qquad (5.21)$$

Statistically, it is expected that the charged associate will form at low concentrations because the dopant ions are randomly distributed. It has been demonstrated, that the binding energy of the associate can significantly alter the ionic conductivity at lower

temperatures because it reduces the concentration of free vacancies [9]. It is therefore necessary to be able to calculate the concentration of free oxygen vacancies as a function of temperature. The method for this calculation has been shown by Kilner and Waters [9] and will be outlined below for the example in equation 5.20.

The free vacancy concentration is controlled by the dissociation reaction:

$$(Gd'_{Ce}V_O^{\bullet\bullet})^{\bullet} \leftrightarrow Gd'_{Ce} + V_O^{\bullet\bullet} \qquad (5.22)$$

The mass action equation can then be written as:

$$K = \frac{[Gd'_{Ce}][V_O^{\bullet\bullet}]}{[(Gd'_{Ce}V_O^{\bullet\bullet})^{\bullet}]} = \frac{1}{W}\exp\left(\frac{-\Delta H_A}{kT}\right) = \frac{E}{W} \qquad (5.23)$$

where ΔH_A is the associate binding enthalpy, *E* represents the exponential term and *W* is the number of possible defect orientations. To make calculations easier, the terms in square brackets now represent site fractions. The corresponding electroneutrality condition is given by:

$$2[V_O^{\bullet\bullet}]\tfrac{1}{2}m + [(Gd'_{Ce}V_O^{\bullet\bullet})^{\bullet}] = [Gd'_{Ce}] \qquad (5.24)$$

The term *m* expresses the ratio of metal sites to oxygen sites to maintain site balance. The total dopant concentration, C_M, is then,

$$C_M = [Gd'_{Ce}] + [(Gd'_{Ce}V_O^{\bullet\bullet})^{\bullet}] \qquad (5.25)$$

Combining equations 5.23-5.25 to eliminate the defect and associate concentrations, gives the equation:

$$[V_O^{\bullet\bullet}]^2 + [V_O^{\bullet\bullet}]\left(\frac{C_M}{m} + \frac{E}{W}\right) - \left(\frac{C_M E}{mW}\right) = 0 \qquad (5.26)$$

The solution to this quadratic is,

$$\left[V_O^{\bullet\bullet}\right] = -\frac{1}{2}\left(\frac{C_M}{m} + \frac{E}{W}\right) + \frac{1}{2}\sqrt{\left(\frac{C_M}{m} + \frac{E}{W}\right)^2 - \frac{4C_M E}{mW}} \qquad (5.27)$$

Electrical conductivity in ionic materials is a result of the motion of ionic species and is therefore proportional to the diffusivity. The ionic conductivity, σ_i of a species, *i*, is given by:

$$\sigma_i = n_i q_i \mu_i \qquad (5.28)$$

where n_i is the carrier density, and q_i and μ_i are the respective charge and mobility of the carrier. For an oxygen ion the carrier density can be written as,

$$n_i = \left[V_O^{\bullet\bullet}\right]\left\{1 - \left[V_O^{\bullet\bullet}\right]\right\}N \qquad (5.29)$$

where N is the number of anion sites per unit volume. The mobility may be expanded atomistically to give,

$$\mu = \frac{\gamma q}{kT}\lambda^2 \nu_0 \exp\left(\frac{-\Delta H_m}{kT}\right) \qquad (5.30)$$

The expression for conductivity now becomes,

$$\sigma = \left[V_O^{\bullet\bullet}\right]\left\{1 - \left[V_O^{\bullet\bullet}\right]\right\}N\frac{\gamma q^2}{kT}\lambda^2 \nu_0 \exp\left(\frac{-\Delta H_m}{kT}\right) \qquad (5.31)$$

The ionic conductivity can be converted into an oxygen diffusion coefficient using the Nernst-Einstein equation but normally a conductivity correlation factor, f_C, must be included. The correlation factor is needed because the availability of mobile defects is different in an electric field and thus the ionic conductivity diffusion coefficient, D_σ, can be expressed as, $D_\sigma = D^* f_C$. The Nernst-Einstein equation thus becomes,

$$D = \frac{kT\sigma}{Nq^2 f_C} \tag{5.32}$$

For low defect concentrations, f_c is approximately unity. The ionic conductivity diffusion coefficient can be formed in terms of atomistic parameters, by substituting equation 5.31 into 5.32, as follows:

$$D_\sigma = \gamma f_C \left[V_O^{\bullet\bullet}\right]\left\{1-\left[V_O^{\bullet\bullet}\right]\right\}\lambda^2 \nu_0 \exp\left(\frac{-\Delta H_m}{kT}\right) \tag{5.33}$$

Similar to diffusion, experimentally measured conductivity also shows an Arrhenius behaviour and an analogous equation to 5.13 can be written for ionic conductivity,

$$\sigma_i = \sigma_0 \exp\left(\frac{-E_a}{RT}\right) \tag{5.34}$$

where σ_0 is the pre-exponential term. Assuming the value of $1-\left[V_O^{\bullet\bullet}\right]$ is close to one, it can be seen that the two diffusion coefficients in equations 5.18 and 5.33, only differ by the correlation factors f_D and f_C. The ratio of the two diffusion coefficients is known as the *Haven Ratio* (H_R) and is simply the ratio between the two correlation factors, i.e.

$$\frac{D_T}{D_\sigma} = \frac{f_D}{f_C} \equiv H_R \tag{5.35}$$

In highly doped systems, point defects and simple defect associates will combine together to form more complex clusters and will eventually lead to defect ordering, an aspect which must be considered before applying these equations.

5.4. Fluorite Related Structures

There are a number of oxides that crystallise in the cubic fluorite structure. Among the lanthanide oxides are CeO_2, PrO_2 and TbO_2 and from the actinide oxides there are ThO_2, UO_2 and PuO_2. Although urania and plutonia have received much attention from the nuclear industry, the most promising electrolyte materials studied have been ceria and thoria. Thoria electrolytes are discussed below but demonstrate considerably lower conductivity values compared to both zirconia and ceria electrolytes.

5.4.1. CeO_2 Electrolytes

The ideal ceria lattice is shown in Fig.5.1. The unit cell formula A_4O_8, shows the tetravalent cations forming a face-centred cubic (FCC) sublattice, with each cation in eight-fold co-ordination with oxygen. The oxygen ions occupy all the tetrahedral sites and therefore have a co-ordination number of four.

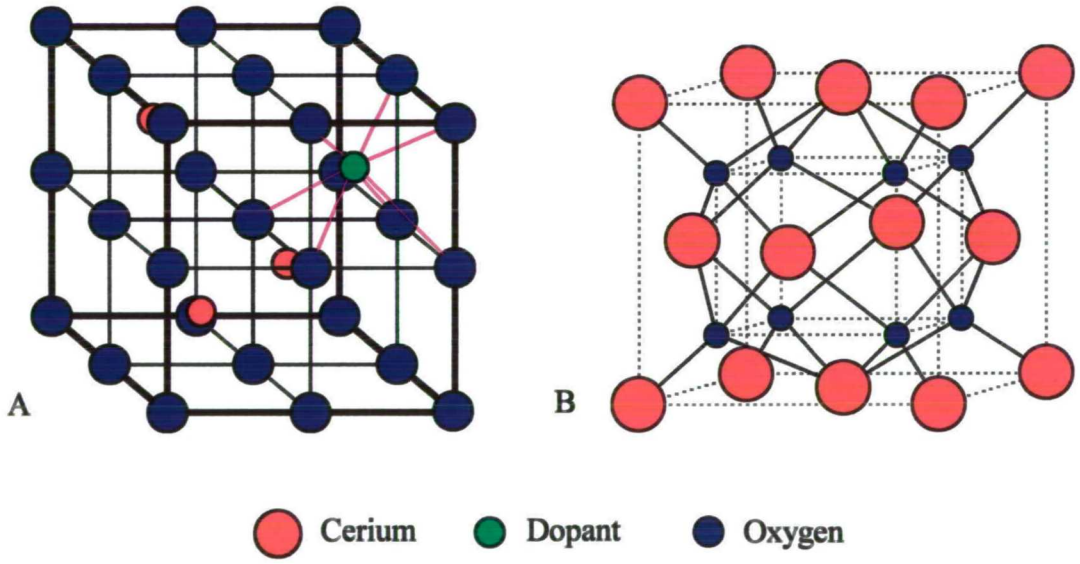


Fig.5.1. A). Ideal unit cell of doped ceria. B). Fluorite structure showing anion co-ordination.

When measured in air, ceria doped with Gd or Sm shows superior ionic conductivity compared to YSZ and is one of the few materials which could replace YSZ. Ceria electrolytes would operate around 500-700°C and allow significant materials

advantages in SOFC applications. A detailed review of ceria electrolytes can be found in the next chapter. A brief summary is given below.

It is well known that ceria electrolytes can be reduced at high temperatures and low oxygen partial pressures and this fact will be considered in more detail in the next chapter. It is thought that at low temperatures (500°C), the electronic conductivity would not lower the efficiency of a SOFC significantly [10, 11]. The effect protons have on the electrical conductivity has only recently received attention. Opinion remains mixed concerning the concentration of protons involved. Initial work at Imperial College indicated that the concentration of protons was very low [12]. Further published research [13] suggests that protons can alter the behaviour of doped ceria in reducing conditions. Additional publications by Norby, e.g. [14], infer a significant concentration of protons. Clearly, more research is necessary to clarify the role of protons in ceria and a defect model is required.

To reveal the nature of doped ceria electrolytes in different oxygen partial pressures, a detailed understanding of the defect behaviour is prerequisite, to predict the contributions of each defect species to the total conductivity in SOFC applications. This understanding allows an estimate of the efficiency with which the SOFC will operate. A useful technique to represent the defect behaviour is on a Brouwer diagram.

5.4.1.1. Brouwer Diagrams

For electrolyte materials that are to be used in changing oxygen partial pressures, it is important to know how the defect concentrations vary. A number of defect reactions have been described above for the Gd-doped CeO_2 system; it is now time to understand the net effect of these reactions when they all occur simultaneously. There are five defects of interest in the Gd-doped CeO_2 system, Gd'_{Ce}, $V_O^{\bullet\bullet}$, O'_i, e' and $h^{\bullet}$, for which the relevant defect forming reactions are:

Intrinsic Anti-Frenkel Defects,

$$O_O^X \leftrightarrow O_i'' + V_O^{\bullet\bullet} \qquad (5.36)$$

Intrinsic Electronic Defects,

$$\text{null} \leftrightarrow e' + h^{\bullet} \tag{5.37}$$

Oxidation/Reduction,

$$O_O^X \leftrightarrow \tfrac{1}{2} O_{2(g)} + V_O^{\bullet\bullet} + 2e' \tag{5.38}$$

The oxidation reaction is essentially the reverse of the reduction reaction; however, when all the oxygen vacancies have been replaced with oxygen atoms, oxygen interstitials will then be incorporated according to the reaction,

$$\tfrac{1}{2} O_{2(g)} \leftrightarrow O_i'' + 2h^{\bullet} \tag{5.39}$$

The Gd concentration in these experiments is essentially "frozen in" because it does not vary with oxygen partial pressure. Therefore, only the reactions which are in equilibrium with oxygen need to be considered.

The respective equilibrium constants are then:

$$K_1 = [O_i''][V_O^{\bullet\bullet}] \tag{5.40}$$

$$K_2 = np \tag{5.41}$$

$$K_{3a} = [V_O^{\bullet\bullet}] n^2 P_{O_2}^{1/2} \tag{5.42}$$

$$K_{3b} = \frac{[O_i''] p^2}{P_{O_2}^{1/2}} \tag{5.43}$$

The full electroneutrality equation can be expressed as:

$$2[O_i''] + n + [Gd_{Ce}'] = 2[V_O^{\bullet\bullet}] + p \tag{5.44}$$

It is now possible to solve these equations, so that the concentrations of each defect at any temperature and P_{O_2} may be calculated, provided the equilibrium constants are known. The solution of these equations has been simplified by an assumption introduced by Brouwer [15], stating that under any equilibrium condition there is only one particular charged defect which dominates on each side of the neutrality equation. This assumption holds when a single defect of each sign has a much higher concentration than other defects of the same sign. The electroneutrality equation can then be reduced to a series of Brouwer Approximations, which for this system are:

1. $n = 2[V_O^{\bullet\bullet}]$
2. $n = p$
3. $[Gd'_{Ce}] = 2[V_O^{\bullet\bullet}]$
4. $[Gd'_{Ce}] = p$
5. $[O_i''] = [V_O^{\bullet\bullet}]$
6. $2[O_i''] = p$

Each of these regimes represents a different range of oxygen activity and can be shown on a Brouwer diagram. The Brouwer diagram is a plot of log [concentration] against $\log P_{O_2}$ and shows the variations in defect concentration at a constant temperature. Regime 5 is unlikely to be seen unless the temperature is close to the melting point and at this temperature it is assumed, that only one of regimes 2 or 5 will dominate, depending on the Frenkel energy and the band gap. In ceria, the Frenkel defects will dominate and therefore regime 2 is not considered. Four Brouwer approximations remain and are shown in Fig.5.2.

The most important regime for electrolyte materials is regime II, where the oxygen vacancy concentration is dependent only on the dopant concentration. The conductivity is directly proportional to the defect concentration, therefore, the conductivity generally follows the defect with the highest concentration. At lower temperatures, the electronic conductivity is sufficiently small in regime II, that the ionic conductivity dominates. This region demonstrates the ionic or electrolytic

domain of the material. For a good SOFC electrolyte, this region needs to extend as far to the lowest oxygen partial pressure as possible.

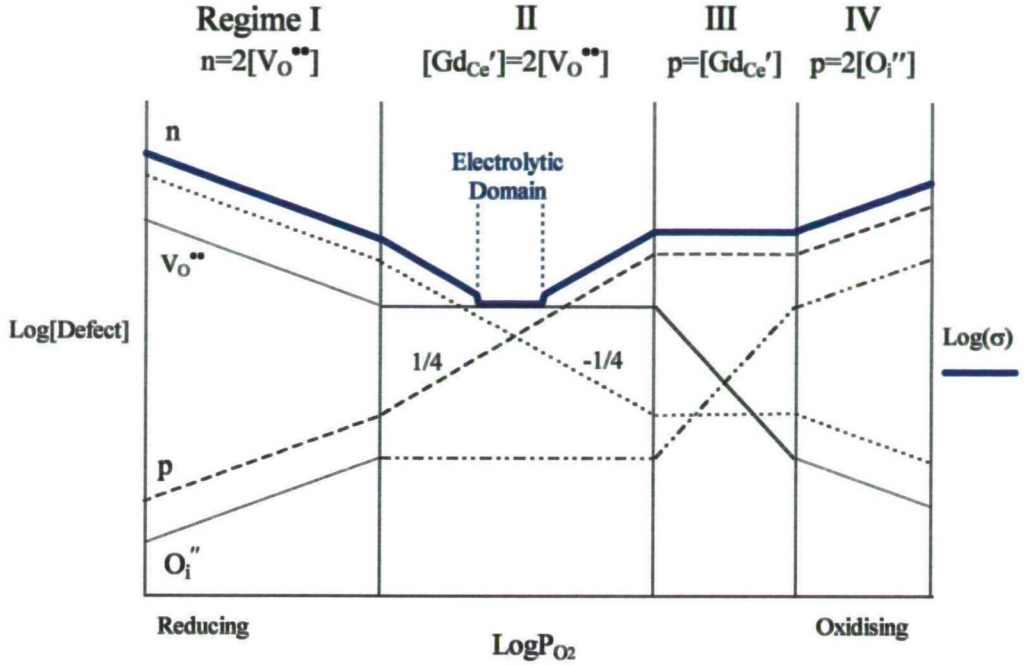


Fig.5.2. Brouwer diagram for Gd-doped ceria also showing the variation in conductivity.

The gradients of the lines in this regime can be calculated using the defect equations and Brouwer approximations as follows,

Brouwer Approximation: $$\left[Gd_{Ce}^{'}\right] = 2\left[V_O^{••}\right] \tag{5.45}$$

Equation 5.42 ($K_3 = \left[V_O^{••}\right] n^2 P_{O_2}^{1/2}$) rearranges to become,

$$n = K_3^{1/2}\left[V_O^{••}\right]^{-1/2} P_{O_2}^{-1/4} \tag{5.46}$$

Therefore $$\sigma \propto n \propto P_{O_2}^{-1/4} \tag{5.47}$$

The electron concentration will show a -1/4 dependence with oxygen partial pressure. Equation 5.41 (K_2=np) shows that the hole concentration will display the reverse dependence, i.e.

$$p \propto P_{O_2}^{1/4} \qquad (5.48)$$

Similar calculations can be made to show the dependencies of each defect in the other regimes.

5.4.1.2. Deviations from Brouwer Assumptions

The assumption made that the activity of a defect can be represented by its concentration is only reasonable at low defect concentrations. At higher concentrations, defect interactions become significant and it is then necessary to introduce a concentration dependent activity coefficient [16]. Also, the assignment of unit activity to normally occupied lattice positions will be in error, when large deviations from stoichiometry exist. In addition, the high dopant concentrations used in most electrolytes, requires consideration of defect associates that will form in the defect equations [17]. The transition between one neutrality condition to another is assumed to be a sharp transition. In reality, the change over from one dominant defect species to another may occur over a wide oxygen partial pressure, which invalidates the simple Brouwer approximation.

5.4.2. $Zr(M)O_2$ Electrolytes

Zirconia and hafnia only form the cubic structure necessary for fast oxygen conduction at very high temperatures and at lower temperatures transform into other structures, e.g. zirconia transforms first into a tetragonal phase and finally a monoclinic phase, as the temperature is reduced. The cubic phase can be stabilised to lower temperatures, by doping to relatively high concentrations, i.e. cubic zirconia is stabilised with around 8mol% $YO_{1.5}$ additions [18]. The high concentration of dopants involved, implies that the dilute solution theory is no longer applicable and substantial defect association is already present. Defect modelling becomes very difficult in these systems and no theoretical analysis fully explains the experimentally observed behaviour in these materials.

Zirconia is the most studied of the solid oxygen ion conducting electrolytes and there are numerous publications concerning its electrical and structural properties, for which many review articles have been written [19, 20]. Many divalent and trivalent dopants have been used to stabilise zirconia, but CaO and more commonly Y_2O_3 (YSZ) have been chosen in most applications, due to their relative abundance and low cost. The highest ionic conductivities have been reported for Sc_2O_3 doped ZrO_2 [21] but the high cost of the scandia has inhibited researchers. The need to lower the temperature of operation of SOFC's may not exclude this material entirely, when the cost of the whole system is taken into consideration.

Many of the properties of doped ceria and zirconia electrolytes follow the same trends. There is considerable evidence of both dopant and impurity segregation to the grain boundaries to allow the formation of low conductivity thin films [22, 23]. Most zirconia solid solutions show a significant grain boundary resistance at low temperatures, which is mainly attributed to the segregation of impurities such as Si, Ca and Al to the boundary region [24, 25]. The nature of these films is still not fully understood but most results indicate the presence of a silicate phase. The continuity of this phase tends to depend on the purity of the starting materials and hence both continuously and partially covered grain boundaries have been observed [26, 27]. The equilibrium thickness of these grain boundary films has been shown to be between 1-2nm [28], although greater thicknesses have also been reported [22]. Higher concentrations of impurities segregate to large isolated pockets or migrate to the external surface. Space charge regions have also been reported to increase the grain boundary resistance [22]. The activation energy of the grain boundary is generally higher than that found for the bulk material, implying a different composition at the grain boundaries. A change in E_a is found in the bulk Arrhenius data, suggesting association of defects is present at the lower temperatures. There has also been a number of papers on ceria-zirconia solid solutions, for both ionic and mixed conducting applications [24]. The higher the ceria concentration, the higher the ionic and electronic conductivities.

YSZ fulfils all the basic requirements of an SOFC electrolyte listed at the beginning of this chapter, showing long term stability in both reducing and oxidising atmospheres,

although there are concerns over the extent of reactivity of this material with other cell components. Many P_{O2} dependent measurements have been performed on YSZ to determine the electronic conductivity and have found this to be negligible. The contribution of the protonic conductivity in YSZ has been studied somewhat less, although recent results of Manning [29] suggest that the protonic conductivity may also be negligible, however there are some discrepancies in these results that cannot be accounted for.

5.4.3. Bi_2O_3 Based Electrolytes

The cubic δ-Bi_2O_3 phase is produced by an order-disorder transition at 729°C and exhibits the highest value of oxygen ion conductivity (approximately $1Scm^{-1}$ at 750°C) reported so far for a solid electrolyte [30]. δ-Bi_2O_3 has a fluorite related structure, where the cations occupy a FCC sublattice, with a complex oxygen ion sublattice in which one quarter of the anion sites are vacant. A number of dopants have been added to stabilise a low temperature form of the δ-Bi_2O_3 phase; the most successful dopants have been Y_2O_3 and Er_2O_3 [31, 32]. However, technological applications of Bi_2O_3-based electrolytes are limited because of the reduction of Bi^{3+} at relatively high oxygen partial pressures [33].

5.4.4. ThO_2 Electrolytes

Thoria based electrolytes display the greatest stability of all the fluorites in reducing conditions, exhibiting electrolytic domains to at least 10^{-22}atm at 1000°C [34]. Like ceria electrolytes, undoped thoria already has a cubic fluorite structure and the addition of aliovalent dopants serves to increase the oxygen vacancy concentration. Both alkaline earth and rare earth dopants have been studied in thoria but the majority of research has dealt with the ThO_2-Y_2O_3 solid solution, which possesses the highest electrical conductivity [18].

Thoria electrolytes are seldom studied today because their ionic conductivities are one to two orders of magnitude lower than that of YSZ [18]. The activation energies for oxygen conduction are significantly higher as well, with the value for $Th(Ca)O_{2-X}$ in

the range 1.16-1.42eV for 1-8mol%CaO [35]. Thoria electrolytes also display electron-hole conduction at oxygen partial pressures greater than 10^{-6}atm, which is a result of the incorporation of excess oxygen into existing vacancies according to the reaction [36]:

$$\tfrac{1}{2}O_2(g) + V_O^{\bullet\bullet} \leftrightarrow O_O^X + 2h^{\bullet} \qquad (5.49)$$

Thoria is no longer considered for electrolyte applications but its extremely stable nature still justifies studies into the defect chemistry of fluorite structures in reducing conditions.

5.4.5. Pyrochlore

The pyrochlore structure ($A_2B_2O_7$), where A is a larger trivalent rare earth or yttrium ion and B is a quadrivalent zirconium or titanium ion, is closely related to that of the fluorite, with one eighth of the anion sites vacant. However, compared to defect fluorites with the same stoichiometry, in the perfect pyrochlore structure, both the cation sublattice and the oxygen sublattice are ordered. The oxygen ion conductivity in the perfect pyrochlore structure is thus low and the oxygen vacancies must become disordered for fast oxygen ion conduction [37]. Disordering is normally achieved by heating to temperatures above the order-disorder transition. A commonly studied pyrochlore is $Gd_2Zr_2O_7$ [38], which disorders at around 1550°C to a defective fluorite system.

The degree of anion disorder remains difficult to predict, where the anions generally follow the ordering of the cation sublattice. Cation disorder can be enhanced by doping with cations of similar size to those in the lattice, which makes the mixing of ions more favourable, e.g. $Gd_2(Zr_XTi_{1-X})_2O_7$ [39]. The largest increase in conductivity is achieved by aliovalent substitution [40], for example in $(Gd_{0.9}Ca_{0.1})_2Ti_2O_7$, which has a conductivity of 5×10^{-2}Scm^{-1} at 1000°C [41]. Unfortunately, disordering of the cation sublattice increases the activation energy because it reduces the number of large tetrahedral sites which act as pathways for oxygen ions. Thus the ideal oxygen ion conducting pyrochlore needs an ordered cation sublattice, with a disordered anion

sublattice. These two competing factors hinder the development of useful pyrochlore electrolytes and at present there is no pyrochlore system which exhibits an oxygen ion conductivity with a superior performance to that of zirconia electrolytes. Some pyrochlores ($Gd_2(Zr_XTi_{1-X})_2O_7$) exhibit a degree of electronic conductivity in reducing conditions and are now being considered for mixed ionic/electronic conduction [42].

5.5. Perovskite Related Structures

The ideal perovskite structure (ABO_3) consists of a small ionic radius cation, B, surrounded by an octahedral arrangement of oxygen ions. The larger A cation occupies the corners of the unit cell, to form an FCC arrangement with the oxygen ions (Fig.5.3). The structure can be composed from a combination of divalent and tetravalent cations, two trivalent cations of different size or a monovalent and pentavalent cation. The perovskite structure is less open than the fluorite structure, with 6-co-ordinated oxygen ions, but it is very stable under variable temperature and redox conditions and retains its structure over a wide range of aliovalent cation substitutions [43]. There are a selection of perovskite structures which exhibit reasonable oxygen ion conductivities but most display mixed ionic/electronic or ionic/protonic conduction [44]. These three classes of perovskite are briefly discussed below.

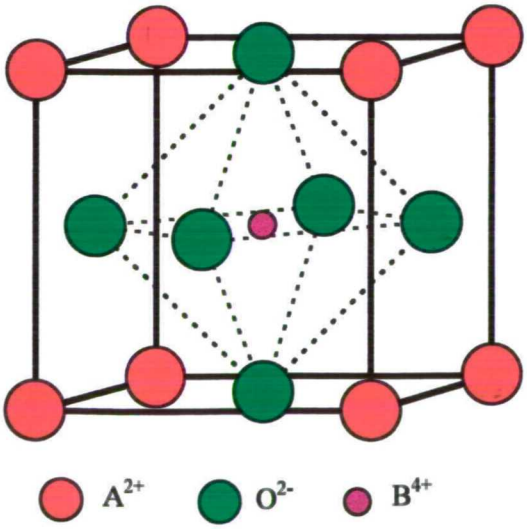


Fig.5.3. The ideal perovskite structure.

5.5.1. Ionic Conductors (LSGM)

Until recently, perovskites had mainly been considered for electrode materials and mixed conducting films because of their stability under many operating conditions. The few purely ionic conductors, such as Ba or Ca-doped $LaAlO_3$, had reasonably high oxygen ion conductivities, e.g. 5×10^{-3} at 800°C [44], but did not exhibit conductivities significantly greater than those of YSZ.

In 1994, two different research groups published work on a new perovskite electrolyte material with a significantly higher oxygen ion conductivity compared to YSZ [45, 46]. This material was based on the perovskite $LaGaO_3$, with Sr doping on the A site and Mg doping on the B site. The highest conductivity below 700°C was found for the composition $La_{0.8}Sr_{0.2}Ga_{0.9}Mg_{0.1}O_3$ and this compound is now commonly referred to as LSGM. This material exhibits a wide electrolytic domain, stability in fuel environments and is not sensitive to moisture and remains a promising material for use in SOFC electrolyte applications. The largest concerns with this material are the long term stability under operating conditions, which will only be known in time, and the high cost of gallium. There are many research groups developing LSGM and early indications suggest that this material could replace YSZ for intermediate temperature (700-800°C) operation devices [47].

5.5.2. Proton Conductors

Pure proton conductors would offer some distinct advantages over YSZ, for the electrolyte material in SOFC applications. Superior conductivity at lower temperatures offers higher theoretical efficiencies and lower cost of peripheral equipment. Pure proton conduction also implies that the fuel does not need to be recycled because the water is not produced on the fuel side. In practice, oxygen ion conduction accompanies proton migration, resulting in water production. Most proton conducting oxides also display considerable electronic conductivity, which would lead to unacceptable losses in operating efficiency. Mixed electronic/protonic conducting perovskites are now being considered as alternative anode materials [48].

The most commonly studied proton conducting materials are based on $SrCeO_3$, $BaCeO_3$, $SrZrO_3$ and $BaZrO_3$ [49]. Doping on the B-site using Gd, Yb, Y or Sc increase the electronic conductivity and controls the material stoichiometry [50], for example in $BaCe_{0.9}Gd_{0.1}O_{3-X}$ and $SrCe_{0.95}Yb_{0.05}O_{3-X}$ [51, 52].

5.5.3. Mixed Ionic and Electronic Conductors (MIEC)

There are a large number of mixed ionic/electronic conducting perovskites. The electronic conductivity is introduced by choosing a transition metal for the B-site, or doping the B-site with a transition metal, e.g. $LaCoO_3$. The A-site is often doped with aliovalent cations to increase the number of oxygen vacancies, e.g. $La_{1-X}Sr_XCoO_3$. The mixed conducting properties of these materials have been considered for electrodes in electrochemical devices and for the electrolyte in oxygen separation membranes (see chapter 4), where the perovskite $La_{1-X}Sr_XCo_{1-Y}Fe_YO_3$ appears very promising [53, 54]. Pure electronic conduction is also observed in perovskite materials such as $La_{1-X}Sr_XMnO_3$ (LSM) but a discussion of these materials is not relevant to this thesis.

5.5.4. Brownmillerite Electrolytes

The brownmillerite structure ($A_2B_2O_5$) is essentially that of the cubic perovskite (ABO_3), with one sixth of the oxygen atoms removed, and therefore contains a large number of intrinsic oxygen vacancies. The smaller B-site atoms should show no preference between octahedral and tetrahedral sites. The large number of oxygen vacancies allow for the possibility of enhanced oxygen ion conduction, making this class of materials promising for fast oxygen ion conductors. Unfortunately, below 800°C the oxygen vacancies become ordered along the [101] direction, effectively trapping the vacancies and preventing rapid ionic conduction. Above this transition temperature, the vacancies become disordered and fast ion transport takes place [55]. Fisher [56], working on $Ba_2In_2O_5$, has shown that successful doping on the B-site can lower this transition temperature. It was found that Sc and Ga doping produced the best results, although the Ga-doped samples sintered poorly, with the optimum composition at $Ba_2In_{1.8}Sc_{0.2}O_5$. Further reduction in the transition temperature was

thought to occur by substitution of the A-site cation for a smaller cation, e.g. Sr [57]. This increases the unit cell volume and allows easier oxygen ion movement, which leads to disordering of the lattice.

By moving one row up in the periodic table, the brownmillerite structured $Sr_2Ga_2O_5$ should be formed. Fisher [58] was unsuccessful in the preparation of this material and suggested that this was due to the small size of the Ga^{3+} ion, which preferred to be located at tetrahedrally co-ordinated sites. Preparation of $Ca_2Ga_2O_5$ has also been unsuccessful [59]. By doping the gallium site ions with larger isovalent cations, it was thought possible to stabilise the gallium ions and produce a good oxygen ion conductor [60]. Further discussion on this subject can be found in chapter 8. Despite the large number of brownmillerite compounds that exist, at present, none can improve upon the properties of YSZ as an electrolyte material.

References

1. G.V.Lewis and C.R.A.Catlow. J.Phys.Chem.Solids. **47**, (1986), 89.
2. B.V.Ratnakumar and S.R.Narayanan. Handbook of Solid State Batteries and Capacitors. Ed. M.Z.A.Munshi. World Scientific Publishing Company. 1995, 4.
3. E.C.Subbarao and H.S.Maiti. Solid State Ionics. **11**, (1984), 317.
4. C.Wagner and W.Schottky. Z.Phys.Chem. **B11**, (1931), 163.
5. H.L.Tuller and A.S.Nowick. J.Electrochem.Soc. 126, (1979), 209.
6. Physical Ceramics. Eds. Y-M.Chiang, D.P.Birnie and W.D.Kingery. John Wiley and Sons, Inc. 1997, 185.
7. Diffusion in Solids. Ed. P.Shewmon. The Minerals, Metals and Materials Society. 1989.
8. F.A.Kröger and H.J.Vink. Solid State Physics, Vol.3. Eds. F.Seitz and D.Turnbull. Academic Press. 1956, 307.
9. J.A.Kilner and C.D.Waters. Solid State Ionics. **6**, (1982), 253.
10. B.C.H. Steele. J.Power Sources. **49**, (1994), 1.
11. I.Reiss. Solid State Ionics. **52**, (1992, 127.
12. J.D.Sirman and M.Sahibzada. Private communications.

13. N.Kiratzis, B.C.H.Steele, J.M.Ralph, M.Sahibzada, A.Atkinson and J.A.Kilner. To be published.
14. T.Norby and P.Kofstad. J.Am.Ceram.Soc. **69**, (1986), 780.
15. G.Brouwer. Philips Res.Rep. **9**, (1954), 366.
16. A.B.Lidiard. Handbuch der Physik, Vol.20. Springer-Verlag. 1957, 246.
17. J.B.Lightstone and G.G.Libowitz. J.Phys.Chem.Solids. **30**, (1969), 1025.
18. T.H.Estell and S.N.Flengas. Chemical Reviews. **70**, 3, (1970), 339.
19. P.Aberlard and J.F.Baumard. Phys.Rev. **B26**, (1982), 1005.
20. A.E.Hughs and S.P.S.Badwal. Solid State Ionics. **46**, (1991), 265.
21. Y.Mizutani, M.Kawai, K.Nomura, Y.Nakamura and O.Yamamoto. Proc. of the Fifth International Symposium on SOFCs. Eds. U.Stimming, S.C.Singhal, H.Tagawa and W.Lehnert. The Electrochem.Soc, (1997), 196.
22. M.J.Verkerk, B.J.Middelhuis and A.J.Burggraaf. Solid State Ionics. **6**, (1982), 159.
23. M.Aoki, Y-M Chiang, I.Kosacki, L.J-R Lee, H.Tuller and Y.Liu. J.Am.Ceram.Soc. **79**, 5, (1996), 1169.
24. G.Chiodelli, G.Flor and M.Scagliotti. Solid State Ionics. **91**, (1996), 109.
25. S.P.S.Badwal and J.Drennan. J.Mater.Sci. **22**, (1987), 3231.
26. J.E.Bauerle. J.Phys.Chem.Solids. **30**, (1969), 2657.
27. T.van Dijk and A.J.Burggraaf. Phys.Status Solidi. **A63**, (1981), 229.
28. D.R.Clark. J.Am.Ceram.Soc. **70**, (1987), 15.
29. P.S.Manning, J.D.Sirman, R.A.De Souza and J.A.Kilner. Solid State Ionics. **100**, (1997), 1.
30. P.D.Battle, C.R.A.Catlow, J.Drennan and A.D.Murray. J.Phys.C: Sol.State Phys. **16**, (1983), L561.
31. P.D.Battle, C.R.A.Catlow, J.W.Heap and L.M.Moroney. J.Solid State Chem. **63**, (1986), 8.
32. M.J.Verkerk, K.Keizer and A.J.Burggraaf. J.Electrochem.Soc. **128**, (1981), 75.
33. T.Takahashi, T.Esaka and H.Iwahara. J.Appl.Electrochem. **7**, (1977), 299.
34. M.F.Lasker and R.A.Rapp. Z.Physik.Chem. **49**, (1966), 198.
35. H.S.Maiti and E.C.Subbarao. J.Electrochem.Soc. **123**, (1976), 1713.
36. J.E.Bauerle. J.Chem.Phys. **45**, (1966), 4162.

37. A.J.Burggraaf, B.A.Boukamp, I.C.Vinke and K.J. de Vries. Recent Developments in Oxygen-Ion Conducting Solid Electrolytes. Ed. C.R.A.Catlow. 1989, 259.
38. H.L.Tuller. J.Phys.Chem.Solids. **55**, 12, (1994), 1393.
39. P.K.Moon and H.L.Tuller. Solid State Ionics. **28-30**, (1988), 470.
40. K.V.Kutty, C.K.Mathews, T.N.Rao and U.V.Varadaraju. Solid State Ionics. **80**, (1995), 99.
41. S.A.Kramer and H.L.Tuller. Solid State Ionics. **82**, (1995), 15.
42. H.L.Tuller, S.Kramer and M.A.Spears. Proc. of the 14th Risø International Symposium of Materials Science. Eds. F.W.Poulsen, J.J.Bentzen, T.Jacobsen, E.Skou, M.J.L.Østergård. (1993), 43.
43. D.M.Smyth. Geophysical Monograph. **45**, (1987), 99.
44. H.Iwahara. Solid State Ionics. **52**, (1992), 99.
45. T.Ishihara, H.Matsuda and Y.Takita. J.Am.Chem.Soc. **116**, (1994), 3801.
46. M.Feng and J.B.Goodenough. Eur.J.Solid State Inorg.Chem. **t31**, (1994), 663.
47. P.Huang and A.Petric. J.Electrochem.Soc. **143**, 5, (1996), 1644.
48. R.A.De Souza. Ph.D. Thesis. University of London, 1996.
49. R.L.Cook and A.F.Sammells. Solid State Ionics. **45**, (1991), 311.
50. T.Scherban and A.S.Nowick. Solid State Ionics. **35**, (1989), 189.
51. B.C.H.Steele. Materials Science and Engineering. **B13**, (1992), 79.
52. I.Kosacki and H.L.Tuller. Solid State Ionics. **80**, (1995), 223.
53. Y.Teraoka, T.Nobunga, K.Okanoto, N.Miura and N.Yamazoe. Solid State Ionics. **48**, (1991), 207.
54. J.A.Kilner, S.Benson, J.Lane and D.Waller. To be Published.
55. J.B.Goodenough. Proc. of the 14th Risø Inter. Symp. of Materials Science. Eds. F.W.Poulsen, J.J.Bentzen, T.Jacobsen, E.Skou, M.J.L.Østergård. (1993), 43.
56. C.A.J.Fisher, B.Derby and R.J.Brook. British Ceramics Proc. Ed. B.C.H.Steele. **56**, (1996), 25.
57. H.Kuramochi, T.Mori, H.Yamamura, H.Kobayashi and T.Mitamura. J.Ceram.Soc.Japan. **102**, 12, (1994), 1159.
58. C.A.J.Fisher. Ph.D. Thesis. University of Oxford, 1996.
59. R.Arpe, R.von Schenk and H.Müller-Buschbaum. Z.Anorg.Allg.Chem. **410**, (1974), 97.
60. J.C.Grenier, M.Pouchard and P.Hagenmuller. J.Solid State Chem. **13**, (1975), 92.

Chapter 6. Ceria and Doped Ceria Electrolytes

6.1. Introduction

In addition to a high ionic conductivity, a key requirement for the electrolytes discussed in chapters 3 and 4 is a high density. A high density is necessary to prevent cross mixing of any gases in a device as a result of open porosity. Generally, high sintering temperatures are required to achieve satisfactory densities, however, high sintering temperatures are undesirable during the co-firing of a complete cell (electrode-electrolyte-electrode) in a single step. Lower temperatures are needed to optimise the nature of the porous electrodes and to reduce the inter-diffusion of cation species.

The beginning of this chapter is concerned with the fabrication techniques employed to produce high density ceria at lower temperatures. The electrical and mechanical properties of the final ceramics are directly related to the manner in which they are manufactured and therefore, the remainder of this chapter consists of a discussion of the numerous studies concerning the electrical behaviour of ceria electrolytes.

6.2. Preparation of Pure Ceria

Pure ceria is a refractory oxide with a melting point of 2600°C. A characteristic of these refractory materials is the high sintering temperatures needed to achieve full densification (1700-1800°C) and much research has been aimed at lowering the sintering temperatures in such materials, e.g. Al_2O_3, ZrO_2, MgO.

The sintering of a compacted powder is normally the final stage in the processing of a ceramic. The production of the powder, its nature and conversion to the final phase(s), determine the temperature at which a fully dense ceramic can be obtained. The standard method for preparing ceria is by ammonia precipitation of cerium salts, e.g.

cerium nitrate [1]. The cerium compound is then washed with water several times to reduce the ammonia content and heated until dry. Variations using mixtures of ammonium hydroxide and ammonium carbonate [1] and urea decomposition [2] have also been used, giving homogeneous precipitation and often sub-micrometer powders.

Once a powdered material has been prepared, it must undergo a calcination step to convert the powder to the final oxide. The nature of the calcined powder is important in determining the ease with which a compact can be sintered. Critical powder characteristics include: particle size, particle size distribution, surface area, particle shape and powder density. Generally, a small particle size and high surface area give good sinterability. It has been suggested, that the optimum calcination temperature is when decomposition of the precipitate is just complete [3]. This temperature usually gives the highest powder surface area, with a small particle size. Calcination temperatures for ceria above 800°C are thought to produce poor quality powders. However, a suitably high temperature is necessary to ensure complete conversion to the oxide. Table 6.1 shows some of the reported calcination temperatures for pure ceria and the resulting sintering temperatures needed for high densities.

Powder Synthesis Route	Calcination Temp/Time	Sintering Temp/Time	Density	Ref
Coprecipitation	600°C/2hrs	1500°C/3hrs	>85%	[1]
Flash Combustion	500°C/5min	1450°C/1hr	>95%	[2]
Sol-Gel	600°C/2hrs	Not reported	Not reported	[4]
Coprecipitation using Hexamethylenetetramine	None	1250°C/6min	>95%	[5]

Table 6.1. Synthesis temperatures and densities of some pure ceria powders.

Once calcined, a powder is commonly pressed into a green body compact. This can be achieved either uniaxially or isostatically, or a combination of both. Increasing the pressure exerted on the powder increases the green density but large uniaxial pressures can lead to a layering effect within the compact, resulting in anisotropic properties during sintering. Isostatic pressing greatly reduces any layering effects. There is some evidence [5] to show that the isostatic pressure need not be very large in order to produce high sintering densities and emphasis is placed on the need for soft,

unagglomerated powders for good sinterability. Agglomeration is ubiquitous in normal powders and most research has demonstrated a higher density in samples which have been compacted at high pressures [6].

The pressed compact is finally sintered into a dense body, where the density will depend on both the sintering temperature and the length of time at this temperature. The density usually increases markedly as the temperature is increased and, to a lesser extent, as the sintering time increases. The atmosphere during sintering can also change the densification rate.

Some very interesting results have been observed by Baumard et al [7], who added small quantities of either Nb_2O_5 or TiO_2 to ceria as sintering aids. It was found that 0.1Wt% additions of TiO_2 achieved densities >99% after sintering at 1200°C/1hr but no evidence of liquid phase sintering was observed. While Nb_2O_5 introduces electronic conductors into the lattice and is thus not suitable in electrolyte applications, additions of TiO_2 to ceria requires no charge compensating defects. Titania demonstrates a higher resistance to reduction compared to ceria but it is uncertain what effect the fuel cell atmosphere would have on this dopant.

6.3. Preparation of Doped Ceria

For ceria to exhibit the conductivities required for SOFC applications, it is necessary to introduce aliovalent cations into the ceria lattice. Preparation of doped ceria is more difficult than that of pure ceria because of the introduction of additional cations. The majority of this thesis is concerned with gadolinia-doped ceria. Gadolinia is a refractory material, often prepared by the precipitation of gadolinium nitrate solution in ammonium oxalate [8], followed by calcination at 900°C and sintering at 1600°C/4hrs, to achieve densities >95%.

Due to the increasing importance of Gd-doped ceria for electrolyte applications, many researchers have been investigating methods to produce highly sinterable powders. The most widely used industrial technique is coprecipitation of the cations from a

suitable solution [9]. Commonly, cerium and dopant nitrate solutions are mixed with ammonium oxalate solutions [3], or oxalic acid [10, 11, 12]. The lowest sintering temperature achieved is currently 1200°C, after sol-gel evaporation of 20mol% Gd, Sm, La or Yb doped ceria at 100°C, and gave a crystalline, homogeneous, solid solution with a particle size of 5nm [13, 14]. The very small particles were thought to be responsible for the low temperatures needed for full densification. More commonly, sintering temperatures between 1400-1600°C are used, for times ranging from 1 hour to several days [15].

Polymeric production of doped ceria is also frequently adopted, using the standard nitrate precursors which are dissolved in water. These methods and other novel processing routes are described in chapter 9 [16].

The preparation technique and following heat treatments for doped ceria, can lead to extremely large variations in the microstructural and electrical properties of the final material. Amongst many other factors, the purity of precursors, degree of homogeneity resulting from the processing technique and particle size must be considered when comparing data from other researchers. The result of these complexities is that researchers often show conflicting data with differing explanations. There is still confusion as to whether the grain boundary conductivities are best explained by a 'blocking' model or a constriction model (these terms are explained fully in section 6.8.1.). The reported concentration of silicon at the grain boundaries also varies widely. High concentrations of silicon produce a glassy silica layer at the grain boundaries, which is thought to be responsible for the high resistance observed. However, ceria with low silicon concentrations also displays a relatively high resistance at the grain boundaries. In addition, producing ceria for electrical applications leads to some competing microstructural requirements. In a typical CGO electrolyte, the grain boundaries show a higher resistance compared to the bulk material at temperatures <500°C, thus a reduction in the number of grain boundaries during sintering, will reduce this resistance [17]. Larger grains generally imply mechanically weaker materials, while small grain sizes achieve the greatest strength but increase the number of grain boundaries. A compromise is necessary concerning the number of grain boundaries needed for optimum properties.

The calcination temperature of doped ceria will largely determine the nature of the powder and its sinterability. Table 6.2 shows a summary of various processing temperatures for differently prepared powders and the resulting densities obtained. It can be seen, that the mechanically mixed oxides generally require higher temperatures to achieve good densities. Van Herle [10] has suggested that the calcination temperature is not important because it only determines the primary particle size. It is suggested, that the particle agglomeration size determines the sinterability of the powder, where submicron size agglomerates achieve the highest densities.

Powder Synthesis Route	Calcination Temp/Time	Sintering Temp/Time	Density	Ref
Coprecipitation	350°C/1hr	1000°C/1½hr	83%	[3]
Coprecipitation	800°C/1hr	1400°C/4hrs	98%	[12]
Coprecipitation	700-800°C/ 1hr	1200°C/4hrs	96%	[10, 11]
Coprecipitation using trichloroacetic acid	620°C	1520°C/24hrs	>98%	[18]
Mechanically Mixed oxide	1000°C/1hr	1300°C/10hrs	~90%	[6]
Coprecipitation	1000°C/1hr	1300°C/10hrs	~90%	[6]
Mechanically Mixed oxide	1500°C/3hrs	1500°C/6hrs	~98%	[19]
Sol-Gel	1000°C/2-3hrs	1400-1450°C /6min	>95%	[20]
Coprecipitation	700°C/2hrs	1550°C/3hrs	>95%	[21]
Mechanically Mixed Oxide	1000°C/12hrs	1500°C/4days	88-95%	[27]
Coprecipitation	1000°C/12hrs	1500°C/4days	88-95%	[27]
Mechanically Mixed Oxide	1400°C/16hrs	1550°C/1hr	70%	[22]
Mechanically Mixed Oxide	1300°C/15hrs	1450°C/15hrs	94%	[22]
Mechanically Mixed Oxide	1300°C/10hrs	1650°C/15hrs	>95%	[23]
Mechanically Mixed Oxide	-	1550°C/6hrs	>95%	[24]
Mechanically Mixed Oxide	1350°C/10hrs	1650°C/15hrs	>95%	[25]
Mechanically Mixed Oxide	1300°C/8hrs	1800°C/2-3hrs	>96%	[26]

Table 6.2. Synthesis temperatures and densities of some doped ceria powders.

Experimentally, it is sometimes found that longer sintering times decrease the grain boundary conductivity [27, 28]. At first, this may seem contradictory because longer sintering times will allow more grain growth and consequently a lower number of grain

boundaries perpendicular to current flow. However, the thickness of the grain boundaries may increase with time and the degree of segregation will also increase. It is evident that the segregation of impurities plays an important role in terms of the grain boundary conductivity, which suggests shorter sintering times are preferable.

In samples where the density is below 95% of the theoretical density, open porosity is still present in the sintered compacts. For these materials a linear correction can be made to the electrical conductivity, σ, to compensate for the porosity [29], as shown in equation 6.1. In samples where the densities are greater than 95%, only closed porosity is present and the linear correction for porosity is not appropriate.

$$\sigma = \sigma_{measured} \times \frac{\rho_{theoretical}}{\rho_{measured}} \qquad (6.1)$$

where ρ is the density.

It is clear, that there are many variables in the production of dense ceramic materials and a large matrix of experiments would be needed to find the optimum conditions. The aim of this thesis was to use the simplest but most effective technique to produce dense ceria materials.

6.3.1. Impurity Effects

In the laboratory preparation of ceramic powders it is almost impossible to eliminate all impurities. Certain impurities can be present in relatively large concentrations and seemingly have very little effect on any observable property, while other impurities, present at a few ppm, can drastically affect the electrical properties. The important point is to determine which impurities cause the most problems in terms of sintering and ionic conduction etc. and to reduce these impurity levels.

The most common impurities detected in both powder and sintered doped ceria are Si, Ca, Na, Mg, K, Al, Fe and, in most cases, a number of other rare earth cations. These impurities all readily form oxides in the presence of oxygen and it is speculated that it

is the oxides that are present in all cerias. Only SiO_2 has received serious attention because of the high resistance exhibited in the amorphous phase. Silicon has a very small ionic radius (0.4Å), creating a very large elastic strain in the ceria lattice which produces a strong driving force for Si to segregate to the grain boundary. The effects of the other impurities and their interactions are still largely unknown.

The concentrations of these common impurities vary between materials because the starting precursors are supplied by different manufacturers, who generally supply materials with a choice of purities. Impurities can also be introduced during each processing stage, i.e. during sintering and milling, but these impurities can normally be minimised using standard precautions. Table 6.3 shows the wide variation in impurity levels detected by different researchers.

Material	Detection Technique	Si ppm	Ca ppm	Na ppm	Mg ppm	K ppm	Fe ppm	Al ppm	Ref
CGO	Emission spectroscopy	400	-	200	25	10	10	-	[3]
CYO	Flame emission AAS	<5	20	120	4	8	20	-	[18]
CGO	-	660	2400	880	-	400	-	200	[12]
CGO	Emission spectroscopy	400-1000	-	-	100	-	-	-	[6]
Ce-YSZ	-	753	-	1050	-	-	-	586	[30]
Ce(Ln)O	Spectroscopic analysis	1000	200	-	-	-	-	500	[31]

Table 6.3. Typical variation in measured impurity levels in ceria solid solutions.

The presence of these impurities in the bulk of the material is unlikely to greatly affect the properties of the electrolyte because of the high level of acceptor doping. There is, however, growing evidence of widespread segregation of many impurities to both the surface and grain boundary regions and further evidence of dopant segregation [21]. This topic is explored in more depth in section 6.4.

6.4. Dopant and Impurity Segregation

The majority of studies in which the surfaces and grain boundaries of doped ceria have been analysed, found significant concentrations of impurities present, compared to that in the bulk of the sample. However, in very pure samples (a few ppm) a grain boundary resistance was still observed. This has been attributed to the presence a space-charge region, in which the concentration of oxygen vacancies is depleted at the interface. In less pure samples, the grain boundary resistance is further increased by the segregation of impurities. The concentration of the dopant at the grain boundaries is usually different from the bulk composition and the role that the dopant plays at the grain boundary is still unclear.

XPS studies [30] have detected an enrichment of Si, Na, Al and dopant (Y) on the surface of powders as the annealing temperature increased, while the Ce signal decreased. This result suggests that Ce does not form part of the segregated phase but is covered by a layer of the other elements. It is speculated that a continuous Y-Na silicate chain was formed, which is capable of incorporating other impurities. Further XPS studies by Harrison [32] have shown that all rare earth dopants in ceria segregate to the surface. The degree of segregation increased as the temperature increased, covering in excess of 2 monolayers at 1450°C.

The results of the surface analysis of sintered CGO pellets using low energy ion scattering [33] found calcium to be most prominent at the surface, with smaller signals for Si and Na. The calcium rich layer extended about one monolayer in thickness. There also appeared to be some Gd enrichment in the near surface region, which extended between 5-10 monolayers before the bulk composition was reached. The segregation of impurities and dopants to the grain boundaries is expected to behave similarly to that at the surface. Thus, a higher Gd concentration would result in a lower conductivity because both gadolinia and highly doped ceria (>30mol%) are poorer ionic conductors.

Analysis of the grain boundary region in ceramics has been performed by Christie [17] using HRTEM on relatively pure CGO. Si and Ca were detected as the predominant

impurities at the grain boundaries, but, lattice images revealed direct grain-to-grain contact with no visible second phase material for all grain boundaries studied. This is the first direct information which suggests that impurity free grain boundaries still retain a high resistance and that the segregation of impurities serves only to increase this resistance.

Steele [34] has analysed the a.c. conductivity of a number of dilute ceria solutions and has found a trend between the dopant ion radius and resistance of the grain boundary. For dopants larger than cerium, i.e. Ca^{2+}, the grain boundary resistance is lower than the bulk resistance and it is suggested that calcium segregation to the grain boundaries produces an increase in the conductivity. For similar sized dopants, i.e. Gd^{3+}, the grain boundary resistance is larger than the bulk resistance but little dopant segregation is expected and the high resistance is related to a space-charge region. For smaller dopants, i.e. Y^{3+}, the grain boundary resistance is again found to be higher than that of the bulk but is now associated with a depletion of the dopant from the boundary region, which not only lowers the oxygen vacancy concentration but also lowers the conductivity.

Duran [12] using microprobe analysis, found the concentration of Gd in both 8% and 16% $GdO_{1.5}$ doped ceria to increase at the grain boundaries. Reiss [6] suggests that a Gd concentration gradient, increasing at the grain boundaries, will exist in all heterogeneously mixed samples and that this gradient is reduced below detection limits in homogeneous samples. More recent reports have shown segregation of dopants in supposedly homogeneous, wet chemically prepared ceria, which suggests that segregation occurs in all samples. The degree of segregation becomes more prominent at high temperatures and thus lowering the preparation/sintering temperature should reduce the segregation of dopants and impurities to the grain boundaries and improve the ionic conduction across them [13].

Gerhardt et al. [31, 35] have analysed a Ce-6%Gd sample using a.c. impedance and demonstrate considerably higher grain boundary conductivities in silicon free samples (<10ppm), while the bulk conductivities remain similar. TEM studies of the higher Si concentration samples showed a thin (<1nm) amorphous Si phase around all grains

and, in addition, thick (50nm) amorphous Si layers which surrounded agglomerates of grains. The thicker grain boundary layers are probably the result of high Si contents (1000ppm), which would form after all the grains have been covered by the initial thin Si layer. As well as an amorphous phase, Si is thought to form one of two stable crystalline phases with the dopant ions at the grain boundaries, e.g. $Y_2Si_2O_7$ and Y_2SiO_5. Increasing the dopant concentration increases the proportion of Si that forms the crystalline phases and therefore less Si is available to form the high resistance amorphous phase. Thus, as the dopant concentration increases, the grain boundary conductivity should increase, too. This is a common observation in most doped ceria samples [35, 36].

6.5. Dilute Solution Theory

When studying the defect behaviour of doped fluorites, it is necessary to distinguish between high and low defect concentrations. In the low defect concentration region, all defects are assumed to be free to move within the lattice and not interact with other defects. In the high defect concentration region, defect interaction will occur, resulting in clustering and, in the extreme, formation of a second phase. Using these descriptions, it has been established that most doped ceria electrolytes fall into the latter category.

It is practically impossible to achieve the ideal low defect concentration region but theoretical and experimental evidence suggest that the low concentration region can be extended to include a limited degree of defect interaction. The electrical properties in these low defect concentration materials can be explained by the *dilute solution theory*. There is some disagreement in the literature, as to what is considered a dilute solution, which further varies for different dopants in ceria. A common assumption is that a dilute solution contains only simple associates (dimers) and charged dopants/defects, randomly distributed and with limited interaction. Associates normally form at low temperatures and so a calculation of the activation energy for conduction needs to consider the migration enthalpy and an association enthalpy term. In most ceria solutions (except very pure), the impurity levels are such that dopant concentrations

>0.1mol% are required to dominate over the electrical effects of impurities [29]. The maximum dilute solution concentration is often put at 1mol% dopant, which leaves a very restricted experimental dopant concentration range for study.

A common trend observed in doped cerias is an approximately linear increase in the ionic conductivity as the dopant concentration increases until a maximum, after which the conductivity decreases. The increase in conductivity is a result of the increased oxygen vacancy concentration as the dopant concentration increases. The maximum is a result of the higher degree of defect interaction, which reduces the number of free oxygen vacancies and leads to a decrease in the conductivity as more complex defect associates form. It therefore seems logical to define a dilute solution as one where the dopant concentration is less than that required to produce a maximum in the isothermal conductivity. Above the maximum, the solution is considered concentrated. For dopants where their solubilities are lower than the level expected to produce the maximum conductivity, e.g. Sc in CeO_2, an additional criterion must be applied. This states that a dilute solution must also be one, in which the dopant is present in a concentration less than its solubility limit.

Although the dilute solution theory can be used to explain the maximum obtained in conductivity for the bulk material, in polycrystalline samples, at low temperatures, the grain boundaries also contribute to the resistance of the electrolyte. In order to determine the best conducting electrolyte both the bulk and grain boundary conductivities need to be optimised and consequently the concentration which gives the highest bulk conductivity may not give the best total conductivity.

6.5.1. Defect Association

The ideal ceria electrolyte is one in which all the oxygen vacancies are free to conduct oxygen ions. In reality, all doped cerias show some degree of defect association, which reduces the number of free oxygen vacancies and ultimately lowers the ionic conductivity. The type of associate formed and the energy which binds the defects together, is determined by the type of dopant. There are two contributions involved in the formation of an associate. Firstly, there is a Coulombic interaction between the

oppositely charged oxygen vacancy and dopant ion and secondly, there is a reduction of the elastic strain in the lattice. Therefore, both the charge and size of the dopant ion are important factors in the formation of associates. In dilute solutions at low temperatures, oxygen vacancies are thought to form simple associates. Larger clusters of dopant-vacancies are statistically unlikely due to the random distribution of the dopant ions. Thus, it follows that for divalent dopants, e.g. Ca, neutral associates are formed, while for trivalent dopants, e.g. Gd, charged associates form, i.e.

$$\left\{Ca''_{Ce}V_O^{\bullet\bullet}\right\} \qquad \text{and} \qquad \left\{Gd'_{Ce}V_O^{\bullet\bullet}\right\}^{\bullet}$$

Kilner [37] has derived the activation energies, E_a, for ionic conductivity for di- and trivalent dopants in ceria at low temperatures and found that for divalent dopants,

$$E_a = \Delta H_m + \Delta H_a/2 \qquad (6.2)$$

while for trivalent dopants,

$$E_a = \Delta H_m + \Delta H_a \qquad (6.3)$$

where ΔH_m is the migration enthalpy and ΔH_a is the association enthalpy. The migration enthalpy in the fluorite structured oxides is very similar (CeO_2, ΔH_m=0.61eV, ZrO_2, ΔH_m=0.68eV), suggesting that the vacancy migration in the fluorite oxides is more dependent on the structure than the dopant type and size. If this is true, then the differences observed experimentally are dependent on the association enthalpies. As the temperature is increased, the defect pairs dissociate, leaving free oxygen vacancies. This change to free vacancies can be seen on an Arrhenius graph of conductivity by a decrease in the activation energy (reduced gradient). In this temperature regime $E_a = \Delta H_m$. For high values of ΔH_a, full dissociation will not occur until much higher temperatures and these materials will display lower conductivities. At very high temperatures, intrinsic anti-Frenkel defects are expected in ceria, but in practice this is not observed below the melting point. The formation of intrinsic defects is usually associated with a high activation energy. An idealised Arrhenius graph for the bulk conductivity in doped ceria is shown in Fig.6.1. Within each region

the activation energy remains constant but there are curved sections on the Arrhenius graph at the transition between each region. The association enthalpies of the divalent dopants are generally higher than those of the trivalent dopants (Ca: E_a = 0.64eV, Gd: E_a = 0.12-0.3eV), owing to higher electrostatic interactions.

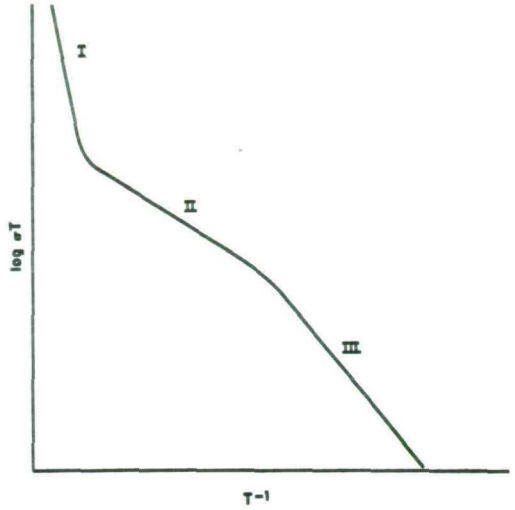


Fig.6.1. Idealised bulk conductivity graph for doped ceria showing regions I (intrinsic), II (extrinsic, dissociated) and III (extrinsic, associated), from Nowick [38].

A number of experimental and theoretical studies on ceria electrolytes with an isovalent series of dopants, show that the activation energy is minimised, when the size of the dopant and cerium ions are similar [39]. Assuming that the migration enthalpy remains constant for all dopants, it appears that dopant ions with a similar radius to the lattice cerium ions form associates with the lowest binding enthalpy. By comparing the ionic radii of a range of dopants in ceria, it is found that the best matched divalent dopant is calcium, while the best matched trivalent dopant is gadolinium. Experimentally, it is found that calcium has the highest conductivity among the divalent dopants and gadolinium has the highest conductivity of the trivalent dopants. Butler [39] was able to calculate the binding energies of an oxygen vacancy with more than one surrounding Gd ion and found that the association enthalpy increased only slightly and in fact became negative when four Gd ions were present, which suggests that this sort of cluster is unlikely.

It has also been found that there is a much greater size dependence for dopant ions smaller than cerium, than for larger dopant cations (see Fig.6.2). A larger reduction in

the lattice strain is created by forming an associate in the case of small dopant cations resulting in a larger elastic energy contribution and consequently, the binding energy for the pair is large. These results suggest that the electrostatic interactions make only a small contribution to the activation energy and it is the lattice relaxation effects which dominate the association enthalpy. At higher temperatures where all defects are free it is expected that the activation enthalpy of all equally doped cerias is similar and is only dependent on the migration enthalpy. The temperature at which defects are considered free, is normally above the temperatures at which the material is likely to be operated.

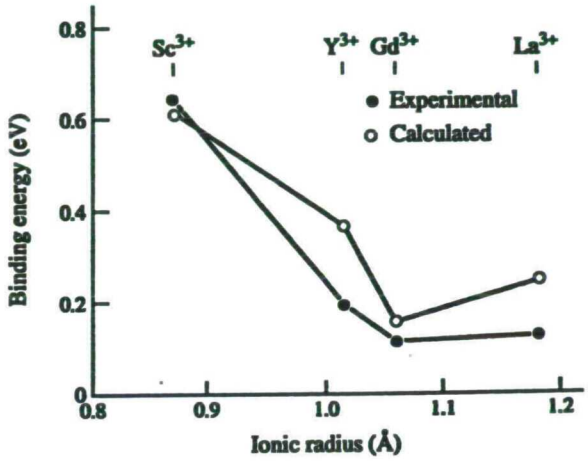


Fig.6.2. Graph showing the experimental and calculated effects of dopant ion size on the association enthalpy in the ceria lattice for trivalent dopants. Ionic radii are obtained from lattice parameters [40].

The simplistic assumption that similarly sized host and dopant ions produce the best conductivities has been extended by Kim [41]. Kim shows that minimising the difference between the host and dopant cations is not sufficient to explain a number of the conductivity results for different dopants and suggests that the valence of the dopant must also be included. Calculations show that the elastic strain in the host lattice is minimised, when the dopant cations have an ionic radius slightly larger than that of the host, denoted by r_c, the critical ionic radius. The value of r_c for divalent and trivalent dopants was calculated to be 0.1106nm and 0.1038nm respectively. Again Ca and Gd doping produced the closest radii, with the results for other dopants now following the trend for higher electrical conductivity as the dopant radius approaches r_c. In addition, these calculations were also used to determine the solubility limits of

different dopants, suggesting that the solubility of a cation increases, the closer its radius is to the host. The dopant size is also important in concentrated solutions but the formation of more complex associates makes theoretical models difficult. Experimental data in this regime will be discussed later.

Kilner [42] has shown that better quality information on the relative radii of the host and dopant cations may be obtained from a lattice parameter map. Fig.6.3 shows a plot of the cubic lattice parameters for a number of host fluorite lattices and the pseudo-cubic lattice parameter for a number of rare earth oxides. It is clear, that ceria has a much larger selection of closely matched dopants compared to zirconia or thoria and this explains why ceria exhibits the highest conductivity in the fluorite structured oxides. Bevan and Summerville [43] have studied the variation in the fluorite lattice parameter, as a function of dopant concentration for trivalent dopants. Fig.6.4 shows how little the lattice parameter changes as gadolinia is added, indicating that the strain energy in the lattice is minimised. It should be mentioned here, that the oxygen vacancies will also affect the lattice parameter because they tend to expand the lattice and so care must be taken when interpreting lattice parameter data.

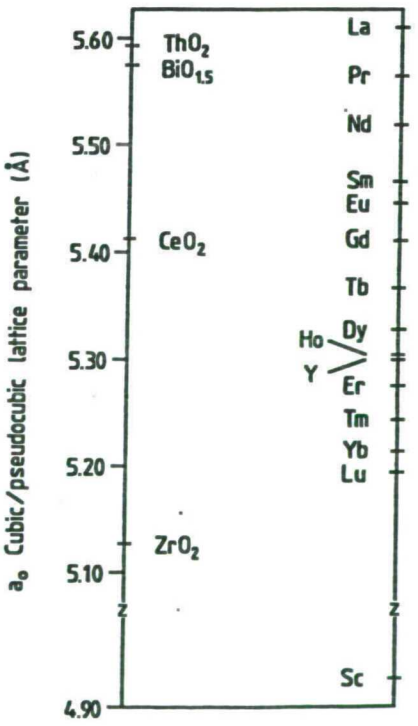


Fig.6.3. Lattice parameter map showing host lattices and rare earth oxide dopants [44].

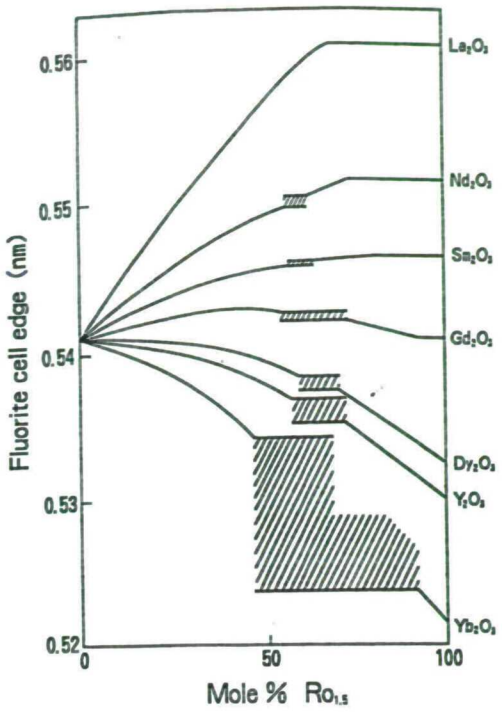


Fig.6.4. Effect of dopant concentration on the ceria lattice parameter [45].

6.6. Cation Mobility/Grain Boundary Mobility in Doped Ceria

The mobility of the oxygen ions in the fluorites is much higher than the mobility of cations and hence, it is the cations that determine the rate of material transfer during processes such as sintering. Dopant cations can also change the rate of grain growth. Surprisingly, there are only a few studies concerning the mobility of cations in ceria and these are generally limited to dilute or near dilute solutions (<1%) [46, 47]. In these studies, diffusion of the cations is thought to occur via an interstitial mechanism, which is enhanced by the introduction of oxygen vacancies, that provide pathways with lower energy barriers for diffusion.

In contrast to smaller dopants, such as scandium and magnesium, larger dopants, such as yttrium, were found to be better at suppressing grain boundary mobility. It was also found, that increasing the dopant concentration (for larger ions) in ceria reduced the grain size, again demonstrating suppression of the grain boundary mobility [19]. This

suppression of mobility can be explained by the creation of a space-charge region and the solute drag effect, explained below.

When considering trivalent dopants in ceria, half of the dopant ions are not associated with oxygen vacancies and have an effective negative charge. For the surface of each grain to be electrically neutral, a counterbalancing positive charge must exist. Coulombic attraction then causes segregation of the negatively charged dopant to the positively charged surface, to form a space-charge region. Implicit in this model is the presence of an enrichment layer of solute and impurity ions at grain boundaries.

In dilute solutions of ceria (1%), the grain boundary mobility was found to be lower than that of undoped ceria. Therefore, enhancement of mobility due to an increase in oxygen vacancies concentration does not fully explain the observed grain boundary mobility. The solute drag must also be considered, in which the dopant concentration gradient between the bulk and grain boundaries offers a strong drag to the boundary mobility, thus retarding grain growth. Therefore it follows, that higher dopant concentrations result in smaller grain sizes. The formation of defect clusters may further increase the drag effect.

Undersized dopants such as Nb^{5+}, Ti^{4+}, Sc^{3+} and Mg^{2+}, have an anomalous effect on grain boundary mobilities. These undersized dopants enhance grain boundary diffusion at concentrations >1%. Sc^{3+} causes a large increase in grain boundary mobility but its size reduced the ionic conductivity, due to association of defects. Ti^{4+} on the other hand, should have no attractive charge in the fluorite lattice and thus show no electrostatic attraction to oxygen vacancies. This may explain the results of Baumard [7], discussed in section 6.2, where high sample densities were achieved at low temperatures with additions of TiO_2.

The cation diffusion coefficients in ceria are about six orders of magnitude lower than those associated with anion diffusion coefficients at 1000°C [48]. The cation transport number in CeO_2-2%Y_2O_3 has been reported to be less than 0.004 at 1000-1100°C [48]. A recent study by Sirman et al. [49] has measured the diffusion of Fe and Co into CGO using secondary ion mass spectrometry (SIMS). The results showed a high activation

energy for cations diffusion (~6eV) and the formation of no reaction products between ceria and Fe and Co. A measured diffusion coefficient of around $10^{-15}cm^2s^{-1}$ confirms the low values discussed previously. The difficulty of accurately measuring such low mobilities explains the lack of published data but more results are essential, if the sintering behaviour of these materials is to be improved.

6.7. Ionic Transference Number

Electrolytes for use in SOFC applications, will experience reduced oxygen partial pressures, which lead to a certain degree of mixed ionic and electronic conduction. In order to specify the proportion of the total conductivity that results from each species, it is convenient to define a parameter known as the *transference* or *transport number*, *t*. In the case of electrolytes, it is the ionic conductivity that dominates and therefore the ionic transference number, t_i, can be defined as,

$$t_i = \sigma_i /(\sigma_i + \sigma_e) \qquad (6.4)$$

where σ_i is the ionic conductivity and σ_e the electronic conductivity. In most electrolyte applications, the ionic transference number should be close to unity. This is the case for most rare earth doped cerias in air below 1000°C [23, 26]. When measuring the total conductivity of a sample, the ionic conductivity can be obtained by multiplying the total conductivity by this ionic transference number.

There are now two standard uses of the ionic transport number to permit comparisons between different electrolytes: either the oxygen partial pressure above which t_i is very high, i.e. 0.99, or the oxygen partial pressure for which t_i=0.5, is quoted. The latter can usually be calculated to a higher accuracy and is the most common value quoted. The electrolytic domain has already been introduced in the previous chapter, as the region on a logσ versus logP_{O_2} graph, where ionic conductivity is dominant. The value of t_i=0.5 can be marked on this type of graph and is commonly referred to as the P(–) point.

6.8. Conduction Mechanisms

It was shown in Chapter 5, that ceria and doped ceria show both ionic and electronic conduction and, in some circumstances, mixed conduction, depending on the conditions within which the material is placed. At lower temperatures and high oxygen partial pressures, the conductivity is predominantly ionic and is independent of P_{O_2}. At high temperatures and low oxygen partial pressures, the conductivity is predominantly electronic and the magnitude of the conductivity is similar to that of pure ceria. The ionic conductivity can normally be expressed by the Arrhenius equation:

$$\sigma_i = \frac{\sigma_O}{T} \exp\left(\frac{-E_i}{RT}\right) \qquad (6.5)$$

By plotting a graph of $\log\sigma_i T$ verses 1/T, the activation energy for the conduction process, E_i, can be calculated from the slope of the line. The pre-exponential term is calculated from the intercept on the y-axis. Using impedance spectroscopy, it is possible to separate the bulk and grain boundary impedances and allow for Arrhenius graphs of the bulk, grain boundary and total conductivities. Values for the activation energies can then be compared. Unfortunately, most published data concentrates on either the bulk or the total conductivities and a complete picture of the material cannot be obtained. Four-point d.c. conductivity measurements are useful for a comparison of the total conductivities between a.c. and d.c. techniques but provide no information on the bulk or grain boundary conductivities. Early studies on ceria have used fixed frequency a.c. techniques. Care must be taken when analysing this type of data because it is difficult to distinguish between bulk and grain boundary data when the temperature is increased. Therefore, any results obtained by this method are of limited value.

6.8.1. Grain Boundary Conductivity

As mentioned already in doped ceria ceramics, 'clean' grain boundaries still exhibit higher resistances compared to that of the bulk material. The higher resistance is a

result of the atomic lattice mismatch between adjacent grains and the resulting electrical disturbance induced in this region. Space-charge regions, analogous to the Schottky barriers in semiconducting materials, serve to retard the movement of oxygen ions across the grain boundary regions and thus to increase their resistance. When segregation and impurity effects are considered at grain boundaries, the situation becomes very complex and a comprehensive understanding of the conduction mechanisms in most ceramic systems is not available.

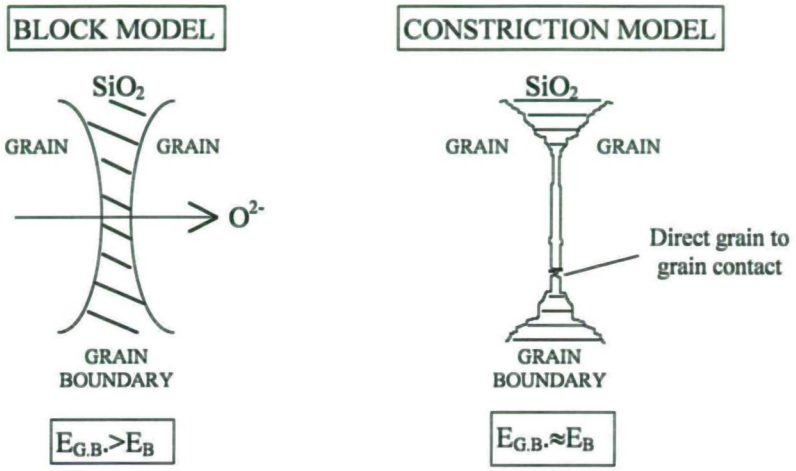


Fig.6.5. Schematic representation of the two grain boundary models.

To explain the grain boundary effects in zirconia and ceria electrolytes, two models have been proposed (Fig.6.5). The constriction model, first considered by Bauerle [50] for YSZ, found that the activation energies of the bulk and grain boundaries were similar and so concluded that their conductivities must also be similar. The model consisted of a non-continuous impurity phase at the grain boundaries, with constricted regions of direct grain to grain contact, displaying a conductivity of similar magnitude to the bulk. A number of studies on ceria electrolytes have shown that the bulk and grain boundary activation energies are different [27, 51]. The alternative blocking or brick layer model has been used for ceria because the higher grain boundary E_a suggests the presence of a different material at the grain boundary, in the form of a continuous layer around the grains.

In a study of calcia doped ceria [52], the brick layer model was used to compare calculated and experimental values for the bulk conductivity. Single crystal and

polycrystalline materials were measured and the bulk resistance calculated according to equation 6.6 (where ρ is the resistivity),

$$\text{Bulk Resistance} = \frac{\text{Number of Grains} \times \text{Grain Size}}{\text{Surface area of sample}} \times \rho_{\text{single crystal}} \qquad (6.6)$$

The model assumes that the grain boundary thickness, l_{gb}, is much less than the grain thickness, L_g. When the grain boundary calculations using a bicrystal were compared to the polycrystalline sample, a sharp disagreement was obtained. The polycrystalline grain boundary resistance was an order of magnitude lower. These results suggested that a continuous grain boundary phase was not possible and a constriction type approach was used to explain the grain boundary effects. In this case, it was thought that the grain boundaries were composed of areas of intimate contact with a low resistance, and air gaps, which were blocking to ion flow. The air gaps were calculated to be ~230Å thick and provided the dominant contribution to the grain boundary capacitance.

When trying to calculate the true resistance of the grain boundaries, it is often difficult to assign a grain boundary thickness for the purpose of calculations. Early reports used $C=\varepsilon_0\varepsilon_R A/l$ (where ε_R is the relative permittivity of the bulk) to show that a simple ratio between measured bulk and grain boundary capacitances (equation 6.7), could indicated how much smaller the grain boundaries were compared to the grain size.

$$\frac{C_b}{C_{gb}} \approx 1/1000 \qquad (6.7)$$

Tanaka [21] used this relationship and the simple blocking model to calculate the grain boundary thickness to be 50nm.

6.9. Alkaline Earth Dopants

There are now a large number of dopants that have been added to ceria. Some of the earliest dopants used to increase the ionic conductivity of ceria were the alkaline earth

oxides. MgO, CaO, SrO and BaO all enhance the conductivity of ceria but it is generally found that CaO doping achieves the highest conductivity. When a dopant is added to ceria above its solubility limit, a second phase will precipitate from the solid solution. In the case of the alkaline earth oxides, the second phases that precipitate are, MgO, CaO, $SrCeO_3$ and $BaCeO_3$ [53]. Lattice parameter measurements show that the solubility limit of CaO in CeO_2 is around 23mol% and is the highest of the alkaline earth oxides because of the close matching between the Ca^{2+} and Ce^{4+} ionic radii. For SrO, the solubility limit is about 8mol%, while those of MgO and BaO are very low. The alkaline earth solubilities are generally lower than the rare earth elements and only CaO doping has seriously been considered in electrolyte applications. Originally, CaO doping was preferred to Y_2O_3 or rare earth oxides, based on its lower cost.

Studies show, that small additions (0-5mol%) of both CaO and SrO to ceria produce a marked increase in the total conductivity [53]. At 10mol%, both dopants show similar total conductivities, whereas magnesia and baria show conductivities two orders of magnitude lower. Above the solubility limit of SrO, a second phase precipitates and the conductivity decreases. CaO doping produces a maximum total conductivity at about 11mol% CaO [54] but the conductivity decreases only gradually up to concentrations of 50mol% CaO [55]. This is a rather surprising result because the solubility limit of CaO in ceria is around 23mol% and thus a large amount of second phase material would be present at a doping level of 50mol%. It would appear, that the second phase thus disperses uniformly within the doped ceria solid solution and causes very little hindrance to the flow of oxygen ions.

Aria [55] and El Adham [54] found that increasing the CaO content increased the ionic domain of ceria in reducing environments, such that at 50mol% the ionic domain extended beyond 10^{-16}atm at 800°C. For calcia doped ceria in the ionic domain, the electronic transference number, t_e<0.1 up to 1000°C and was found to decrease linearly with temperature [27]. The ionic transference numbers for both CaO and SrO doped CeO_2 were close to unity between 600-900°C. For CaO doping between 2-50mol%, t_i remained between 0.98-1, over a similar temperature range [56, 57]. The ionic transference numbers for MgO and BaO doped ceria were between 0.5-0.8 over this temperature range [53], which can be explained by their lower ionic conductivities.

The ability of ceria to accept very large dopant concentrations of calcia without significant decrease in the maximum ionic conductivity and the suppression of electronic conductivity in reducing atmospheres at these high dopant levels, warrants further research into this material. The high calcia concentrations could also significantly reduce the cost of the electrolyte.

6.9.1. Scandia and Yttria Doped Ceria

Both scandia and yttria have received attention as dopants in ceria. Scandia shows some anomalous effects on the electrical conductivity, due to its small size and these will briefly be discussed below. Yttria doped ceria displays a conductivity only slightly lower than the best rare earth dopants but achieves a significant cost reduction. For SOFC applications where ceria may be coated by a thin layer of YSZ, yttria doping will also reduce the problem of cation inter-diffusion within a cell.

Most of the research on yttria doped ceria shows the same trends as those of the rare earths, which are described in the next section. However, there are some experiments which add to the knowledge of doped ceria. There are few studies that investigate the nature of a complex defect cluster. Two techniques that have been used with limited success are EXAFS [58] and neutron diffuse scattering [59]. The latter technique has been used in the study of yttria doped ceria. In 10-30mol%$YO_{1.5}$ doped CeO_2, it was found that experimental and defect model calculations were in good agreement for a cluster consisting of two oxygen vacancies along a ⟨111⟩ diagonal, associated with 3-4 nearest neighbour yttrium ions [60].

EXAFS studies performed on Sc and Gd doped ceria [58] were able to probe the local environment of individual ions and showed that Gd was randomly distributed in a 20mol% solid solution, with no ordering. In Sc doped ceria, extensive ordering had occurred, which is a result of the lower solubility limit of scandia in ceria and the very small ion size of Sc^{3+}, causing clustering of these ions which reduces the lattice strain. In a mixed Sc-Gd doped ceria, the Sc^{3+} ion had scavenged all of the oxygen vacancies introduced by the Gd^{3+} ion, leaving Gd largely unassociated. These results strongly

suggest that for diffusion and ionic conductivity, it is the local structure and short range order that is most important.

A study by Wang [27, 51] using Y doping, proposes the large grain boundary resistances measured at low temperatures and low dopant concentrations to be a result of dopant scavenging from the grain boundaries by impurities. The composition of the grain boundaries would then be close to that of pure ceria, which has a much lower ionic conductivity compared to doped ceria. In addition, the grain boundary E_a was calculated as >2eV, which is close to the single crystal ceria value of 2.4eV. It was also found that the grain boundaries are more susceptible to reduction than the lattice, which would be the case for near pure ceria at the boundaries. The increased reduction at the grain boundaries in this case, suggests that the impurities are not involved in the high resistances of these boundaries because of their highly stoichiometric nature.

The introduction of charged defects and defect associates into doped ceria, constitutes the formation of electric and elastic dipoles in these materials. Using dielectric or anelastic relaxation techniques, it is possible to measure the resonant frequency of each dipole as a function of temperature. Each different dipole displays a peak at a certain temperature and it is therefore possible to assign the nature of the dipole for each peak. Experiments and theoretical calculations have been performed on a number of dopants in the dilute solution regime (<1mol%) and have shown very close agreement. Generally, at a frequency of 8kHz, a relaxation peak can be observed for all trivalent dopants between 165-450K. It has been shown, that this relaxation peak is a result of dopant-vacancy associates. The relaxation activation energy for the reorientation jump, i.e. for a jump in which an oxygen vacancy remains bound to the dopant ion, is found to be 0.41eV for Sc^{3+}. This value is considerably less than that for Y^{3+} or Gd^{3+} of 0.65-0.67eV [61, 62] and Ca^{2+} of 0.82eV [63].

Much of the relaxation research has concentrated on the properties of scandia doped ceria. Electrical measurements have shown this material to have a very low conductivity compared to other trivalently doped cerias. This low conductivity has been attributed to the high dopant-vacancy association enthalpy of this material. In this, Sc^{3+} acts as a scavenger for oxygen vacancies, in an attempt to reduce the high

lattice strain energy caused by the introduction of this dopant. Relaxation measurements have shown that scandia has a unique low temperature peak (125K), which results from an isolated, off centre Sc^{3+} ion (or, more correctly, a displacement of the adjacent oxygen ions). The relaxation enthalpy, H_R, for this process was calculated to be ~0.2eV. All other dopants must therefore occupy the correct lattice positions in the cubic structure and do not give rise to a relaxation peak of this type.

Higher temperature relaxation peaks are also found for Sc^{3+} and are attributed to larger defect clusters. It therefore appears likely, that scandium-oxygen vacancy associates remain bound to temperatures >1000°C and that they also form more complex clusters, which remain to high temperatures. Other trivalent dopants do not show higher temperature relaxation peaks at concentrations <1mol% and the assumption that the dopant ions are essentially frozen in below 1000°C, in a random distribution, is valid. This does not seem to be the case for scandia.

For concentrations >1mol%, defect clusters will be present for all dopants and the relaxation enthalpy is larger than for simple associates [64]. Therefore, it may be energetically more favourable for an oxygen vacancy to jump to a new dopant ion, than for it to re-orientate around the existing dopant ion. Also, some defect clusters will have zero electric dipole moment and so will not contribute to dielectric relaxation (or impedance spectroscopy) measurements.

Some double doping experiments have been performed using Sc^{3+} and Y^{3+} as the dopants. It is found that the Sc^{3+} ions scavenge all of the oxygen vacancies introduced by the Y^{3+} ions. It is not possible to determine the effects of lattice strain reductions with these dopants because both have an ionic radius lower than the critical radius for the ceria lattice.

6.10. Rare Earth Dopants

Over the past two decades, ceria doped with rare earth oxides has been shown to produce higher conductivities compared to the alkaline earth oxides. While there are

some reports of ceria doped with La_2O_3 [65, 66], Pr_2O_3, Nd_2O_3, Eu_2O_3, Tb_2O_3, Dy_2O_3, Ho_2O_3, Er_2O_3, Tm_2O_3, Yb_2O_3 and Lu_2O_3 [67, 68, 69, 70], most of the research has concentrated on Gd_2O_3 and Sm_2O_3. These two dopants achieve the highest conductivities in ceria and while there is still some controversy as to which dopant is the best, the differences between them are marginal.

There are many trends that are observed in the electrical conductivity of these materials but there are no reports that fully analyse these trends. The following section provides a discussion of these trends that, unless stated, apply to both divalent and trivalent dopants.

AC impedance studies allow both the resistance and capacitance of the bulk and grain boundaries to be determined. When an Arrhenius plot of the bulk conductivity is drawn, a change in the slope of the graph occurs at a certain temperature [71]. The change in gradient is generally considered to be the transition from associated to unassociated behaviour of the dopant and oxygen vacancies [71]. The grain boundary conductivity is always observed to be linear with temperature and no change in slope has been reported [52]. At low temperatures, the grain boundary conductivity is normally lower than the bulk conductivity but has a higher activation energy. Thus, at a certain temperature there will be a cross-over in their conductivities. Above this temperature, the grain boundary conductivity becomes less blocking to current flow compared to the bulk. The result of this change-over is that the total conductivity displays a change in slope at a certain transition temperature, exhibiting a lower activation energy at higher temperatures [53]. The measured transition temperature varies by several hundred degrees between results presented by different researchers, which has a number of explanations.

Overs [3] and Riess [6] suggest this variation is a result of non-uniform distribution of the dopant in each grain. This is unlikely because the variation in bulk conductivities shows very little difference between researchers [18]. The most likely cause of variation can be attributed to the grain boundaries. The wide variation in measured grain boundary conductivities and activation energies for nominally the same compositions can easily account for large differences in the transition temperature.

Further, it is normally shown that the grain boundaries have lower activation energies at higher dopant concentration, which shifts the transition temperature to higher values [54].

For di- and trivalent dopants, the bulk conductivity commonly displays a maximum between 6-11mol% dopant concentration, although the peak becomes broader at higher temperatures. For divalent dopants, the bulk activation energy remains approximately constant with increasing dopant concentration. The maximum in conductivity results from an increased number of oxygen vacancies, which at a certain concentration start to form more complex defect clusters and thus lower conductivity. For trivalent dopants, the bulk activation energy displays a minimum at approximately the same concentration as that which produces the maximum conductivity. However, the maximum conductivity and minimum activation energy are not always associated with similar dopant concentrations because the pre-exponential is also a function of temperature. The maximum conductivity, therefore, depends on temperature as well as dopant concentration. The minimum in E_a is thought to be the result of interactions between the partially compensated associates and the free dopant ions. As the dopant concentration increases, higher energy vacancy traps are introduced, increasing the activation energy.

Faber [67] suggests, that the relaxation of neighbouring ions around a defect screens the coulombic field of the defect charge and thus prevents any long range electrostatic interactions between defects. Instead, each defect has a critical radius, R_c, over which it will interact with other defects. This radius has been found to extend to 3rd or 4th nearest neighbour sites. When an oxygen vacancy enters this sphere of influence, the activation energy for conduction decreases. As more concentrated solutions are formed, more low energy pathways are created. A competing reaction in more concentrated solutions is the deep trapping of oxygen vacancies with more than one dopant ion. In sufficiently concentrated solutions all the oxygen vacancies are deeply trapped and E_a increases. These two reactions result in a minimum in E_a. The value of R_c determines the value of ΔH_A and appears to be high for similar sized dopants to cerium, e.g. Gd, where ΔH_A is minimised.

The grain boundary conductivity generally increases with increasing dopant concentration. There are some reports that show a maximum in the conductivity at high dopant concentrations (>25mol%) [36], while others papers report a vanishing grain boundary component [72]. The activation energy for the grain boundary is found to display a minimum for both divalent and trivalent dopants [27, 52], although the minimum is generally very broad and occurs at high dopant concentrations (16-26mol%) [54].

Therefore, the total conductivity displays a maximum at a concentration slightly lower than that of the grain boundary conductivity (~20mol% [36]), with a broad minimum in the activation energy.

Christie [17] has performed a detailed analysis of conductivity as a function of grain size. While the bulk E_a remained constant with increasing grain size, the grain boundary E_a increased. The capacitances measured for the bulk, grain boundary and total responses should remain constant over the temperature range of the experiment [27, 35]. The bulk capacitance was found to be constant for different grain sizes, although the grain boundary capacitance increased linearly with grain size [17]. The measured capacitance is only an apparent capacitance for all the grain boundaries and a correction factor must be used to calculate the true capacitance of a single grain boundary. The number of grain boundaries can be calculated from equation 6.8.

$$\text{Number of Grain Boundaries} = \frac{L}{d_g} - 1 \qquad (6.8)$$

where L is the thickness of the sample and d_g is the average grain size. The measured capacitance can then be used to calculate the grain boundary thickness, δ_g, using equation 6.9 which has been derived by Bonanos [73].

$$\frac{\delta_{gb}}{d_g} = \frac{C_g}{C_{gb}} \qquad (6.9)$$

where C_g and C_{gb} are the capacitance of the bulk and grain boundary. Using this equation, the grain boundary thickness was calculated to be 3nm and remained constant for all grain sizes. Equation 6.9 is only strictly correct if the bulk and grain boundary relative permittivities are equal, which is unlikely when a second phase is present at the grain boundaries and care must be taken when using these figures. A similar process can then be used to calculate the true grain boundary conductivity, using equation 6.10.

$$\sigma_{gb}^{true} = \frac{\delta_{gb}}{d_g}\sigma_{gb} \qquad (6.10)$$

It was found that the true grain boundary conductivity remained constant as the grain size increased, indicating that the decrease in the total grain boundary conductivity is primarily due to an increased number of grain boundaries. It is speculated that a chemical processing route leads to thinner grain boundaries and thus increased capacitance, *C*, according to equation 6.11.

$$C=\varepsilon_0\varepsilon_R A/l \qquad (6.11)$$

Experimentally, it was found that both resistance and capacitance were increased for the chemically prepared material, compared to a solid state preparation [18]. Thinner grain boundaries indicate a lower resistance ($R=\rho l/A$). To account for this increased resistance, it is speculated that either the dopant segregates to the grain boundary in the mixed oxide samples, giving a higher dopant concentration, or the dopant is removed in the chemically prepared material, reducing the concentration. A reduction in the dopant concentration relative to Ce suggests less current carrying oxygen vacancies, resulting in an increased resistance.

6.11. Multiple Doping in Ceria

Co-doping and double doping in ceria has been mentioned previously, where Sc and Y and Sc and Gd were added to ceria to evaluate the effects of lattice strain on the

association energies. Scandia is perhaps a poor dopant to add to ceria, not only because of its very small size but also due to its low solubility limit. This work has therefore concentrated on less extreme dopants, in order to reduce the lattice strain to near zero and maximise the bulk conductivity. The dopants chosen were Sm-Y and La-Yb. Preliminary results are reported in a paper by Ralph [74] and discussed in depth in chapter 13.

A recent study by Mori [75] prepared a Ce-25mol%Sm sample and compared this to a sample doped with 23.4mol%Sm-1.5mol%Cs-0.1mol%Li. Doping with alkali metals is usually avoided because of low solubilities in ceria and their high volatility. It was suggested, that the alkali metals form a solid solution with ceria but at such low concentrations, XRD would not be able to detect the presence of any second phases. Mori claims the alkali metal doped samples have higher total conductivities. Unfortunately, the microstructures of the samples are not discussed and the higher conductivity could easily be the result of larger grains in the alkali doped material. It would be interesting to see if a purely alkali metal doped ceria has a high ionic conductivity.

6.11.1. Other Dopants

A number of other dopants have been used for purposes other than ionic conductivity. TiO_2 doping has been used as a sintering aid and experiments with a mixed ceria-zirconia electrolyte have also been reported, as discussed previously. A number of dopants have been used to promote electronic conductivity in ceria, for use as an anode material, such as Nb_2O_3, SnO_2 and Pr_2O_3 [76]. Other dopants used in ceria include Rh_2O_3 [77], In_2O_3 and Cd_2O_3 [78].

6.12. Electronic Conductivity

Probably the single most important disadvantage that all ceria electrolytes have when applied to SOFC applications, is the relatively easy reducibility of the cerium ion. The reduction of ceria introduces electronic carriers into the electrolyte, which not only

reduce the electrical efficiency of the fuel cell but lead to increased mechanical stresses across the electrolyte, which can cause cracking. Compared to the number of studies that have aimed at optimising the ionic conductivity in ceria, the number of papers that target the reduction in electronic conductivity are very low. The reason for this is that there is no easy route to stabilise the 4+ valence state of ceria.

To date, there have been two approaches used to reduce the electronic conductivity but there is still no satisfactory answer. The first idea was originally developed by Tuller [79], who suggested that it might be possible to trap the electrons created as ceria is reduced, which would lower their mobility and make their contribution to the total conductivity smaller. To create these electron traps, a dopant is needed that reduces at slightly higher potentials to the cerium ion. The effective positive charge on the dopant attracts electrons, which reduces the dopant, trapping electrons and thus lowering their mobility. The success of this technique depends on how deep the electron traps are and a number of dopants have been considered, i.e. Pr, Sm, Fe, Mn. Of these, Pr^{4+} has received the greatest attention. The original work of Maricle [80] showed a large reduction in the electronic conductivity in CGO when 1mol%Pr was added, which extended the electrolytic domain to lower oxygen partial pressures. It was claimed that the P(–) value had been lowered by several orders of magnitude. Unfortunately, repeated attempts by other researchers were not able to recreate such improvements and although it seems that Pr doping does lower the electronic conductivity, it is not sufficient for an SOFC.

The introduction and reduction of Pr^{4+} can be described by the reaction in 6.12.

$$Ce'_{Ce} + Pr^{\times}_{Ce} \leftrightarrow Pr'_{Ce} + Ce^{\times}_{Ce} \qquad (6.12)$$

For a significant reduction of Pr, the equilibrium constant for this reaction must be large. Navarro [81] states, that the reaction constant is only slightly larger than that for the reduction of ceria and thus only a small improvement in the electrolytic domain can be expected. Navarro also shows that Pr doping increased the ionic conductivity of CGO and suggests that most of the improvements seen in the P(–) value can be attributed to increases in the ionic conductivity. Consequently, the choice of Pr as a

dopant appears to be incorrect. More recently, Pr doped ceria has been considered as an electrode material, due to its increased electronic conductivity [82].

The second idea for reducing the electronic conductivity, involves the introduction of an ionically conducting but electronically blocking grain boundary layer. The grain boundary would not stop the reduction of ceria but would reduce the mobility of the electrons created. This approach is discussed further in chapters 8 and 14. There are, at present, no published reports of this technique by other researchers.

Mogensen [83] states that oxygen vacancies introduced through doping suppress the number of oxygen vacancies from the reduction of ceria. In other words, the reaction in equation 6.13 is driven further to the left as the dopant concentration increases, resulting in a lower electronic conductivity. The result that increasing dopant concentrations can increase the resistance to reduction for ceria, has been observed by most researchers.

$$O_O^X \leftrightarrow V_O^{\bullet\bullet} + \tfrac{1}{2} O_{2(g)} + 2e' \qquad (6.13)$$

Levy [84] suggests that the oxygen vacancies interact with electrons, which tend to lower their mobility. However, the improvement is limited to, at best, an order of magnitude in P(–).

6.12.1. Grain Boundary P_{O_2} Dependencies

There are very few studies that have analysed the effects of reduced oxygen partial pressure on the grain boundary conductivity. For this, it is necessary to use low temperatures to limit the degree of electronic conduction and to resolve the grain boundary component. At low temperatures, it is often difficult to reach equilibrium gas pressures within reasonable time-scales and the more common approach is to measure the total conductivity at higher temperatures.

The conductivity of the bulk material is generally assumed to follow a -1/4 dependency, with respect to the oxygen partial pressure. Wang [27] reports a stronger

oxygen partial pressure dependence for the grain boundaries, which shows a -1/3 relationship.

6.12.2. P-Type Conductivity in Doped Ceria

The p-type conductivity in CGO is normally considered negligible in fuel cell applications and a study by Costa [85] shows this to be true, with a measured p-type conductivity of $1.1\text{-}1.6\times10^{-6}Scm^{-1}$ at 850°C. The activation energy for p-type conduction was calculated as 3.5-3.7eV and is about twice as high as that for YSZ. Below 900°C, the p-type conductivity in CGO is lower than that of YSZ.

6.13. Mechanical Stability

The mechanical properties of doped ceria have received very little attention. This sections aims at providing some basic mechanical data, which will be considered in the analysis in Appendix A, where a more in-depth discussion of the mechanical properties are dealt with. Duran et al [12] have observed transgranular fracture in CGO (8 and 16mol% $GdO_{1.5}$), which was considered an unusual mode of fracture in ceramics with a grain size as small as 1-2μm and, therefore, a high grain boundary density. Values of the fracture toughness, K_{IC} and Young's Modulus, E for >98% dense samples and 3-4μm grain size are as follows (the K_{IC} values are higher than those reported for YSZ):

Material	$K_{IC}/MPam^{-1/2}$	E/Nm^{-3}
Ce-4%Gd	3.2	175
Ce-8%Gd	2.2	166

Table 6.4. Fracture toughness and Young's modulus for CGO [12].

Another mechanical property which is pertinent to the study of SOFC's, is the thermal stability of the ceria electrolytes with the other components of the cell. It is generally found that the thermal expansion coefficients of ceria in air, are larger than those of YSZ and provide a better matching to existing electrode materials. Table 6.5 shows some typical values. Unfortunately, in reducing conditions the reduction of ceria

causes a large change in the expansion coefficient, which can lead to cracking. Mogensen [83] suggests this effect can be minimised by doping to high concentrations (40-50mol%). This subject is dealt with further in Appendix A.

Material	Thermal Expansion Coefficient/$10^{-6}K^{-1}$
CeO_2	12.3
Ce-20%Gd	12.5
Ce-40%Gd	12.1
Ce-50%Er	11.4
Ce-10%Ca	12.8
Ce-20%Ca	13.6
Zr-15%Y	10.8

Table 6.5. Thermal expansion coefficients between 50-1000°C, from [86].

References

1. A.S.Abd El Halim, N.M.Abdelmonem, N.A.Afify and G.Abd El Hamid. Powder Metallurgy International. **21**, 1, (1989), 29.
2. H.K.Varma, P.Mukundan, K.G.K.Warrier and A.D.Damodaran. J.Mater.Sci.Lett. **9**, 4, (1990), 377.
3. A.Overs and I.Riess. J.Amer.Ceram.Soc. **65**, 12, (1982), 606.
4. W.P.Hsu, L.Ronnquist and E.Matijevic. Langmuir. **4**, 1, (1988), 31.
5. P.-L.Chen and I.-W.Chen. J.Am.Ceram.Soc. **76**, 6, (1993), 1577.
6. I.Riess, D.Braunshtein and D.S.Tannhauser. J.Am.Ceram.Soc. **64**, 8, (1981), 479.
7. J.F.Baumard, C.Gault and A.Argoitia. J.of the Less-Common Metals. **127**, (1987), 125.
8. S.El-Houte and M.E.S.Ali. Powder Metallurgy International. **19**, 2, (1987), 20.
9. T.Seguelong. Private communications.
10. J.Van herle, T.Horita, T.Kawada, N.Sakai, H.Yokokawa and M.Dokiya. J.Am.Ceram.Soc. **80**, 4, (1997), 933.
11. J.Van herle, T.Horita, T.Kawada, N.Sakai, H.Yokokawa and Dokiya. Solid State Ionics. **86-88**, (1996), 1255.

12. P.Duran, C.Moure and J.R.Jurado. J.Mater.Sci. **29**, 7, (1994), 1940.
13. A.K.Bhattacharya, R.G.Biswas, A.Hartridge, K.K.Mallick and J.L.Woodhead. Electroceramics: Production, Properties and Microstuctures. Eds. W.E.Lee and A.Bell. British Ceramics Proceedings No.52, 1994, 257.
14. A.K.Bhattacharya, A.Hartridge, K.K.Mallick and J.L.Woodhead. J.Mater.Sci. **31**, (1996), 5005.
15. K.Yamashita, K.V.Ramanujachary and M.Greenblatt. Solid State Ionics. **81**, (1995), 53.
16. C.C.Chen, M.M.Nasrallah and H.U.Anderson. J.Electrochem.Soc. **140**, 12, (1993), 3555.
17. G.M.Christie and F.P.F.van Berkel. Solid State Ionics. **83**, (1996), 17.
18. A.L.Dragoo and L.P.Domingues. J.Am.Ceram.Soc. **65**, 5, (1982), 253.
19. D.D.Upadhyaya, R.Bhat, S.Ramanathan, S.K.Roy, H.Schubert and G.Petzow. J.Euro.Ceram.Soc. **14**, 4, (1994), 337.
20. W.Huang, P.Shuk and M.Greenblatt. Solid State Ionics. **100**, (1997), 23.
21. J.Tanaka, J.F.Baumard and P.Abelard. J.Am.Ceram.Soc. **70**, 9, (1987), 637.
22. R.T.Dirstine, R.N.Blumenthal and T.F.Kuech. J.Electrochem.Soc. **126**, 2, (1979), 264.
23. H.Yahiro, Y.Eguchi, K.Eguchi and H.Arai. J.Appl.Electrochem. **18**, 4, (1988), 527.
24. G.B.Balazs and R.S.Glass. Ionic and Mixed Conducting Ceramics 2nd International Symposium, The Electrochemical Society Inc. (1994), 478.
25. S.Hamakawa, T.Hayakawa, A.P.E.York, T.Tsunoda, Y.S.Yoon, K.Suzuki, M.Shimizu, and K.Takehira. J.Electrochem.Soc. **143,** 4, (1996), 1264.
26. T.Kudo and H.Obayashi. J.Electrochem.Soc. **122**, 1, (1975), 142.
27. D.Y.Wang and A.S.Nowick. J.Solid State Chemistry. **35**, (1980), 325.
28. G.B.Balazs and R.S.Glass. Ionic and Mixed Conducting Ceramics 2nd International Symposium, The Electrochemical Society Inc. (1994), 478.
29. R.N.Blumenthal, F.S.Brugner and J.E.Garnier. J.Electrochem.Soc. **120**, 9, (1973), 1230.
30. G.M.Ingo, G.Mattogno, N.Zacchetti, P.Scardi and R.Dal Maschio. J.Mater.Sci.Lett. **10**, (1991), 320.

31. R.Gerhardt, A.S.Nowick, M.E.Mochel and I.Dumler. J.Am.Ceram.Soc. **69**, 9, (1986), 647.

32. P.G.Harrison, D.A.Creaser, B.A.Wolfindale, K.C.Waugh, M.A.Morris and W.C.Mackrodt. Catalysis and Surface Characterisation. Eds. T.J.Dines, C.H.Rochester and J.Thomson. 1992, 76.

33. P.J.Scanlon, R.A.M.Bink, F.P.F.Berkel, G.M.Christie, L.J.van Ijzendoorn, H.H.Brongersma and R.G.van Welzenis. To be Published.

34. B.C.H.Steele and E.P.Butler. British Ceramic Proceedings. **36**, (1985), 45.

35. R.Gerhardt and A.S.Nowick. J.Am.Ceram.Soc. **69**, 9, (1986), 641.

36. J.M.Ralph and J.A.Kilner. Proc. of the 2nd European SOFC Forum. Ed. B.Thorstensen. (1996), 773.

37. J.A.Kilner and B.C.H.Steele. Nonstoichiometric Oxides. Ed. O.T.Sorensen, Academic Press. 1981, 233.

38. A.S.Nowick. Diffusion in Crystalline Solids. Eds. G.E.Murch and A.S.Nowick. Academic Press. 1984, 143.

39. V.Butler, C.R.A.Catlow, B.E.F.Fender and J.H.Harding. Solid State Ionics. **8**, (1983), 109.

40. H.Tuller. J.Phys.Chem.Solids. **55,** 12, (1994), 1394.

41. D-J.Kim. J.Am.Ceram.Soc. **72**, 8, (1989), 1415.

42. J.A.Kilner. Solid State Ionics. **8**, (1983), 201.

43. D.J.M.Bevan and E.Sommerville. Handbook on the Physics and Chemistry of Rare Earths, Vol.3. Eds. K.A.Gschneider and L.Eyring. Elsevier Science. 1979, 401.

44. J.D.Faktor. PhD. Thesis. University of London, 1980.

45. H.Inaba and H.Tagawa. Solid State Ionics. **83**, (1996), 1.

46. P.-L.Chen and I.-W.Chen. To be Published in J.Am.Ceram.Soc.

47. P.-L.Chen and I.-W.Chen. J.Am.Ceram.Soc. **77**, 9, (1994), 2289.

48. T.H.Estell and S.N.Flengas. Chem.Rev. **70**, (1970), 339.

49. J.D.Sirman, D.Waller and J.A.Kilner. Proc. of the 5th International Symposium on SOFC's. Eds. U.Stimming, S.C.Singhal, H.Tagawa and W.Lehnert. The Electrochem.Soc. (1997), 1159.

50. J.E.Bauerle. J.Phys.Chem.Solids. **30**, (1969), 2657.

51. D.Y.Wang and A.S.Nowick. Advances in Ceramics. **1**, (1981), 130.

52. K.El Adham and A.Hammou. Solid State Ionics. **9&10**, (1983), 905.

53. H.Yahiro, T.Ohuchi, K.Eguchi and H.Arai. J.Mater.Sci. **23**, (1988), 1036.

54. K.El Adham and A.Hammou. J.Chim.Phys. **79**, 9, (1982), 633.

55. H.Arai, T.Kunisaki, Y.Shimizu and T.Seiyama. Solid State Ionics. **20**, (1986), 241.

56. K.Eguchi, T.Kunisaki and H.Arai. J.Am.Ceram.Soc. **69**, 11, (1986), C282.

57. M.A.Seitz and T.B.Holliday. J.Electrochem.Soc. **121**, 1, (1974), 122.

58. P.Li, I.-W.Chen, J.E.Penner-Hahn & T.-Y.Tien. J.Am.Ceram.Soc. **74**, (1991), 958.

59. M.P.Anderson, D.E.Cox, K.Halperin and A.S.Nowick. Solid State Ionics. **9&10,** (1983), 953.

60. B.E.F.Fender. Chemical Applications of Thermal Neutron Scattering. Ed. B.T.M.Willis. Oxford University Press, London. 1973, 250.

61. R.Gerhardt-Anderson and A.S.Nowick. Transport in Nonstoichiometric Compounds. Eds. G.Simkovich and V.S.Stubican. Plenum Press. 1985, 111.

62. D.Y.Wang and A.S.Nowick. J.Phys.Chem.Solids. **44**, 7, (1983), 639.

63. R.Gerhardt-Anderson, F.Zamani-Noor and A.S.Nowick. Solid State Ionics. **9&10,** (1983) 931.

64. R.Gerhardt, W.K.Lee and A.S.Nowick. J.Phys.Chem.Solids. **48**, 6, (1987), 563.

65. T.Takahashi. Physics of Electrolytes, Vol.2. Ed. J.Hladik. Academic Press, London. 1972, 540.

66. B.C.Morris, W.R.Flavell, W.C.Mackrodt, and M.A.Morris. J.Mater.Chem. **3,** 10, (1993), 1007.

67. J.Faber, C.Geoffroy, A.Roux, A.Sylvestre and P.Abelard. Applied Physics A: Solids and Surfaces. **49**, 3, (1989), 225.

68. R.T.Dirstine, R.N.Blumenthal and T.F.Kuech. J.Electrochem.Soc. **126**, 2, (1979), 264.

69. H.Yahiro, K.Eguchi and H.Arai. Solid State Ionics. **36**, (1989), 71.

70. G.B.Balazs and R.S.Glass. Solid State Ionics. **76**, 1-2, (1995), 155.

71. D.Y.Wang, D.S.Park, J.Griffith and A.S.Nowick. Solid State Ionics. **2**, (1981), 95.

72. J.Van herle, T.Horita, T.Kawada, N.Sakai, H.Yokokawa and M.Dokiya. J.Euro.Ceram.Soc. **16**, (1996), 961.

73. N.Bonanos, B.C.H.Steele and E.P.Butler. Impedance Spectroscopy: Emphasing Solid State Materials. Ed. J.R.Macdonald. John Wiley and Sons, Inc. 1987, 205.

74. J.M.Ralph, J.Przydatek, J.A.Kilner and T.Seguelong. Ber.Bunsenges. Phys.Chem. **101**, 9, (1997), 1403.

75. T.Mori and H.Yamamura. J.Am.Ceram.Soc. **79**, 12, (1996), 3309.

76. C.Ftikos, M.Nauer and B.C.H.Steele. J.Euro.Ceram.Soc. **12**, 4, (1993), 267.

77. A.Martinez-Arias, J.Soria and J.C.Conesa. J.Catalysis. **168**, 2, (1997), 364.

78. A.K.A.Pryde, S.Vya, R.W.Grimes, J.A.Gardner and R.Wang. Physical Review B. **52,** 18, (1995), 13214.

79. D.L.Maricle, T.E.Swarr and H.L.Tuller. US Patent 5,001,021, (1991).

80. D.L. Maricle, T.E. Swarr and S. Karavolis. Solid State Ionics. **52,** (1992), 173.

81. L.Navarro, F.Marques, and J.Frade. J.Electrochem.Soc. **144,** 1, (1997), 267.

82. Y.Takasu, T.Sugino and Y.Matsuda. J.Appl.Electrochem. **14**, 1, (1984), 79.

83. M.Mogensen, T.Lindegaard, U.R.Hansen and G.Morgensen. Ionic and Mixed Conducting Ceramics 2nd International Symposium, The Electrochemical Society Inc. (1994), 448.

84. M.Levy and J.Fouletier. Solid State Ionics. **12**, (1984), 467.

85. A.D.S.Costa, J.A.Labrincha and F.M.B.Marques. J.Mater.Sci.Lett. **15**, (1996), 1716.

86. M. Mogensen, T. Lindegaard U.R. Hansen, G. Mogensen. J.Electochem.Soc. **141**, 8, (1994), 2122.

Chapter 7. Electrolyte Films

7.1. Introduction

The components within each positive electrode-electrolyte-negative electrode (PEN) structure of a fuel cell stack, are generally in the form of thick films (<1mm thickness). For the planar design, the films must be flat and have a uniform thickness. One component usually acts as the substrate and also conveys the mechanical support for each cell. Both the electrodes and the electrolyte have been used as the substrate onto which the other components can then be laid. There have been many techniques developed to produce both the substrate films and the films which are placed on top of the substrate. One of the main driving forces in the production of these films has been the reduction in their thickness. The reasons for this are both economic and technical. Thinner films use less material per PEN structure and so helps to lower the cost of the whole stack. Producing thinner films also helps to lower the ohmic resistances of each component, especially that of the electrolyte, and enables the fuel cell to operate at lower temperatures.

Two of the largest problems faced in the production of thin films, are the differences in thermal expansion of each material, which can lead to cracking of the plates during manufacture and interdiffusion between the materials. The electrolyte has the highest sintering temperature and is commonly prepared first to reduce thermal stress build up. The electrodes are added afterwards and sintered at a lower temperature, to achieve the required porosity and reduce interdiffusion. In this scenario, the electrolyte must act as the mechanical support, which necessitates thicknesses between 200-400μm. At these thicknesses the electrolyte material has a relatively high resistance and it is desirable to reduce its thickness for lower temperature operation. Below 200μm the electrolyte is no longer self supporting and one of the electrodes must act as the support.

The sintering temperature of the electrodes is around 200°C below that of the electrolyte, in order to obtain the correct porosity in the material. Using one of the

electrodes as the support, requires the sintering temperature of the electrolyte to be lowered but to still maintain a dense impermeable structure. In practice, this has not been possible and so the electrodes have been sintered at higher temperatures. This increases the degree of interdiffusion and results in the formation of second phases at the interfaces, which have markedly increased the polarisation losses.

The benefit of using an electrode as the support, is that sintering of a whole cell can be carried out in one step, saving both time and money. However, the performance benefits of the two step process, with the self supporting electrolyte, have maintained research for both processing routes.

Another factor that must be considered in making these thin films, is the microstructure of the supporting substrate. The electrolyte has a dense surface and the growth of porous electrodes is relatively easy. The porous electrodes present more of a challenge when applying a dense electrolyte on their surface.

The production and testing of fuel cell plates is largely restricted to industrial companies, due to the quantities of material needed. For the low temperature SOFC structures, there is still active laboratory based development. At lower temperatures, the use of metal alloys becomes available and so it is necessary to evaluate the production of ceramic films on to metals. Metal alloys would provide excellent mechanical support and allow thin ceramic films to be used.

Thin and thick films play an important role in SOFC devices and the preparation of both the supporting substrate film and the non-supporting films, are challenges which face the commercialisation of SOFC's today. The discovery that very thin buffer layers can substantially decrease the electrode polarisation losses (see section 3.4.5.), further strengthens the need to develop appropriate thin film techniques.

This chapter will review some of the research on the production of ceria and zirconia thin and thick films. A report on a thin film technique used in this study to deposit doped ceria onto ferritic stainless steel, will also be discussed.

7.2. ZrO_2 and CeO_2 Films

One of the simplest and least expensive techniques to prepare both YSZ and doped ceria films, is screen printing [1]. Basically, the electrolyte powder, dispersed in an organic binder, is forced through a screen onto a substrate of the desired shape. The printed pattern is then dried, before the organic binder is burnt out and the powder sintered to a coherent film [~30μm]. Thicker films can be made by successive printings and firings and both porous and dense films are possible [1].

Another relatively simple and cost effective technique that has received increasing attention, is that of tape casting, followed by tape calendering [2]. The electrolyte (YSZ or CGO) is mixed with a binder and plasticiser and then rolled into a tape. A supporting anode tape is produced in a similar way and the two tapes are rolled together, resulting in an electrolyte thickness between 1-10μm. The tape is then sintered, before the cathode layer is slurry coated onto the electrolyte and sintered. Uniform layer thicknesses are achievable with a fully dense electrolyte. No cracking or delamination of the layers has been observed and there is no detectable interdiffusion between the layers. The electrical characteristics of the cells have been shown to achieve high current densities and no performance degradation up to 1100°C.

Electrochemical vapour deposition (EVD) is used extensively in tubular SOFC technology to deposit the thick electrolyte layer. Generally, EVD is both an expensive and time consuming process but it allows reproducible, fully dense and highly crystalline films to be grown. EVD is used somewhat less in the construction of planar SOFC's because the thickness of the electrolyte film is prohibitively large. However, in ceria based fuel cells, a thin layer of YSZ on the anode side of the electrolyte increases the stability of ceria in the reducing atmospheres. Initial work on EVD films to evaluate the kinetics of depositing ceria electrodes onto dense yttria doped ceria has also been demonstrated [3]. The deposited layers were found to be dense and polycrystalline with a grain size around 8μm. Deposition of a 2μm layer took only a few minutes, which makes this technique more economically viable. It is unlikely that EVD will be used to grow the doped ceria electrolyte layer, which is much thicker, because of the time intensive process involved. EVD of YSZ layers with thicknesses

around 10μm, normally require >2hrs and analysis has shown penetration of up to 4μm into the pores of porous substrates [4].

A recent report [5] has suggested, that a YSZ/CGO composite electrolyte has no intrinsic advantage over a simple thin YSZ electrolyte. In this report, a bismuth oxide film was used as the electrolyte, with doped ceria as the anode. The ceria layer was self supporting with a thin (5-60μm) erbia doped bismuth oxide layer coated onto the cathode side. Bismuth oxide is not usually considered for SOFC applications, due to its instability even at relatively high oxygen partial pressures, as discussed in chapter 5. This report claims that the P_{O_2} gradient across the thick, dense ceria layer was sufficiently large, that at the interface of the anode and electrolyte, the P_{O_2} was high enough to prevent the reduction of the bismuth ion. Although significantly higher open circuit potentials were obtained, compared to a doped ceria electrolyte, the power densities achieved were very low in comparison to YSZ electrolytes.

Spin coating of a buffer layer between a YSZ electrolyte and a LSCF electrode have been reported to reduce polarisation losses at the interface [6]. Samaria doped ceria thin films, approximately 0.1μm thick, were spin coated onto LSCF, producing dense, homogeneous, crack free films from a polymeric precursor. The thickness of the film can be controlled by the solution viscosity, rotating disk spinning speed and time. High density films were produced at sintering temperatures as low as 600°C/1minute, which resulted in typical grain sizes of 0.1μm. It has been suggested, that the catalytic properties of the LSCF acted as nucleation sites, allowing the doped ceria nuclei to form at these relatively low temperatures. In addition, it was found that ceria and LSCF were unreactive up to 1200°C.

7.3. CeO_2 Thin Films and Deposition Techniques

Ceria has yet to be commercially accepted as an electrolyte material in a SOFC but it has been used in a number of other applications, in the form of thin films. Gas sensors incorporating ceria films, have been used in car exhausts (lamda probes), to monitor the P_{O_2} of exhaust gases and allow the efficient burning of fuel to reduce emission

levels. Sputtering techniques (i.e. reactive r.f. sputtering) have been used to deposit thin films of ceria onto an alumina substrate [7, 8], resulting in film thicknesses between 0.5-1.5μm. Thicker films of ceria and yttria doped ceria (5-50μm) have been grown using spin coating and screen printing techniques [8]. Good adhesion and high densities were obtained after sintering at 1400°C/2hours. The polycrystalline films had very similar electrical properties to that of the bulk material, showing good matching in the oxygen vacancy and electron activation energies for migration.

7.4. Pulsed Laser Deposition

Pulsed laser deposition (PLD) has found widespread use in the growth of high temperature superconducting oxide thin films [9]. The ability of PLD to grow oxide films without deviation in composition from the target material, has established this technique in the accurate growth of thin films. PLD is also compatible with relatively high P_{O_2} values, enabling the control of oxygen non-stoichiometry in as-grown films.

There are a significant number of research papers concerning laser deposition of ceria onto silicon [10]. Highly textured ceria (111) films are usually grown with thicknesses between tens of nanometers to hundreds of nanometers. Generally, no reaction phases are detected between the ceria and silicon up to 850°C. Yashimoto [11], using a related technique called laser molecular beam epitaxy (laser MBE), was able to grow both polycrystalline and single crystal ceria films on Si(111) substrates. The films were grown at 20°C, with a thickness of 270nm. Full crystallinity was exhibited in the films and very sharp interfaces were observed between ceria and silicon.

Previous work carried out at Imperial College and UCL has studied the various parameters required to grow crystalline CGO films onto Si(100) substrates, using PLD [12]. The original aim of this work was to grow dense submicron films for low temperature operation SOFC's. However, many of the submicron films displayed pinhole defects in their microstructure, which would allow permeation of gases. It is possible, that slight changes in the set-up of the deposition parameters could remove

these defects, but it was decided to concentrate on CGO film thicknesses ~1μm, to eliminate the pinhole problem.

The PLD experiments were performed under an initial vacuum pressure of 10^{-6}mbar. Two different lasers were used during these experiments: A LPX-300i KrF excimer laser and a Quantel frequency quadrupled Nd:YAG laser. The parameters of each laser are shown in table 7.1. Laser fluences between 0.5-10J/cm^2 were obtained by focusing the laser spot to the area described in the table. The laser fluences were measured using Gentec and Molectron energy meters.

Laser	λ (nm)	Pulse duration (FWHM)/ (ns)	Energy per Pulse (J)	Pulse repetition rate (Hz)	Spot dimensions (mm)
Excimer	248	25	1.2	10	3×1
Nd:YAG	266	3.5	0.09	10	1 (diameter)

Table 7.1. Laser parameters.

Previously used target materials ($Ce_{0.9}Gd_{0.1}O_{2-X}$) were prepared in-house, by a similar route to those used in this study. In this study, amorphous citrate prepared pellets were used as the target materials, with the following compositions: $Ce_{0.9}Gd_{0.1}O_{2-X}$, $Ce_{0.8}Gd_{0.2}O_{2-X}$, and $Ce_{0.7}Gd_{0.3}O_{2-X}$. The CGO thin films were then ablated onto a ferritic stainless steel (24%Cr, 0.1%Cu, 0.45%Mn, 0.62%Ni) substrate, which was heated to 650°C in a previously optimised P_{O_2} = 1×10^{-4}torr. The steel had been polished down to a 1μm finish using a diamond paste. Ferritic stainless steel is a candidate material for the bipolar plate in low temperature SOFC's and this study aimed to assess the deposition of oxides onto the steel, using PLD. The ferritic stainless steel could also be used as the anode in a SOFC; consequently, the deposition of CGO was evaluated. The future aim was then to study the deposition of CGO onto porous steel, to produce an anode-electrolyte structure. Once deposited, the films were analysed by XRD, SEM and AFM. Finally, platinum electrodes were applied for a.c. impedance analysis.

A SIMS study of the previously deposited films, indicated that the Gd concentration was higher than that of the target material, suggesting that the ablation of CGO does

not proceed with perfect stoichiometric transfer. It was also observed, that certain impurity levels (e.g. K, Ca, C and Cl) were lower in the CGO film compared to the target composition. Additional data [13] has shown, that the longer pulse duration of the excimer laser caused heating to a lower depth in the substrate, compared to the Nd:YAG laser. Repeated heating produced phase changes in the surface of the substrate, with a resulting difference in film stoichiometry. By changing some of the deposition parameters, on both lasers, the stoichiometry of the CGO films in this study were found to be close to that of the target materials.

References

1. J.F.Baumard, C.Gault and A.Argoitia. J.of the Less-Common Metals. **127**, (1987), 125.
2. N.Q.Minh & C.R.Horne. 14th Riso International Symp. on Material Science. Eds. F.W.Poulsen, J.J.Bentzen, T.Jacobsen, E.Skou and M.J.L.Ostergard. (1993), 337.
3. J-F. Jue, J.Jusko and A.V.Virkar. J.Electrochem.Soc. **139**, 9, (1992), 2458.
4. J.Meijerink, G.Z.Cao, H.W.Brinkman, K.J.de Vries and A.J.Burggraaf. 14th Riso International Symposium on Material Science. Eds. F.W.Poulsen, J.J.Bentzen, T.Jacobsen, E.Skou and M.J.L.Ostergard. (1993), 331.
5. E.D.Wachsman, P.Jayaweera, N.Jiang, D.M.Lowe and B.G.Pound. J.Electrochem.Soc. **144**, 1, (1997), 233.
6. C.C.Chen, M.M.Nasrallah and H.U.Anderson. J.Electrochem.Soc. **140**, 12, (1993), 3555.
7. U.Lampe, J.Gerblinger and H.Meixner. Censors and Actuators. **B**, 7, (1992), 787.
8. H.J.Beie and A.Gnoerich. Sensors and Actuators. **B4**, 3-4, (1991), 393.
9. B.Dam, J.H.Rector, J.Johansson, S.Kars and R.Griessen. Applied Surface Science. **96-98**, (1996), 679.
10. A.G.Akimov, D.B.Bogomolov, A.E.Gorodetskii, L.P.Kazanskii, A.N.Khodan, I.L.Krylov, J.P.Langeron, N.A.Melnikova, D.Michel, J.L.Vignes and J.Perriere. Thin Solid Films. **238**, 1, (1994), 15.
11. M.Yoshimoto, K.Shimozono, T.Maeda, T.Ohnishi, M.Kumagai, T.Chikyow, O.Ishiyama, M.Shinohara and H.Koinuma. Jap.J.Appl.Phys. **34**, (1995), L688.
12. L.G.Coccia, G.C.Tyrrell, J.A.Kilner, D.Waller, R.J.Chater and I.W.Boyd. Applied Surface Science. **96-98**, (1996), 795.
13. D.Waller, L.G.Coccia, G.C.Tyrrell, J.A.Kilner and I.W.Boyd. To be published.

Chapter 8. Glass Additions

8.1. Introduction

A number of texts are available, which discuss in detail the production and conductivity properties of glasses and the reader is referred to these for an in-depth analysis [1, 2, 3, 4]. The aims of this chapter are to briefly summarise the subjects of liquid phase sintering and conductivity in glasses and then to explore possible glass additions in CGO. It is interesting to note, that much of the research in the field of conducting glasses was reported 20-30 years ago and since then there appears to be only a few reports on this topic. Recently, there have been some reviews on the subject [5, 6, 7] but these basically echo the research of the previous literature. The conduction mechanisms in glasses are still poorly understood [8, 9] and so there seems a need for further research into ionically conducting glasses.

A glass is an amorphous material and is formed by the sufficiently rapid cooling of a melt. The glass is thus in a metastable state and will recrystallise if exposed to high enough temperatures. Often a number of glass phases separate in the liquid state into individual phases, each of which may crystallise or remain glassy upon cooling.

There are a number of ways of making a glass, the most common used is that of cooling a melt. Other techniques used include:- Condensation of a vapour phase onto a cold substrate (CVD), disordering of a crystalline solid by irradiation and ion bombardment and deposition from a solution (the sol-gel process). In this study, only cooling from a melt has been employed, due to its simplicity and ready availability of equipment.

8.2. Liquid Phase Sintering

The addition of low melting point phases to ceramics to lower the manufacturing temperature is not a new idea and has been used in the production of many common ceramics, e.g. TiO_2 in $BaTiO_3$. Compared to ceramics, glasses generally have lower melting temperatures and are therefore candidate materials for use as liquid phase sintering aids. As well as the ability of glassy liquid phases to lower the production temperatures, some glasses can also act as ion conductors. Unlike polycrystalline ceramic conductors, glasses are isotropic and are not complicated by the presence of grain boundaries. These glasses are then suitable for use as, or in, solid electrolytes. The variety of conduction mechanisms by which glasses are thought to carry current are described in the following sections.

Liquid phase sintering or reactive liquid sintering is commonly used to produce ceramics, both structural and technical. The low temperature dependence of most electrical ceramics allow liquid phases to reduce the processing temperature in components, such as ceramic varistors, capacitors and thermistors. There are also reports [10] of liquid phase sintering aids used in $LaCrO_3$, the bipolar plate of a SOFC. The essential requirements for a good liquid phase additive are an appreciable solubility for the matrix material, low viscosity for rapid diffusion kinetics and a contact angle that allows the liquid to wet and penetrate between the constituent particles. In zirconia and ceria ceramics, minor silica impurities result in a small amount of liquid phase during sintering, giving slight local variations in densification. Some care has to be taken when choosing the liquid phase in ceramic applications, where high temperatures are to be encountered, because of the ability of the glass to re-melt if the temperature exceeds its original melting point. This situation is most important for refractory oxides but in most electrical applications of ceramics this is not really a problem. In these ceramics, devitrification of the glass is more problematic. When a liquid phase is used, the final product will always contain some porosity but this is normally limited to only a few percent.

8.3. Conductivity in Glasses

The conductivity in glasses has been studied for over a century but the understanding of the mechanisms by which current can flow is poorly understood, compared to that in conducting ceramics. The types of conductivity that are found in glasses can basically be divided into two groups:- Ionically conducting glasses, which are dominated by the alkali ions and electronically conducting glasses, which are a much more recent discovery.

Most glasses contain three basic components, *network-formers,* e.g. SiO_2 and B_2O_3, *network-modifiers*, e.g. Na_2O and K_2O, and *intermediates*, e.g. Al_2O_3. Pure silica glass (fused silica) has a very low conductivity due to a continuous random network structure and complete connectivity of the very strong O-Si-O bonds. A typical two dimensional structure of pure B_2O_3 is shown in Fig.8.1.

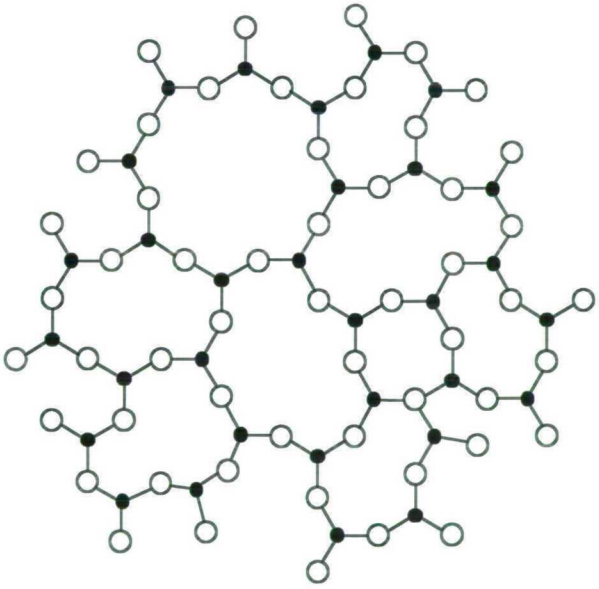


Fig.8.1. Two-dimensional representation of a boron oxide glass.

The addition of network modifiers breaks some of the Si-O bonds and introduces ions into the system, that are orders of magnitude more mobile than the network-former ions. Therefore, the possibility of ionic and electronic glasses are made possible by adding the correct dopants into the structure.

8.3.1. Ionically Conducting Glasses

Ionically conducting glasses have been extensively studied, with the majority of research centred on the alkali glasses. There is, however, limited work on other alkali-free glasses which are also ionic conductors and a review of the current status will be given below. Most glasses are based on the SiO_2 system modified by sodium ions, which break the very strong Si-O bonds, creating non-bridging oxygen ions in the structure (Fig.8.2.).

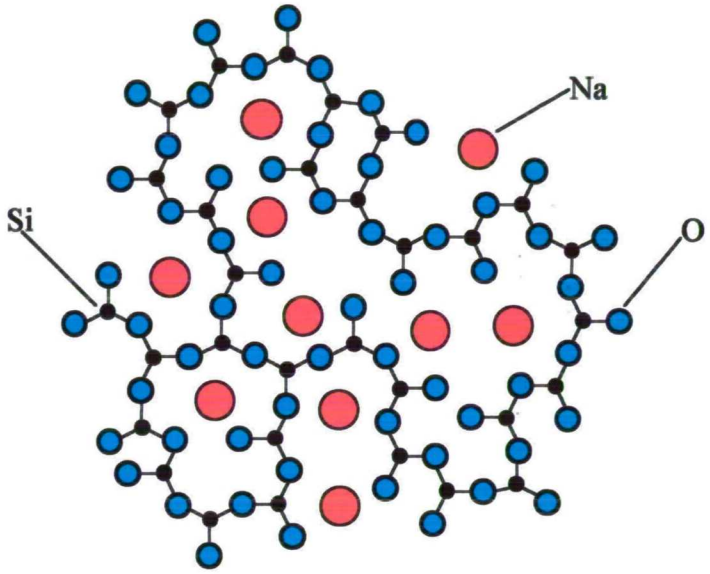


Fig.8.2. Two dimensional representation of a sodium silicate glass.

The sodium ions are then electrostatically attached to the oxygen ions whilst remaining able to hop through the structure, to constitute the ionic current. All alkali ions show this behaviour, resulting in similar conductivities. Although lithium ions achieve the highest conductivity, due to their small ionic radius, sodium has been used most extensively. The size of the holes in which the alkali ions are situated are determined during the formation of the network and are thus completely dependent on the cation size. In these glasses, the transference number of the alkali ions is found to be unity. In the alkali "free" glasses, the transference number of the conducting ions is less certain because of controversy over the ions present and the mechanisms for conduction. It is thought that in fused silica, impurity levels of only parts per million of sodium are required for the sodium ion to dominate the conductivity, while around

5% additions of transition metal oxides exhibit a degree of electronic conductivity [11].

More recently, the addition of silver ions into silicate glasses have shown greater ionic conductivities compared to the alkali ions and intensive research into a number of related glasses has been undertaken in the area of solid electrolytes. Following studies on many silicate and other glass systems, the effects of different ion substitutions have now been determined. Substitution of alkali ions increase the conductivity greatly (as already discussed), while alumina slightly increases the conductivity. Additions of ZnO, PbO, MgO, Fe_2O_3 (single valence state only), BaO, CaO and B_2O_3 all decrease the conductivity.

As a result of stronger Coulombic interactions with the negative charges in the network, the mobility of divalent and higher valent ions in silica is normally relatively low compared to the alkali ions and consequently research into these systems is sparse. The alkali-free glasses, e.g. $BaO\text{-}SiO_2$ and $CaO\text{-}SiO_2$, are ionic conductors, where the ionic migration is thought to be due to the Ba^{2+} and Ca^{2+} ions respectively [12, 13]. Another series of alkali free glasses are known as the Cabal glasses, based on the system $CaO\text{-}B_2O_3\text{-}Al_2O_3$. The network in these structures is formed by B_2O_3 and Al_2O_3. The addition of CaO then has two effects on the structure of the glass as the concentration increases, which is described by Owen [3], as a simple screening model. With low CaO concentrations, the additional oxygen from the CaO is taken up by increasing the boron atoms co-ordination from 3- to 4-fold. This change in co-ordination number continues up until the limit, at which each four co-ordinated boron atom is surrounded by four, three co-ordinated boron atoms. The structural changes in the glass up to this limit are known as the accumulation region. Above this limit a destructive region is found, whereby the addition of oxygen from the CaO is taken up by the breaking of B-O-B bonds, with the formation of non-bridging oxygen atoms. In the accumulation region, the resistivity was found to be invariant with the CaO concentration; it decreased rapidly in the destruction region as the CaO concentration increased [14]. Based on the oxygen dependency of these glasses, the conductivity mechanism is suggested to be due to the field-induced drift of oxygen ions. A network

forming oxygen moves into a network modifying oxygen site (interstitial site), accompanied by an equal but opposite migration.

It has been shown [15], that these glasses segregate on a submicroscopic scale into borate and aluminate phases. This is a common factor in many glass systems, with similar conduction mechanisms in both phases. In the glasses prepared by Owen, excess boron oxide was needed to compensate for the highly volatile nature of this compound, and were then melted at 1300-1350°C.

Oxygen ion migration has also been reported in sodium borate glasses [9]. During electrolysis at Pb anodes, a layer of PbO was observed, indicating the preference of O^{2-} ion migration over that of Pb^{2+} ions into the glass. The conduction mechanisms proposed for the oxygen ions were similar to those described for the Cabal glasses.

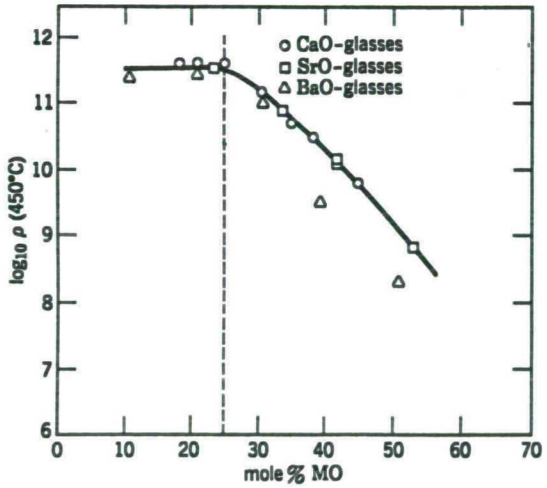


Fig.8.3. A comparison of d.c. resistivity in some alkaline earth boroaluminate glasses at 450°C [3].

Reports of the electrical properties in the related glass systems $SrO-B_2O_3-Al_2O_3$ and $BaO-B_2O_3-Al_2O_3$ by Hirayama [16] show good agreement to those of Owen, as demonstrated in Fig.8.3. The vertical dotted line marks the boundary between the accumulation region on the left and the destruction region on the right. The resistivities decrease as the alkaline earth oxide concentration increases. Fig.8.4. shows a comparison of the activation energies for these glasses, which are again in good agreement. Hence, the conductivity in the alkaline earth boroaluminate glasses

appears to be independent of the alkaline earth metal used, but critical on the concentration.

The Cabal glasses are noted for their high electrical resistivities, some of which are higher than the purest grade fused silica. The conductivity of oxygen ions is thus relatively low but consistent with current theories, considering the large size and charge of the oxygen ions. Additions of lead and barium are known to increase the resistivity in some glasses but allow reasonably low working temperatures and viscosities and prevent problems of devitrification [1].

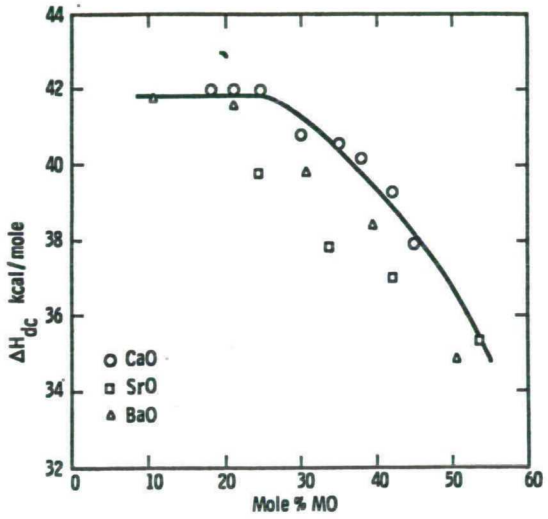


Fig.8.4. Activation energies for d.c. conductivity in some alkaline earth boroaluminate glasses [3].

8.3.2. Electronically Conducting Glasses

Some glasses have been discovered which exhibit semi-conducting properties but still possess high resistivities (e.g. $10^{12}\Omega$cm at 20°C). These glasses were developed by the semiconductor industry for the ease with which they can be made into intricate shapes and can be divided into two classes: oxide glasses and non-oxide glasses (normally referred to as chalcogenide glasses).

The semi-conducting oxides are based on compounds, which are also semi-conductors in their crystalline form, such as V_2O_5, and FeO. These oxides are generally difficult to prepare in a glassy form and are usually added to a network former. The systems

V_2O_3-P_2O_5 and FeO-P_2O_5 are the most commonly encountered, where P_2O_5 is an insulator. Conduction is thought to occur by electron or polaron hopping between ions of dissimilar valence, e.g. from Fe^{2+} to Fe^{3+}. Thus, the V_2O_3 system is considered to be an n-type semiconductor, while the FeO system is considered to be p-type semi-conducting. Electronically conducting oxide glasses prepared with TiO_2, CoO and MnO in borate and silicate matrices have also been studied [17, 18, 19].

Electronic conduction in non-oxide glasses is most often encountered in the chalcogenide glasses, based primarily on sulphur, selenium and tellurium. Additional modifiers and intermediates include As, Sb, Bi, Tl, P and the halogens, e.g. As_2Se_3, Sb_2S_3 and As_2Te_3. As well as being semi-conducting, these glasses also show photoconducting behaviour, which has found uses in the Xerox printing process. Unlike the oxide glasses which are ionic, the chalcogenide glasses are generally covalent and thus the mechanisms by which electrons migrate are different. Conduction does not involve a hopping mechanism. It is thought more likely that a band model is operative, where a high density of localised states extend from the conduction and valence bands into the band gap of the material. Conduction is then thermally activated and occurs when the carriers acquire sufficient energies to cross the band gap energy. Some chalcogenide glasses can also be very sensitive to impurity levels, a similarity shared with their crystalline counterparts, which may introduce active donor or acceptor states within the band gap. Generally, the chalcogenide glasses are insensitive to impurities and therefore allow less rigorous preparation procedures compared to the standard semi-conductors [1]. In relation to the chalcogenide glasses the oxide glasses are, on the whole, relatively less sensitive to the presence of impurities.

Clearly, for the studies in this research, it is important to avoid choosing glass compositions which contain any of these electronically conducting glasses. The aim is to find a glass, which has a relatively low melting point, is purely ionic and which therefore blocks electrons.

8.4. Strontium Gallate Glasses

Most glasses discussed so far have been based on the network formers, SiO_2, B_2O_3, and P_2O_5, but these are not the only easily formable glasses available and other oxides, such as GeO_2 and Ga_2O_3, can also form glasses. To introduce non-bridging oxygen ions into the network, a modifier must be added. The alkali ions are not convenient for an oxygen ion conducting glass but there are a number of other metal oxides, which also act as modifiers. These include, CaO, SrO and BaO. It is worth noting, that Ga_2O_3 is usually considered a modifier and so the precise nature of any particular additive depends on the nature of the specific situation in which it is being incorporated. The most closely related glasses to the alkaline earth gallates that have been studied are those of the Cabal glasses, which are essentially alkaline earth borates. It is thus reasonable to assume, that the conduction mechanism in the gallates is similar to the borates (both group III elements), viz. oxygen ion migration.

It is important to remember, that the structure of strontium gallate glasses is not known and so other conduction mechanisms may exist. It is feasible, although energetically very unfavourable, that oxygen molecules are able to diffuse through the network. This could explain the high resistivities exhibited by these glasses. Alternatively, oxygen ions may migrate via oxygen vacancies within the network, which are created at the non-bridging oxygen bonds. Conduction from the Sr^{2+} ion is thought to be very low, due to the large ionic radius and electrostatic attraction to the non-bridging oxygen ions.

Reports on other strontium gallate systems also indicate oxygen ion conductivity. An investigation by Yamaguchi [20], concerning the modified spinel structured polycrystalline Sr-hexa-gallate (possesing a β-alumina structure, $SrZnGa_{10}O_{17}$), showed excess oxygen ions were created as the structure was converted to β-alumina by the substitution of the spinel forming agent with Zn^{2+}. Oxygen ion migration is thus considered the major ionic species responsible for ionic conductivity. Experiments were also performed after the material had been soaked in a molten Na solution. Sodium ion conductivity then dominated, which indicates the need for low levels of sodium impurities in strontium gallate systems.

The use of a sintering aid in ceria solutions was sparked by previous studies on the related material, stabilised zirconia. Chiou [21] and Goodenough [22] used reactive liquid or glass additions in an attempt to lower the sintering temperatures. Chiou experimented with a number of glass compositions, sintering temperatures and times and found the glass based on $CaO\text{-}BaO\text{-}B_2O_3\text{-}SiO_2\text{-}Al_2O_3$ achieved the greatest improvement in densification over that of a standard CSZ. Sintering at 1350°C gave a density greater than that of CSZ sintered at 1500°C (~95%). Sintering for short times (1-2hrs) was sufficient to reach the high density; longer periods of time gave no improvements in the density. The optimum concentrations of glass additive were in the range 3-5mol% and it was found that in some cases, lower concentration of glass actually produced samples with a poorer density than that of pure CSZ. The glass additives were shown not to effect the bulk or grain boundary conductivities.

Goodenough, who has studied the electrolyte system lanthanum gallate doped with Sr and Mg (LSGM), discovered that the $SrO\text{-}Ga_2O_3$ system exhibited a low melting point eutectic (1270°C) at the composition $Sr_2Ga_2O_5$ [23]. It was decided to use this compound as an additive to the conventional electrolyte YSZ, in an attempt to lower the sintering temperature, using a liquid phase. The strontium gallate was prepared at 1210°C but was found to disproportionate on cooling into a predominately $Sr_3Ga_4O_9$ phase. A.C. impedance results showed this ceramic to have a low conductivity ($2\times10^{-6}Scm^{-1}$ at 800°C) but emphasis was placed on lowering the sintering temperature. The ceramic was then ground and added to the YSZ prior to sintering at 1350°C for two days. For a 3mol% $Sr_2Ga_2O_5$ sample, a density around 96% of the theoretical was achieved, which again was greater than that of a pure YSZ sintered at 1450°C. The bulk conductivities of these materials were slightly lower than that of YSZ, a common feature when a less effective dopant is added, whereas the grain boundary conductivites were considerably enhanced. The highest total conductivity was achieved with a 3mol% addition of the $Sr_2Ga_2O_5$. However, the grain size in the doped material was approximately 10μm compared to only 1-2μm for the pure YSZ. The effect of the grain size would result in considerably fewer grain boundaries in the doped sample, thus reducing the number of grain boundaries that must be crossed by any oxygen ions. The effect of this would be to lower the total resistance of the grain boundaries. Further analysis of the data shows that the reduction in the number of

grain boundaries only partly accounts for the increased conductivity and thus the dopant itself must also enhance conduction at the boundaries. It was suggested, that the disproportionated $Sr_2Ga_2O_5$ may be stabilised as predominantly a single, oxygen deficient phase at the grain boundary. An increase in the oxygen mobility at the grain boundary, would then account for the increased conductivity observed.

From the literature available there appears to be a number of potential glasses with sufficiently low melting points, that could be used as a sintering aid in CGO. The ability of these glasses to be good oxygen ion conductors at the grain boundaries, would appear unlikely. Oxygen ion conducting glasses show very large resistivities and are most likely to demonstrate either little improvement or a worse conductivity at the grain boundaries compared to an undoped CGO. The slight worsening in conduction would, however, be negligible if the glass was able to block the flow of electrons in CGO, under reducing conditions. The reduction of ceria is still one of the main problems facing CGO if it is to be used in SOFC technology. A grain boundary phase which can greatly reduce the mobility of the electrons is very desirable and glasses are just one class of materials being considered.

It is relatively easier to produce a glass with the composition $Sr_2Ga_2O_5$, but the structure and conduction mechanisms remain unknown. An alternative approach would be to cool the melt sufficiently slowly such that conversion to the ceramic form of $Sr_2Ga_2O_5$ resulted. The ceramic $Sr_2Ga_2O_5$ would have the brownmillerite structure (discussed in chapter 5), containing oxygen vacancies and thus may exhibit a higher conductivity when compared to the glass form.

On cooling $Sr_2Ga_2O_5$ below the eutectic, the equilibrium phase will disproportionate into $Sr_3Ga_4O_9$ and $Sr_3Ga_2O_6$. Fisher [24], suggested that the inability to synthesis $Sr_2Ga_2O_5$ was the result of the small size of the Ga^{3+} ion, which preferred tetrahedral co-ordination. It was suggested that the brownmillerite structure can be stabilised, using dopants to force the Ga^{3+} ion into octahedral co-ordination within the structure. The conductivity of oxygen in the disproportionated mixed phase, was shown to be very low [22] and methods to stabilise the brownmillerite structure have been investigated in this thesis.

Based on preliminary results from this thesis, Kiratzis [25] first discussed the merit of reducing the electron mobility in ceria electrolytes, by introducing an electron blocking phase at the boundaries. It was thus decided to try and repeat the experiments of Goodenough in the ceria system, for both lowering the sintering temperature and improving the grain boundary conductivity. Although it has been reported that strontium can react with gadolinium to form its own brownmillerite phase, $Sr_2Gd_2O_5$ [26], Fisher [24], has shown this not to be the case. No phase diagram exists for the SrO-Gd_2O_3 system, but the compounds that have been reported, were only formed at temperatures above 1600°C. It is unlikely that the strontium and gadolinium will react at lower temperatures. It is thought that the gallates will be stable in reducing environments, because of investigations into the lanthanum gallate system [15, 27]. Thus the possibility exists, that strontium gallate may also act as an electron blocking layer as ceria is reduced. Consequently, both ceramic and glass forms of nominally the same material were prepared and analysed in this study, with the primary goal of reducing the electronic conductivity in CGO.

References

1. Introduction to Ceramics. Eds. W.D.Kingery, H.K.Bowen and D.R.Uhlmann. John Wiley and Sons, Inc. 1976.
2. J.D.Mackenzie. Electrical Conductivity in Ceramics and Glasses - Part B. Ed. N.M.Tallan. M.Dekker, Inc. 1974, 560.
3. A.E.Owen. Progress in Ceramic Science. Ed. J.E.Burke. Pergamon Press Ltd. 1963, 77.
4. W.A.Koehler and P.R.Jones. Handbook of Engineering Materials. Eds. D.F.Miner and J.B.Seastone. John Wiley and Sons, Inc. 1955, 3-346.
5. Physical Ceramics. Eds. Y-M.Chiang, D.Birnie and W.D.Kingery. John Wiley and Sons, Inc. 1997.
6. Amorphous Inorganic Materials and Glasses. Ed. A.Feltz. VCH Publishers. 1993.

7 Glass Science. Ed. R.H.Doremus. John Wiley & Sons Inc. 1994.

8 C.A.Angell. Solid State Ionics. **18-19**, (1986), 72.

9 M.D.Ingram. Physics and Chemistry of Glasses. **28**, 6, (1987), 215.

10. M.R.Morelli, B.Derby, R.J.Brook. Proc. of the 4th Euro Ceramics, Electroceramics. **5,** (1996), 97.

11 O.V.Mazurin, G.A.Pavlova, E.YaLev and E.K.Leko. Zh.Tekh.Fiz. **27**, (1957), 2702.

12 K.K.Evstrop'ev and V.A.Khar'yuzov. Dokl.Akad.Nauk SSSR. **136,** (1961), 140.

13 M.Schwartz and J.D.Mackenzie. J.Am.Ceram.Soc. **49**, (1966), 582.

14. A.E.Owen. Phys.Chem.Glasses. **2**, 3, (1961), 87.

15. A.E.Owen. Phys.Chem.Glasses. **2**, 5, (1961), 152.

16. C.Hirayama. J.Am.Ceram.Soc. **45**, 6, (1962), 288.

17 A.Feltz and B.Unger. Z.Chem. **24**, (1984), 100.

18 J.D.Mackenzie. J.Am.Ceram.Soc. **47**, (1964), 211.

19 P.W.McMillan. Adv.Glass Tech. **1**, (1962), 333.

20. S.Yamaguchi, Y.Iguchi and A.Imai. Solid State Ionics. **40/41**, (1990), 87.

21. B-S.Chiou, W.Y.Hsu and J-G.Duh. Ceramics International. **14**, 1, (1988), 7

22. M.Feng and J.B.Goodenough. J.Am.Ceram.Soc. **77**, 7, (1994), 1954.

23. V.P.Kobzareva, L.M.Kovba, L.M.Lopato, L.N.Lykova and A.V.Shevchenko. Russian J.Inorganic Chem. **21**, 6, (1976), 903.

24 C.A.J.Fisher. Ph.D. Thesis. University of Oxford, 1996.

25. N.Kiatzis, B.C.H.Steele, J.M.Ralph, M.Sahibzada, A.Atkinson and J.A.Kilner. To be published.

26 A.F.Sammells, R.L.Cook, J.H.White, J.J.Osborne and R.C.MacDuff. Solid State Ionics. **52**, (1992), 111.

27. M.Feng and J.B.Goodenough. Eur.J.Solid State Inorg.Chem. **t31**, (1994), 663.

Section 2

Experimental

Chapter 9. Powder Preparation

9.1. Introduction

Chapter 6 demonstrated the importance of the preparation method for ceramic powders, in order to obtain the desired properties. There are now many techniques available for producing powders, with resulting variations in homogeneity, particle size and degree of agglomeration. The most commonly used methods to prepare oxide powders are briefly described below. The first three methods have been used to prepare powders for study in this thesis, however, the majority of powders have been made by the amorphous citrate route.

9.2. Solid State Technique

The mixing of oxide or carbonate powders is the oldest and simplest technique available for producing a mixed metal oxide powder and many researchers in the past have used this method to produce doped ceria ceramics [1, 2, 3, 4, 5, 6, 7, 8, 9, 10, 11, 12, 13, 14]. Generally, the oxide powders are milled together for a long period of time (24hrs), to reduce the particle size of the two constituent powders, before calcination at high temperatures (1000-1200°C). The calcined powder is normally crushed and milled again before a further calcination step and this process is repeated until a single phase material remains. The small particle sizes and high temperatures are necessary to promote cation movement, such that a single phase powder results. Although this technique is simple, relatively inexpensive and capable of large scale production of ceramic powders, there are some significant disadvantages.

Problems with the agglomeration of particles, inhomogeneous cation distributions and the formation of second phases, lead to variations in grain growth during sintering and thus to poorly sinterable powders. The long milling times required for good

homogeneity can often lead to high levels of impurities. This can result in large variations in material properties between different batches of powder. For the production of electrical ceramics, this technique is becoming obsolete and the following chemical processes are more commonly encountered.

Powders produced by the mixed oxide in this thesis include: A CGO powder mixed with a deliberate doping of SiO_2 (see chapter 12) and CGO powder with additions of strontium gallate and strontium boron gallate powders, both in glass and ceramic form (see chapter 14). Solid state processing was used for these powders because alternative techniques were either not possible or impractical for these samples. In the case of the silica doped material, attempts to use the amorphous citrate route resulted in sintered materials which melted and bonded to the alumina crucible and were extremely inhomogeneous. It is thought that this is a result of silica and sodium (present in the sodium silicate, "water glass" precursor) vaporisation from the solid solution and the subsequent formation of a low melting point phase. The same results were not observed when silica powder was used in the mixed oxide route. For the strontium gallate experiments, a solid solution of CGO and strontium gallate was not desired. The aim in this experiment was to form a grain boundary phase of strontium gallate, for which the mixed oxide route was the most appropriate. A more advanced technique was also used for these latter powders which is described in section 9.6.2.

9.3. Co-Precipitation Technique

The co-precipitation of cations from solution can produce powders with excellent sinterability, however, when there are more than two cation species involved, some difficulties can be experienced. Typically, metal nitrate precursors are dissolved in distilled water to ensure molecular mixing of the cations. A basic solution (ammonia, ammonium hydroxide, etc.) is then used to precipitate metal hydroxides, which form as a result of the rapid change in pH. There are three permutations allowing combination of the nitrate and basic solutions:

1 The base is added to the salt solution

2 The salt solution is added to the base

3 The salt solution and base are added continuously

It is suggested that the best results are obtained by the continuous mixing of both solutions [15].

Once the metal hydroxides precipitate from solution, links are formed between each hydroxide and chains begin to grow. Cross-linking then enables a three dimensional network to form, resulting in a gel which incorporates both the cations and nitrate ions from the precursors. By washing the gel 3 or 4 times in water, followed by centrifuging to separate the precipitate from the nitrate ions, isolation of the precipitate can be achieved. It is then necessary to wash the precipitate in an alcohol, e.g. ethanol, to prevent hard agglomerates from forming. The alcohol is thought to prevent water molecules from bonding to adjacent particles, thus reducing the degree of agglomeration [16, 17, 18]. The gel is then dried, before calcination to the final oxide powder.

Co-precipitation produces powders which are soft and have a fine particle size but they sometimes show chemical inhomogeneity, due to the segregation of cations. Ideally, all the cations should precipitate from solution at the same pH. Precipitation of cations at different pH values, leads to an inhomogeneous mixture of the metal cations. Further, some metal hydroxides are soluble in water and thus will not precipitate, resulting in a different oxide powder composition to the one desired.

A number of researchers have used the co-precipitation route to produce singularly doped ceria with highly sinterable powders [19, 20, 21, 22, 23, 24, 25, 26, 27, 28, 29]. In this study, only one powder was produced at Imperial College by a co-precipitation route, a calcium co-doped CGO powder, $Ce_{0.8}Gd_{0.19}Ca_{0.01}O_X$. Details of the process are explained below.

1 Nitrates of Ce(>99%), Gd(99.9%) and Ca(99.997%) were weighed in the requisite proportions and then dissolved in de-ionised water.

2 The nitrate solution was then dropped into a solution of ammonia (pH≥13).

3 The resulting gel was then washed 4 times in ammonia/water solutions with decreasing ammonia concentrations. After each washing, a centrifuge was used to separate the precipitate and the liquid was decanted off.

4 A final washing in methanol was then performed.

5 The gel was dried under a UV lamp in air, ground and then milled in methanol for 2 hours.

6 Calcination of the dried powder was then performed at 900°C for 2 hours.

The resulting powder was single phase but contained hard agglomerates and the sintered compact showed a large degree of inhomogeneity. Atomic absorption spectroscopy showed very low levels of Ca and inspection of the literature revealed that $Ca(OH)_2$ was soluble in water and hence it would not precipitate, as expected, from solution. To allow a credible comparison between the properties of the Ca doped and undoped materials, it was decided not to use this processing method. This method was also very time consuming and not suitable for the production of large numbers of compositions in the laboratory.

9.4. Amorphous Citrate Technique

All powders prepared at Imperial College, excluding those mentioned above, were processed using the amorphous citrate route, which was developed by Pechini [30]. The process involves the chelation of the precursor metal cations with a hydroxycarboxylic acid (e.g. citric acid), which forms a polymer precursor, with the cations homogeneously dispersed. Often a polyhydroxyl alcohol (e.g. ethylene glycol) is then added to increase the degree of foaming during the formation of the polymeric resin, providing a better mixing of the cations. The polymer solution is then dried to form a viscous solution, which on further heating leads to polyesterification, the removal of residual water and the formation of an expanded polymer resin. Heating at higher temperatures causes a breakdown in the polymer resin, before calcination converts the powder to the final oxide.

The homogeneity of the metal cations in solution is maintained during the heating stages by fixing the cations to the polymeric resin. The resin has a high viscosity, which prevents cation segregation and the formation of hard agglomerates and results in a homogeneous distribution of cations. The large quantity of organic material present, generally requires higher calcination temperatures compared to the co-precipitation technique, to effectively remove the residual carbon.

The particular method employed in this study was similar to that of Anderton [31] and Baythoun [32] and has been adopted by some other researchers [33, 34]. The starting precursors were all metal nitrates purchased from the Aldrich Chemical Co. as follows:

a). $Ce(NO_3)_3.6H_2O$ (99.99%)
b). $Gd(NO_3)_3.6H_2O$ (99.9%)
c). $Ca(NO_3)_3.2.61H_2O$ (99.997%)

The correct proportions of each nitrate were then dissolved in de-ionised water. A magnetic stirrer and slightly elevated temperatures were used to obtain a clear solution, before citric acid (99.54%, also from Aldrich), which had been dissolved in de-ionised water, was then added to the nitrate solution. The ratio of the citric acid to metal cation content was one to one, such that there was an excess of citric acid.

The citric acid-nitrate solution was then stirred and heated to 100°C to remove excess water, leaving a viscous solution, that transformed to the polymer resin on further heating. Increasing the temperature to 400°C broke the polymer chains and caused the resin to char. Calcination to the final oxide was then performed at 900°C for 2 hours.

The addition of the citric acid to the nitrate solution allowed an organometallic complex to form. Each citric acid molecule has four potential sites for cation substitution (see Fig.9.1), but not every site will be used in the reaction and therefore an excess of citric acid is needed. As the resin is heated, the complex decomposes exothermally, breaking the carbon bonds. The resulting powder contains the cations homogeneously distributed, which enables the formation of oxide powders with a uniform composition on the molecular scale.

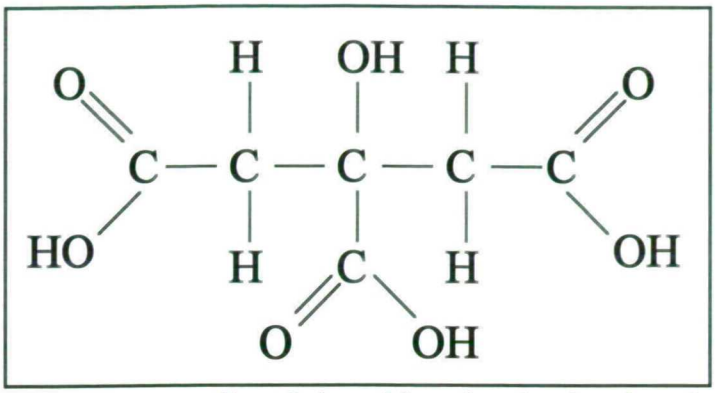


Fig.9.1. Molecular structure of a citric acid molecule showing the four potential hydroxide substitution sites.

9.5. Combustion Synthesis Technique

The production of an oxide powder with a high surface area in a single heating step, is very advantageous. Combustion synthesis using glycine can achieve such a reaction. Metal nitrates are added to glycine and dissolved in distilled water and the excess water is evaporated off, until a viscous liquid results. Further heating causes thickening of the liquid, followed by swelling, until an expanded foam is formed. At this stage, the foam ignites and a self sustaining combustion reaction produces the oxide powder. The glycine forms a complex with the metal ions, ensuring a homogeneous distribution of cations and serves as the fuel for combustion. The major problem with this technique is that the combustion of the precursors is very vigorous, even when small quantities of powder are prepared and it would therefore not be feasible to make sufficient powder in a reasonable time.

9.6. Powders Prepared at Rhône-Poulenc (RP)

All RP powders that have been used in this study have been prepared via a co-precipitation route, which is described below. One exception to this is the CGO powder with strontium gallate additions which is described separately. It is not

possible to divulge the precise preparation route of these powders for commercial reasons, however, it is possible to give a brief outline.

9.6.1. Co-Precipitation Route

Nitrates of the various metal cations were dissolved in distilled water and then added to a solution of ammonium hydroxide and ammonium hydrogen carbonate. The solution was then heated at 80°C until a polymer resin resulted, after which the product was calcined at 800° for 2 hours, to produce the final single phase oxide.

9.6.2. Powder Atomisation

In order to obtain an homogeneous coating of strontium gallate around all the particles of a standard Ce-10%Gd powder, it was necessary to employ a powder atomisation technique. The correct mixture of cations were used to create an atomised stream, through which the CGO powder was passed, producing an homogeneous layer around each CGO particle. The strontium gallate consisted of two phases which were converted to the correct single phase on heating to the melting point.

9.7. ECN Powder

One ceria powder composition was supplied from ECN in the Netherlands. The powder was prepared using a co-precipitation route, however, the details of the preparation are not available. The powder was analysed to demonstrate the differences in properties, for powders from different sources. The following composition was studied: $Ce_{0.8}Gd_{0.18}Pr_{0.02}O_{2-X}$.

9.8. Sintering

All powders were uniaxially pressed in a steel die to form a compact shape, using a pressure of 1/2 ton. The green compacts were then placed into air-tight rubber jackets

and isostatically pressed to 300MPa. The pellets were then sintered in air at 1550°C for 5 hours, to obtain the maximum density [35]. The samples were sintered in alumina trays, which had been covered with powder of the same composition as the pellets, to prevent diffusion of impurities from the alumina during sintering.

References

1. T.Kudo and H.Obayashi. J.Electrochem.Soc. **123**, 3, (1976), 415.
2. B.Cales and J.F.Baumard. J.Phys.Chem.Solids. **45**, 8-9, (1984), 929.
3. S.J.Hong and A.V.Virkar. J.Am.Ceram.Soc. **78**, 2, (1995), 433.
4. J.E.Shermilt, H.M.Williams, M.J.Edirisinghe, J.R.G.Evans and B.Ralph. Scripta Materialia. **36**, 8, (1997), 929.
5. C.Milliken, S.Elangovan and A.C.Khandkar. Ionic and Mixed Conducting Ceramics 2nd International Symposium. Eds. T.Ramanarayanan, W.Worrell and H.L.Tuller. The Electrochem.Soc. (1994), 466.
6. S.Hamakawa, T.Hayakawa, A.P.E.York, T.Tsunoda, Y.S.Yoon, K.Suzuki, M.Shimizu, and K.Takehira. J.Electrochem.Soc. **143,** 4, (1996), 1264.
7. P.Sarkar and P.S.Nicholson. J.Am.Ceram.Soc. **72**, 8, (1989), 1447.
8. G.B.Balazs and R.S.Glass. Solid State Ionics. **76**, 1-2, (1995), 155.
9. H. Yahiro, K. Eguchi and H. Arai. Solid State Ionics. **36**, (1989), 71.
10. D.L. Maricle, T.E. Swarr and S. Karavolis. Solid State Ionics. **52**, (1992), 173.
11. R.T.Dirstine, R.N.Blumenthal and T.F.Kuech. J.Electrochem.Soc. **126**, 2, (1979), 264.
12. H.L. Tuller and A.S. Nowick. J.Electrochem.Soc. **122**, 2, (1975), 255.
13. M.Levy and J.Fouletier. Solid State Ionics. **12**, (1984), 467.
14. C.Ftikos, M.Nauer and B.C.H.Steele. J.European Ceram.Soc. **12**, 4, (1993), 267.
15. P.A.Lesing. Am.Ceram.Soc.Bull. **68**, 5, (1989), 1002.
16. M.J.Readey, R.Lee, J.W.Halloran and A.H.Heuer. J.Am.Ceram.Soc. **73**, 6, (1990), 1499.
17. S.L.Dole et al. Mats.Sci.and Eng. **32**, (1978), 277.
18. M.S.Kaliszewski and A.H.Heuer. J.Am.Ceram.Soc. **73**, 6, (1990), 1504.

19. R.Gerhardt-Anderson and A.S.Nowick. Solid State Ionics. **5**, (1981), 547.
20. D.Y.Wang, D.S.Park, J.Griffith and A.S.Nowick. Solid State Ionics. **2**, (1981), 95.
21. Y.Takasu, T.Sugino and Y.Matsuda. J.Appl.Electrochem. **14**, 1, (1984), 79.
22. J.Faber, C.Geoffroy, A.Roux, A.Sylvestre and P.Abelard. Applied Physics A: Solids and Surfaces. **49**, 3, (1989), 225.
23. A.D.Logan and M.Shelef. J.Mater.Research. **9**, 2, (1994), 468.
24. J.Fouletier and M.Henault. Solid State Ionics. **9-10**, (1983), 1277.
25. B.C.Morris, W.R.Flavell, W.C.Mackrodt, and M.A.Morris. J.Mater.Chem. **3,** 10, (1993), 1007.
26. M.P.Anderson, D.E.Cox, K.Halperin and A.S.Nowick. Solid State Ionics. **9&10,** (1983), 953.
27. D.S.M.Bevan, W.W.Barker, R.L.Martin and T.C.Parks. Proc. of the 4th Conference on Rare Earth Research. Ed. L.Eyring. Gordon and Breach, New York. (1965), 441.
28. J.Tanaka, J.F.Baumard and P.Abelard. J.Am.Ceram.Soc. **70**, 9, (1987), 637.
29. P.Li, I.-W.Chen, J.E.Penner-Hahn and T.-Y.Tien. J.Am.Ceram.Soc. **74**, 5, (1991), 958.
30. M.Pechini. United States Patent No. 3,330,697, (1967).
31. D.J.Anderton and F.R.Sale. Powder Metallurgy. **1**, (1979), 14.
32. M.S.G.Baythoun and F.R.Sale. J.Mater.Sci. **17**, (1982), 2757.
33. T.Kenjo, Y.Horiuchi and S.Osawa. J.Electrochem.Soc. **137**, 8, (1990), 2423.
34. M.Mogensen, T.Lindegaard, U.R.Hansen and G.Morgensen. Proc. of the Ionic and Mixed Conducting Ceramics 2nd International Symposium. The Electrochem. Soc. (1994), 448.
35. R.Gerhardt and A.S.Nowick. J.Am.Ceram.Soc. **69**, 9, (1986), 641.

Chapter 10. Characterisation Techniques

10.1. Introduction

This chapter describes the techniques and equipment used in the characterisation of all the samples studied in this thesis. The beginning of the chapter briefly discusses the initial powder and sintered ceramic studies performed, emphasising any special procedures required. More in-depth discussions are then included on the main analysis techniques, including electrical testing, TEM, SIMS and LEIS. The end of this chapter then describes the characterisation techniques used for thin film analysis. Results and discussion of data obtained from these techniques is included in the following chapters.

10.2. Thermogravimetry of Precursor Material

The nitrate precursors and citric acid used in the preparation of powder at Imperial College have been discussed in the previous chapter. Most of these precursors absorb a certain degree of water, if left in air and so it was important to ascertain the correct water of crystallisation stoichiometry in these materials, so that accurate additions of each could be made in producing the desired CGO powders. The calcium nitrate water content had previously been determined using an evaporation technique (the nitrate concentration was assumed to be close to that expressed by the manufacturers). The water content was found to be 2.61moles.

For the cerium and gadolinium nitrates, the water of crystallisation content was determined by thermogravimetry (TG) and differential thermal analysis (DTA). The nitrate concentration was also determined using this technique. A Stanton Redcroft Simultaneous Thermal Analyser STA-780 Series was used, capable of weighing down to 0.01mg. Measurements were made in air, in the temperature range 25-600°C, using platinum crucibles and an alumina reference for calibration. The changes in weight

loss as the sample temperature was raised, were then quantified to calculate the percentage of reactant.

10.3. Composition Analysis

10.3.1. Inductively Coupled Plasma

The concentration of 58 elements has been determined in selected ceria powder compositions using this technique. The inductively coupled plasma (ICP) was combined with atomic emission spectroscopy (AES) to quantify the Gd concentrations. Using an internal standard, an uncertainty of 5% was achieved. A similar method was used to calculate the concentrations of Si, Ca, Al and Mg; however, in these cases, an external standard was used, giving an uncertainty of 10%. The remaining elements were analysed semi-quantitatively using ICP and mass spectrometry (MS), giving an uncertainty of 20%.

The powders were prepared for ICP, by first adding the powders and HCl into a PTFE beaker and then rapidly heating in a microwave to dissolve the powder.

10.3.2. Atomic Absorption Spectroscopy

Atomic absorption spectroscopy (AAS) was used to determine the concentrations of Ca and Si in a number of the powder compositions. A Perkin Elmer 2380 Atomic Absorption Spectrophotometer with a double beam was employed. Calcium and silicon cathode lamps were used for the metal determination, following the aspiration of the metallic salt solutions into a nitrous oxide/acetylene flame.

Initial attempts to dissolve the oxide powders using nitric acid and hydrochloric acid proved unsuccessful. A more satisfactory result was obtained when sulphuric acid was used and the solution heated. The powders did not completely dissolve, however, the majority of Ca is expected to be in solution because of its high solubility. In order to determine the silicon concentrations, the powders were dissolved in heated

hydrofluoric acid. The powders were still not fully dissolved and so the total Si concentration could not be calculated. The solutions did, however, allow the concentration of "free" silicon (i.e. in SiO_2) to be calculated. It is thought that the undetectable silicon will form part of a complex silicate structure, which is less likely to contribute to grain boundary impurity effects. The problems experienced with the dissolution of these powders could be solved by the use of a digestion vessel, which, at elevated temperatures, increases the pressure within a small volume containing the powder and acid and significantly increasing the solubility limit of the acid. It is recommended that further AAS be carried out using this technique.

10.4. Particle Size Analysis

The calcined powder particle size distribution was determined by a laser light scattering technique, using a Malvern Instruments Mastersizer MS1005 fitted with a lens capable of measuring particle sizes in the range 0.1-80μm. The powders were ultrasonically dispersed in distilled water prior to characterisation, with a few drops of a dispersant added to reduce the degree of agglomeration. This technique is based on the fact that laser light will be scattered by particles in suspension. The angle of scattering is related to the particle size and the intensity of the scattered light at any given angle is related to the proportion of particles of that size in the suspension. All powders were characterised using this technique, to help explain any differences observed during sintering.

10.4.1. Specific Surface Area Measurements

Specific surface area measurements of a selection of powders were made using the nitrogen gas adsorption or BET technique. A Quantachrome NOVA 2000 Analyser was used, which had a surface area range between 0.01-2000m^2/g. The technique utilises low temperature adsorption, or the uptake of nitrogen gas on a powder surface at the temperature of liquid nitrogen. The surface area is determined by the volume of gas required to form a monolayer on the powder surface.

10.4.2. Scanning Electron Microscopy

The morphology of a selection of ceria powders was examined using a JEOL JSM-220A scanning electron microscope in the secondary electron mode. Powder samples were mounted onto aluminium stubs using a thin film of epoxy resin and coated in gold, to avoid charging of the sample by the electron beam.

10.5. Dilatometry

10.5.1. Sintering Dilatometry

To study the sintering behaviour of a number of Imperial College and Rhône-Poulenc powders, dilatometry was performed to assess the shrinkage behaviour of the powders during sintering. A SETARAM CRPHT vertical dilatometer was used to record the shrinkage data in air, over the temperature range 20-1550°C and at a heating rate of 10°C/min. Cylindrical samples were isostatically pressed to 300MPa and the ends polished flat. The length of the samples were kept between 5-8mm. Platinum foil was placed between the sample and the alumina holder to prevent any contamination or reactions. The dilatometer software compensated for the expansion of the sample holder for each measurement.

10.5.2. Thermal Expansion Coefficients

The thermal expansion behaviour of several sintered ceria samples of different composition were measured, using a Netzcsh 402E horizontal dilatometer in air. Measurements were made on polished bars between 15-30mm in length, that had been prepared as described in chapter 9. Data was recorded between 20-1200°C at a heating rate of 10°C/min. The dilatometer had been calibrated with an alumina sample, to compensate for the expansion of the alumina sample holder.

10.6. X-Ray Diffraction

Both powder and sintered ceramic samples were examined by x-ray diffraction (XRD). A Philips PW1710 diffractometer using CuK_α radiation of wavelength 1.54178Å was utilised to identify the phase purity, crystal structure and lattice parameters of each composition. Silicon (111) served as an external calibration standard and the ceramic samples were rotated during analysis, to increase the number of orientations of the crystal grains available to the incident x-rays. Samples were analysed over the angular range 10° to 130° 2θ at a scan rate of 2.4° 2θ/min and the diffraction patterns were collected with the aid of Philips PC-APD software. The diffraction patterns were then compared to the documented pattern for ceria in the JCPDS index. The true lattice parameter was determined by a linear regression of lattice parameter verses $\cos^2\theta$ for peak values above 70°2θ, to obtain the lattice parameter at $\cos^2\theta=0$.

10.6.1. High Temperature X-Ray Diffraction

The development of a second phase in the gadolinia doped ceria samples, described by Bevan [1], was studied using high temperature XRD. Two samples were analysed, a low dopant concentration ($Ce_{0.97}Gd_{0.03}O_{2-x}$) and a high dopant concentration ($Ce_{0.7}Gd_{0.3}O_{2-x}$). A Philips X'Pert diffractometer equipped with an Anton Paar HTK-16 high temperature camera was used to record the diffraction patterns. Measurements were recorded at 100°C intervals between 300-1000°C, with an equilibration time of one hour. Slow scans (3 hours) were performed at 500°C and 1000°C for the high dopant concentration sample to analyse fine details.

10.7. Density Measurements

The bulk density of the sintered ceramic pellets was calculated using the Archimedes' method described below:

1. The pellet is heated in an oven to remove any water.
2. The dried pellet is then weighed in air (M_{air}).

3. The pellet is placed into a beaker of distilled water in a vacuum desiccator for one hour.
4. The pellet is weighed suspended from a thin wire in a beaker of distilled water (M_{water}).
5. The wire suspended in the water is then weighed (M_{wire}).
6. The surface water is removed from the pellet and the pellet is re-weighed ($M_{wet/air}$).

The bulk density of the sintered ceramic is then calculated according to equation 10.1,

$$\rho_{bulk} = \frac{M_{air}}{M_{wet/air} - (M_{water} - M_{wire})} \times \rho_{water/T} \qquad (10.1)$$

where $\rho_{water/T}$ is the density of water at the temperature of the measurement. The measured density is normally expressed as a percentage of the theoretical density ($\rho_{theoretical}$), which is calculated from equation 10.2.

$$\rho_{theoretical} = \frac{(MW \times Z)_n}{N_A \times V_{unit\ cell}} \qquad (10.2)$$

where MW is the molecular weight and Z is the number of these atoms in the unit cell, for all n atoms, N_A is the Avagadro number and $V_{unit\ cell}$ is the volume of the unit cell calculated from the lattice parameter for the ceria solid solution.

10.8. Grain Size Determination using Optical Microscopy

The mean grain sizes of the sintered ceramic pellets were determined using the grain intercept method [2]. Samples were first polished in steps down to a 1μm diamond finish before thermal etching between 1435-1450°C for 20 minutes. Grain size measurements were then determined from optical photographs, which were taken with a Zeiss-Jenalab optical microscope with a CCD video camera module. Images were recorded using UTHSCSA Image Tools IT version 1.25 software.

10.9. A.C. Impedance Spectroscopy

10.9.1. Introduction

A.C. impedance spectroscopy has been used as the primary technique for measurement of the electrical properties of all doped ceria ceramics. The theory of this technique will be discussed in greater detail in chapter 12. This section will explain the sample preparation and experimental set-up.

10.9.2. Sample Preparation

The sintered pellets were first ground using 1200 grit SiC paper to obtain flat, smooth faces on either side of each pellet. Platinum paste was then applied to each face and baked at 950°C for 1/2hour, to ensure a good contact with the pellets. Electrical measurements were made via platinum wires attached to fine platinum meshes, which provided the current contacts to each electrode on the pellets. The pellets and contacts were held in position with springs, which applied a compressive force. The sample holder is shown schematically in Fig.10.1. Impedance spectra were obtained using a Solartron 1260 frequency response analyser over the frequency range 0.1-10^7Hz. Measurements were made in the temperature range 150-500°C in air. The amplitude of the applied excitation voltage was maintained at 50mV to ensure a linear response.

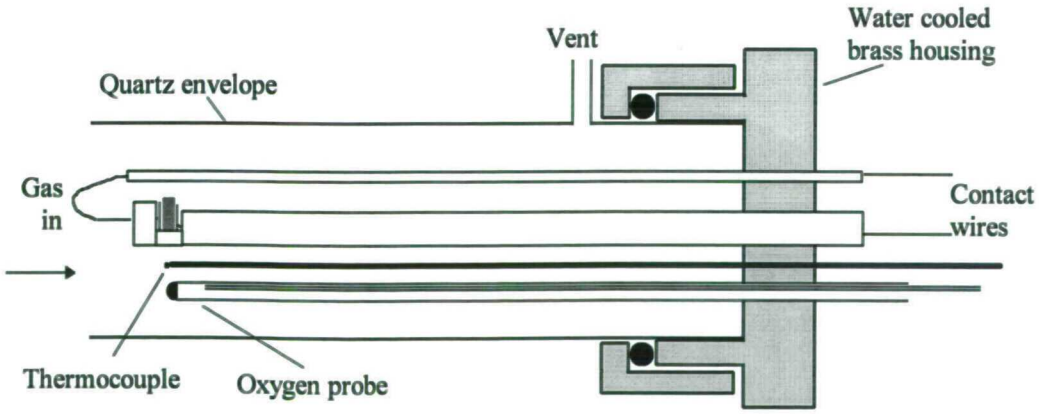


Fig.10.1. Schematic of the a.c. impedance sample holder (from Lane [3]).

Each spectra shows two high frequency semi-circles which represent the response of the grain interior and grain boundary of these materials. Suitable fitting of these semi-circles permits the resistance of these components to be measured and plotted on an Arrhenius graph of logσT versus 1/T. The gradient of each line can then be used to calculate the activation energy for ionic conduction.

10.10. Four-Point D.C. Resistivity

Using a 4-point d.c. resistivity technique, the electrical conductivity of dense ceramic bar samples was measured for several ceria compositions, as a function of both temperature and oxygen partial pressure. Each bar was ground to produce flat, parallel faces with the approximate dimensions 4mm × 4mm × 30mm. The dimensions of each bar were accurately measured using a digital micrometer. Four platinum wires were then attached along the length of the bar (Fig.10.2): The two outermost wires were wrapped around the bar for the current supply. Platinum paste was also applied to the bar around the wires to ensure a good electrical contact. The two central wires were located accurately on the bars by making small notches to rest the wires onto, and then wrapping the wires around as before. The precise distance between the central two wires was measured using a digital micrometer.

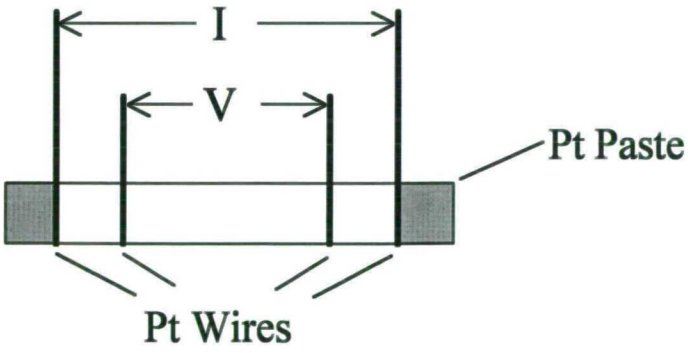


Fig.10.2. Schematic of the bar samples used for electrical resistivity measurements.

The bar was then placed onto an alumina tube, with the correct length to allow the sample to be placed into the hot zone of a furnace. Four platinum wires ran through the tube, connected at one end to the sample and at the other end to a digital voltmeter

and a Solartron 1186 Electrochemical Interface for the supply of a constant current. A thermocouple and zirconia probe were situated close to the sample and all three were enclosed in a quartz glass envelope, which was placed inside the furnace. The oxygen partial pressure inside the quartz envelop was controlled by mixing different ratios of CO/CO_2 and H_2/CO_2 at known flowrates with digital mass flow meters. The apparatus can be seen in Fig.10.3. The current was kept between 1-3mA, so that the voltage did not exceed 1V. Above 1V, ceria can be reduced, which increases the electronic conductivity.

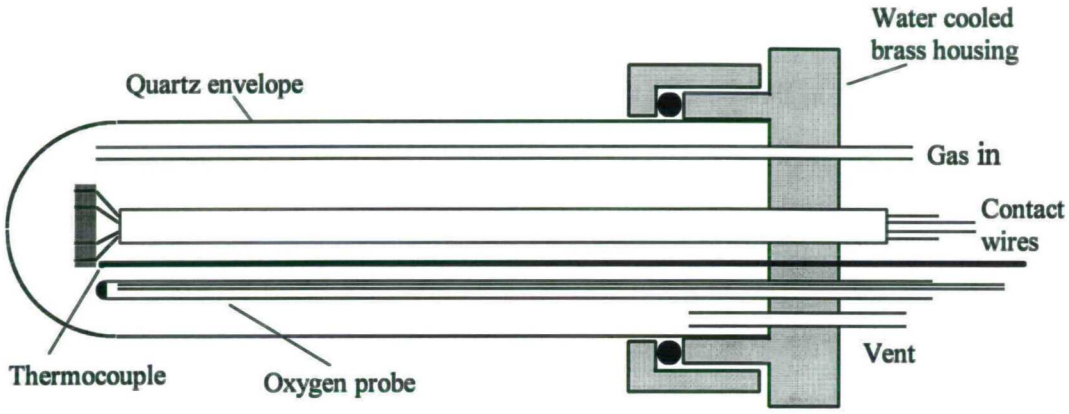


Fig.10.3. Schematic of the 4-point d.c. electrical conductivity holder (from Lane [3]).

At a given temperature and oxygen partial pressure the conductivity (σ) can be calculated from equation 10.3.

$$\sigma = \frac{l}{RA} \qquad (10.3)$$

where A is the cross sectional area of the bar, l is the length between the two potential wires and R is the measured resistance, which can be calculated from Ohm's law (V=IR). The oxygen partial pressure can be calculated from the emf generated at the oxygen probe, using the Nernst equation.

10.11. Electrical Measurements at Rhône-Poulenc

Impedance spectroscopy and four point d.c. resistivity measurements were performed, using the same sample preparation methods as previously discussed. Identical equipment was used for the a.c. impedance measurements, while a Keithley High Performance Multimeter Model 2001 was used as the constant current in the d.c. resistivity measurements. Oxygen partial pressures were calculated by accurately controlling the gas flow rates and data available in the literature [4]. D.C. resistivity data was also recorded in air over the temperature range 300-900°C for a selection of compositions. All data collection was automated using in-house designed programs.

10.12. Transmission Electron Microscopy

Grain boundaries, as mentioned in chapter 6, act as regions of discontinuity and sinks for dopant and impurity segregation. It is then critical, to look into grain boundaries and analyse the structure and chemical composition present, to elucidate on the electrical behaviour observed. The thickness of grain boundaries in ceria ceramics is estimated at 2–3nm [5]. This small size makes it very difficult to observe the grain boundaries unless high resolution (HR) TEM is employed and for this reason, there are very few reports on direct observation of grain boundaries.

The preparation of ceramic samples for transmission electron microscopy (TEM), presents many more difficulties compared to the preparation of metal samples, due to the extremely thin sections required. The brittle nature of ceramics often leads to fracture, as the ceramics become thinner. Ion beam thinning is usually employed to reduce the thickness of a sample to electron transparency but the bombardment of the incident ions can often leave the sample with extrinsic deformation features. The identification of true grains can be performed by tilting the sample in three dimensions and observing the contrasting effects in the transmission image. Once the grain boundary region is recognised, the correct orientation of the grain boundary and adjacent grains parallel to the electron beam must be achieved, before a high resolution lattice image can be obtained. It is at this stage, where a certain degree of serendipity

is required because few grain boundaries allow correct alignment with the electron beam.

10.12.1. TEM Preparation

A number of routes were used to prepare samples for TEM analysis but all samples had to have a diameter of 3mm or less, in order to place them into the sample holder.

10.12.1.1. Preparation Route 1

A sintered pellet was first ground to between 150-200μm (below this thickness, the samples become difficult to handle) and then cut with a diamond impregnated wire saw into rectangular shaped pieces 2mm×1.5mm. These pieces were then placed into a steel grid (non-magnetic) with a 3mm diameter and rectangular hole in the centre for the ceramic sample (Fig.10.4).

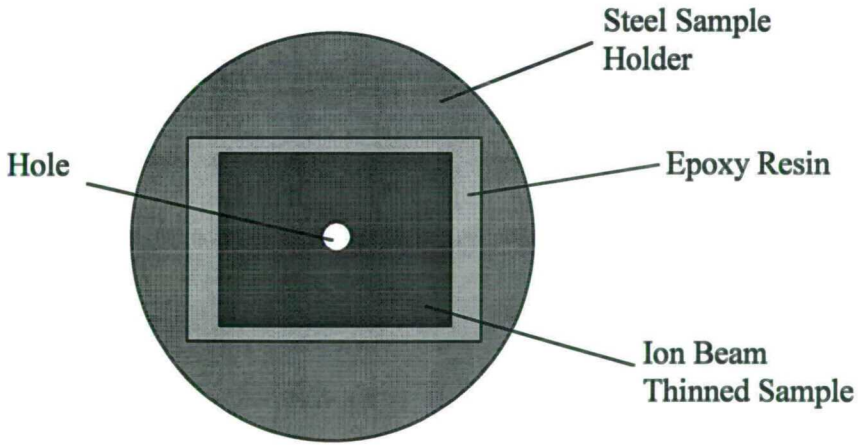


Fig.10.4. Schematic representation of a mounted TEM sample.

A quick setting epoxy resin (Araldite) was used to fix the ceramic into the hole of the metal grid. The glue was left to set overnight, before the glue and sample were ground further to between 80-100μm. The centre of each sample was then reduced further by a technique known as 'dimpling', which must be performed on both sides of a specimen for optimum results. A dimpling grinding wheel rotates perpendicular to the sample surface while the sample also rotates, such that the centre is ground at the quickest rate. In theory, dimpling is finished when a small hole appears at the centre of

the sample, however, in practice, fracture normally occurs at this stage and thus a 10-20μm thickness should remain at the centre. Ion beam thinning is then a standard, less aggressive technique to thin the centre of the sample to a thickness of 0-200nm. Two ion beams (one directed on the top surface and one on the lower) of 5keV and 0.5nA are used on a rotating sample in a vacuum of 2×10^{-4}torr. The incident angle of the ion beam onto the sample starts at 12° and is then reduced to 8°. Finally, the sample has a thin carbon film deposited onto the analysis surface to prevent charging problems.

10.12.1.2. Preparation Route 2

An ultrasonic circular drill was used to cut 3mm diameter specimens from a sintered pellet. The specimens were mounted onto a metal stub, which allows the samples to be ground to between 40-80μm. Following this, dimpling could be performed until a small hole was visible at the centre, without fracture. Ion beam thinning was then used, as described above, to produce a sufficiently thin section at the centre of the sample, followed by carbon coating.

10.12.1.3. Preparation Route 3 (Rhône-Poulenc facilities)

A sintered pellet was crushed into small particles and then mixed with a carbon impregnated resin and set for 24 hours. An ultramicrotomic cutting device was then used to obtain thin sections 50nm in thickness. The cut sections were ready for examination, needing no ion beam thinning or carbon coating.

Preparation routes 2 and 3 were most successful in terms of good images and data, although the density of material in route 3 is rather low and thus reduces the probability of finding correctly aligned grain boundaries.

In order to obtain a complete set of data on each sample analysed, it was necessary to use three different transmission electron microscopes. The Ce-6%Gd R-P sample was analysed on a JEOL FX2000 MK1 TEM, with electron diffraction and a Link Systems chemical analysis unit, operating at 200kV and a minimum spot size around 5nm in diameter. The Ce-26%Gd and Ce-19%Gd-1%Ca samples were analysed at R-P using

a Philips CM30 TEM, equipped with a PGT XEDS spectrometer for chemical analysis. XEDS analysis was performed in STEM mode using a 7nm probe, operating at 300kV. The Ce-3%Sm-3%Y and Ce-3%La-3%Yb samples were analysed using both the FX2000 MK1 mentioned above and the FX2000 MK2 operating at 200kV, which provides easier imaging and electron diffraction collection. All attempts to find correctly aligned grains and grain boundaries were unsuccessful but some orientations still allowed high resolution images of the grain boundaries and these micrographs are shown in the results.

10.13. Measurement of Oxygen Diffusion Coefficients

It was shown in chapter 5 that the oxygen self-(tracer) diffusion coefficient, D*, could be directly related to the oxygen ion conductivity, σ_i, provided the concentration of oxygen sites in the ideal crystal lattice is known. To enable the oxygen self-diffusion coefficient to be calculated, ceria samples have been annealed in a labelled isotope exchange process and then the concentration profile of the labelled isotope measured, using a secondary ion mass spectrometer (SIMS). A brief description of the oxygen isotope exchange and SIMS analysis is given below. Detailed explanations of these techniques and their limitations can be found in the literature [6, 7].

10.13.1. Sample Preparation and Oxygen Isotope Exchange

Pellets with densities >95% were prepared using the route described in chapter 9. The thickness of each pellet was approximately 3mm. A standard surface finish was obtained on one face of each of the pellets, by grinding and then polishing the pellets with successively finer grades of diamond paste, down to 0.25μm. The samples were then ultrasonically cleaned in acetone.

For the oxygen isotope exchange experiments, the stable oxygen isotope ^{18}O was chosen because it is the most suitable oxygen tracer for SIMS analysis. The exchange experiments were performed in an UHV rig, where the samples were placed in a silica tube, such that a tubular furnace could be rolled on and off to allow fast heating and

cooling rates. Once the main chamber had been evacuated, research grade oxygen of natural isotopic abundance was introduced. The pre-heated furnace was then rolled on to the tube and the samples pre-annealed, for approximately an order of magnitude longer than the tracer exchange anneal. This ensured that the material was in equilibrium at the chosen temperature and oxygen partial pressure. The samples were then quenched and the chamber evacuated, before the labelled ^{18}O was introduced and the samples were annealed at the same temperature as before. After the desired time, the furnace was rolled off and the samples quenched.

The anneal temperature is monitored by a thermocouple situated close to the sample and logged onto a computer as a function of time. The annealing time and temperature are then calculated from the temperature-time profile, using an expression derived by Killoran [8], which takes into account the time periods required to heat up and cool down the sample. The concentration of the ^{18}O in the ^{18}O enriched gas atmosphere is measured with a mass spectrometer attached to the exchange apparatus. This is necessary to obtain accurate values for the surface exchange coefficient, *k*.

10.13.2. Secondary Ion Mass Spectrometry

The diffusion profile within the annealed ceramics was measured, using secondary ion mass spectrometry (SIMS) which can differentiate between the ^{16}O and ^{18}O oxygen isotopes and record their concentrations as a function of length or time. An Atomika 6500 Ion Microprobe was used for the SIMS analysis, the details of which are shown in Fig.10.5. There are essentially three sections: the primary ion beam, the main chamber and the secondary ion detection system. A primary ion beam of Xe^+ with an energy of 15keV was used for all samples. The primary ion beam is accelerated towards the sample and collides with the surface, losing energy to atoms on the surface and near surface. Some of the surface atoms are subsequently sputtered from the sample in random directions. These secondary ions are then accelerated towards a mass analyser and through a quadrapole mass filter to a channeltron detector, which records the count rate of ions with assigned mass/charge ratios.

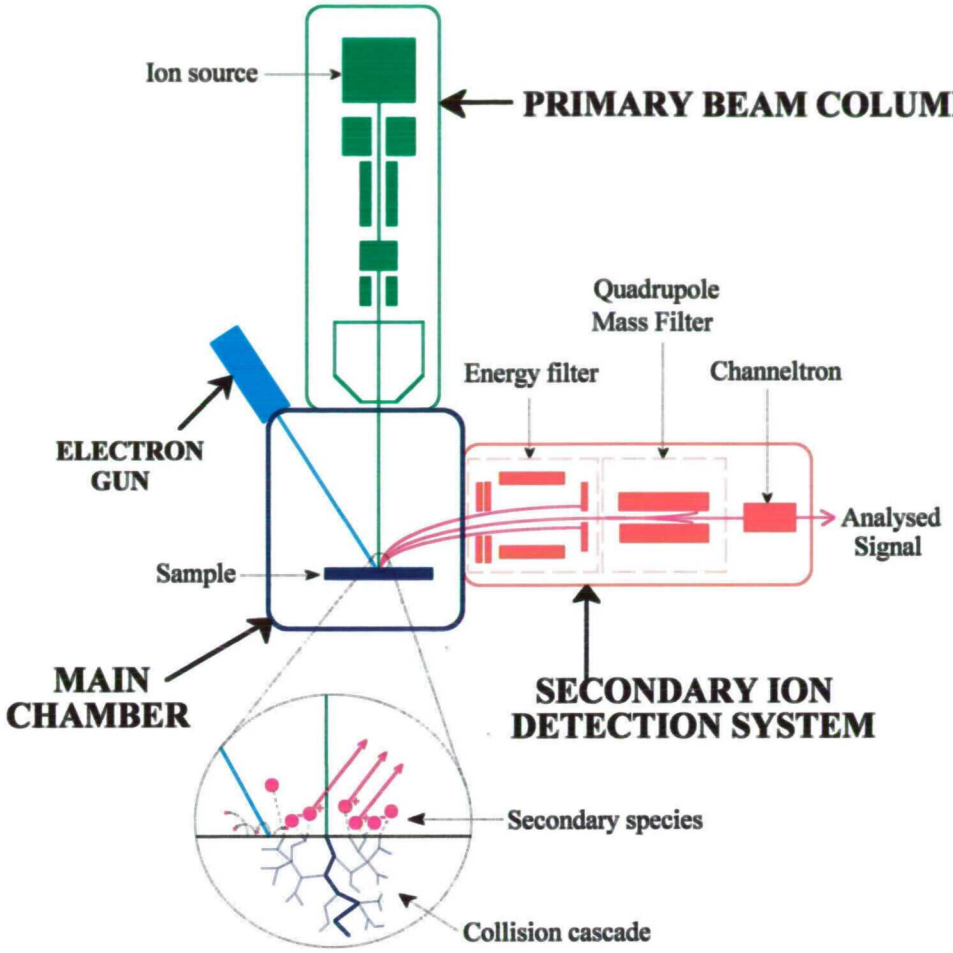


Fig.10.5. Schematic diagram illustrating the key features of the Atomika 6500 SIMS (from Patel [9]).

The main chamber pressure is maintained below 10^{-9}mbar throughout the analysis, to avoid scattering of the primary and secondary ion beams. The ceria samples studied in these experiments are all insulators and their surfaces will accumulate charge from the bombardment of the primary ion beam. It was therefore necessary, to use an electron gun to provide a high intensity, low energy beam of electrons onto the sample surface during analysis, for charge compensation. Using the electron gun restricted the area of analysis on each sample to less than 1000μm^2, outside which sufficient charge compensation was not possible and the profiles became very noisy.

Doped ceria ceramics have reasonably high diffusion coefficients and, therefore, long diffusion profiles. A linescanning technique was thus used in the SIMS to measure the concentrations of ^{16}O and ^{18}O through the depth of the sample. This method involves

cutting the exchanged sample perpendicular to the original polished exchanged surface and then polishing this newly revealed surface again to 0.25μm (Fig.10.6).

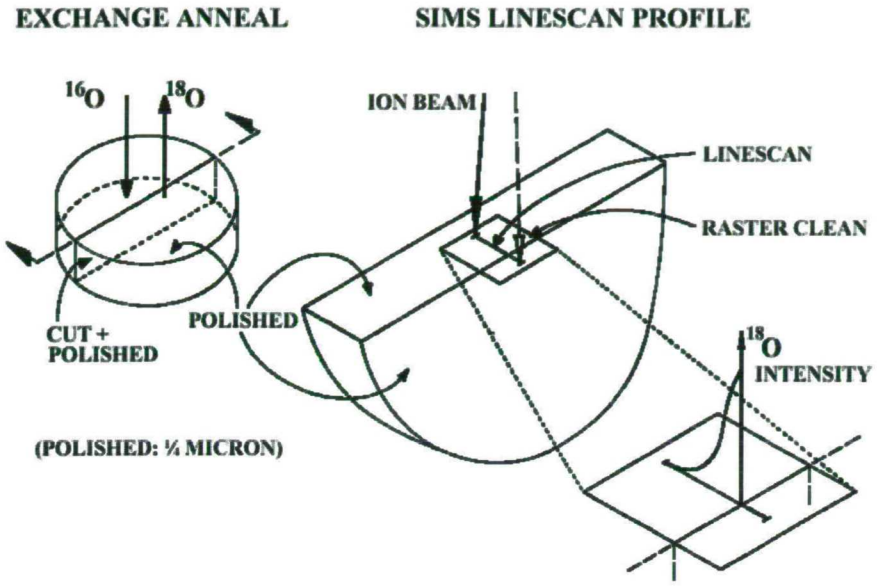


Fig.10.6. Schematic diagram of the SIMS line-scanning technique (from Chater et al. [7]).

The primary ion beam is then scanned along the surface, starting from the exchanged surface and finishing when the ^{18}O concentration drops to the natural ^{18}O background level (0.2%). The surface concentration of ^{18}O for each sample was measured, using a depth profiling technique, described by Chater et al. [7]. Samples with a relatively low surface concentration, were placed back-to-back with an unannealed sample for linescanning. This was to ensure, that the profile finished at the background concentration in the annealed sample. For the higher surface concentration samples, two annealed pieces were linescanned back-to-back. This enabled more linescans to be recorded per analysis and allowed the start of each diffusion profile to be more easily determined.

The isotopic fraction, C(x), at any point in the linescan is then simply given by:

$$C(x) = \frac{\text{Number Density of } ^{18}O \text{ atoms}}{\text{Number Density of } \left(^{18}O + ^{16}O\right) \text{ atoms}} \qquad (10.4)$$

The normalised ^{18}O isotopic fraction, C'(x), was then fitted to the solution of Fick's second law of diffusion, using equation 10.5, obtained by Crank [10]. The solution assumes a semi-infinite medium, a constant isotope concentration during the anneal and a surface exchange reaction that is proportional to the difference in isotope concentration between the gas and the solid. The derivation of this equation can be found in reference [3].

$$C'(x) = \frac{C(x) - C_{bg}}{C_g - C_{bg}} = \mathrm{erfc}\left(\frac{x}{2\sqrt{D^* t}}\right) - \exp\left(hx + h^2 D^* t\right)\mathrm{erfc}\left(\frac{x}{2\sqrt{D^* t}} + h\sqrt{D^* t}\right) \tag{10.5}$$

where C_{bg} is the ^{18}O background concentration, C_g is the concentration of ^{18}O in the gas phase, erfc is the complimentary error function, x is distance from the surface, D* is the oxygen self-diffusion coefficient, t is the time for the ^{18}O anneal and h=k/D*.

A depth profile that corresponds to the solution of the diffusion equation indicates, that solid state bulk diffusion is being measured. Deviation from the predicted behaviour indicates the presence of other diffusion paths. The parameters D* and k can be obtained by a non-linear least squares fit of the experimental data to equation 10.5. The error in D* is always found to be greater than that of k and an accuracy in D* of 10% requires a minimum diffusion length of 50μm when using the smallest ion beam (5μm diameter) [6].

10.14. Low Energy Ion Scattering

10.14.1. Introduction

Low energy ion scattering (LEIS) is a surface analysis technique, which selectively probes the outermost atomic layer of a solid to yield information about the elemental surface composition. An inert gas ion beam is scattered from the surface of a material, as a result of a binary elastic scattering collision with surface atoms. The use of inert gases ensures that the scattered ions mainly result from collisions with the outermost

atoms and are in an ionised state. With a knowledge of the incident beam energy, mass of the ion and surface atom and the scattering angle, the energy loss of the incident ion can be calculated. The scattering energy is proportional to the mass of the target atoms and thus the distribution of scattered ion energies reflects the composition of the sample surface.

10.14.2. Sample Preparation

Four sintered samples were prepared for LEIS measurements. Due to the nature of the technique, the surfaces of 'as sintered' materials can be analysed, thus removing the need for polishing. However, a polished and annealed sample was also analysed as a standard, to ensure that surface roughness caused no differences. The samples and sample holder were cleaned in ethanol for 1 hour in an ultrasonic bath. The samples were then transferred to the vacuum chamber and annealed between 340-380°C for 30 minutes in an oxygen atmosphere, before the final transfer into the main chamber.

An elemental study of the surface monolayers of several CGO pellets were analysed using the ERISS (Energy Resolved Ion Scattering Spectroscopy) LEIS apparatus in Eindhoven. Experiments are performed in a UHV chamber with an electron gun aimed at the sample surface for charge compensation. The scattered ions are first energy resolved with a double cylindrical toroidal analyser, before detection using a series of channel plates to record the count rate of ions. The data was then analysed with a program written in-house. It was necessary to use three different mass beams so that all the target elements could be resolved. Each beam shows the highest resolution for target elements with a similar atomic weight to that of the beam. A 3keV $^{3}He^{+}$ beam was initially used to detect the presence of residual carbon on the surface. A 3keV $^{4}He^{+}$ beam was then used to analyse low to medium atomic weight elements. A $^{20}Ne^{+}$ beam was finally utilised to separate the signals for the cerium and gadolinium ions. All beam currents were initially 1nA and were increased to sputter at a faster rate. The apparatus was capable of annealing samples up to temperatures of 500°C.

In-situ x-ray photoelectron spectroscopy (XPS) was also performed, to analyse the elements present at a greater depth than that obtainable with LEIS. This provided

information about the elements present in the bulk of each sample. XPS is based on the emission of photoelectrons from atoms when irradiated with X-rays. The energy of the emitted photoelectron then carries unique information concerning the nature of the stimulated atom. A VG Scientific type 427 Twin Anode was used to generate Mg K_α X-rays and the emitted electrons were detected with the same set-up used for LEIS. All LEIS and XPS measurements were made by Mr Marc Ponjée at Eindhoven.

10.15. Thin Film Analysis

The deposition of CGO thin films onto ferritic stainless steel substrates has been discussed in chapter 7. XRD was first performed on the films to confirm the identity of the phases present and to study signs of texturing after deposition. Analysis was performed by Dr. D. Waller.

The thickness of each film was then determined using a surface profilometry technique, for which a Taylor-Hobson Talystep was used. The Talystep is a mechanical instrument that uses a finely sprung stylus, which is dragged across the surface of the specimen, producing a scaled print out, from which the thickness can be calculated.

Both SEM (using a JEOL JSM-220A scanning electron microscope) and atomic force microscopy (AFM) were used to investigate the morphology of the thin films. Porosity, pin holes, cracks and grain boundaries were the main defects which were analysed for.

The AFM consists of a fine probe which scans across the surface of the sample, revealing the surface morphology by measuring the force acting on the scanning tip. The tip is not in contact with the surface and so the force is determined by the interactions between the tip and the surface. The surface can thus be measured to a vertical resolution of 1nm, and a lateral resolution of 5nm. A Quesant QScope 250^{TM} AFM was used in air for these experiments.

The thin films were finally prepared for electrical testing by painting a thin layer of conductive silver paste onto the films. The silver electrodes were dried under a UV lamp instead of being baked on (as in the standard preparation), to prevent the silver paste from diffusing through any pinholes in the thin films. Impedance spectroscopy was then performed on each film between room temperature and 150°C, using the set-up described previously.

References

1. D.J.M.Bevan and E.Summerville. Handbook on the Physics and Chemistry of Rare Earths. Ed. K.A.Gschneider and L.Eyring. North-Holland Publishing Company, 1979, 401.
2. M.I.Mendelson. J.Am.Ceram.Soc. **52**, 8, (1969), 443.
3. J.A.Lane. Ph.D. Thesis. University of London, 1995.
4. K.P.Abraham. Ph.D. Thesis. University of London, 1959.
5. G.M.Christie and F.P.F.van Berkel. Solid State Ionics. **83**, (1996), 17.
6. R.A.De Souza. Ph.D. Thesis. University of London, 1996.
7. R.J.Chater, S.Carter, J.A.Kilner and B.C.H.Steele. Solid State Ionics. **53-56**, (1992), 859.
8. D.R.Killoran. J.Electrochem.Soc. **109**, (1962), 170.
9. S.B.Patel. Ph.D. Thesis. University of London, 1994.
10. J.Crank. Mathematics of Diffusion. Oxford University Press. 1975, 36.

Section 3

Results

And

Discussion

Chapter 11. Sample Preparation

11.1. Introduction

Chapters 5 and 6 show the wide variations in electrical properties for doped ceria, when identical compositions are processed using different processing methods. For this reason, it is essential to have a full understanding of the properties for each composition, before it is possible to compare similar compositions. The results discussed in this chapter and chapter 13 aim at providing a complete picture of all the compositions that will be tested in the proceeding chapters. It is thought, that any differences which are not accounted for by these results can then be attributed to true differences, which result from changes in composition.

11.2. Thermogravimetry

The precursor nitrates that are used in the preparation of the various CGO compositions are hygroscopic. It was therefore necessary to determine the water of crystallisation in each material, to ensure that the correct stoichiometric ratio of cerium and gadolinium was added. Thermogravimetry was used to measure the water content as described in chapter 10. The graphs obtained for the cerium nitrate and gadolinium nitrate precursors are shown in Fig.11.1.

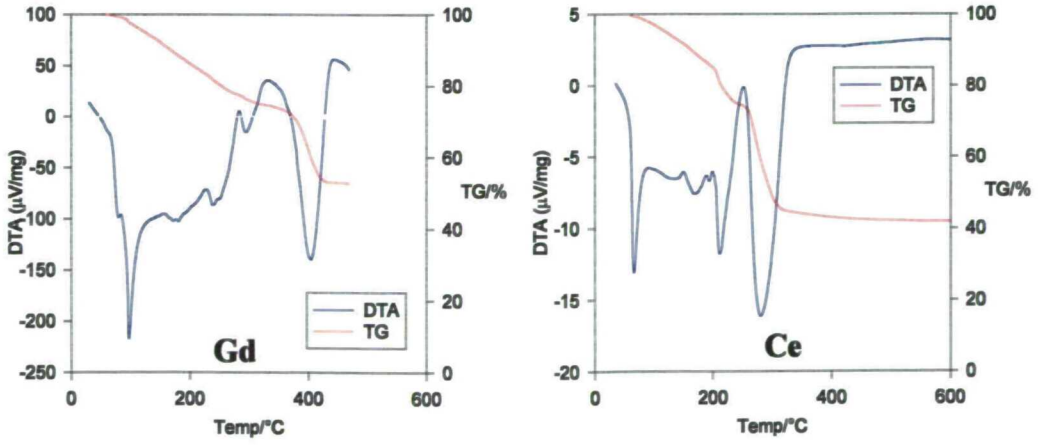


Fig.11.1. Typical thermogravimetric graphs for Gd and Ce nitrate.

The largest weight loss in Fig.11.1 occurred at the highest temperature and is due to the evaporation of the nitrate. Endothermic peaks at lower temperatures result from the loss of water. Using the thermogravimetric data, it is possible to determine the total weight percent of water lost and compare that to the expected weight percent of water. Table 11.1 shows this comparison and demonstrates that both values are in good agreement within the experimental error. The calculated values were thus considered to be sufficient and used when adding the different precursors. The calcium nitrate water content had previously been determined using an evaporation technique (the nitrate concentration was assumed to be close to that expressed by the manufacturers). The water content was found to be 2.61moles.

Precursor	Expected Weight %	Calculated Weight %
Cerium Nitrate	24.9	25.3±1.0
Gadolinium Nitrate	23.9	25.2±1.5

Table 11.1. Theoretical and measured weights of water in the nitrate precursors.

11.3. Composition Analysis

11.3.1. Inductively Coupled Plasma (ICP)

The concentration of 58 elements has been determined in selected ceria powder compositions using the inductively coupled plasma technique discussed in chapter 10. A gadolinium doped and calcium codoped ceria powder were chosen to establish the concentrations of the impurities present. The impurities in samples with the same dopants are expected to be similar, due to identical processing routes. Table 11.2 lists the levels of the main impurities discussed in chapter 6. The remainder of the 58 elements studied were below the detection limit of this technique (<0.5ppm).

This experiment illustrates, that within experimental error, the Gd concentration is the same as the nominal composition for both of the samples studied. The Ca concentration in the codoped material is less than that expected but is still significantly higher compared to the undoped sample. In both samples, the level of Si was below

the detection limit of 30ppm, which implies very low levels of this element. The 3mol% Gd sample shows significantly higher levels of Na, Mg, Ba and Al, while the codoped material has a high level of Ti. The expected high levels of other rare earths are also present, most notably that of La in the calcium codoped sample.

Element	$Ce_{0.97}Gd_{0.03}O_X$/ppm	$Ce_{0.8}Gd_{0.19}Ca_{0.01}O_X$/ppm
Gd	(2.92at%)	(17.83at%)
Ca	359	(0.26at%)
Si	<30	<30
Na	253	3.6
Mg	48	<1
Al	147	<15
Ti	14	210
Ba	34	0.7
La	200	1476
Pr	37	35
Nd	42	10
Sm	3.8	0.6
Eu	2.4	1.4
Ho	1.7	9.4
Er	3.1	16

Table 11.2. Concentration of elements in doped ceria samples measured by ICP.

11.3.2. Atomic Absorption Spectroscopy (AAS)

AAS was only used to determine the calcium and silicon levels, using the equipment described in chapter 10. The results for both CGO and Ca codoped CGO are shown in Table 11.3. The free silicon level in all samples was below the detection limit of the instrument (25ppm), which is in agreement with the results from ICP and confirms a very low level of Si in all samples.

The Ca level in the codoped material is again lower than expected but in agreement with the ICP results. The Ca level in the 3mol% Gd is slightly lower than the value recorded using ICP, although it is of similar magnitude. The Ca concentrations in both of the codoped materials is shown to be similar and permits a direct comparison of

electrical measurements between these materials. The Ca concentrations in the 10 and 20mol% Gd samples is higher because a less pure cerium nitrate precursor was used (>99%). There appears to be a trend towards lower Ca concentration as the Gd concentration increases. The lower purity 10 and 20mol% Gd samples also seem to follow this trend. It is not known why there should be this trend but the effects it may have on the electrical conductivity are considered in chapter 12.

Material	Concentration of Ca/ppm
CeO_2 (99.99%)	<25
$Ce_{0.97}Gd_{0.03}O_X$	230
$Ce_{0.94}Gd_{0.06}O_X$	240
$Ce_{0.9}Gd_{0.1}O_X$	700
$Ce_{0.87}Gd_{0.13}O_X$	220
$Ce_{0.84}Gd_{0.16}O_X$	170
$Ce_{0.8}Gd_{0.2}O_X$	400
$Ce_{0.77}Gd_{0.23}O_X$	30
$Ce_{0.74}Gd_{0.26}O_X$	60
$Ce_{0.7}Gd_{0.3}O_X$	<25
$Ce_{0.9}Gd_{0.09}Ca_{0.01}O_X$	2600
$Ce_{0.8}Gd_{0.19}Ca_{0.01}O_X$	2500

Table 11.3. Concentration of Ca in doped ceria samples calculated from AAS.

11.4. Particle Size Analysis, Surface Area and Morphology

Chapter 6 demonstrated that the size, morphology and degree of agglomeration of the calcined powders are all important characteristics when high density ceramics are required. The particle size measurement technique has been discussed in chapter 10. The particle sizes of all the CGO powders studied are recorded in Table 11.4. It can be seen that there is a large variation in particle size, with the codoped materials exhibiting the smallest particles.

The surface area for a 23mol% Gd powder has been measured using the technique described in chapter 10. The specific surface area was calculated as $7.5 m^2 g^{-1}$

$\pm 0.05 m^2 g^{-1}$. This value is low compared to the values obtained from industrially produced powders (see chapter 13) and suggests a higher degree of agglomeration.

Composition	Mean Particle Size (D_{50})/μm (Error ±0.5μm)
CeO_2 (99.99%)	5.99
$Ce_{0.97}Gd_{0.03}O_X$	3.75
$Ce_{0.94}Gd_{0.06}O_X$	6.41
$Ce_{0.9}Gd_{0.1}O_X$	3.13
$Ce_{0.87}Gd_{0.13}O_X$	5.22
$Ce_{0.84}Gd_{0.16}O_X$	12.22
$Ce_{0.8}Gd_{0.2}O_X$	4.27
$Ce_{0.77}Gd_{0.23}O_X$	4.72
$Ce_{0.74}Gd_{0.26}O_X$	5.56
$Ce_{0.7}Gd_{0.3}O_X$	7.35
$Ce_{0.9}Gd_{0.09}Ca_{0.01}O_X$	0.7
$Ce_{0.8}Gd_{0.19}Ca_{0.01}O_X$	3.98

Table 11.4. Mean particle sizes for CGO powders.

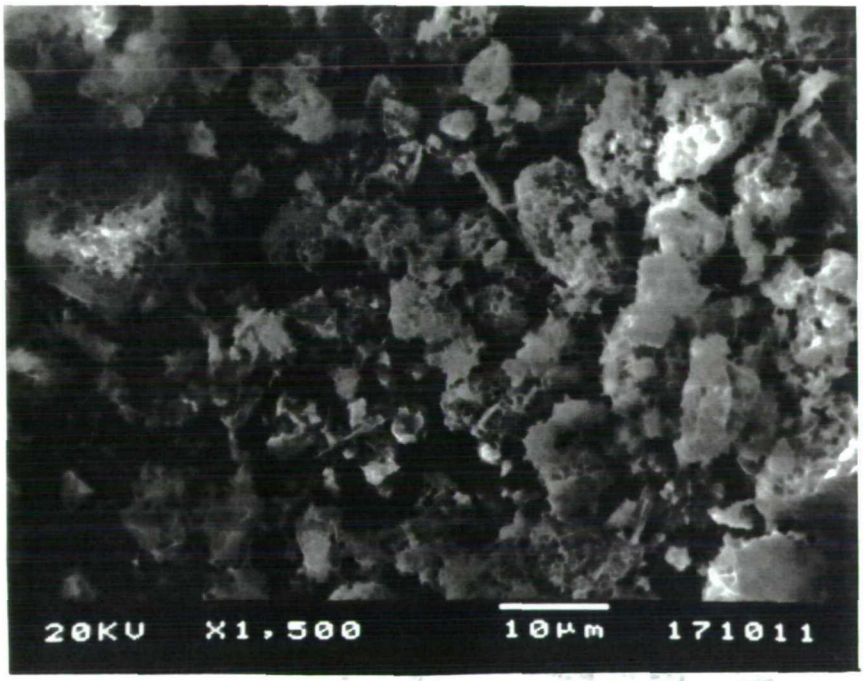


Fig.11.2. Typical SEM morphology of a calcined CGO powder ($Ce_{0.94}Gd_{0.06}O_{2-X}$).

Fig.11.2 shows a typical SEM micrograph of a powdered CGO sample, which clearly displays a large degree of agglomeration between particles. All CGO samples showed similar degrees of agglomeration and consequently the effect of this on sintering should be similar for all samples. There was also no appreciable difference in the degree of agglomeration for the codoped powders. The smaller particle sizes recorded for the codoped powders are probably the result of softer agglomerates, which are disrupted more in the ultrasonic bath before measurement.

11.5. Dilatometry

11.5.1. Sintering Characteristics

Dilatometry was used to study the sinterability of a number of CGO powders. The percent of shrinkage is measured as a function of temperature, using the equipment described in chapter 10. In general, an s-shaped curve is obtained, with a plateau region at high temperatures. The beginning of this plateau region provides an indication of the sintering temperature needed to reach a density >95%, i.e. closed porosity. The percent shrinkage allows a qualitative comparison between the green densities achievable for each powder, with the greatest amounts of shrinkage assigned to the lowest green density samples. It should be noted, that a low green density does not necessarily imply that a high sintering temperature is needed to obtain a high final density because it is the rate of material transfer at any particular temperature which determines the final density. Fig.11.3 shows shrinkage curves for a number of CGO compositions, including the Ca codoped materials.

Table 11.5 lists the densities of all the sintered samples, which have been calculated as described in chapter 10. The $Ce_{0.9}Gd_{0.09}Ca_{0.01}O_{2-X}$ sample achieved the highest density of all the samples prepared. This can be explained by the shrinkage curve, which reaches the plateau region at the lowest temperature. The plateau starts at 1400°C, after which there is no further increase in shrinkage, which suggests that both open and closed porosity are virtually eliminated at this temperature. The sintering curve for $Ce_{0.8}Gd_{0.19}Ca_{0.01}O_X$ is markedly different, showing that the sintering plateau is only

just being reached at 1550°C. It is expected that this sample has a larger percentage of closed porosity, which would explain the lower measured density.

The densities of the 6% and 26%Gd doped samples are both ≥95%. The shrinkage curves for these samples show that the plateau region appears to start around 1550°C. This suggests that sintering temperatures ≥1550°C must be used for these samples to achieve high densities. The 16%Gd sample produced the lowest density of all the samples (90%). The shrinkage curve for this sample displays an unusual expansion behaviour above approximately 1450°C. It is thought that this behaviour may be due to errors in the experimental set-up and a repeat measurement is required to clarify the shrinkage behaviour of this sample.

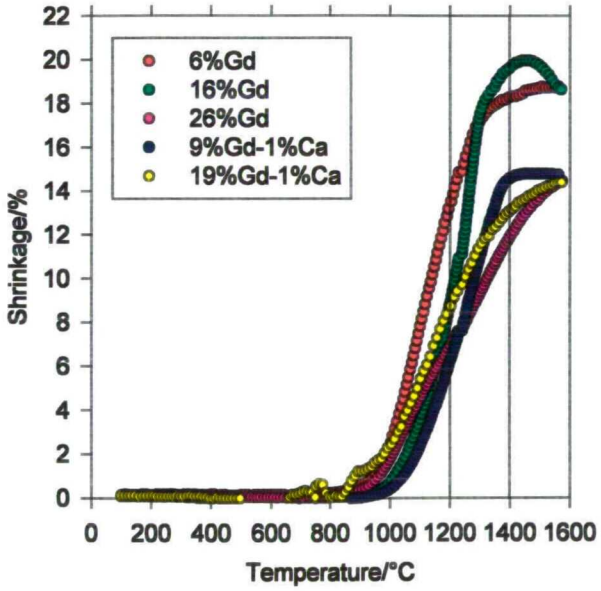


Fig.11.3. Dilatometric shrinkage curves for CGO and Ca doped CGO.

Table 11.5 shows that the density of all the samples studied was >90%, with the majority of samples >95%. All samples were considered to be sufficiently dense to allow conductivity measurements to be performed, with a minimal error from porosity. The grain sizes of all the sintered pellets are also recorded in Table 11.5. Most samples have a grain size between 3-5μm, which corroborates the fact that these samples were at a similar stage of densification. The grain size of the $Ce_{0.9}Gd_{0.09}Ca_{0.01}O_{2-X}$ sample is slightly larger, which reflects the fact that full

densification was achieved at a lower temperature for this sample and suggests faster material transport in this sample.

Composition	Bulk Density/gcm^{-3} (±0.30gcm^{-3})	Density/% of theoretical (±3%)	Grain Size/μm (±0.5μm)
CeO_2 (99.99%)	6.83	96	7.92
$Ce_{0.97}Gd_{0.03}O_X$	6.62	92	5.00
$Ce_{0.94}Gd_{0.06}O_X$	6.99	97	4.08
$Ce_{0.9}Gd_{0.1}O_X$	6.89	95	3.24
$Ce_{0.87}Gd_{0.13}O_X$	7.18	99	4.56
$Ce_{0.84}Gd_{0.16}O_X$	6.51	90	3.53
$Ce_{0.8}Gd_{0.2}O_X$	7.11	98	4.23
$Ce_{0.77}Gd_{0.23}O_X$	6.89	95	4.23
$Ce_{0.74}Gd_{0.26}O_X$	6.90	95	3.89
$Ce_{0.7}Gd_{0.3}O_X$	7.17	98	4.71
$Ce_{0.9}Gd_{0.09}Ca_{0.01}O_X$	7.22	100	6.75
$Ce_{0.8}Gd_{0.19}Ca_{0.01}O_X$	6.82	94	4.04

Table 11.5. Density and average grain size of CGO and Ca-doped CGO pellets.

Fig.11.4 shows typical micrographs for two CGO samples. The sizes of the grains are fairly uniform, with very little porosity visible within grains. The grain boundaries show a distribution of micropores. These results are consistent with well sintered pellets and densities >95%.

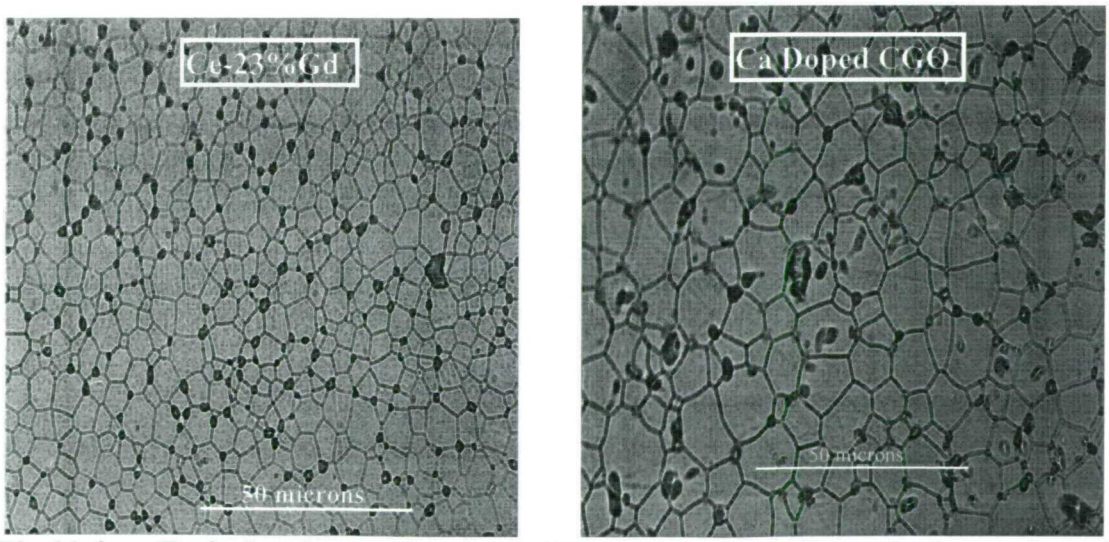


Fig.11.4. Typical micrographs for polished and thermally etched samples of $Ce_{0.77}Gd_{0.23}O_X$ and $Ce_{0.9}Gd_{0.09}Ca_{0.01}O_X$. Dark spots indicate closed porosity.

Fig.11.4 also shows the $Ce_{0.9}Gd_{0.09}Ca_{0.01}O_{2-X}$ sample, which has visibly larger grains and virtually no porosity, as predicted from the density and dilatometry measurements. When analysing the grain boundary conductivity data for this sample, a grain boundary correction must be made, according to section 6.10, before comparison with other compositions.

11.5.2. Thermal Expansion Coefficients

Fig.11.5 shows a graph of the thermal expansion coefficients plotted against the dopant concentration. The two points at 6mol% are those for the doubly doped ceria material supplied by Rhône-Poulenc ($Ce_{0.94}Sm_{0.03}Y_{0.03}O_X$ and $Ce_{0.94}La_{0.03}Yb_{0.03}O_X$). The values are calculated between the standard temperature range 50-800°C, using the equipment described in chapter 10. The graph shows that all compositions have a thermal expansion coefficient between 12.2–12.6×$10^{-6}K^{-1}$, which is in close agreement to the values already reported in the literature (12.5×$10^{-6}K^{-1}$ [1]). These results indicate that the thermal expansion coefficient of ceria is not strongly dependent on the doping concentration or dopant type.

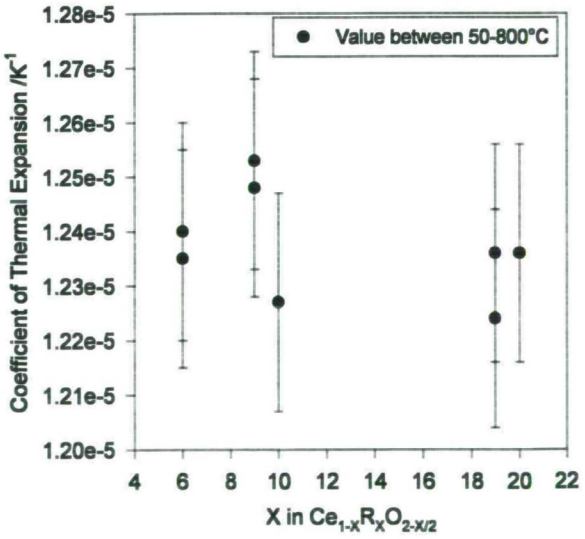


Fig.11.5. Thermal expansion coefficients in a number of doped ceria samples.

11.6. XRD

Fig.11.6 shows an XRD trace obtained for a typical CGO sample. A single cubic fluorite ceria phase was observed for all compositions at room temperature, with a shift in the peak angles, from that of pure ceria, to lower 2θ values. The shift in peak values is caused by the dissolution of the dopant into the lattice and increases as the dopant concentration increases. The d-values are found to increase as the dopant concentration increases, which implies that the lattice parameter (a_0) also increases.

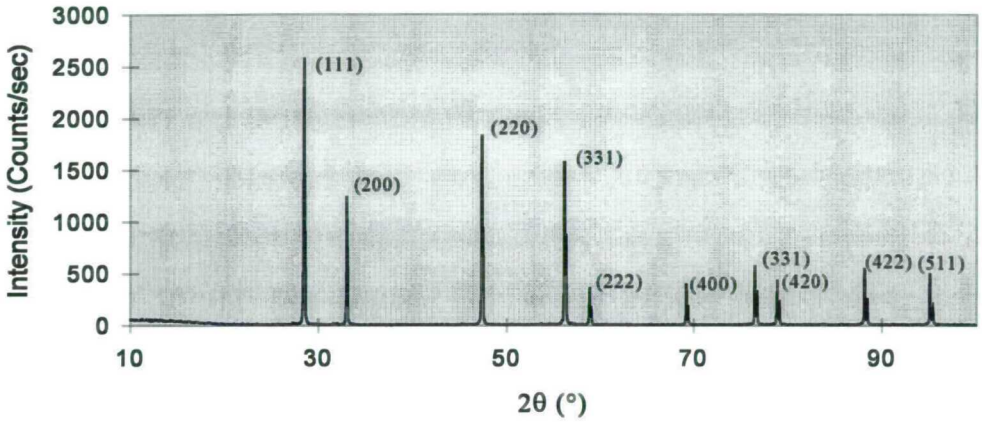


Fig.11.6. Typical XRD trace for doped ceria.

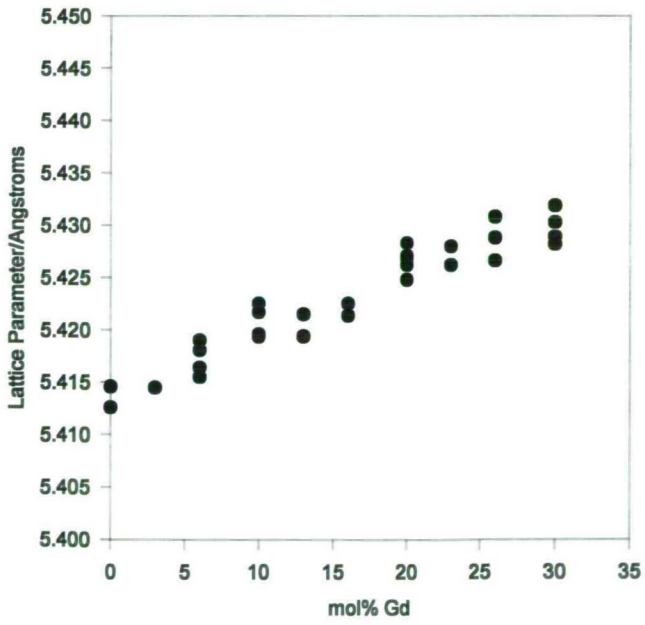


Fig.11.7. Variation of lattice parameter with dopant concentration.

Fig.11.7 shows how the lattice parameter varies with concentration. There is a linear increase in a_0 with concentration up to 20mol%, which is in agreement with the results of Bevan [2] but the graph appears to approach a broad plateau at 30mol%, which is lower than that observed by Bevan. The deviation from linearity is due to the formation of the Gd_2O_3 rare earth C-type phase. Bevan, having annealed samples at high temperatures for several days, claims to detect this second phase at concentrations as low as 20mol% Gd. In all the samples analysed here, no second phase was observed, implying that these solutions had not reached an equilibrium condition. The presence of the plateau in the lattice parameter is suggested to be the result of two competing factors. Firstly, a geometrical strain term related to the differences in ionic radii between cerium and gadolinium, which increases the lattice parameter and secondly, an attractive defect interaction term, which strongly contracts the unit cell.

11.6.1. High Temperature XRD

High temperature XRD showed no second phase peaks for $Ce_{0.97}Gd_{0.03}O_{1.985}$ or $Ce_{0.7}Gd_{0.3}O_{1.85}$ at any temperature up to 1000°C, during fast scanning. The peak angles were again shifted to lower 2θ values, compared to pure ceria, with a linear increase in the lattice parameters with temperature. However, a number of shoulder peaks were revealed at higher angles, during a slow scan for the $Ce_{0.7}Gd_{0.3}O_{1.85}$ sample, measured at 1000°C (see Fig.11.8). This is consistent with the formation of a C-type second phase. Unfortunately, it is not possible to determine if this second phase is the same as a C-type Gd_2O_3 phase because the structure of this phase is very similar to the parent fluorite ceria phase, resulting in very similar diffraction patterns. On quenching this sample from 1000°C to room temperature, the shoulder peaks disappeared, indicating that the second phase only forms at higher temperatures. No similar shoulder peaks were obtained on a slow scan at 500°C.

It can be concluded from these results that the difficulty in detecting a C-type second phase is due to the slow mobility of the cations in the lattice. In order to achieve an equilibrium condition it is necessary to anneal at high temperatures for a long time. The sintering times used in this study are relatively short and therefore allow only short range ordering of the cations. When this is combined with the virtually identical

diffraction spectra of the C-type phase, the presence of this second phase would be below the detection limits of XRD at room temperature (which is about 5%).

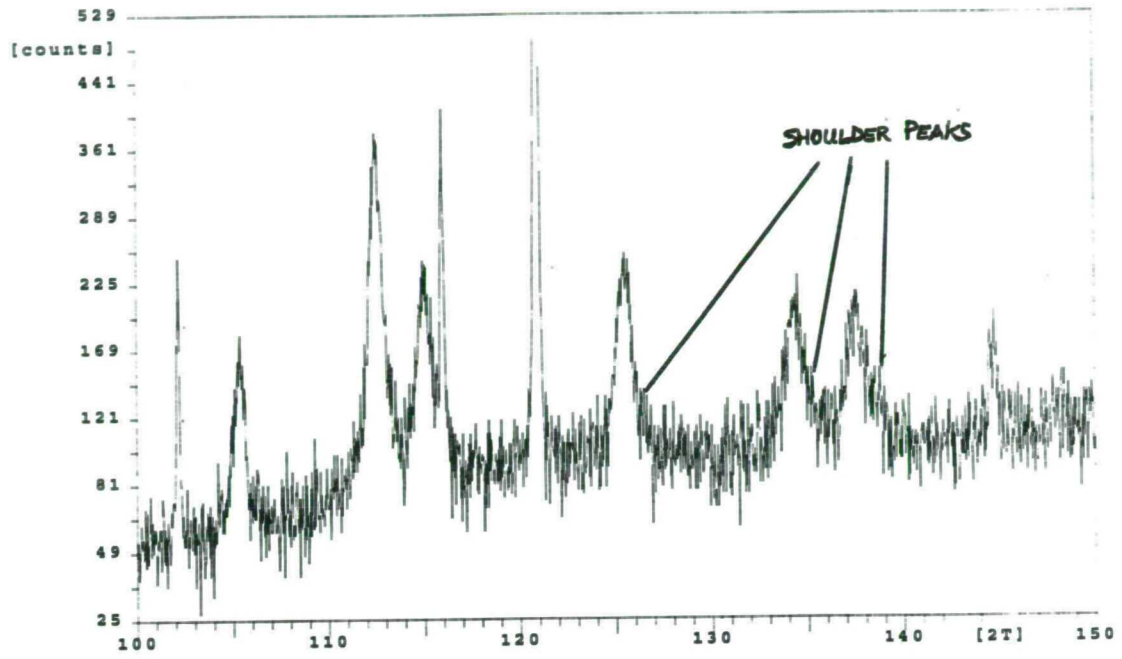


Fig.11.8. XRD spectra for $Ce_{0.7}Gd_{0.3}O_{1.85}$ at 1000°C, displaying shoulder peaks from a second phase.

References

1. M.Mogensen, T.Lindegaard U.R.Hansen and G.Mogensen. J.Electrochem.Soc. **141**, 8, (1994), 2122.
2. D.J.M.Bevan and E.Sommerville. Handbook on the Physics and Chemistry of Rare Earths. Volume 3. Eds. K.A.Gschneider and L.Eyring. Elsevier Science. 1979, 401.

Chapter 12. Effects of Gd Doping in Ceria and the Production of CGO Thin Films

12.1. Introduction

The results and discussion in the following chapters contain many impedance plots, comparing the electrical properties of a number of doped ceria samples. The beginning of this chapter aims at providing a more in-depth review of the impedance spectroscopy technique, to aid in a better understanding of the results. The data presented in this chapter are solely devoted to that of gadolinia doped ceria, with a detailed study of the grain boundaries. For a more detailed description of impedance spectroscopy, the reader is referred to a number of texts [1, 2, 3]. The end of this chapter concentrates on the electrical properties of CGO thin films and their microstructure.

12.2. AC Impedance Spectroscopy

The preparation of the sample and analysis equipment were described in chapter 10. This section now aims to provide a description of the response of an electrolyte to an alternating field.

When a small sinusoidal voltage, V(t) is applied across a sample, a resulting sinusoidal current, I(t) will flow, which leads the voltage by some phase angle, ϕ. The phase difference results from either the dielectric response time of the material or to polarisation effects at the grain boundaries. The impedance of the sample, Z can then be calculated according to equation 12.1.

$$Z = \frac{V(t)}{I(t)} \qquad (12.1)$$

Unlike resistance, impedance is frequency dependent and is expressed in complex number form as:

$$Z = |Z|e^{-j\phi} \tag{12.2}$$

or in Cartesian co-ordinates,

$$Z = |Z|\cos\phi - j|Z|\sin\phi \tag{12.3}$$

where $|Z| = V_0/I_0$, V_0 and I_0 being the amplitude of the voltage and current. The real (Z') and imaginary (Z") impedances can then be expressed according to equations 12.4 and 12.5, respectively.

$$Z' = |Z|\cos\phi \tag{12.4}$$

$$Z'' = |Z|\sin\phi \tag{12.5}$$

Equation 12.3 can now be written more simply as equation 12.6,

$$Z = Z' - jZ'' \tag{12.6}$$

Most electrolytes are polycrystalline, consisting of grains and grain boundaries. Generally, the relaxation of charged species in the bulk and grain boundary will occur at different rates and thus it is possible to separate their impedances as a function of frequency. The impedance of each process will consist of a resistive and capacitive component, which allows the impedance of the bulk relaxation to be expressed as,

$$\frac{1}{Z} = \frac{1}{R} + j\omega C \tag{12.7}$$

where R is the resistance and C the capacitance. Equation 12.7 can be shown to be the equation of a circle (see Appendix B), with a radius of R/2 and a centre at (R/2, 0). If ω, R, and C are all greater than zero, a semi-circle will be obtained on the *x* axis,

when plotted as a function of frequency. Both the bulk and grain boundary will produce semi-circular responses. The grain boundary response will be displaced from the bulk response depending on the relaxation rate of the charged species. It is normal to compare the relaxation rates of different processes in terms of rate constants or relaxation times, τ, which are defined as, $\tau = RC$.

The resistance of the grain boundary region can be a result of a second phase or a constriction resistance (explained in section 6.8.1), which results in the development of a space-charge region as the oxygen ions concentrate at the boundary. The capacitance of the grain boundary region is therefore associated with the polarisation at the interface.

The relaxation time associated with the grain boundary is normally higher than that related to the bulk. If the grain boundary relaxation time is significantly larger than that of the bulk, the two processes will be well separated on an impedance plot. In ceria there are two or three orders of magnitude difference in relaxation times and so normally, two, well resolved semi-circles are obtained.

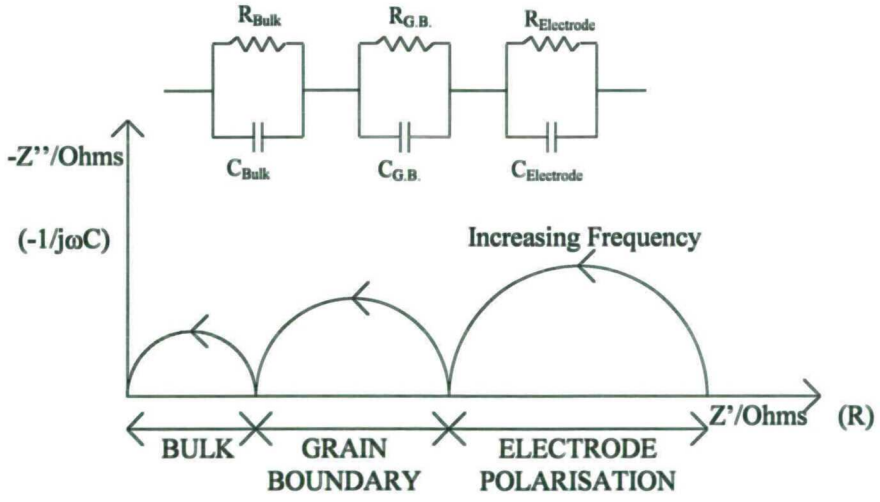


Fig.12.1. Ideal impedance spectra for a polycrystalline electrolyte, showing the equivalent R-C circuit for each process.

As mentioned, equation 12.7 produces a semi-circle when plotted on an impedance plot as a function of frequency. This equation can be mathematically derived (see

appendix B) from the impedance of a resistor and capacitor connected in parallel. It is therefore common to model electrolyte materials using electrically equivalent lumped R-C circuits. Fig.12.1 shows the equivalent circuit for an ideal electrolyte and resulting impedance spectrum. The electrode process has been simplified as another parallel RC circuit but is usually more complicated. A discussion of the electrode processes is outside the scope of this thesis. An electrolyte material, however, rarely displays ideal resistor and capacitor behaviour and the equivalent circuits serve more as a guide than an absolute.

12.2.1. Empirical Observations of Impedance Data

The experimentally measured impedances of a sample normally show some degree of depression below the real axis, which corresponds to a narrow distribution of R-C elements, or relaxation times, for that particular process [4]. This is normally the result of inhomogeneities within a material. Thus, representing each process by a single relaxation time is not strictly correct but represents an average value. However, this is normally sufficient to allow approximate calculations to be made. The depression angle, α, has been found to be independent of temperature for ceria [5] but increases as the homogeneity of the material decreases. Thus, mixed oxide prepared materials generally show larger depression angles because of a poorer distribution of the dopant. The depression angle is therefore related to the width of the relaxation time distribution and provides an indication of the degree of heterogeneity in a sample.

The resistance of the bulk material is normally taken as the intercept on the x-axis between the two highest frequency semi-circles. In practice, neither semi-circle intercepts the x-axis due to some overlap in the semi-circles and fitting a semi-circle to the data can lead to errors in the resistance. Faber [6] states that a better determination of the bulk (or grain boundary) resistance can be obtained by taking the abscissa of the minimum observed between the two semi-circles.

At high frequencies it is often observed that the imaginary impedance in doped ceria becomes positive. It is thought that the positive Z" is a result of the inductance created in the parallel wires of the sample holder, and becomes significant above a frequency

of 1MHz. The inductance, estimated to be 0.9mH, prevents good resolution of a bulk semi-circle [5] and the high frequency intercept of the grain boundary semi-circle must be used instead.

12.3. Electrical Properties

The electrical conductivity of the following compositions have been studied with a.c impedance spectroscopy in air, using the equipment described in chapter 10: pure ceria, 3, 6, 10, 13, 16, 20, 23, 26 and 30%Gd doped ceria. The bulk and grain boundary contributions have been separated using the technique discussed in section 12.2. An estimate of the accuracy of the apparatus was performed by first measuring the impedance of a high tolerance resistor and capacitor connected in parallel and secondly, by measuring the impedance of a sample repeatedly, at the same temperature, after a number of heating cycles. The results from the first measurement returned values that were the same as the quoted values for the resistor and capacitor (within the tolerance stated). The measurements on the real sample showed that the bulk conductivity varied by only 1%, whereas the grain boundary results showed a variation of 30%, which is due to the higher uncertainty in fitting to the less resolved grain boundary semi-circle. The resistance of the platinum wires was also tested using an empty cell and was found to be <3Ω below 600°C.

The results presented in this section show the conductivities for the bulk, grain boundary and total data. It should be emphasised that this work provides the first comprehensive set of conductivity measurements for CGO as a function of Gd concentration and a number of important points arise from these data.

12.3.1. A.C. Impedance Spectroscopy - Bulk Data

Fig.12.2 shows the impedance spectra for several CGO samples. Both the bulk and grain boundary responses show well resolved semi-circles. The bulk semi-circle response can be seen to increase with Gd concentration, whereas the grain boundary response decreases.

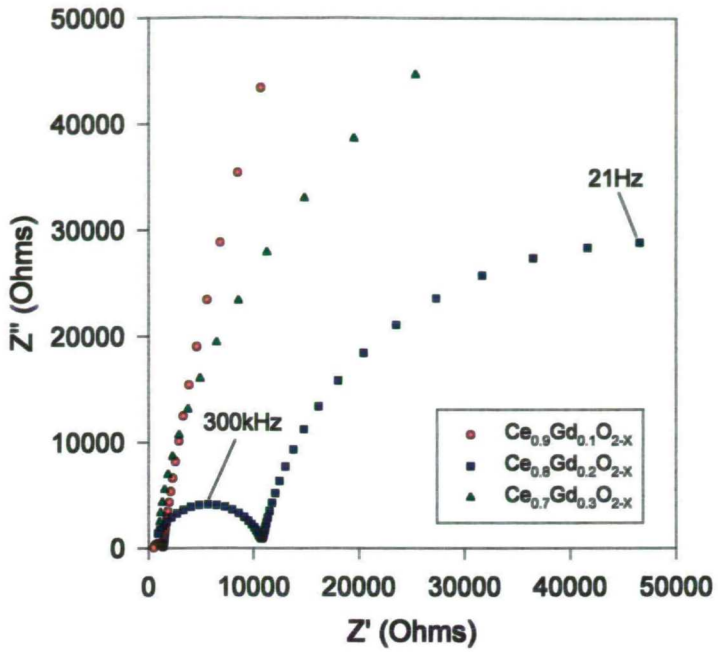


Fig.12.2. Impedance spectra for several CGO samples, measured in air at 250°C.

The results for the bulk, grain boundary and total resistances of all compositions have been converted into conductivity values and plotted on Arrhenius graphs, according to equation 5.35. Fig.12.3 shows the Arrhenius graph for the bulk conductivity. It is clear that the pure ceria sample displays the lowest conductivity over the entire temperature range, which reflects the low concentration of intrinsic oxygen vacancies present in ceria. In all cases, doping with Gd increases the conductivity by the introduction of charge compensating oxygen vacancies.

The bulk conductivity appears to reach a maximum value between 6-10mol% Gd, which is in agreement with most researchers for trivalent dopants. Careful analysis of each composition shows a curvature in each experimental curve at a temperature of approximately 350°C. The curvature appears to be largest for low dopant concentrations and similar results have been found for Y-doped ceria [6, 7]. This curvature can be explained by the change from associated behaviour, to unassociated behaviour at higher temperatures, as discussed in section 6.5.1. Chapter 6 showed that Gd-doped ceria has the lowest association enthalpy of all the trivalent dopants, which indicates that the defect associates are readily dissociated. It is likely, therefore, that in these experiments, the materials do not display completely associated behaviour at low

temperatures. However, Fig.12.3 shows that logσT increases approximately linearly with 1/T, which strongly suggests that fully associated behaviour is being measured.

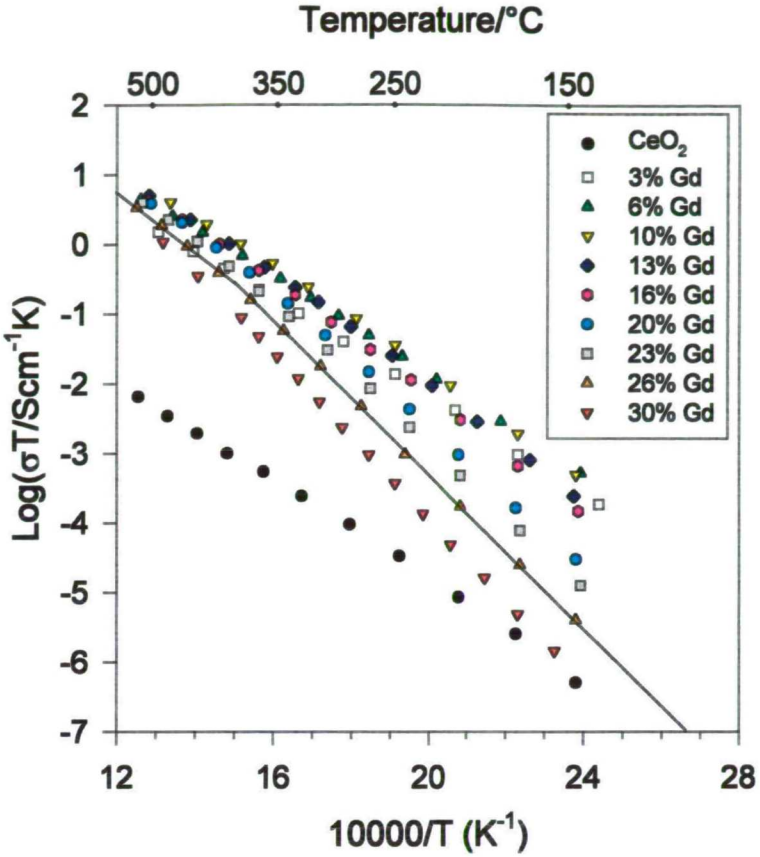


Fig.12.3. Arrhenius graph of the bulk conductivity for a series of CGO samples with increasing Gd concentrations. Ce-26%Gd displays lines obtained by regression analysis, used to calculate the low and high temperature gradients.

Equations to describe the low and high temperature behaviour have been derived by several researchers for dilute concentration solutions. Wang [7] and Hohnke [8] demonstrate the linear dependence of ionic conductivity on dopant concentration at high temperatures, according to equation 12.8.

$$\sigma T \approx 2 \times 10^{6} x \exp\left(\frac{-H_m}{kT}\right) \qquad (12.8)$$

where x is the dopant mole fraction and H_m is the migration enthalpy. However, in the low temperature regime, both authors show that the conductivity and activation enthalpy should be independent of dopant concentration (equation 12.9).

$$\sigma T \approx 5 \times 10^5 \exp\left(-\frac{H_m + H_a}{kT}\right) \qquad (12.9)$$

where H_a is the association enthalpy. Hohnke claims that equation 12.9 closely matches the experimental data for dopant concentrations below 7mol% Gd but at higher dopant concentrations it is necessary to include terms for short and long range defect interactions. The experimental data of Hohnke showed that the activation enthalpy remained constant for low dopant concentrations. However, the conductivity increased with dopant concentration, which differs from the dopant independent behaviour expected from equation 12.9. With this increase in conductivity it is difficult to understand how agreement with the theoretical model is obtained. Wang has shown that the experimental data do not agree with this low temperature model. Even dilute $Ce(Y)O_{2-X}$ solutions (<1mol% Y), displayed a large increase in conductivity as the dopant concentration increased and was attributed to the decrease measured in the activation enthalpy. Similar results have also been found by Faber [6] for a number of trivalent dopants in ceria. The results presented in Fig.12.3 agree with these reported experimental results, showing the conductivity to increase with dopant concentration until a maximum is reached.

Fig.12.3 also shows a remarkable convergence point in the bulk conductivity at a temperature of approximately 550°C, for all doped ceria concentrations. At this focus point the conductivity is independent of the dopant concentration. A similar convergence in bulk conductivity has also been observed by Hohnke [8] for doped zirconia, hafnia and ceria systems. For CGO, the convergence temperature was reported to be much higher (~1300°C), while that for $Zr(In)O_{2-X}$ was around 580°C. It is possible that the convergence observed by Hohnke for CGO is due to an increase in the electronic conductivity. At these high temperatures, the reduction of ceria will be significant, thus introducing electronic conductivity into the material, which would then dominate over the ionic conductivity and mask any differences. The discrepancy between the focus temperature reported by Hohnke and these results, suggests that Hohnke may have been using inhomogeneous samples. Clustering of large numbers of

defects into discrete areas, would result in an increase in the transition temperature for unassociated behaviour.

The low and high temperature slopes on the bulk conductivity plot (Fig.12.3) can be fitted using regression analysis (shown on Fig.12.3 for Ce-26%Gd), to provide a value for the activation enthalpy for ionic conduction in both regions. The data points used in each region were in close agreement with the fitted straight line, giving an estimated accuracy in the calculated activation energies of ±0.05eV. Fig.12.4 displays the values of the activation enthalpies as a function of dopant concentration. The low temperature activation enthalpies also contain a term for the association enthalpy (discussed earlier) and therefore display higher enthalpy values.

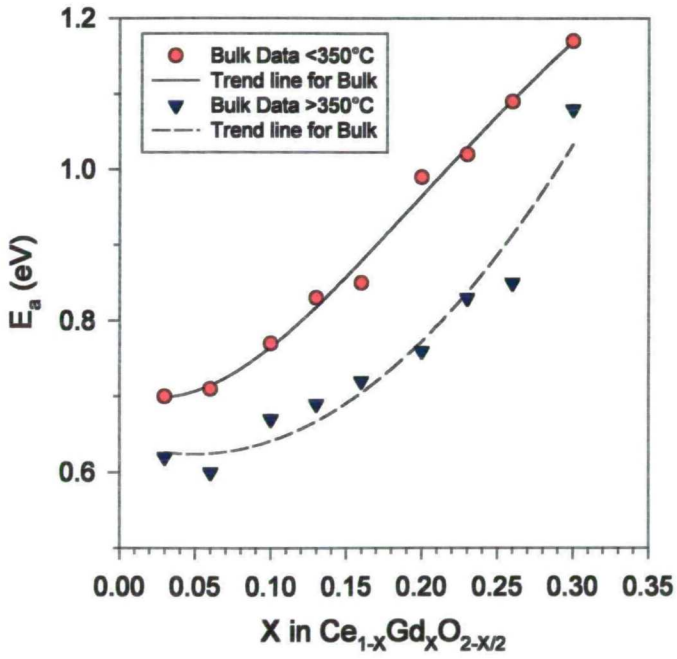


Fig.12.4. Comparison of the bulk activation energies for ionic conduction as a function of dopant concentration, in the high and low temperature ranges.

The values for the activation enthalpy below 350°C increase almost linearly with dopant concentration above 6mol% Gd. Below this concentration the activation energy levels off, which agrees with the experimental data of Hohnke [8]. The data of Wang [7] and Faber [6] show shallow minima in the dilute solution region for a number of trivalent dopants. There are too few data points in the dilute solution region (<6mol%) in the present work to determine if a shallow minimum occurs.

The values recorded above 350°C appear to remain constant until 6mol% Gd, before increasing fairly linearly with Gd concentration. It is expected that the higher temperature activation enthalpies are due to the migration of the oxygen ions only and should therefore remain constant, as discussed in chapter 5 and experimentally found by Hohnke. The results presented in Fig.12.4 indicate that in dilute solutions (<6mol% Gd), we are measuring the migration enthalpy for oxygen ions. Above this concentration complex defect interactions are still present, which increases the activation enthalpy and thus the simple associate defect model becomes untenable at high dopant concentrations.

The change in gradient observed in the bulk conductivity plot may therefore represent the dissociation temperature of simple associates (dimers), while more complicated defect clusters are still present. In the dilute solutions there are unlikely to be any complex associates and thus the high temperature gradient is a measure of the migration enthalpy. At higher dopant concentrations there is a greater probability of complex associates forming. The size of the complex associate, i.e. number of defects present, will increase linearly with dopant concentration, therefore, a linear rise in activation enthalpy may be expected. This is in fact found to be the case in the present data. If we assume that the high temperature activation enthalpy for low dopant concentrations is equal to the migration enthalpy, then by subtracting this value from the low temperature activation enthalpies, it is possible to calculate the association enthalpies as a function of dopant concentration. Table 12.1 shows the calculated association enthalpies for each composition.

The very high association enthalpies (i.e. 0.56eV for Ce-30%Gd) in the most concentrated solutions are unlikely, and indicate, that the migration enthalpy for ceria increases with dopant concentration. The increase in the migration enthalpy may be the result of a precipitated second phase (C-type Gd_2O_3), which has a higher migration enthalpy. Therefore, the low temperature activation energy may contain contributions from the intrinsic migration enthalpy, the association enthalpy and a second phase migration enthalpy. The last two enthalpies are thought to be dopant concentration dependent and will be most significant in the higher dopant concentration solutions.

Composition	Association Enthalpy/eV
3% Gd	0.09
6% Gd	0.10
10% Gd	0.16
13% Gd	0.22
16% Gd	0.24
20% Gd	0.38
23% Gd	0.41
26% Gd	0.48
30% Gd	0.56

Table 12.1. Calculated association enthalpies for CGO.

If attention is now given to the pre-exponential term, according to equations 12.8 and 12.9, at high temperatures the pre-exponential should increase linearly with dopant concentration, whereas at low temperatures it should remain constant. Hohnke [8] and Faber [6] suggest an exponential dependence on dopant concentration at low temperatures, while Wang reports an exponential increase up to 30mol% Y before the pre-exponential levels off. Fig.12.5 shows how the pre-exponential varies with dopant concentration for this study, both in the high and low temperature regions.

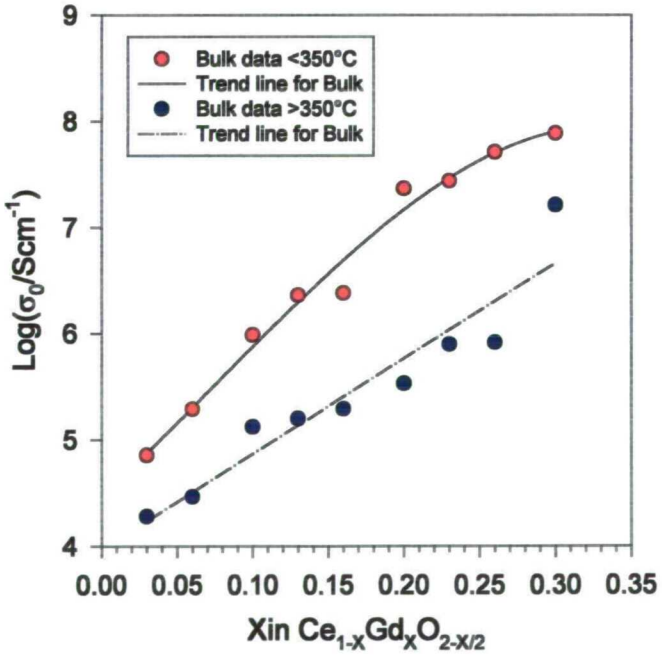


Fig.12.5. Comparison of the high and low temperature bulk pre-exponential terms as a function of dopant concentration for CGO.

Although there is some scattering in the data, the high temperature bulk result shows an exponential increase in the σ_0 term and not the linear increase predicted by theory. The low temperature bulk data shows two different exponential dependencies, with a change-over around 20mol% Gd. The exponential dependency for σ_0 is in good agreement with the previously mentioned researchers, however, the appearance of two slopes is not expected. A change in slope is most likely to be the result of a change in the jump frequency, ν_0, or the jump distance, λ, but it is not possible to determine the exact nature with this data.

Previous data by Hohnke [9, 10] who investigated $Zr(In)O_{2-X}$ has shown that there is a relationship between the activation energy and the pre-exponential. A graph of $Log\sigma_0$ verses E_a produced a fairly linear relationship. Fig.12.6 shows the same graph for the data obtained in this research, both in the high and low temperature regions. The high temperature data clearly shows a linear relationship. The low temperature data does not show the same linear dependence because of the change in slope in $log\sigma_0$ described previously.

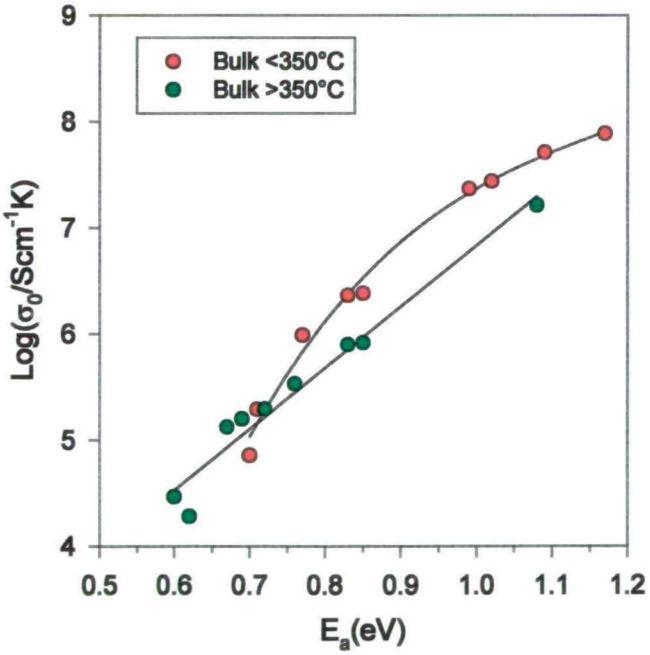


Fig.12.6. Relationship between the pre-exponential and activation enthalpy for the bulk component of CGO, both below and above 350°C.

This type of behaviour follows a rule known as the Meyer-Neldel rule and has been seen before in other classes of materials [11, 12]. For a series of samples that obey this rule it can be shown that there is a convergence in the conductivity at a common temperature, according to equation 12.10 [11].

$$\mathrm{Log}(\sigma_0) = \frac{E}{2.303RT_0} + C \qquad (12.10)$$

where E is the activation enthalpy, R the gas constant, T_0 the convergence temperature and C a constant. Using the data in Fig.12.6, the convergence temperature is calculated as 552°C. This temperature is in good agreement with convergence observed in Fig.12.3.

It is suggested by Nowick [11] that the convergence temperature marks the boundary between associated and unassociated behaviour on the conductivity plot. However, the convergence temperature for the results presented here appears to be above the temperature seen for the transition to unassociated behaviour. There are very few electrolytes studied that follow the Meyer-Neldel rule but it appears that CGO may be one. With the low numbers of electrolytes that follow this rule, is difficult to find trends that determine the conditions needed for a convergence temperature.

To conclude the discussion on the bulk data, an explanation for the conductivity maximum is needed. For dopant concentrations below the maximum observed in the logσT verses 1/T plot, increasing dopant concentration causes a reduction in the association enthalpies due to favourable interactions between defects (see section 6.10). As the dopant concentration increases further, larger defect clusters form which trap oxygen vacancies, increasing the association enthalpy and thus reducing the conductivity. From the results in this study it is also evident that the pre-exponential term is a function of dopant concentration and is related to the activation enthalpy via the Meyer-Neldel rule. The conductivity is most affected by the pre-exponential term in the low temperature associated region.

12.3.2. A.C. Impedance Spectroscopy - Grain Boundary Data

The conductivity measured at the grain boundaries is more difficult to explain compared to the bulk data because the exact composition and microstructure of the boundary are seldom known. Indeed, the composition of the grain boundary is unlikely to remain constant but vary continuously over the entire sample, which adds to the complexity of interpretation. Fortunately, the bulk and grain boundary electrical responses are easily resolved using impedance spectroscopy, so that the grain boundary resistance can be accurately measured. The Arrhenius graph for the apparent grain boundary conductivity is displayed in Fig.12.7. The most striking difference between this graph and that for the bulk conductivity (Fig.12.3), is the absence of any convergence temperature. Fig.12.8 shows that the activation enthalpies for conduction are very similar for all compositions, except for that of pure ceria, which displays a slightly higher value. A shallow minimum between 10-15mol% Gd is observed in the activation enthalpy.

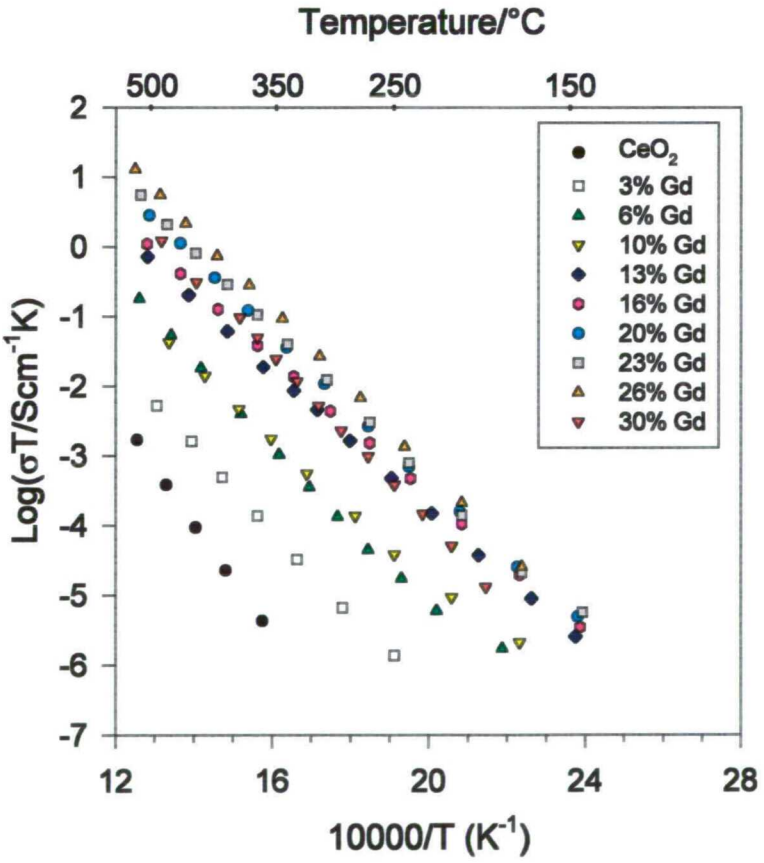


Fig.12.7. Arrhenius graph of the grain boundary conductivity for a series of CGO samples with increasing Gd concentrations.

The activation enthalpies for the grain boundary conductivity are considerably higher than either of the bulk activation enthalpies, for low dopant concentrations (<10mol% Gd). With increasing dopant concentration, the difference between the bulk and grain boundary activation enthalpies decreases, until 30mol% Gd, where the values are very similar.

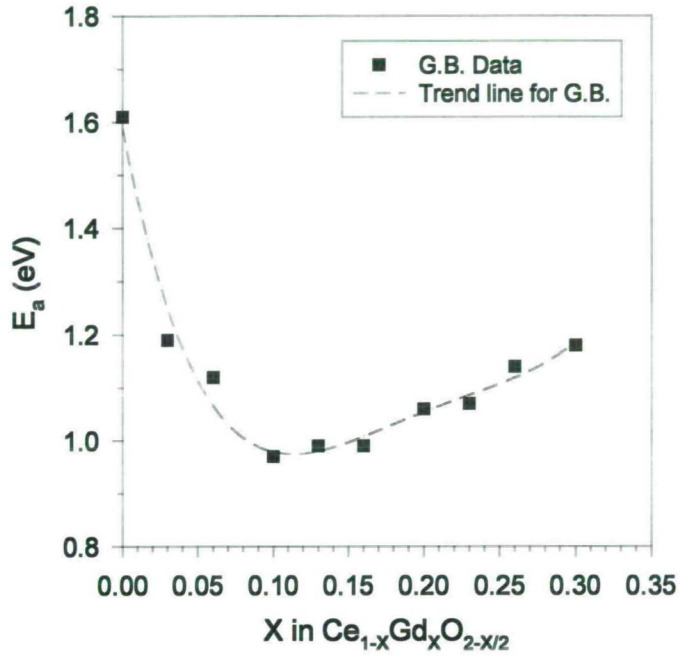


Fig.12.8. Grain boundary activation enthalpies for ionic conduction as a function of dopant concentration.

Considering the two models proposed in chapter 6 to interpret the grain boundary data, i.e. blocking and constriction models, the present data displays characteristics of both models. At low dopant concentrations, the grain boundary activation enthalpy is higher than that of the bulk value, which indicates the blocking model should be used. The blocking model considers a continuous phase surrounding all grains, having a different composition to that of the bulk. At 30mol% Gd, the bulk and grain boundary activation enthalpies are the same, indicating that the constriction model is more appropriate. The constriction model considers a secondary phase at the grain boundary which is discontinuous and permits the conduction of oxygen ions via discrete areas of direct grain-to-grain contact. The closely matching values obtained for the grain boundary activation enthalpy for all compositions, suggests the presence of similar second phase compositions at the boundaries.

Returning to the Arrhenius plot in Fig.12.7, it is observed that the grain boundary conductivity increases with dopant concentration but reaches a maximum at 26mol% Gd, after which the conductivity decreases. In this case it appears that the increase in conductivity is not related to the activation enthalpies (which are similar) but must be dependent on the pre-exponential. Fig.12.9 shows the variation of the grain boundary pre-exponential with dopant concentration and demonstrates an exponential increase for σ_0, similar to that found for the bulk.

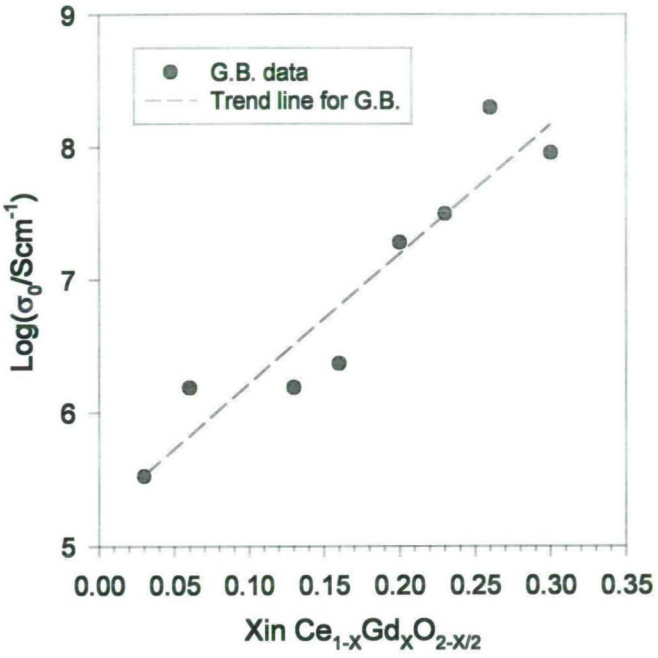


Fig.12.9. Grain boundary pre-exponential term as a function of dopant concentration for CGO.

For a true comparison of the grain boundary conductivities, it is necessary to re-calculate the conductivities considering the small variations in the grain size between samples shown in chapter 11 and the grain boundary thickness. The discussion in section 6.10 showed how both the variation in grain size and grain boundary thickness could be used to calculate the true grain boundary conductivity. Using equation 6.9 it was possible to determine the grain boundary thickness for each sample. This value varied between 2nm and 5nm, which shows good agreement to the recent results of Christie [13], except for the 6%Gd sample which had a value of 10nm. Equation 6.10 was then used to calculate the true grain boundary conductivity using the correct grain boundary thicknesses.

Fig.12.10 shows the Arrhenius plot comparing the apparent and the true grain boundary conductivities. Apart from some small deviations due to the slightly different grain sizes and grain boundary thicknesses, the shape of the true grain boundary conductivity follows that of the apparent conductivity. As expected the magnitude of the true grain boundary conductivity is much lower but a maximum is still present at 26mol% Gd. The results of Christie [13] showed a marked difference between the apparent and true grain boundary conductivities with increasing grain size. It was found that the true grain boundary conductivity remained approximately constant as the grain size increased. Fig.12.10 shows that increasing Gd concentrations *do* have an effect on the true grain boundary conductivity. The true grain boundary conductivities are much lower than the bulk conductivities, which suggests that a high resistance second phase is present at the grain boundaries.

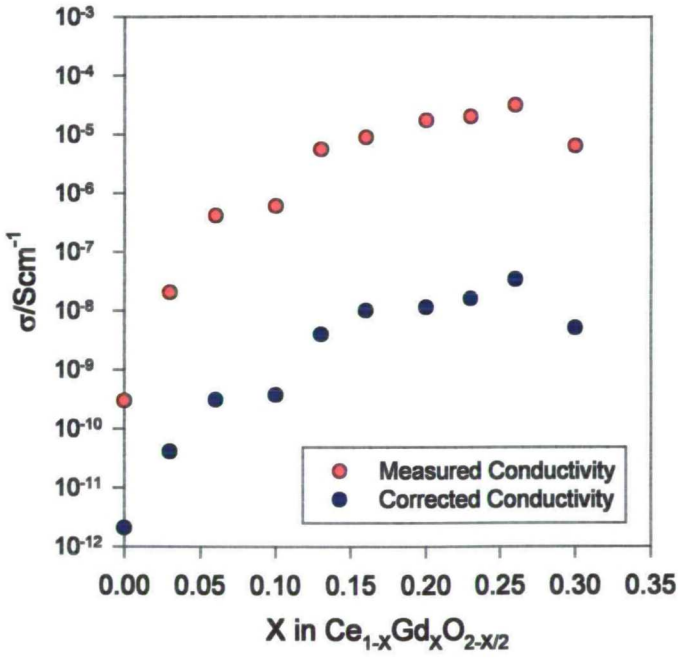


Fig.12.10. Comparison of the measured and corrected grain boundary conductivities for CGO at 300°C.

Some care must be exercised when using equation 6.9 to calculate the grain boundary thickness because this equation assumes that the bulk and grain boundary relative permittivities are equal:

$$\frac{\varepsilon_{g.b.}}{\varepsilon_{bulk}} = 1 \qquad (12.11)$$

Clearly, if a second phase is present at the grain boundaries $\varepsilon_{g.b.} \neq \varepsilon_{bulk}$. The value of the bulk relative permittivity for ceria is around 22. The value of any grain boundary phase which incorporates say SiO_2, is likely to be below 10. The grain boundary thicknesses calculated in this study therefore represent the maximum value possible. Smaller thicknesses would result in even lower grain boundary conductivities but the shape of the curve in Fig.12.10 is unlikely to be changed.

It is difficult to determine from the impedance data alone, the reasons why the grain boundary conductivity reaches a maximum. At this stage it is only possible to speculate on the factors that need consideration, i.e. segregation of impurities and dopant, grain boundary thicknesses, amorphous or crystalline second phases. Section 12.5 reports on the findings of the TEM work performed at the grain boundary. It is appropriate, therefore, to discuss the possible explanations for the grain boundary conductivity in light of this knowledge and so a full discussion of this point is included in section 12.5.

12.3.3. A.C. Impedance Spectroscopy - Total Data

The discussion so far has focused on the individual contributions to the total conductivity. Technologically, it is the total conductivity of an electrolyte that is of most importance in applications. By adding the bulk and grain boundary resistance components, the total resistance is obtained. This can be converted into conductivity and displayed on an Arrhenius plot in the usual manner. Fig.12.11 shows the Arrhenius conductivity plot for the CGO samples analysed in this thesis. The graph appears to be very similar to the grain boundary conductivity graph shown in Fig.12.7.

For all samples with a dopant concentration below 20mol% Gd, the grain boundary conductivity is at least an order of magnitude below that of the bulk conductivity and will be the dominating contribution to the total conductivity. Above 20mol% Gd the grain boundary conductivity is equal to or greater than that of the bulk and thus the bulk conductivity starts to dominate. This results in a change in the total conductivity graph compared to the grain boundary conductivity graph.

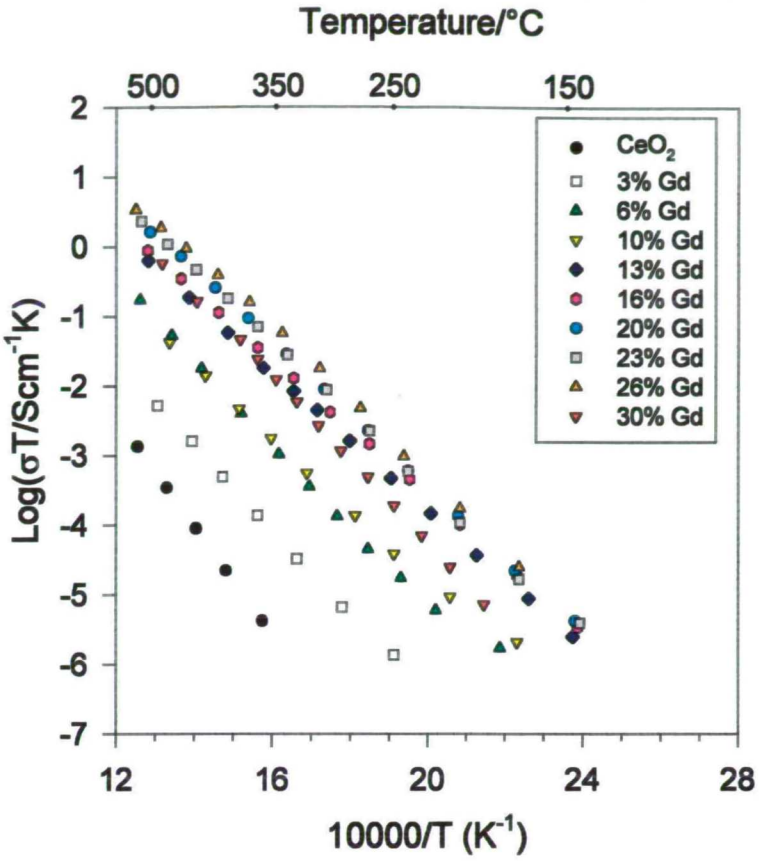


Fig.12.11. Arrhenius graph of the total conductivity for a series of CGO samples with increasing Gd concentrations.

Fig.12.12 displays an isothermal conductivity plot at 500° for the bulk, grain boundary and total conductivities, as a function of Gd concentration. This temperature is chosen because it represents the temperature that it is hoped to operate an SOFC stack using CGO electrolytes. It shows more clearly the relationships between the bulk, grain boundary and total conductivities discussed above. The bulk conductivity produces a curve with a shallow maximum between 6-10mol% Gd. It is interesting to note that at this temperature there is very little difference in bulk conductivity over the entire concentration range.

The grain boundary conductivity produces a more acute maximum at 26mol% Gd. The total conductivity follows the grain boundary conductivity until the bulk contribution becomes significant. This produces a broader maximum in the total conductivity graph between 20-26mol% Gd. A similar maximum has been reported previously by Yahiro [14] for a series of ceria-samaria solid solutions. The decrease in conductivity above the maximum was found to be less dramatic than that below the

maximum. Also, the total conductivity maximum became broader as the temperature increased, a result which is true of the Gd doped samples in this thesis.

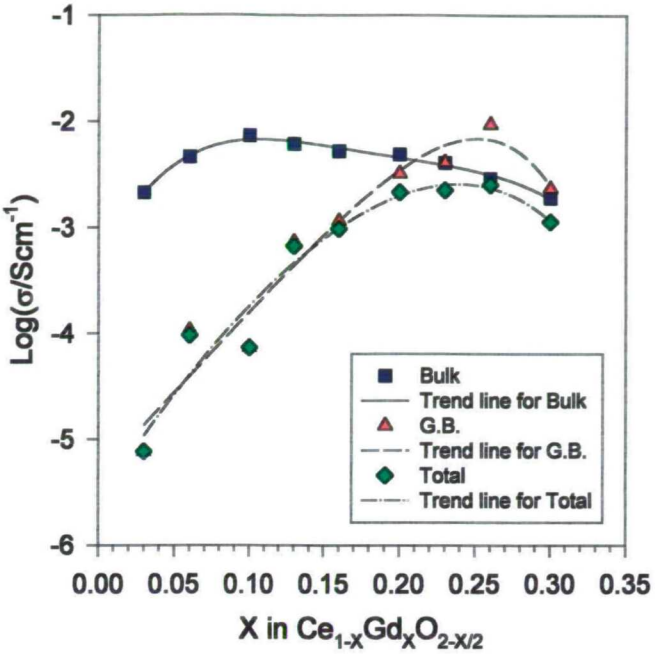


Fig.12.12. Isothermal conductivity of CGO at 500°C as a function of Gd concentration, showing data for the bulk, grain boundary and total contributions.

From the results in Fig.12.12, it would appear that the CGO composition with the highest conductivity is Ce-26%Gd. It is suggested that the 10% and 20% Gd compositions presently considered for SOFC applications are not the optimum compositions for maximum conductivity.

12.3.4. Silica Additions

Chapter 6 discussed the impact of impurities in ceria, especially at the grain boundaries. The high grain boundary resistances measured were reported to be due to the presence of an amorphous silica phase, which had developed from the segregation of Si to the grain boundaries. A number of researchers have reported higher grain boundary conductivities in high purity materials but there is no direct evidence that this is a result of lower Si levels at the grain boundary. Impedance spectroscopy does not allow chemical determination of species but by deliberately doping a CGO sample

with silica, it is possible to detect if the dopant has any effect on the bulk or grain boundary conductivities.

As a reference, it was decided to measure the impedances of a pure ceria and pure gadolinia sample and compare these to a standard Ce-10%Gd sample. The Arrhenius graph for these three samples is shown in Fig.12.13. Clearly, both the bulk and grain boundary conductivities for pure ceria are lower than the total conductivity for CGO (10%Gd). The bulk conductivity for gadolinia is at least two orders of magnitude below that of pure ceria. The grain boundary conductivity was too high to be measured over the temperature range of the experiment. The formation of gadolinia rich phases at the grain boundary is therefore undesirable and segregation of Gd to the grain boundaries should be prevented.

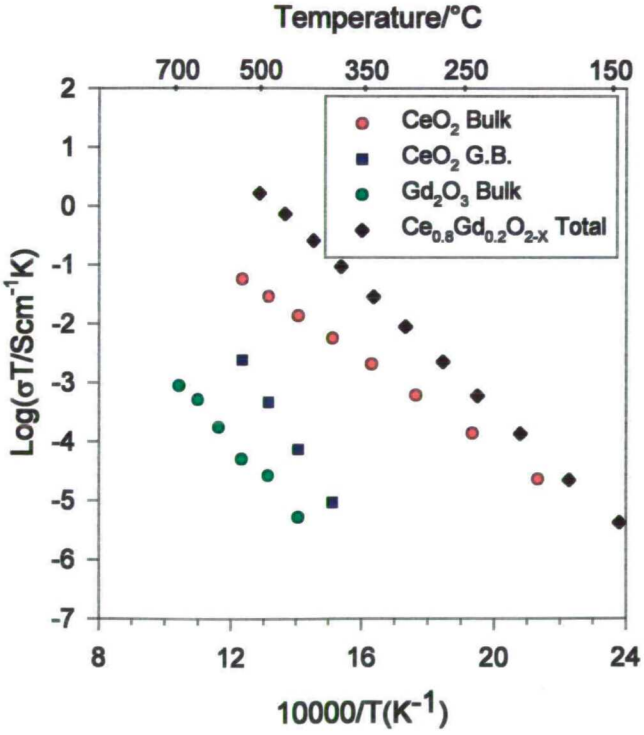


Fig.12.13. Comparison between the conductivities of pure ceria and pure gadolinia against a standard Ce-10%Gd sample.

To assess the effects of silica in CGO, a 5mol% addition of SiO_2 was added to a Ce-10% Gd powder and mechanically mixed. A pellet was then prepared via the normal route for impedance analysis. The Arrhenius plot of conductivity for this sample, compared to a normal CGO sample, is shown in Fig.12.14.

The bulk conductivities are virtually the same at low temperatures and only deviate slightly at the highest temperatures. This result suggests that a large proportion of the silica may have segregated to the grain boundaries. Further evidence for this is the decrease in the grain boundary conductivity by over an order of magnitude for the silica doped CGO. Assuming the purity of the CGO in both samples is the same, this result strongly suggests that silica plays an important role at the grain boundaries. It should be remembered that the silica addition will also contain some impurities and these too may have contributed to the grain boundary conductivity. These results suggest that low silica impurity levels are desirable to achieve the highest conductivities.

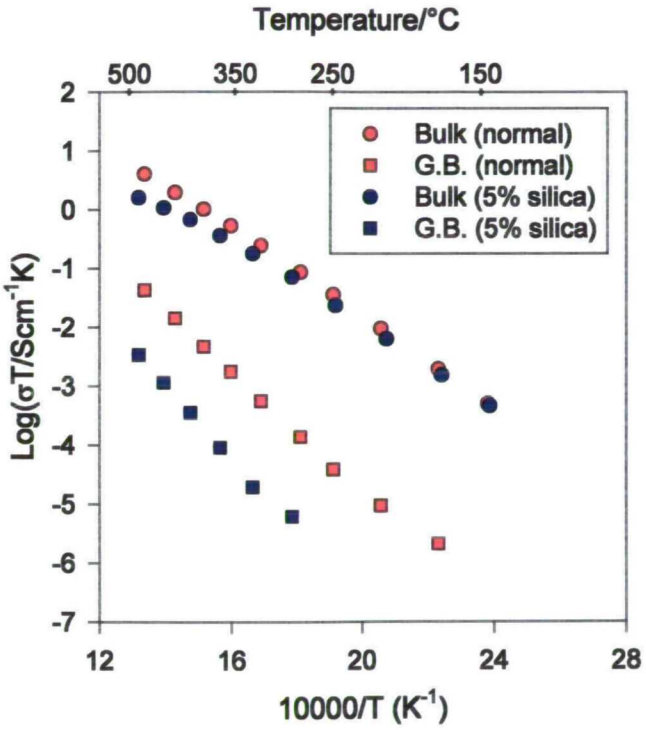


Fig.12.14. Comparison of the bulk and grain boundary conductivities for a normal Ce-10%Gd sample and a silica doped CGO sample.

12.4. Low Energy Ion Scattering (LEIS)

LEIS and XPS measurements have been performed on four samples prepared at IC:- Ce-6%Gd, Ce-26%Gd and two Ce-9%Gd-1%Ca pellets. The first three samples were analysed as-sintered, while the fourth sample had been polished down to a 1/4 micron

finish using diamond paste and then annealed at 1430°C for 1/2 hour. A brief description of the LEIS and XPS techniques and equipment used, is given in chapter 10.

Care must be taken when analysing LEIS spectra because the peak heights of each element do not indicate the concentration of a particular element. The variation in sensitivity of different elements, using different beams, further complicates the analysis. To compare concentrations, the area under each peak must be used, after subtracting the value for the background (which is a gently curving arc in these experiments). When the composition on the surface changes, the peak areas change, but it is not possible to quantify the number of atoms involved, without a comparison with known standard samples.

In each LEIS spectrum a large background peak can be seen. Incoming ions that are not scattered from the surface, are normally neutralised below the surface layer (for inert gases). However, some neutral species can be reionised and escape the surface as secondary ionised ions. It is these ions which are responsible for the background peak. It is generally found that as surface impurity layers become thinner, more secondary ionised ions can escape the surface and the background height increases. The background height reaches a maximum when only one monolayer of surface impurities remain. For CGO, the appearance of Ce on the surface lowers the background signal because cerium does not readily produce secondary ionisation with inert gas beams. This behaviour was observed for the samples used in this study. Some spectra also display a large peak to the far left of the spectrum. This peak is called a sputter peak and is due to the presence of sputtered ions which do not give a LEIS spectrum, i.e. hydrogen ions when using the helium beams and all low mass elements for the neon beam.

The surfaces of all samples were first analysed using a $^{3}He^{+}$ beam scanning over an area 3mm×3mm, to detect for hydrocarbon and silica deposits, which are normally present within the first monolayer. Fig.12.15 displays LEIS spectra for as-sintered Ce-6%Gd and Ce-9%Gd-1%Ca for this initial area scan. The Ca-doped material shows no carbon or silicon deposits on the surface, while the Ce-6%Gd sample displays a small

carbon peak. After several measurements the carbon signal disappeared, which indicates that carbon is a surface deposit. Distinct peaks are displayed for Na, Al, Ca, K and O, which are all common surface contaminants in oxide materials. The position expected for the Ce+Gd peak is marked on the spectrum, although no peak is actually visible. This result is consistent with a surface layer containing the elements mentioned above covering the bulk Ce and Gd.

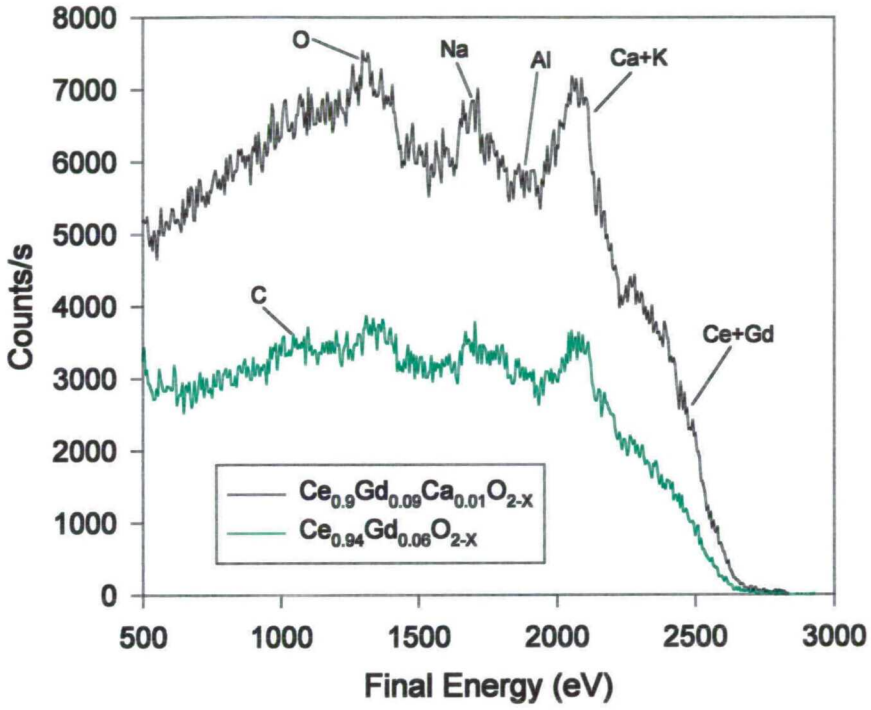


Fig.12.15. LEIS spectra for as-sintered Ce-6%Gd and Ce-9%Gd-1%Ca showing the initial area scans (3×3mm) using $^{3}He^{+}$ beam (3keV, I=1nA).

Fig.12.16 shows the LEIS spectrum for Ce-6%Gd using the $^{4}He^{+}$ beam at different ion doses. The low ion doses (10^{14}-10^{15}ions/cm^2) are obtained from large area scans, while the high ion doses (10^{17}-10^{18}ions/cm^2) use a spot measurement (0.1mm^2). The same elements are observed as before and remain in each spectrum as the ion dose increases. Normally, the impurity signals diminish after the first monolayer has been sputtered off the surface and the signals from the bulk elements dominate. In the present case this is not true because the impurity signals are still present when several tens of monolayers have been sputtered. Also, it is common to observe impurity peaks diminishing at different rates because of the differences in depth distribution for each element. This is not observed in any of the spectra presented here.

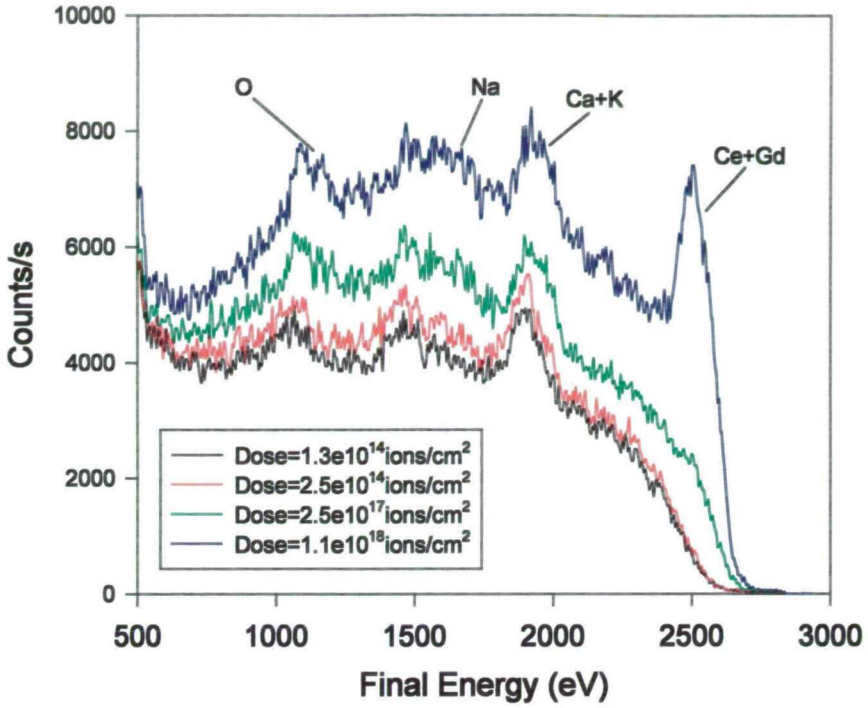


Fig.12.16. LEIS spectrum for as-sintered Ce-6%Gd using a $^4He^+$ beam, showing the development of the Ce+Gd peak and the presence of a thick surface region (several tens of monolayers thick). Ion beam doses as indicated (3keV, I=2-3nA).

The appearance of impurity signals at high ion doses suggests that the segregated surface layer is considerably thicker than one monolayer. In addition, the ratio of the peak heights remains approximately constant between measurements, which implies that these elements have formed a single composition on the surface. The presence of such a thick segregated layer containing a large number of elements is unusual because of the time needed for segregation of these atoms. After the first monolayer has been formed the segregation of further atoms through this layer is less favourable. After several monolayers have formed it seems unlikely that further segregation would occur.

One answer to the problem of having such thick surface layers is that the surface is not a crystalline phase but a glassy structure. Glasses are generally more difficult to sputter than crystalline materials and thus require a higher ion dose to achieve the same sputter depth. Several tens of monolayers sputtered in a polycrystal could in fact be only a few monolayers in a glass, for the same dose. It is clear, however, that a thick surface phase is present, which cannot be accounted for by surface contamination.

This surface phase will have formed during sintering when very high temperatures are experienced and atom mobilities become significant.

To determine the ease of formation of the surface layer, the Ce-6%Gd sample was sputtered overnight using the Ne beam, over an area of 9×9mm, to remove the surface layer. The total ion dose was calculated as $3.4e10^{16}$ions/cm^2. Spectra using $^4He^+$ were then measured on the cleaned surface. The sample was then heated to 500°C for 2 hours in an oxygen atmosphere. Further spectra were then obtained using a $^4He^+$ beam. Fig.12.17 shows the initial LEIS area scans for the as sintered, sputter cleaned and annealed surfaces of the Ce-6%Gd sample.

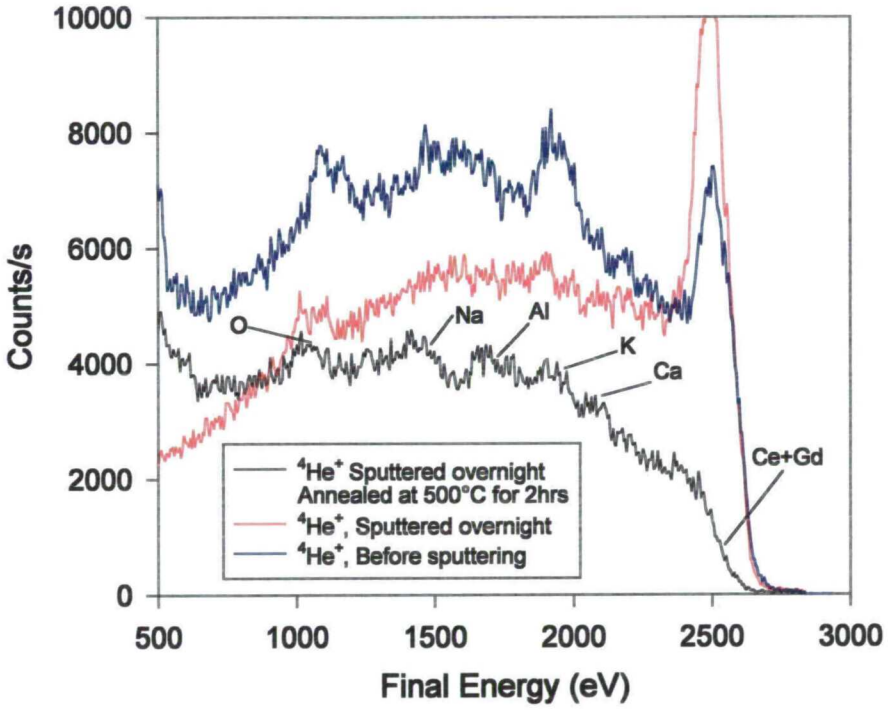


Fig.12.17. LEIS spectra for the as-sintered, sputtered and annealed surface of a Ce-6%Gd pellet. Segregation peaks disappear after sputtering but re-appear after the short anneal (3keV, I=2-4nA).

Fig.12.17 shows that the peaks from the surface layer have virtually disappeared in the sputtered sample, which indicates that the bulk composition has been reached. The annealed spectrum reveals the return of the same peaks previously seen in the as-sintered sample and suggests that a small degree of segregation has occurred, even at

500°C. The implication is that segregation of impurities is inevitable in doped ceria electrolytes used in SOFC's and thus every care must be taken to avoid contamination.

It was not possible to resolve the Ce and Gd signals into two separate peaks using the He beams because He is not sensitive to high atomic mass elements. A result of this poor sensitivity is that it is not possible to detect the presence of the dopant Gd in the surface region. It is possible that Gd has also segregated to the surface to some degree but LEIS measurements are not able to positively confirm this.

The large Ce+Gd peaks observed in the He measurements were better resolved when a Ne beam was used. Fig.12.18 shows the LEIS spectrum for Ce-26%Gd using a Ne^+ beam, which clearly shows a Gd shoulder on the Ce peak. The major disadvantage in using the Ne beam is that the sensitivity for the low atomic mass elements is lost. All of the segregated impurities seen with the He beams have a low mass and so this detail disappears when using a Ne beam. In addition, a spot measurement is used in Fig.12.18, which has a high dose and will have sputtered through the surface impurity layer.

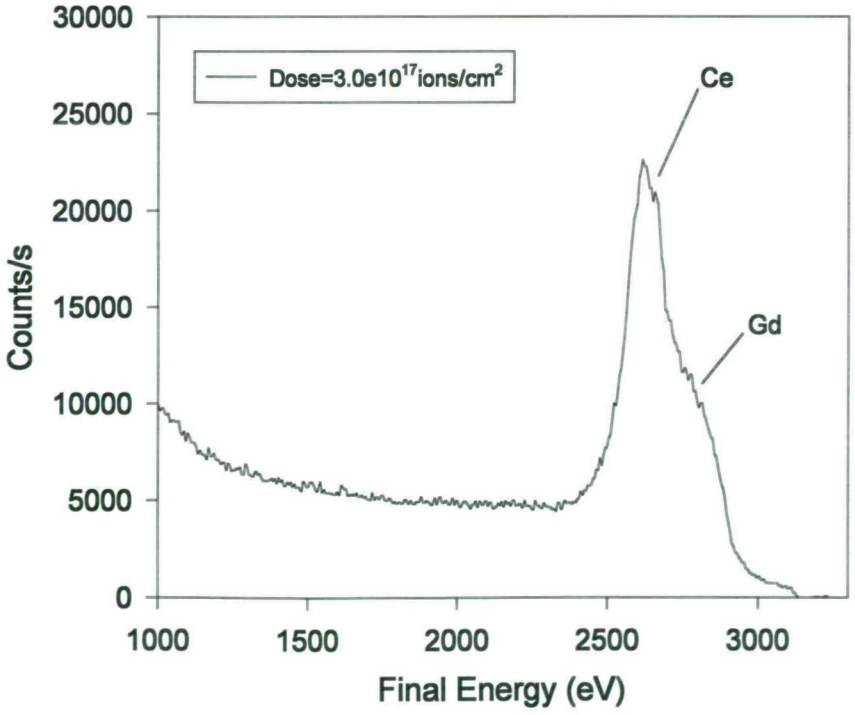


Fig.12.18. LEIS spectrum obtained from a spot measurement using a Ne^+ beam, showing a Gd shoulder on a Ce peak, for a Ce-26%Gd sample (4.75keV, I=3nA).

Fig.12.19 shows the LEIS spectra for the Ca doped sample taken using a $^4He^+$ beam. The spectra reveal that the same elements are present in the surface layer as were found for the Ce-6%Gd sample. When using the $^4He^+$ beam the impurity element peaks remained in the spectra to very high ion doses. The development of the Ce+Gd peak also required a higher ion dose. These results indicate the presence of a thicker surface layer on the Ca-doped CGO sample.

Impurities and dopants in ceria are both known to segregate to higher energy surfaces [15] and this study provides evidence for the segregation of a large number of atoms to the surface of ceria. Grain boundaries are also high energy surfaces and segregation to these surfaces is also expected. Using the information from the LEIS data it is reasonable to assume that a grain boundary layer would form with a similar composition to that found on the surface of the pellet.

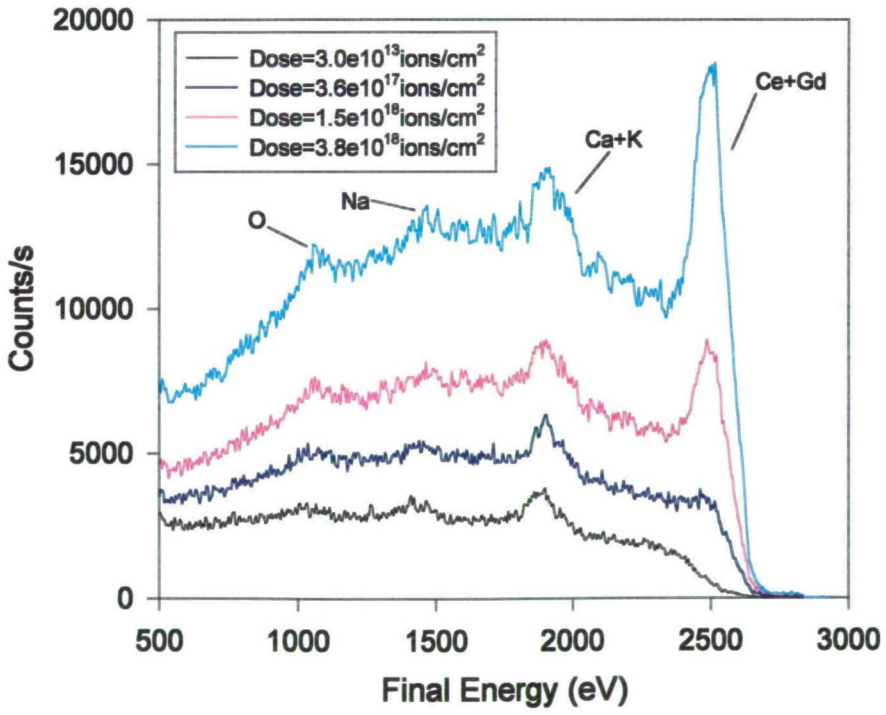


Fig.12.19. LEIS spectra showing the development of the Ce+Gd peak for a Ca-doped CGO pellet and a thick surface layer, using $^4He^+$ spot measurements (3keV, I=1-8nA).

The electrical measurements presented earlier in this chapter and those discussed in chapter 14, show the grain boundary conductivity for the Ca codoped material to be considerably higher than the Ce-6%Gd sample. An explanation of these results using

the LEIS data, is the presence of a thicker grain boundary phase for the Ca codoped material, which can incorporate more impurity atoms. The grain boundary phase would reduce the amount of glassy silica present, which has a very high resistance. The Ce-6%Gd is therefore speculated to have more glassy silica present. In addition, the thick boundary phase may also contain Ce and Gd which may increase its conductivity further over a glassy silica phase. The data are, however, contradictory to the impedance data, where a higher capacitance is calculated for the Ca-codoped material, which implies a lower grain boundary thickness, according to the familiar expression, $C=\varepsilon_0\varepsilon_R A/l$.

It is not possible to determine the structure of the surface layer using LEIS but these results imply a complex oxide structure, which can accommodate a large number of different elements. The high doses needed to sputter through the surface layer suggests that this layer may have a glassy structure.

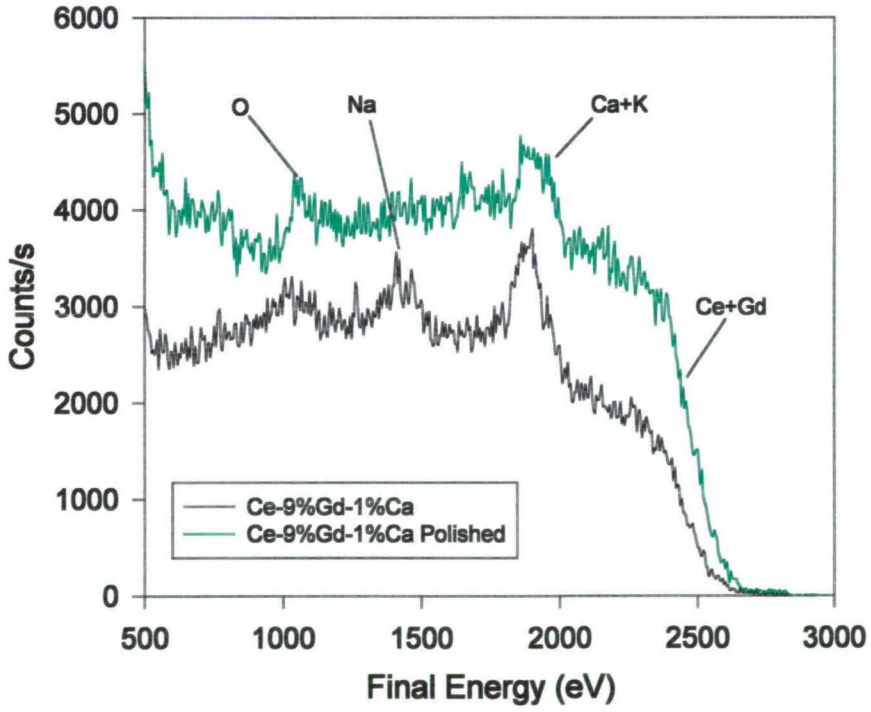


Fig.12.20. LEIS spectra to show the comparison between as-sintered and polished and annealed Ca-doped CGO, using a $^4He^+$ area scan (3keV, I=1-3nA). Dose=3×10^{13}ions/cm^2 for both compositions.

The final LEIS spectrum (Fig.12.20) shows the effects of polishing and annealing samples prior to analysis. It is clear that the polished sample has less well defined impurity peaks but all the peaks are the same as those of the as-sintered sample. It is clear that the background signal is higher for the polished pellet. From the earlier discussions, this indicates that the segregated surface layer is thinner. The polished pellet was exposed to a lower temperature for a shorter time compared to the as-sintered pellet. From this it is be expected that the polished sample would have a thinner segregated surface layer.

12.4.1. XPS

XPS was performed on all samples using the equipment described in chapter 10. Fig.12.21 shows the XPS spectrum for the as-sintered Ce-6%Gd pellet. The same impurities detected using LEIS were observed in the XPS spectrum, i.e. Na, K, Al, and Ca but traces of other impurities were also found e.g. Cl, Si. The Ce-6%Gd sample sputtered overnight with a Ne beam, showed a similar spectrum but showed less development of the impurity peaks, especially Si and Cl.

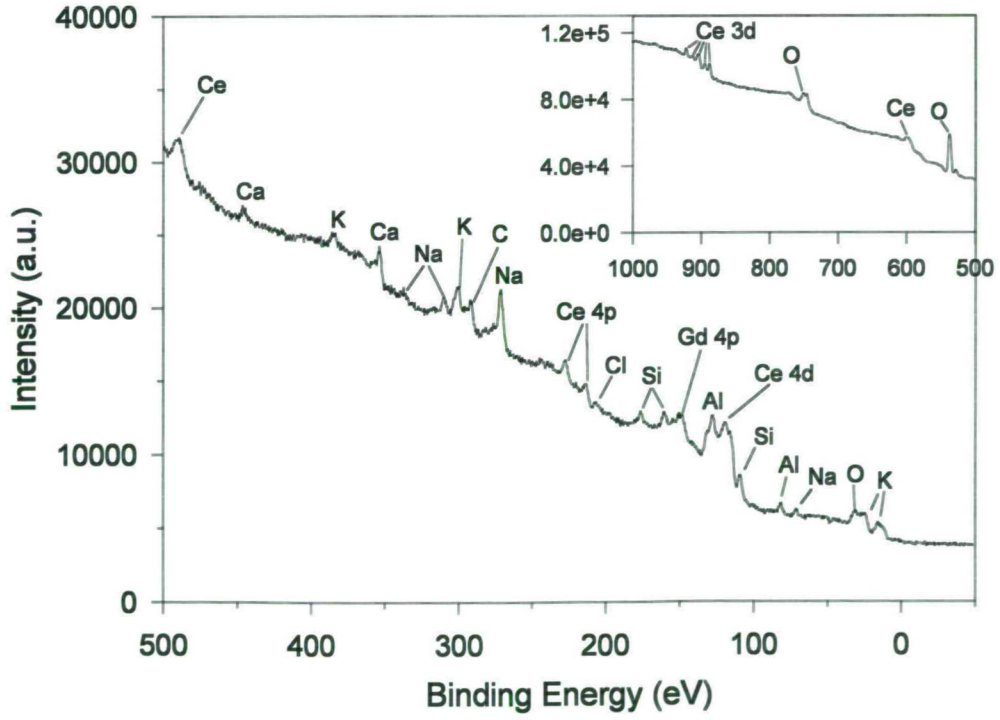


Fig.12.21. XPS spectrum for as-sintered Ce-6%Gd using a Mg K_α beam. Inset shows peaks at higher binding energies.

XPS performed on the remaining samples showed similar spectra to Fig.12.21, confirming the composition of the surface layer determined using LEIS. These results demonstrate that the surface of all IC prepared materials contain similar impurities.

The ICP measurements shown in chapter 11, show that Gd-doped ceria has a significant concentration of sodium. This is in agreement with the LEIS and XPS data which show a strong Na peak. Using ICP, the Ca codoped CGO is shown to contain a considerably lower concentration of Na. A sodium peak is still present in the LEIS spectra which suggests that Na has a strong tendency to segregate to the surfaces.

12.5. TEM

Two Gd-doped ceria samples were analysed using TEM: $Ce_{0.74}Gd_{0.26}O_{2-X}$ and $Ce_{0.8}Gd_{0.19}Ca_{0.01}O_{2-X}$. The samples were prepared and characterised at Rhône-Poulenc as described in chapter 10. The results of microanalysis for both samples, showed that silicon was not detectable at the grain boundaries. The smallest size of the microprobe attainable (7nm), resulted in a large signal from both of the adjacent grains, during each grain boundary measurement. If the grain boundary regions were very thin (<1nm), the composition of the grain boundary may be masked by the data from the grains.

To obtain an image of the grain boundary structure of this thickness, it is necessary to find an orientation that permits lattice imaging of the two adjacent grains and a grain boundary parallel to the electron beam. It was not possible to find such an orientation in these samples because the preparation reduced the number of grain boundaries that could be observed. It was possible, however, to achieve high resolution images of the grain boundaries aligned parallel to the electron beam, which allow an approximate determination of the width of the grain boundaries and the presence of any second phase material. Fig.12.22 shows a high resolution image of the Ce-19%Gd-1%Ca sample. The thickness of the grain boundary is clearly very small (<1nm) and there is no visible evidence of a second phase. Careful examination of the grain boundary reveals light and dark fringes but these are due to the disorientation between the two

grains. The thickness of the grain boundaries remained constant for all areas analysed, including triple grain points where no second phase was detected.

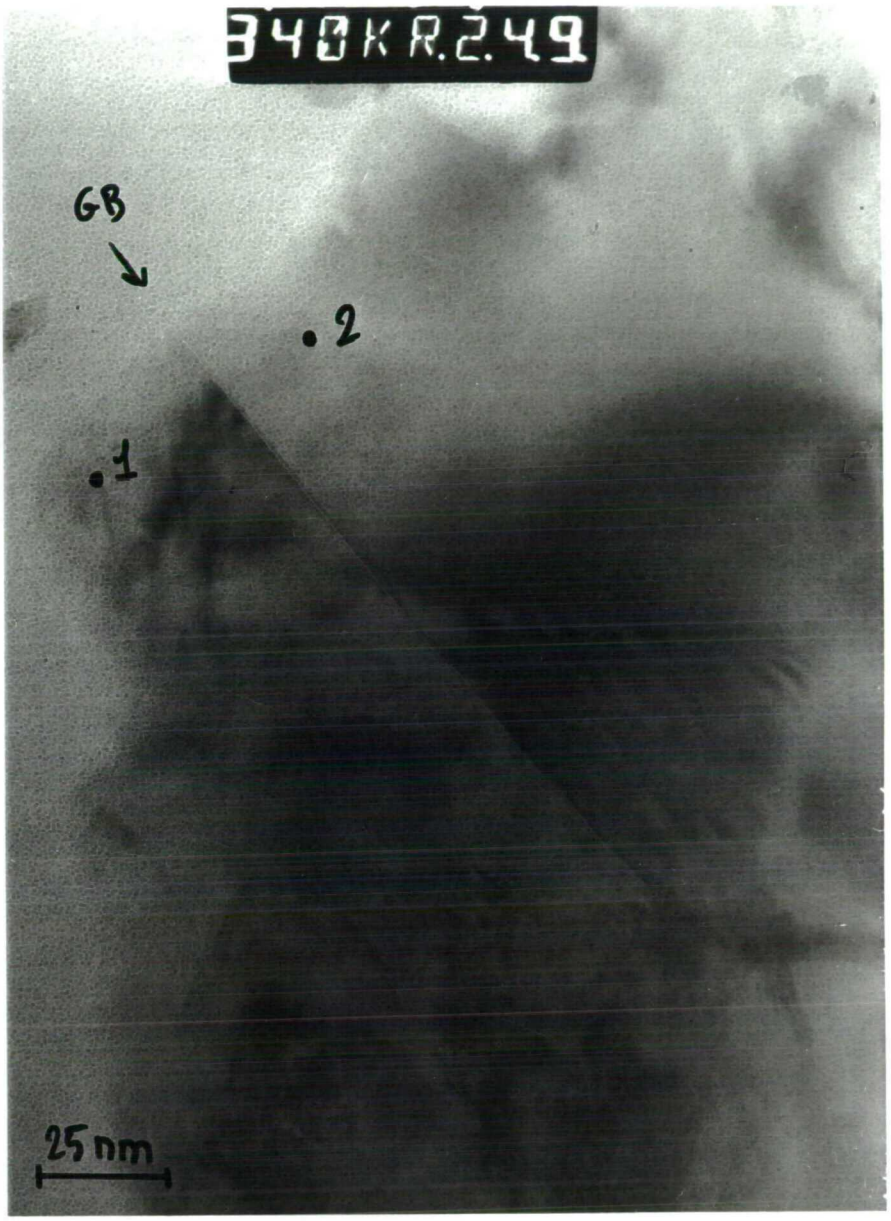


Fig.12.22. Bright field HRTEM image of a $Ce_{0.8}Gd_{0.19}Ca_{0.01}O_{2-X}$ sample with grain boundary aligned parallel to electron beam.

The electron diffraction patterns for all the grains studied showed fully crystalline phases. There were no amorphous phases detected at the grain boundaries. These results suggest that, in both samples, the grain boundary thickness is much smaller than previously expected and the thickness of any distinct segregated phase must be <1nm. It is possible that segregation of impurities and dopants is not significant in these materials but this appears to be in contradiction to the LEIS results, which showed

strong segregation of most impurities to the surface. The driving force for segregation to the grain boundaries is less than that to the surface and it is expected that a grain boundary layer would be thinner than a surface layer. The impurity concentration in these materials is relatively low and it is possible that there is only a monolayer coverage of impurity phase around the grain boundaries, or even incomplete coverage. The grain boundary phase would then be less than 1nm in thickness.

In these experiments the grain size was approximately 4μm and the pellet dimensions were, 1mm thickness and 10mm diameter. Assuming the grains to be spherical and the grain boundary to be linear and of thickness 1nm, the total number of grains and hence the volume of grain boundary can be calculated. The total number of grains in a typical sample is 2.34×10^{9}grains, which gives a grain boundary volume of silica for complete coverage of $5.89\times10^{-11}m^{3}$. The density of silica (quartz) is $2.65gcm^{-3}$, thus the mass of silica required is 1.56×10^{-4}g. The mass of the pellet was 0.5g and thus the weight percent of silica in the pellet is 0.03Wt% SiO_2. This corresponds to a value of approximately 850ppm of silica. Although this is only a rough calculation it appears that silica does not cover all grains in these materials (Si concentration <25ppm) and thus the constriction type of model looks more appropriate.

The LEIS results also revealed the same elements present in the surface layers for all 3 compositions studied, which suggest similar compositions and structures for each layer. It is expected that the grain boundary layers would form the same compositions at the grain boundaries. The differences observed in the electrical properties at the grain boundaries must therefore result from the degree of coverage of the grain boundaries with the impurity phase.

The Ca-codoped material had a grain size approximately twice that of the other samples studied and consequently, a smaller grain boundary area to cover. LEIS results showed this material formed the thickest surface layer. This material also displays the highest grain boundary conductivity (see chapter 14), which indicates that it is the presence of the grain boundary layer that increases the conductivity. If this is true, the higher Gd doped concentrations should have a higher coverage of impurity phase at the grain boundary. Fig.12.23 shows a schematic representation of a possible

grain boundary structure that may be present in these materials. The only method that would allow determination of this fact is high resolution lattice imaging.

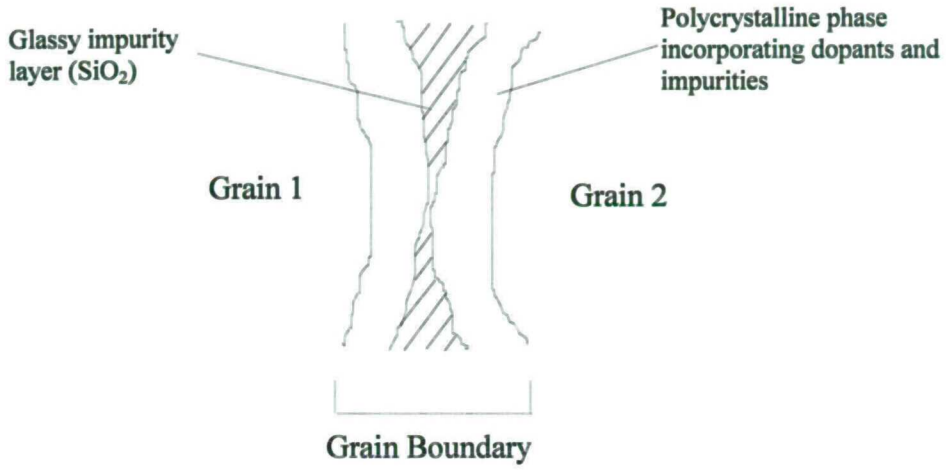


Fig.12.23. Schematic representation of the grain boundary in doped ceria.

12.6. Conclusions

The results from the LEIS and TEM analysis have shown that silica is not the most abundant impurity at the surface or grain boundary of CGO. It is clear from both the impedance and LEIS data that an impurity layer is present at the grain boundaries. The question remains as to the nature of the this grain boundary phase. It is at this point that some contradiction in the data from different techniques occurs. LEIS measurements predict a thick impurity layer at the grain boundary (several monolayers). Calculations from impedance spectroscopy suggest a thickness of 2-5nm, while the TEM results imply a grain boundary layer <1nm in thickness. With no amorphous structure visible in electron diffraction patterns it is speculated that the grain boundary impurity layer is predominantly crystalline. LEIS measurements suggest that the composition of this impurity layer is likely to be a complex Na-Ca-oxide, which may form a glassy structure. The differences observed in the grain boundary conductivities are thought to result from differences in grain boundary layer thickness and continuity and the degree of segregation of impurities and Gd. It should be remembered, however, that LEIS and a.c. impedance measurements average over a large number of grains. For TEM analysis only one or two grain boundaries are

selected, which statistically reduces the significance of these results. Further attempts to analyse the grain boundary region are reported in chapter 13.

12.7. Thin Films

The majority of this thesis is concerned with the electrical properties of samples which are considerably thicker than that required for device operation. As discussed in chapter 7, both thin and thick films of CGO are being used in SOFC stacks and research on a number of deposition techniques is being performed. This section concentrates on the production of CGO films using the pulsed laser deposition technique discussed in chapter 7. Each of the thin film compositions were deposited by laser ablation for 90 minutes. The resulting thicknesses of each film are given in Table 12.2. Fig.12.24 show a typical XRD spectrum for each thin film. The film is polycrystalline but has a high degree of texturing in a [111] direction.

Composition	Film Thickness/μm
$Ce_{0.9}Gd_{0.1}O_X$ (1)	0.236
$Ce_{0.9}Gd_{0.1}O_X$ (2)	0.736
$Ce_{0.8}Gd_{0.2}O_X$	1.550
$Ce_{0.7}Gd_{0.3}O_X$	1.335

Table 12.2. Film thicknesses.

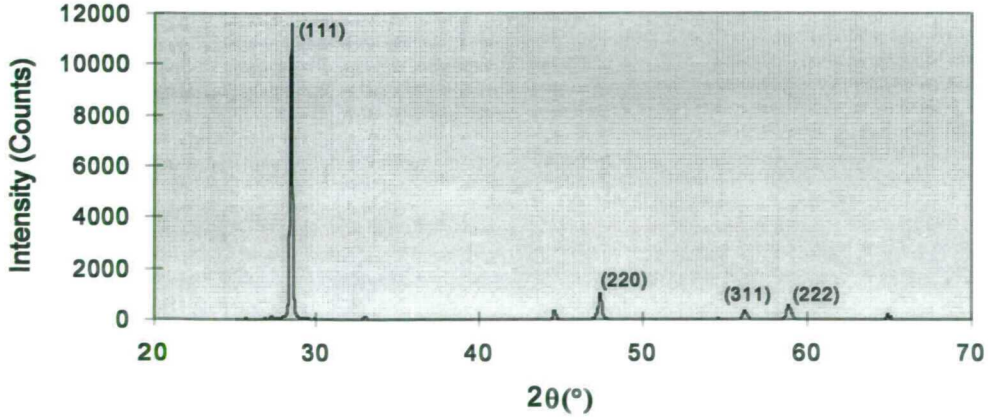


Fig.12.24. Typical XRD trace for thin film CGO on a ferritic stainless steel substrate. Measurement courtesy of Dr.D.Waller.

SEM analysis on the first 10%Gd sample revealed several pinholes in the film and these were thought to be responsible for the short circuit conditions observed under electrical testing (this sample had silver electrodes that were baked on at 700°C). AFM (Fig.12.25) and SEM analysis of the remaining films showed a very dense structure with no visible pinholes.

A.C. impedance measurements were performed below 200°C to allow the bulk responses to be seen. No clear grain boundary component was visible for any of the samples and a large overlap with the electrode response was observed. This overlap complicated the interpretation of the bulk resistance but normally an adequate fit could be obtained.

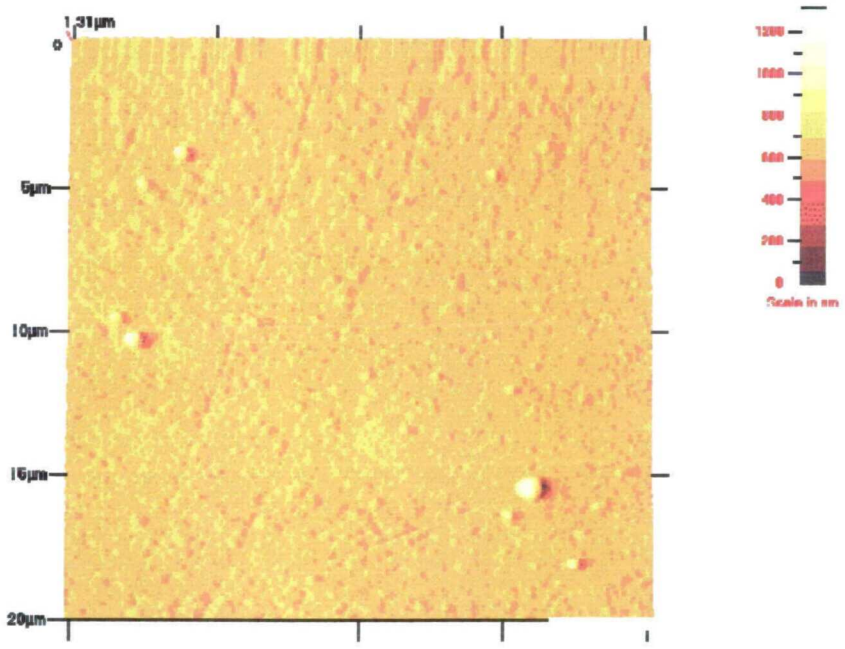


Fig.12.25. AFM image of the surface of a CGO thin film, showing a very flat topography and no pinholes.

Fig.12.26 shows the impedance data for each film composition at 130°C. A fully resolved bulk semi-circle is not obtained for the 10%Gd sample, which displays the lowest resistance. The inset shows a similar poorly resolved bulk semi-circle for the 20%Gd sample at a higher resistance. The bulk response for the 30%Gd sample is only observed at higher resistances.

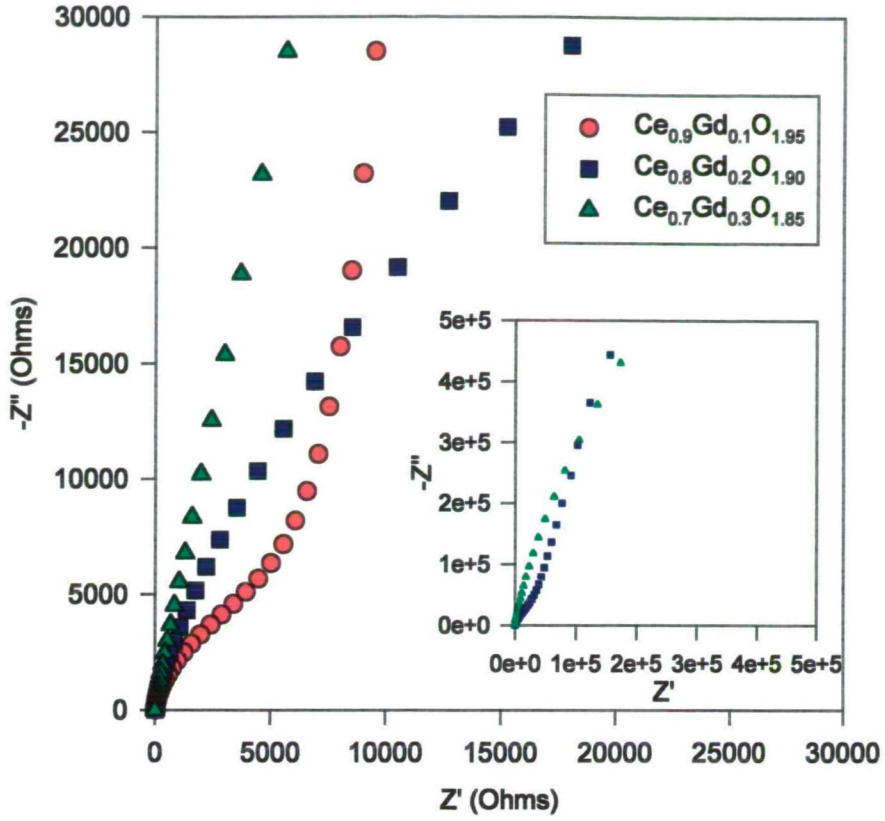


Fig.12.26. Impedance Data of all laser ablated CGO thin films at 130°C. Inset shows the poorly resolved bulk component for the 20%Gd sample.

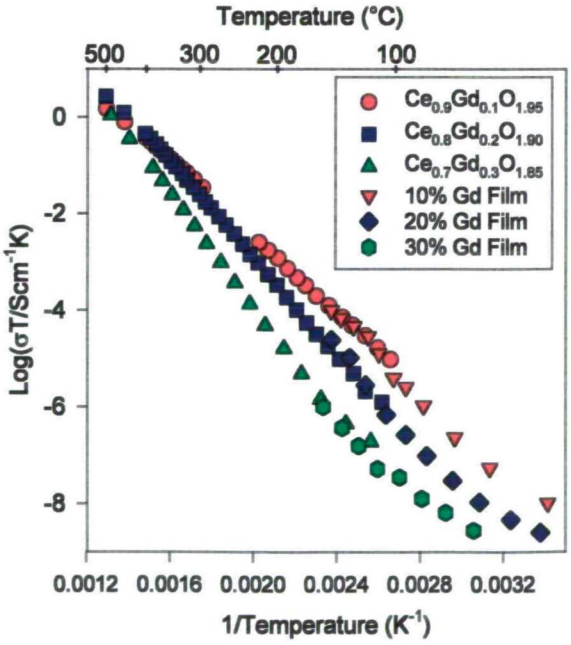


Fig.12.27. Arrhenius conductivity plots for the laser ablated thin films compared to the conductivity data from pellets of the same composition.

The bulk data were then used to construct a conductivity plot for each film. The thin film data is compared with the data from pellets in Fig.12.27, which shows a good agreement between the two. The curvature observed in the thin films at low temperatures is thought to be the result of errors in the measured sample temperature. At low temperatures a long equilibration time is needed and the results indicate that equilibrium conditions had not been achieved for the lowest temperature measurements.

The data presented in this section provide evidence that thin films of CGO can be grown satisfactorily using PLD. Polycrystalline CGO with electrical properties similar to those measured on much thicker samples can be produced, with no porosity. The differences observed in the impedance data between the thin films and pellets, is most probably due to the texturing present in the thin films. It is thought that all grains will be elongated parallel to the direction of current flow in the thin film, which suggests that no, or very few grain boundaries are present perpendicular to the electrodes. This would account for the absence of any grain boundary response in the impedance spectra. The grain size of the thin films studied here will be less than 1μm because of the growth technique employed. The sharp diffraction peaks observed in the XRD spectrum indicates a grain size of at least 200nm.

At present PLD is not a suitable technique for the mass production of thin films because the deposition rate is very slow compared to the simpler and less expensive techniques discussed in chapter 7. The problem of depositing CGO onto porous substrates has not been undertaken in this study but again the unfavourable deposition rate is likely to prohibit use of PLD.

References

1. Impedance Spectroscopy: Emphasising Solid State Materials. Ed. J.R.Macdonald. John Wiley and Sons, Inc. 1987.
2. R.Gerhardt. J.Phys.Chem.Solids. **55**, 12, (1994), 1491.

3. J.T.S.Irvine, D.C.Sinclair and A.R.West. Adv.Mater. **2**, 3, (1990), 132.
4. D.Y.Wang and A.S.Nowick. J.Solid State Chemistry. **35**, (1980), 325.
5. D.Y.Wang and A.S.Nowick. J.Electrochem.Soc. **126**, 7, (1979), 1166.
6. J.Faber, C.Geoffroy, A.Roux, A.Sylvestre and P.Abelard. Applied Physics A: Solids and Surfaces. **49**, 3, (1989), 225.
7. D.Y.Wang, D.S.Park, J.Griffith and A.S.Nowick. Solid State Ionics. **2**, (1981), 95.
8. D.K.Hohnke. Solid State Ionics. **5**, (1981), 531.
9. D.K.Hohnke. Fast ion transport in solids. Eds. P.Vashishta, J.N.Mundy and G.K.Shenoy. North-Holland, Amsterdam. 1979.
10. D.H.Hohnke. J.Phys.Chem.Solids. **41**, (1980), 777.
11. A.S.Nowick, W-K.Lee and H.Jain. Solid State Ionics. **28-30**, (1988), 89.
12. T.Dosdale and R.J.Brook. Solid State Ionics. **8**, (1983), 297.
13. G.M.Christie and F.P.F.van Berkel. Solid State Ionics. **83**, (1996), 17.
14. H.Yahiro, Y.Eguchi, K.Eguchi and H.Arai. J.Appl.Electrochem. **18**, (1988), 527.
15. P.G.Harrison, D.A.Creaser, B.A.Wolfindale, K.C.Waugh, M.A.Morris and W.C.Mackrodt. Catalysis and Surface Characterisation. Eds. T.J.Dines, C.H.Rochester and J.Thomson. 1992, 76.

Chapter 13. Double Doping in Ceria

13.1. Introduction

The concepts for using two dopants in ceria have been explained in Chapter 6. In brief, it is thought that using dopants with different ionic radii may maximise the bulk electrical conductivity in doped ceria, by reducing the strain in the lattice to near zero. This chapter presents and discusses the results of the electrical measurements and compares them to the oxygen self-diffusion coefficients obtained using SIMS analysis. TEM is then used to explore the properties of the grain boundaries. The beginning of this chapter discusses the essential powder and sintered ceramic characteristics.

13.2. Powder Characterisation

The powders used in the double doping experiments have been supplied by Rhône-Poulenc. Generally, the level of impurities in all these powders is much lower than those reported in chapter 11, with the concentration of Si<50ppm and that of Ca<200ppm. The one exception is Ce-2%Sm-4%Y which has a concentration of Si<200ppm. The concentrations of the other rare earth elements were also lower for these compositions.

The particle sizes and surface areas of all the powders are shown in Table 13.1. It can be seen that the particle sizes are all very similar and generally smaller than the particle sizes reported in chapter 11. The specific surface areas of these powders are also much higher than the powders prepared at Imperial College.

The typical morphology for these powders is shown in Fig.13.1. These powders show considerably less agglomeration compared to the Imperial College prepared powders. The small particle sizes and high surface areas should give improved sintering properties and this is demonstrated in Fig.13.2. In comparison to the shrinkage curves

in chapter 11, the plateaux are reached at lower temperatures, which indicates only small amounts of closed porosity remain.

Composition	Particle Size (D_{50})/μm (Error ±0.5μm)	Specific Surface Area/m^2g^{-1} (±0.5 m^2g^{-1})
$Ce_{0.94}Sm_{0.02}Y_{0.04}O_X$	3.12	28
$Ce_{0.94}Sm_{0.03}Y_{0.03}O_X$	2.41	30
$Ce_{0.94}Sm_{0.04}Y_{0.02}O_X$	2.47	28
$Ce_{0.94}La_{0.02}Yb_{0.04}O_X$	2.83	34
$Ce_{0.94}La_{0.03}Yb_{0.03}O_X$	2.83	39
$Ce_{0.94}La_{0.04}Yb_{0.02}O_X$	3.70	39
$Ce_{0.94}Gd_{0.06}O_X$	2.68	24
$Ce_{0.9}Sm_{0.05}Y_{0.05}O_X$	1.66	27
$Ce_{0.94}Gd_{0.19}Fe_{0.01}O_X$	1.67	30

Table 13.1. Particle sizes and surface areas of double doped ceria powders.

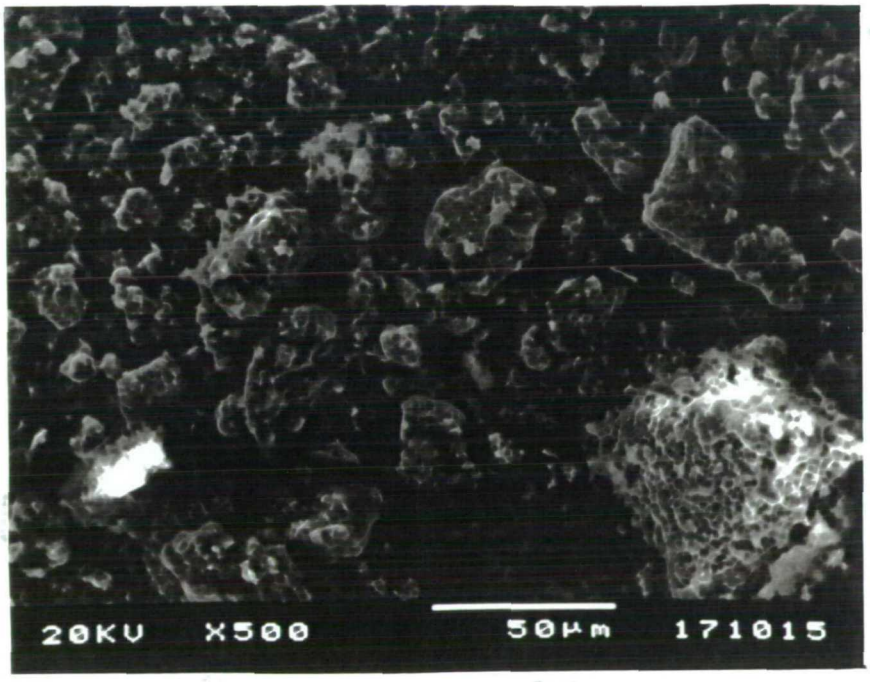


Fig.13.1. SEM micrograph showing the morphology of a double doped ceria powder.

The Gd and Sm doped ceria materials appear to sinter the best, with the plateau starting around 1100°C. The higher doped Sm material is slightly worse, with a plateau starting at 1200°C and the La doped material produces the poorest powder,

where the plateau starts at 1300°C. In all cases it would appear that these materials are capable of sintering to high densities at temperatures much lower than 1550°C, which makes these powders more attractive for SOFC applications.

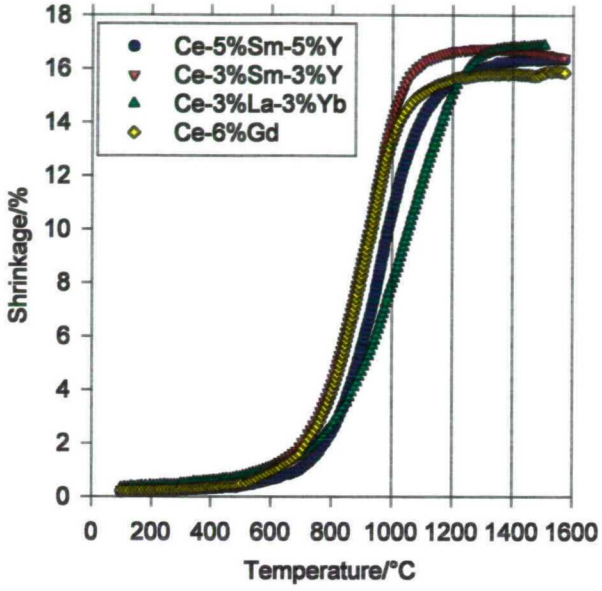


Fig.13.2. Dilatometric shrinkage curves for CGO and double doped ceria materials supplied by Rhône-Poulenc.

Composition	Bulk Density/gcm^{-3} (±0.30gcm^{-3})	Density/% Theoretical (±3%)	Grain Size/μm (±0.5μm)
$Ce_{0.94}Sm_{0.02}Y_{0.04}O_X$	7.19	100	1.99
$Ce_{0.94}Sm_{0.03}Y_{0.03}O_X$	6.98	98	2.02
$Ce_{0.94}Sm_{0.04}Y_{0.02}O_X$	7.01	98	2.08
$Ce_{0.94}La_{0.02}Yb_{0.04}O_X$	7.09	98	2.31
$Ce_{0.94}La_{0.03}Yb_{0.03}O_X$	7.09	98	2.12
$Ce_{0.94}La_{0.04}Yb_{0.02}O_X$	7.15	99	2.09
$Ce_{0.94}Gd_{0.06}O_X$	7.08	99	2.35
$Ce_{0.9}Sm_{0.05}Y_{0.05}O_X$	7.09	98	-
$Ce_{0.94}Gd_{0.19}Fe_{0.01}O_X$	7.17	100	-

Table 13.2. Density and average grain size of CGO and double doped ceria pellets.

The densities of the sintered pellets are recorded in Table 13.2, which shows that all compositions reach a very high density. Table 13.2 also shows the average grain sizes of all the compositions. The grain sizes are all within a very small range (~2μm) and

the peaks were shifted towards lower values compared to the pure ceria sample. The true lattice parameters were calculated from the data and are shown in Fig.13.4. Each composition is plotted as a function of the larger radii dopant to aid clarity. It appears that the overall lattice strain has been reduced compared to the CGO sample, for the $Ce_{0.94}Sm_{0.04}Y_{0.02}O_X$ sample. This confirms that the global lattice strain can be reduced closer to pure ceria using the double doping strategy and the effect this has on the electrical properties will be discussed in the following sections.

13.3. Electrical Properties

Similar to the impedance data reported in chapter 12, the impedance data for the double doped ceria samples are measured for the bulk, grain boundary and total conductivities. The impedance data for the two different doping systems are displayed on separate graphs for clarity, both of which show data for the reference Ce-6%Gd sample. A higher concentration double doped Sm-Y sample is also analysed to determine whether similar trends occur in the electrical properties.

This section also explores the performance of the double doped material at higher temperatures and under the reducing conditions that are encountered in SOFC stacks. A value for the P(-) point is calculated.

13.3.1. A.C. Impedance Spectroscopy - Bulk Data

The bulk and grain boundary impedances are measured using the a.c. impedance technique described in chapter 10. Fig.13.5 shows the Arrhenius plot of the bulk conductivity for the double doped samples. The bulk conductivity of the reference CGO sample remains higher than that of all the double doped compositions below 500°C, including the $Ce_{0.94}Sm_{0.04}Y_{0.02}O_X$ sample, which displayed a lower global lattice strain. This result implies that it is the local lattice strain effects around each dopant ion that determine the bulk conductivity. The conductivity of the La-Yb doped ceria is lower than that of the Sm-Y doped ceria. The introduction of Sm and Y into

ceria causes less local strain in the lattice compared to La and Yb, which is further proof that the local lattice strain effects dominate over the global lattice strain in ceria.

Fig.13.5 shows that the bulk conductivity increases as the larger dopant concentration increases. Balazs [1] shows that the association enthalpy of singly doped ceria is higher for the smaller dopants (Y, Yb), compared to the larger dopants (Sm, La) used in this study. This result indicates that the smaller dopant preferentially associates with the oxygen vacancies created in the lattice. Using defect chemistry, a double doped ceria sample can be represented by $Ce(x,y)O_2$, where x is the larger dopant concentration and y the concentration of the smaller dopant. The neutrality condition in this material can then be expressed as,

$$2\left[V_O^{\bullet\bullet}\right] = x + y \tag{13.1}$$

The formation of simple defect associates can be represented by,

$$V_O^{\bullet\bullet} + M_{Ce}^{'} \Leftrightarrow \left\{M_{Ce}^{'} V_O^{\bullet\bullet}\right\}^{\bullet} \tag{13.2}$$

where M is either dopant. If y is the smaller dopant then,

$$y = \left\{M_{Ce}^{'} V_O^{\bullet\bullet}\right\}^{\bullet} \tag{13.3}$$

For values of y>x, all the oxygen vacancies are associated with the smaller dopant. For values of x>y, some of the oxygen vacancies are also associated with the larger dopant and this should result in a higher conductivity. In the present study, concentrations above 3mol% of the larger dopant, leave insufficient concentration of the smaller dopant to associate with all of the oxygen vacancies created. Therefore, some of the oxygen vacancies will form associates with the larger dopant ion. It is expected, therefore that the association enthalpy of the double doped materials decreases as the larger dopant ion concentration increases. Sm-doped ceria also displays a higher conductivity compared to La-doped ceria [1]. This information explains why Ce-4%Sm-2%Y displays the highest conductivity of the double doped ceria samples.

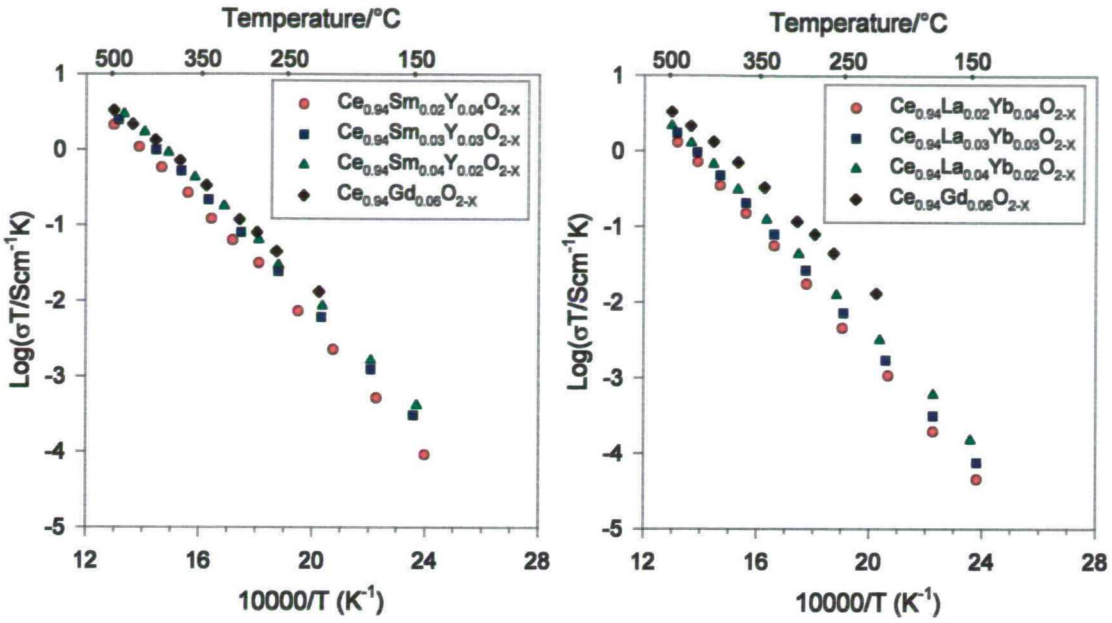


Fig.13.5. Arrhenius plots of the bulk conductivity, obtained by impedance spectroscopy, for $Ce(Sm,Y)O_2$ and $Ce(La,Yb)O_2$, both showing a reference CGO (see legends).

It was shown in chapter 6 that both Sm and Gd doping in ceria produce similar bulk conductivities and it is therefore, not surprising that the highest Sm-doped sample has a conductivity similar to that of the reference CGO.

The curvature observed in chapter 12 for the bulk conductivity in CGO at around 350°C, is also found in all double doped compositions. The gradient above 350°C is again lower and it is thought that this also represents the transition from associated to unassociated behaviour of the defects. The values of the low and high temperature activation enthalpies are recorded in Table 13.3. The results presented in chapter 12 showed that for dopant concentrations below 6mol%, the high temperature activation enthalpy represented the migration enthalpy of oxygen ions in ceria. By simply subtracting the high temperature activation enthalpy from the low temperature value, a measure of the association enthalpy is obtained (also shown in Table 13.3).

The low association enthalpies calculated in Table 13.3 suggest that only simple associates are present. The association enthalpy for the Sm-Y doped ceria decreases as the Sm concentration increases as predicted earlier. The same trend is not observed for the La-Yb doped ceria, which suggests that the high temperature activation enthalpy

does not represent entirely unassociated defect behaviour. Inspection of the low temperature activation enthalpies shows a clear trend towards lower enthalpies as the larger dopant concentration increases.

Composition	Bulk E_a (<350°C)/eV	Bulk E_a (>350°C)/eV	Association Enthalpy (eV)	G.B. E_a/eV
$Ce_{0.94}Sm_{0.02}Y_{0.04}O_X$	0.85	0.68	0.17	0.95
$Ce_{0.94}Sm_{0.03}Y_{0.03}O_X$	0.82	0.72	0.10	0.92
$Ce_{0.94}Sm_{0.04}Y_{0.02}O_X$	0.77	0.68	0.09	0.94
$Ce_{0.94}La_{0.02}Yb_{0.04}O_X$	0.85	0.77	0.08	1.03
$Ce_{0.94}La_{0.03}Yb_{0.03}O_X$	0.83	0.75	0.08	0.98
$Ce_{0.94}La_{0.04}Yb_{0.02}O_X$	0.79	0.71	0.08	1.04
$Ce_{0.94}Gd_{0.06}O_X$	0.70	0.53	0.17	1.23
$Ce_{0.9}Sm_{0.05}Y_{0.05}O_X$	0.81	0.68	0.13	1.01

Table 13.3. Calculated values for the low and high temperature bulk activation enthalpies, the association enthalpy and the grain boundary activation enthalpy.

From the data in this analysis it would appear that gadolinia doping in ceria produces the lowest local lattice strain in ceria and it seems unlikely that any improvement can be made to the bulk conductivity, by using more than one dopant ion type. However, the high temperature bulk activation enthalpy for CGO shown in Table 13.3 is considerably lower than that for Ce-4%Sm-2%Y and inspection of Fig.13.5 indicates that above 500°C, the double doped ceria will have a higher bulk conductivity. The possibility exists that these double doped materials may potentially be better than CGO for application above 500°C.

13.3.2. A.C. Impedance Spectroscopy - G.B. Data

The preparation of all the Rhône-Poulenc samples was identical, with very similar impurity levels (except for Ce-2%Sm-4%Y). Table 13.2 also shows that the densities and grain sizes of the sintered pellets were all very similar. It can be assumed, therefore, that there are equal numbers of grain boundaries encountered during impedance analysis for all samples. The grain boundary correction made in chapter 12 is thus not necessary here to observe the trends in the grain boundary conductivities.

Fig.13.6 shows the Arrhenius grain boundary conductivity graphs for the double doped samples.

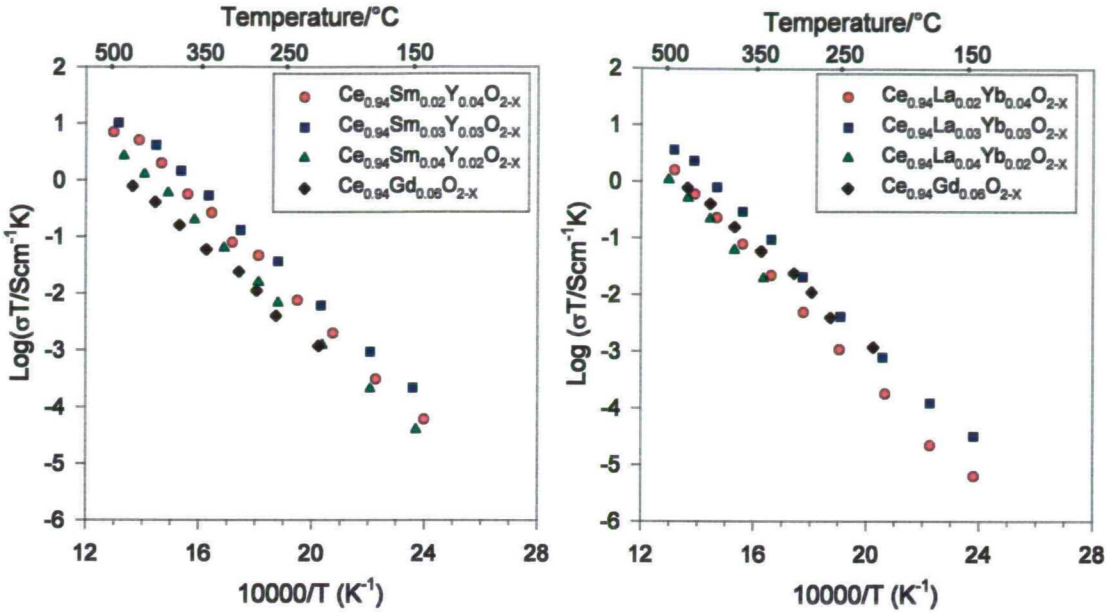


Fig.13.6. Arrhenius plots of the grain boundary conductivity, obtained by impedance spectroscopy for $Ce(Sm,Y)O_2$ and $Ce(La,Yb)O_2$, both showing a reference CGO (see legends).

The grain boundary conductivities show an unexpected result, with the CGO conductivity up to an order of magnitude lower than of some double doped samples. In chapter 12 it was shown that the bulk conductivity for CGO was highest at around 6mol%Gd but the grain boundary conductivity was significantly lower than the bulk. Ideally, it would be better to use this lower dopant concentration if the grain boundary conductivity could be improved because the highest total conductivity would be achieved. In the Sm-Y doped ceria samples it appears that an improvement in the grain boundary conductivity has been made, with only a slight reduction in the bulk conductivity.

Table 13.3 shows the calculated activation enthalpies for the grain boundary conductivities. The activation enthalpies for the grain boundary are higher than those for the bulk, similar to the CGO values reported in chapter 12. This suggests that there is a grain boundary impurity layer which displays a higher resistance compared to the bulk material. The grain boundary thicknesses calculated using equation 6.9, for these

materials ranged between 1-11nm, which is similar to the CGO samples studied in chapter 12.

The maximum grain boundary conductivity, for both Sm-Y and La-Yb doped ceria, occurs when the two dopant concentrations are equal. This result is difficult to interpret using the impedance data alone. If the larger dopant ion is responsible for the increase in the bulk conductivity, then according to the results in chapter 12 for CGO, the grain boundary conductivity should increase with total dopant concentration, over this dopant range. The presence of the second smaller dopant clearly changes the predicted behaviour. An explanation for the improved grain boundary conductivity over that of CGO and the possible causes of the observed maximum are further explored later in this chapter, when an in-depth TEM analysis is performed.

13.3.3. A.C. Impedance Spectroscopy - Total Data

The previous section showed that a significant improvement had been made in the grain boundary conductivity for the Sm-Y doped samples compared to that of CGO. In fact, above 300°C the grain boundary conductivities are higher than the bulk conductivities. The total conductivity reflects this fact by showing a much stronger dependence on the bulk conductivity over the entire temperature range and especially above 300°C. Fig.13.7 shows an Arrhenius plot of the total conductivity for the doubled doped materials. Again, the Sm-Y doped ceria samples show a higher total conductivity compared to the CGO sample. The increase is not as large as that observed for the grain boundary conductivties because of the lower bulk conductivity contribution. The best total conductivity is obtained for the Ce-3%Sm-3%Y sample, which still displays a significant improvement over that of the CGO reference sample.

It must be emphasised again that it is the total conductivity which will ultimately determine the usefulness of an electrolyte for SOFC applications. Considering this fact, it is anticipated that double doping in ceria may play an important role in the development of ceria electrolytes, particularly for the improvements that can be obtained in the grain boundary conductivity.

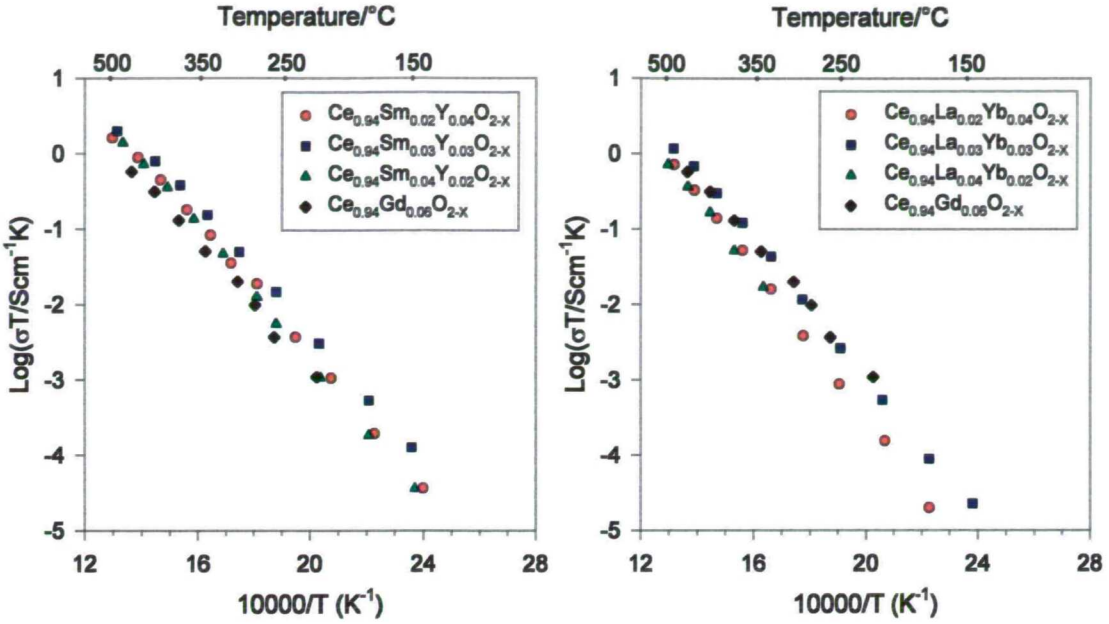


Fig.13.7. Arrhenius plots of the total conductivity, obtained by impedance spectroscopy, for $Ce(Sm,Y)O_2$ and $Ce(La,Yb)O_2$, both showing a reference CGO (see legends).

Chapter 12 suggested that high Gd concentration (26mol% Gd) CGO electrolytes were needed to obtain a sufficient improvement in the grain boundary conductivity, but the bulk conductivity in these samples is lower than the maximum found between 6-10mol%Gd. In the Sm-Y samples the optimum bulk concentration is used and this is combined with a grain boundary conductivity that is similar to the high concentration CGO samples. Clearly, double doping in ceria warrants further attention for electrolyte applications.

In an attempt to explain the improvements in the grain boundary conductivity for the Ce-3%Sm-3%Y sample, a second sample was prepared with a higher total dopant concentration. A 10% doped ceria sample was made with equal concentrations of Sm and Y (5%). Impedance analysis was performed on this sample and compared to the results obtained for the lower concentration double doped ceria. Fig.13.8 shows the comparison between these two material, for the bulk and grain boundary conductivities.

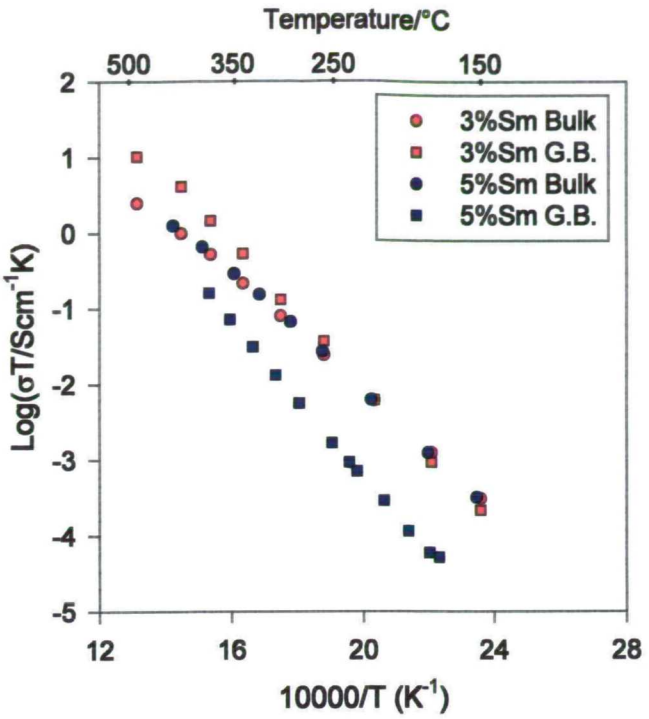


Fig.13.8. Graph of the bulk and grain boundary conductivity, showing a comparison between Ce-3%Sm-3%Y and Ce-5%Sm-5%Y.

A similar improvement in the grain boundary conductivity was expected for the higher doped sample. The total conductivity would then be similar for the two samples. Fig.13.8 shows that the bulk conductivities are similar (as expected), but the grain boundary conductivity for the higher doped material is about an order of magnitude lower. It appears that the grain boundary improvement is not related to the presence of equal concentrations of dopants. Attempts to improve the grain boundary conductivity by altering the ratios of the dopant ions in the higher doped material have not been performed. This information would be necessary before any conclusions could be made for the higher doped sample.

13.3.4. Comparison Between IC and Rhône-Poulenc Prepared Powders

Having produced Ce-6%Gd powders both at IC and Rhône-Poulenc, it is possible to compare the electrical properties of two differently prepared powders. Fig.13.9 shows the Arrhenius plot of the bulk and grain boundary conductivities for both powders.

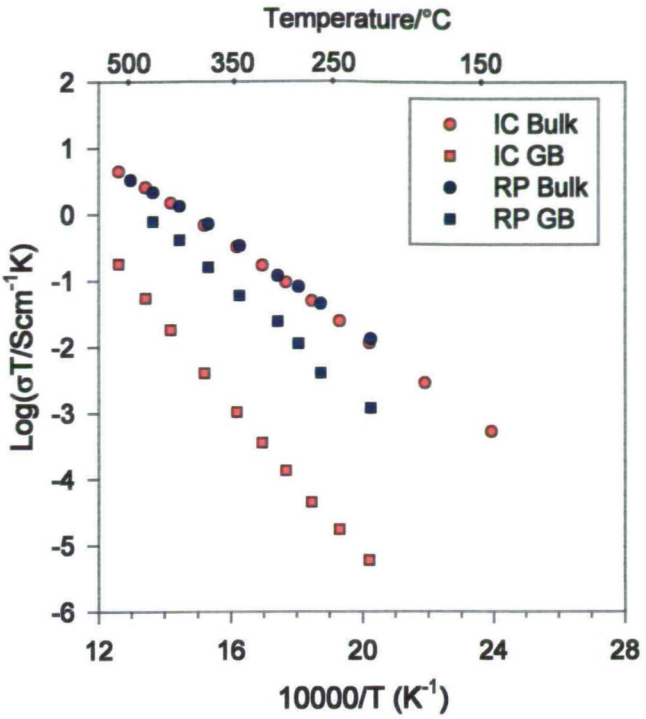


Fig.13.9. Comparison of the electrical properties between IC and Rhône-Poulenc prepared powders for Ce-6%Gd.

The bulk conductivities show excellent agreement, which has been previously observed for other CGO compositions [2]. The grain boundary conductivity is substantially lower for the IC prepared powders and demonstrates the wide variations that can be obtained between industrially and laboratory prepared powders. The increased grain boundary conductivity is not related to the grain size because the Rhône-Poulenc powder actually has a smaller grain size, implying more grain boundaries in these samples. The differences must therefore result from differences in the impurity concentrations. The Rhône-Poulenc powders have a higher purity. Higher purity samples have previously been shown to increase the grain boundary conductivity (see chapter 6). The difference in the grain boundary conductivity gradients (activation enthalpies) also suggests the presence of different concentrations of impurities at the grain boundary.

13.3.5. D.C. Conductivity in Air

The electrical measurements performed so far have used impedance spectroscopy. Due to the dimensions of the samples this has limited the maximum temperature, for which

useful information can be obtained, to around 500°C. To increase the temperature range of this technique, thicker samples with smaller electrode areas are required. A.C. impedance was therefore conducted on a bar shaped sample. The total conductivity of a Ce-3%Sm-3%Y sample could then be measured up to 700°C.

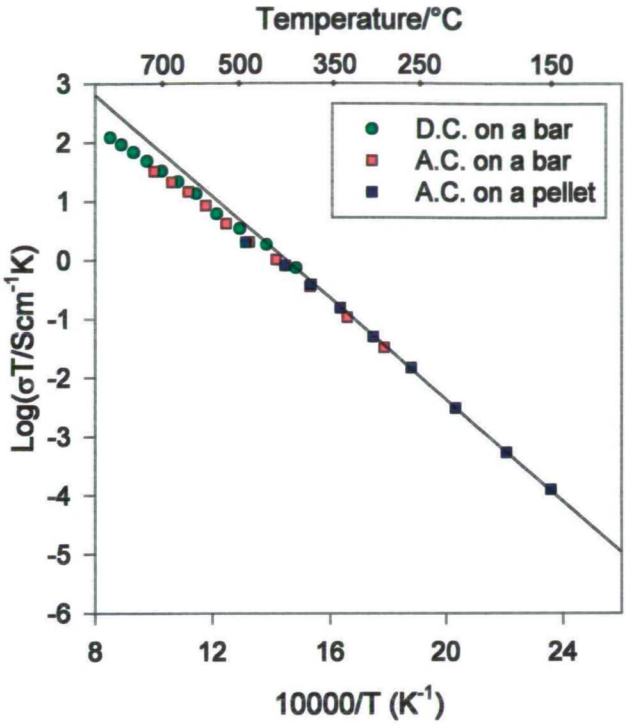


Fig.13.10. Graph to show the good agreement between ac measurements and dc measurement over the temperature range 150°-900°C, on a Ce-3%Sm-3%Y sample. The straight line pronounces the curvature in data at higher temperatures.

The total conductivity is composed of both the bulk and grain boundary contributions. D.C. conductivity measurements provide a direct value of the total conductivity, without having to separate the electrode contributions. Therefore, a good match between the total conductivity obtained between the d.c. and a.c. techniques, confirms a correct fitting of the bulk and grain boundary components in the a.c. technique. D.C. conductivity measurements have been performed on a Ce-3%Sm-3%Y sample in air between 400-900°C, using the equipment described in chapter 10. Fig.13.10 shows the results of the total conductivity obtained from impedance measurements on a pellet and a bar and the d.c. measurements on a bar.

Fig.13.10 show excellent agreement between all three measurements of the total conductivity, which confirms the accurate fitting of the bulk and grain boundary components for the impedance data. A change in gradient around 500°C can be seen on this graph. The gradient at higher temperatures becomes lower and reflects the change from grain boundary dominated conductivity at lower temperatures, to bulk dominated conductivity at higher temperatures. Table 13.3 showed that the bulk activation enthalpy was lower than the grain boundary value and, therefore, a smaller gradient is expected at higher temperatures for the total conductivity. Further discussion concerning the relationship between a.c. and d.c. conductivity is reported in chapter 14.

13.3.6. D.C. Conductivity in Reducing Conditions

The discussions in chapter 12 and this chapter have so far only been concerned with the electrical properties of doped ceria in air. The aim has been to optimise the total conductivity. In a fuel cell atmosphere, the electrolyte must also display resistance to reduction, to prevent the introduction of electronic conductivity, which lowers the efficiency. Probably, the most significant problem for ceria electrolytes is their relatively easy reducibility compared to zirconia electrolytes. Thus a study of any potential ceria electrolyte is not complete without measuring its performance in reducing atmospheres.

Currently, 700°C is the temperature at which ceria electrolytes are being tested for SOFC applications. At this temperature the most reliable results are obtained using d.c. conductivity to measure the total conductivity. Fig.13.11 shows the electrical behaviour of Ce-3%Sm-3%Y and Ce-3%La-3%Yb in reducing conditions, obtained using the equipment described in chapter 10. These results are compared to two standard CGO samples, which are discussed further in chapter 14.

Compared to CGO, the electrolytic domain (discussed in chapter 5) does not seem to have been increased to lower P_{O_2} values for the double doped materials. In addition, an unusual plateau is developed between 10^{-10}-10^{-15}atm for both of the double doped materials. This result implies that there is an additional component to the electrical

conductivity, which is introduced at a P_{O2} above that expected for the reduction of the cerium ion (P(-)~10^{-18}atm). It is possible that measurements were taken before the gas mixtures had reached an equilibrium P_{O2} value, but this is thought to be unlikely because equilibration times of ~24 hours were used. Also, similar results were obtained for both increasing and decreasing P_{O2} conditions.

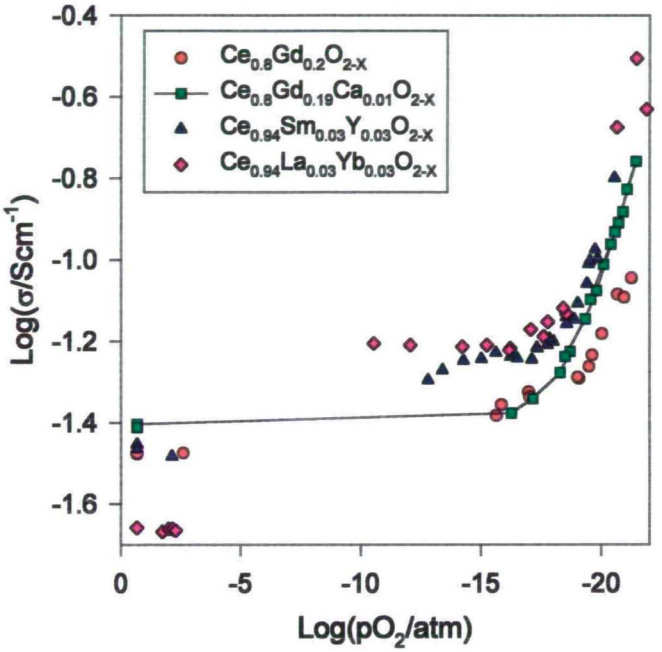


Fig.13.11. Conductivity graph comparing the double doped material from Rhône-Poulenc with the material from IC, in reducing H_2/CO_2 atmospheres at 700°C. The line is used as a guide to show the typical behaviour for doped ceria.

One option for this additional component is that one of the dopant ions can also be reduced. This is thought unlikely because all of the dopant ions are extremely stable and only Sm and Yb are known to exist in two valence states (+2 and +3). It is also possible that there is some degree of protonic conductivity introduced, which would increase the conductivity. The exact explanation for this plateau is still not known but needs to be considered further before these double doped materials are used in SOFC applications.

Using the data in Fig.13.11, a graph of (ionic conductivity, σ_{ionic}/total conductivity, σ_{total}) verses log(P_{O2}) can be constructed, in order to determine the P(-) value discussed in chapter 6. Fig.13.12 shows this graph for Ce-3%Sm-3%Y.

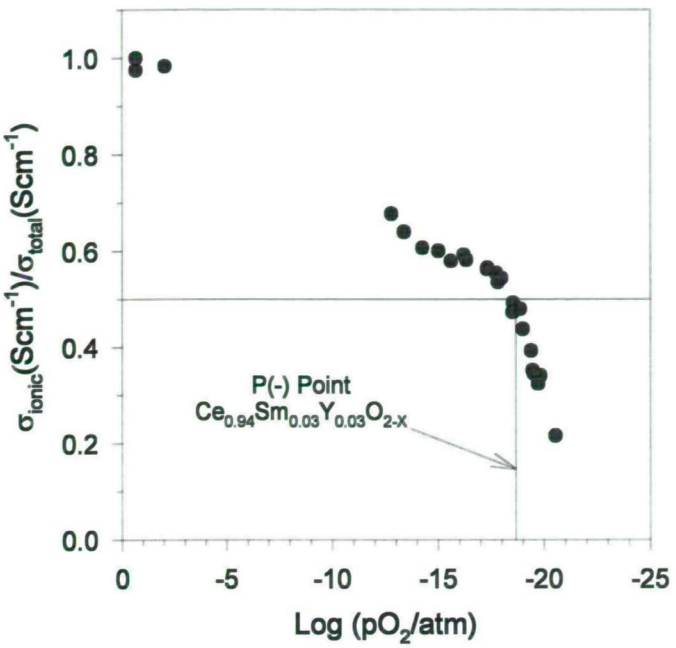


Fig.13.12. Graph showing the P(-) value for a double rare earth doped ceria.

The P(-) value is indicated on the graph at a value of $P_{O_2}=8\times10^{-18}$atm. Although this value is in agreement for that normally calculated for CGO, it is likely that this is larger than the true value due to the plateau observed in Fig.13.11. These results indicate that double doping in ceria does not significantly alter the electrolytic domain, which will restrict the use of these electrolyte materials to low temperature applications (500°C), or applications where higher P_{O_2} values (>10^{-19}atm) are encountered.

13.4. SIMS Data

13.4.1. Isotope Exchange

The procedures for the oxygen isotope exchange experiment have been described in chapter 10. A temperature-time profile, measured from the in-situ thermocouple, for a Ce-6%Gd sample, is shown in Fig.13.13. The corrected temperature and time for anneal using the Killoran technique [3] is also shown in Fig.13.13. The corrected temperatures and times of all the exchange experiments are included in Table 13.4.

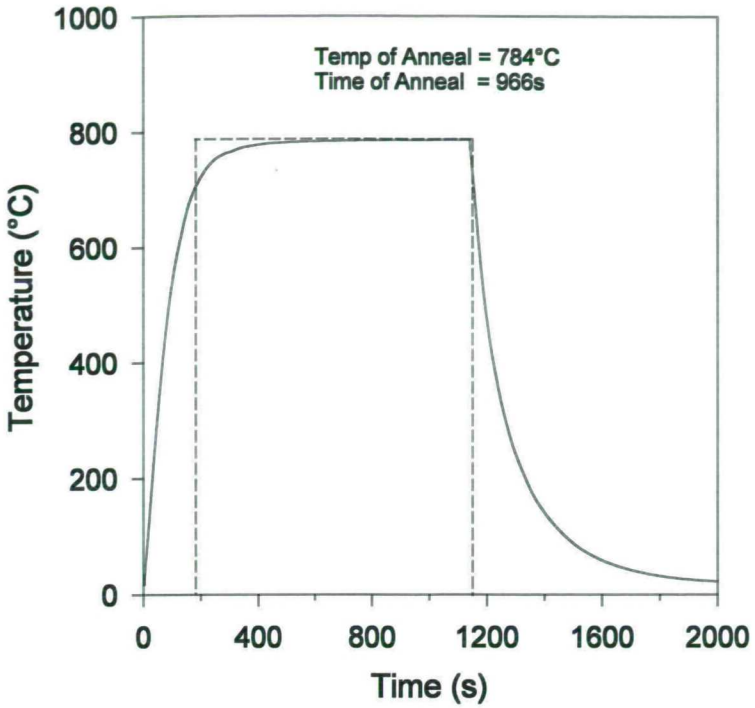


Fig.13.13. Experimental and fitted (dotted line) temperature-time profiles for the $^{18}O/^{16}O$ isotopic exchange of $Ce_{0.94}Gd_{0.06}O_{2-x}$.

The concentration of ^{18}O in the ^{18}O enriched gas (C_g) was measured before the anneal at 80.0%, using a mass spectrometer. The background concentration of ^{18}O in the sample prior to the anneal (C_{bg}) was assumed to be 0.2%. This data is required to obtain a fit to the diffusion profiles discussed in the next section.

Composition	Temperature/°C (±1°C)	Time of anneal/s (±5s)
$Ce_{0.94}Gd_{0.06}O_{2-x}$	784	966
$Ce_{0.94}Sm_{0.03}Y_{0.03}O_{2-x}$	772	942
$Ce_{0.94}La_{0.03}Yb_{0.03}O_{2-x}$	772	942

Table 13.4. Temperatures and corresponding times for $^{18}O/^{16}O$ anneals for several Rhône-Poulenc materials.

13.4.2. Diffusion Profile Measurements

The SIMS linescanning technique was used to measure the concentration of ^{16}O and ^{18}O isotopes in the exchanged samples, as described in chapter 10. The raw data were converted to a normalised ^{18}O isotope ratio, C′(x), using equations 10.4 and 10.5 and

plotted against the linescan length to show the ^{18}O diffusion profile in each sample. The tracer diffusion coefficient and surface exchange coefficient are obtained by fitting the data to the solution of the diffusion equation (10.5), by a non linear least squares fit, using the assumptions described in chapter 10. The experimental and least squares fitted profiles for $Ce_{0.94}La_{0.03}Yb_{0.03}O_{2-X}$ are displayed in Fig.13.14. The linescan length has been adjusted because it was assumed that the start of the profile is at the point of maximum value for C′(x), on the exchanged surface.

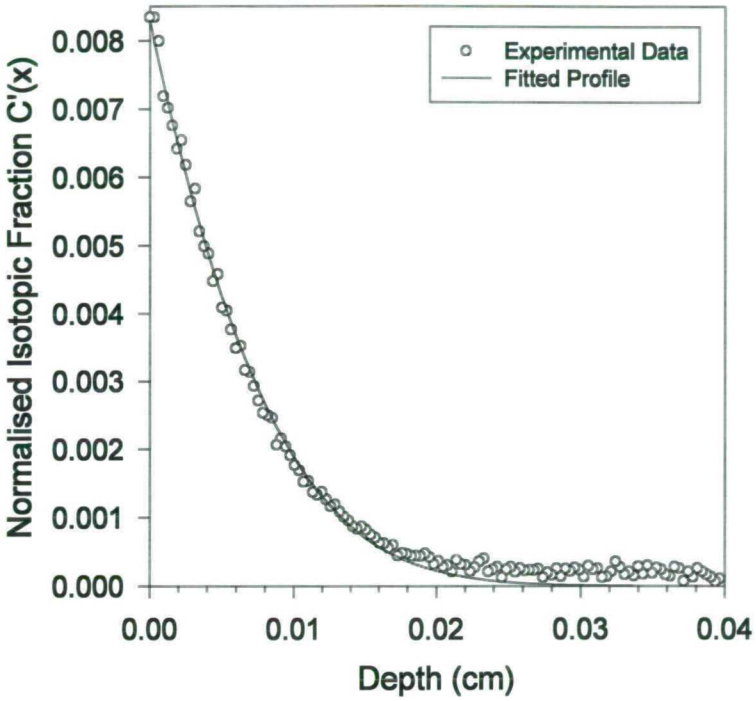


Fig.13.14. Experimental diffusion profile for $Ce_{0.94}La_{0.03}Yb_{0.03}O_{2-X}$ and the least squares fit of this data to equation 10.5.

It can be seen that the shape of the fitted data is similar to the experimental profile, which indicates bulk diffusion is being measured. The concentration of ^{18}O at the surfaces of all the samples studied is low and only slightly above the natural isotopic background. Consequently, all three samples displayed some degree of scattering in their diffusion profiles, as a result of poor counting statistics.

A measure of the quality of the data obtained by SIMS linescans is how closely the measured and fitted profiles agree. The tail of the experimental diffusion profile in Fig.13.14 does not reach zero, i.e. background ^{18}O concentration, but remains at a

constant value just above zero. This may indicate the presence of faster diffusion paths, such as grain boundaries, or pores, which extends the ^{18}O profile further into the sample than expected for bulk diffusion. The microstructural results shown in section 13.2 indicate high density samples, with only a small degree of closed porosity. The small deviation from the background concentration (0.2%) for this sample, indicates that the true background concentration in this material may be slightly higher. A diffusion depth profile was therefore performed on an unannealed sample to measure the true background ^{18}O concentration. It was found, as expected, that the background ^{18}O concentration was slightly higher at 0.22%. This confirms that the tail obtained in Fig.13.14 is only a SIMS artifact and that the background ^{18}O concentration had been reached. From this data, it can be assumed that only bulk diffusion is being measured in this sample. All samples displayed this tail behaviour but showed good fits to the beginning of each profile. The diffusion coefficients obtained from the regression analysis may therefore be an overestimate of the true bulk value. The values obtained from the SIMS measurements, for the tracer diffusion coefficient and surface exchange coefficient in each sample, are given in Table 13.5.

Material	Temp/°C	D_T/cm^2s^{-1}	k/cms^{-1}	D^*/cm^2s^{-1}	D_σ/cm^2s^{-1}	H_R	f_c
$Ce_{0.94}Gd_{0.06}O_{2-X}$	784	1.55e-7	3.57e-8	2.38e-7	7.52e-8	2.06	0.32
$Ce_{0.94}Sm_{0.03}Y_{0.03}O_{2-X}$	772	3.21e-7	2.83e-8	4.94e-7	1.61e-7	2.00	0.33
$Ce_{0.94}La_{0.03}Yb_{0.03}O_{2-X}$	772	5.84e-8	5.83e-8	8.98e-8	1.07e-7	0.55	1.19

Table 13.5. Tracer diffusion coefficients, D_T, surface exchange coefficients, k, self-diffusion coefficients, D*, conductivity diffusion coefficients, D_σ, Haven ratios, H_R and conductivity correlation factors, f_c, for several RP materials.

Table 13.5 also shows the calculated values for the oxygen self-diffusion coefficient and the conductivity diffusion coefficient (converted from bulk impedance conductivity measurements at the respective temperatures), using the equations described in chapter 5. The results obtained for D* and k are displayed in Fig.13.15 and compared to the results of Manning et al. [4] who analysed a Ce-10%Gd sample.

The first observation that can be made about this data, is that the oxygen self-diffusion coefficients decrease in the order: $Ce(Sm\text{-}Y)O_2$>$Ce(Gd)O_2$>$Ce(La\text{-}Yb)O_2$. This order is similar to that found for the bulk electrical conductivity (at the same temperature),

where the Sm-Y doped samples displayed the highest conductivities. When the Ce-10%Gd data are analysed a change in this trend is seen. The bulk conductivity of Ce-10%Gd is similar to of Ce-6%Gd but the diffusion data shows a higher diffusion coefficient for the Ce-6%Gd material.

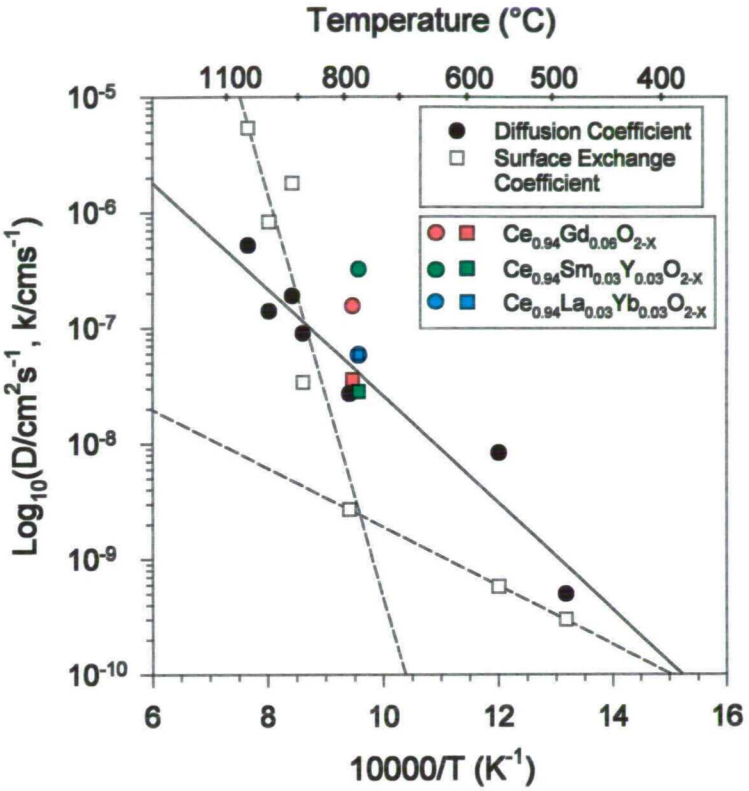


Fig.13.15. Arrhenius plot of the self-diffusion coefficient, D*, and the surface exchange coefficient, k, for several RP materials, compared to a Ce-10%Gd sample measured by Manning et al. [4] (black circles and white squares). The straight lines show trends in the data.

The conductivity diffusion coefficients (D_σ) for the three samples, show conflicting data compared to the tracer diffusion coefficients. It has been shown in previous publications [5], that the diffusion coefficients converted from electrical conductivity measurements are normally higher than those obtained by direct diffusion measurements. This difference is expected because of the relative magnitudes of the correlation factors, f_d and f_c. Above 700°C it is assumed that complete dissociation of defects has occurred, where f_d=0.65 and therefore the Haven ratio becomes less than unity. The difference between D_T and D_σ could be due to electronic conductivity but is more likely to be the result of dipoles which will reorient in an ac field, contributing an

electrical conductivity but not to the bulk diffusion process. This reorientation of dipoles has been discussed previously by Weller and Schubert [6]. It is possible that some defect clusters remain at high temperatures, forming the dipoles that increase the conductivity.

It is interesting to mention here that Fig.13.10 shows an excellent agreement between the d.c and a.c. total conductivity. D.C. conductivity measurements preclude the dipole contribution and thus any substantial dipole component in the a.c. data would result in a poor matching between the two types of data. With such a close matching between a.c and d.c. conductivity data, the dipolar contribution must be small.

The data for $Ce(La\text{-}Yb)O_2$ display the expected higher conductivity diffusion coefficient, with a Haven ratio of 0.55. However, data for $Ce(Sm\text{-}Y)O_2$ and $Ce(Gd)O_2$ show the reverse trend, with a lower D_σ and a Haven ratio ~2. The differences calculated for D_σ and H_R are sensitive to variations in temperature. However, a change in temperature of ±5°C does not significantly alter these results and larger errors in temperature are unlikely. It is more difficult to understand why this should be the case but it is possible that species other than O^{2-} may be involved. If a certain fraction of oxygen ions are being transported as O^- or neutral oxygens, then a lower conductivity would be measured. The discussions in chapter 6 indicated that most of the oxygen vacancies present in ceria, at low temperatures, carry a +2 charge and thus the oxygen ions must diffuse through the lattice as doubly ionised species. At higher temperatures (>500°) it was less clear and the possibility of singly ionised oxygen vacancies was not discounted.

Fig.13.15 also displays the surface exchange coefficients for each sample. Within experimental error, the three Rhône-Poulenc materials have the same k values. These values are at least an order of magnitude greater than the value measured by Manning et al. for Ce-10%Gd and can be explained by the different impurity concentrations present in these powders. LEIS and TEM results from chapter 12 showed that all common impurities segregated to grain boundaries and surfaces of sintered ceramic samples. Therefore, slight differences in impurity elements and concentrations between samples, will lead to different surface layer thicknesses and compositions.

The surface exchange coefficient is very sensitive to the surface composition and large differences in k should be expected when powders from different sources are measured.

The surface exchange coefficient is an important parameter for many catalytic and surface dependant applications. For SOFC electrolytes it is desirable to produce thin films to ensure a high conductivity. However, there is a characteristic electrolyte thickness which determines when the bulk transport controlled reaction, changes to a surface kinetic rate limiting reaction. This electrolyte thickness, l_c can be determined by,

$$l_c = \frac{D^*}{k} \qquad (13.4)$$

For many fluorite based electrolytes, $l_c \approx 100\mu m$ [7]. This implies that fabricating electrolytes less than 100μm thick will not be advantageous unless k can be increased. Methods to increase k include depositing surface active species and increasing the effective surface area using a graded porous structure.

13.5. TEM

Three samples were prepared and analysed using TEM at IC: $Ce_{0.94}Gd_{0.06}O_{2-X}$, $Ce_{0.94}Sm_{0.03}Y_{0.03}O_{2-X}$ and $Ce_{0.94}La_{0.03}Yb_{0.03}O_{2-X}$ (made from Rhône-Poulenc powders). High resolution images of suitable areas for all three samples were obtained, before a series of microprobe analyses and electron diffraction patterns were performed in a linescanning technique, across a number of grain boundaries. Measurements were made within adjacent grains and at the grain boundaries to compare differences in chemical composition and crystal structure.

Fig.13.16 shows a TEM image of a Ce-6%Gd grain structure, over which a linescan analysis was performed. The diffraction patterns for points 1-3 are given in Fig.13.17 and clearly illustrate a ring structure at the grain boundary, which is not present in

either of the adjacent crystalline grains. All grain boundaries displayed these diffraction rings, which indicates the presence of an amorphous phase.

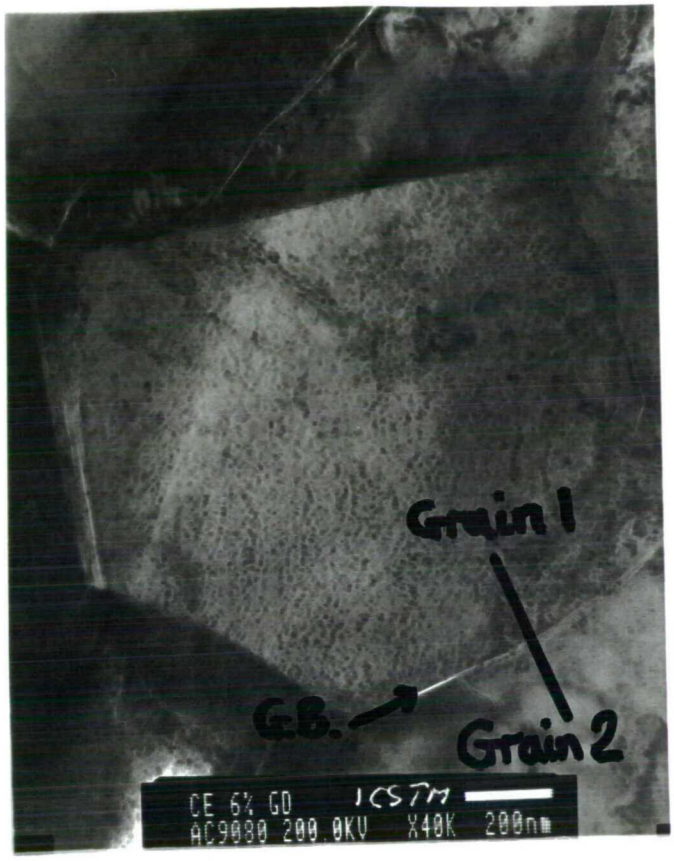
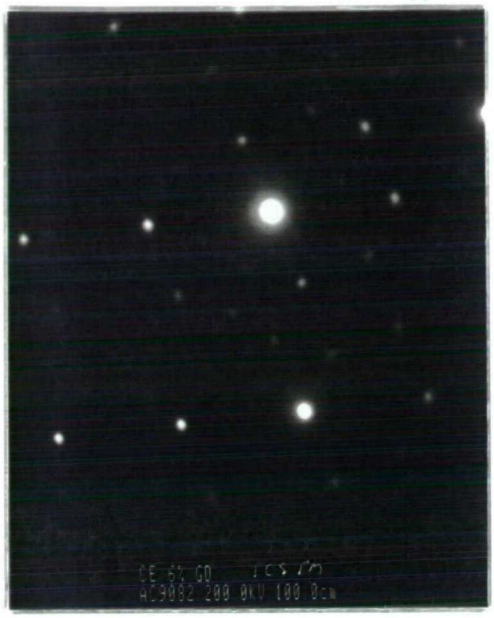


Fig.13.16. Bright field TEM image of a linescanned Ce-6%Gd sample, with the analysed grain boundary indicated by the numbered straight line.

The grain boundary diffraction pattern is a composite image of the patterns from the two grains and any grain boundary phase. By subtracting the diffraction spots of the two grains from the grain boundary pattern, it is possible to determine if an additional phase is present at the boundary. This analysis was performed for a number of grain boundaries and revealed that, in all cases, extra spots were present indicating that a grain boundary phase is likely. The sparsity of the remaining diffraction spots prevented a structural determination of this phase but the data indicates that there may be both a crystalline and an amorphous phase present at the grain boundaries.



Grain 1



Grain 2



Grain Boundary

Fig.13.17. Electron diffraction patterns corresponding to the numbered regions in Fig.13.16, showing amorphous rings at the grain boundary.

Microprobe analysis on this material confirmed the presence of silica at the grain boundaries, at concentrations as high as 6at%. The Ce and Gd concentrations were both found to be variable at the grain boundaries, with values ±4at% of the nominal

composition. No silicon was detectable in the grains, where the dopant concentration was approximately 6at%.

The double doped materials displayed a different behaviour to the Gd doped ceria. Fig.13.18 shows a high resolution image of a Ce-3%La-3%Yb sample and indicates the position of the linescanned grain boundary. The diffraction patterns displayed in Fig.13.19 show fully crystalline grains and grain boundaries. There are no amorphous rings visible, which is clearly different to the Gd-doped sample analysed above. Using the procedure described previously to detect the presence of a grain boundary phase, a number of diffraction spots remained after subtraction of the two grain diffraction patterns. Again, insufficient diffraction spots were left to determine the crystal structure of the boundary phase. However, the low intensity and low number of diffraction spots is consistent with a small concentration of impurity phase at the grain boundary and suggests that the grain boundary phase must exist as a thin layer.

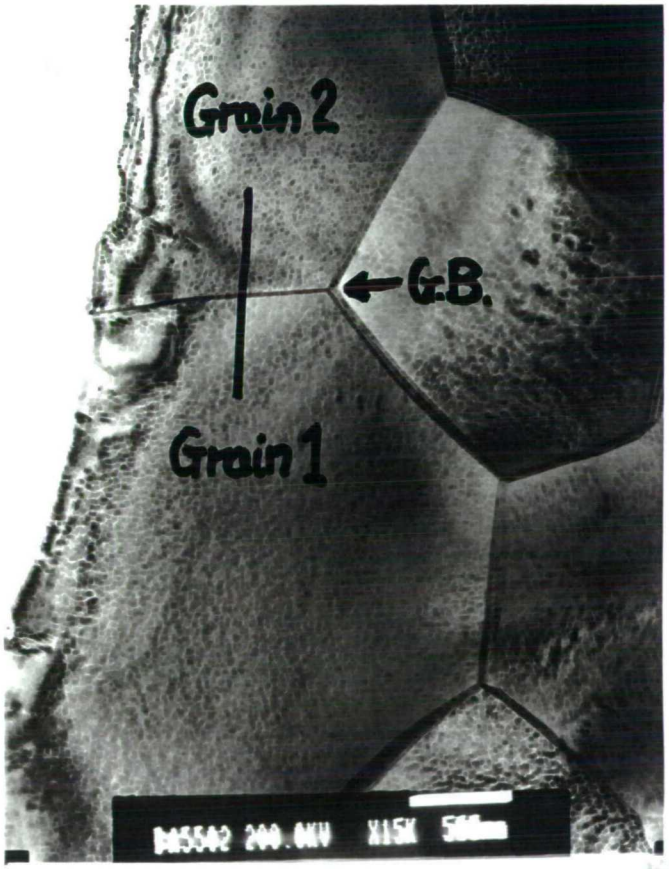


Fig.13.18. Bright field TEM image of a linescanned Ce-3%La-3%Yb sample, with the analysed grain boundary indicated by the numbered straight line.



Grain 1



Grain 2



Grain Boundary

Fig.13.19. Electron diffraction patterns corresponding to the numbered regions in Fig.13.18. There are no amorphous rings visible at the grain boundary.

The HTREM image in chapter 12 demonstrated an impurity grain boundary layer <1nm in thickness and no preferential segregation to triple grain points. The results in this chapter agree with these findings because Fig.13.18 shows a very thin grain

boundary and no visible segregation to triple grain points. The results for the Sm-Y doped ceria sample show similar data to that found above for the La-Yb doped ceria.

The microprobe analysis for the double doped materials was not as straight forward as that for the Gd-doped sample. Silicon was detected at all the grain boundaries analysed, with variable concentrations of up to 3at%, but no silicon was detected within the grains. Due to the similar peak energies of the dopants in each material, it was difficult to separate the dopant signals. The only conclusion concerning the dopant concentration at the grain boundaries that can be made is that the total dopant concentration was usually higher than the nominal composition by approximately 2at%. It should be remembered that the beam diameter was 5nm for all the microprobe analyses and thus the atomic concentrations measured are averaged over the whole beam area. If the grain boundary thickness is assumed to be <1nm, there will be a considerable contribution from the grains. Therefore, the true grain boundary dopant and impurity concentrations may be much higher.

13.6. Conclusions

The results presented in this chapter show that double doping in ceria, can produce materials which have higher conductivities compared to the standard CGO electrolytes currently used. Although it has been shown that a reduction in the global lattice strain does not improve the bulk conductivity, a significant improvement in the grain boundary conductivity can be obtained using Sm-Y doped ceria. Chapter 12 showed that the grain boundary conductivity dominated the total conductivity in lightly doped CGO samples, therefore, improvements in the grain boundary conductivity are more significant than only small improvements in the bulk conductivity.

The TEM results have also shown that CGO samples may contain both an amorphous and crystalline structure at the grain boundaries. The double doped ceria samples appear only to have a crystalline phase present. Silicon was also detected at the grain boundaries of all samples, suggesting that both the amorphous and crystalline phases are likely to contain Si. The CGO samples containing amorphous silica at the grain

boundaries are expected to display poorer conductivities, which is confirmed by the conductivity data. This suggests that the Sm-Y doped ceria is able to incorporate impurities (especially silica) into a crystalline structure which exhibits a higher conductivity compared to amorphous silica.

References

1. G.B.Balazs and R.S.Glass. Solid State Ionics. **76**, 1-2, (1995), 155.
2. J.M.Ralph. Unpublished results.
3. D.R.Killoran. J.Electrochem.Soc. **109**, (1962), 170.
4. P.S.Manning, J.D.Sirman and J.A.Kilner. Solid State Ionics. **93**, (1997), 125.
5. P.S.Manning, J.D.Sirman, R.A.De Souza and J.A.Kilner. Solid State Ionics. **100**, (1997), 1.
6. M.Weller and H.Schubert. Solid State Ionics. **86**, (1992), 569.
7. B.C.H.Steele. Current Opinion in Solid State & Material Science **1**, (1996), 684.

Chapter 14. Ca-Codoping and the Reduction of Electronic Conductivity using Glass Additions

14.1. Introduction

This chapter begins with a discussion of the effects of small additions of Ca to CGO, in an attempt to incorporate impurities at the grain boundaries, such as silica, into a higher conductivity phase. The compositions with the best total conductivities from chapter 12, 13 and 14 are then compared. The remainder of this chapter then concentrates on the reduction of the electronic conductivity in CGO. Firstly, dopants with variable valence are used to create electron traps and a comparison between a number of dopants is tried. Finally, strontium gallate additions to CGO are explored as a possible electron blocking layer at the grain boundary.

14.2. Ca-Codoping in CGO

Impedance spectroscopy is used to analyse the electrical behaviour of CGO samples with small additions of calcia. Calcia was chosen because it would only cause a small reduction in the bulk conductivity (see section 6.9). It was thought that the calcium would segregate to the grain boundary, forming a Ca rich region. Gadolinium and calcium could then form a grain boundary oxide phase, which may be able to incorporate the majority of the impurity ions into its structure. The conductivity of a Gd-Ca-O phase is likely to have a higher oxygen ion conductivity compared to silica or other impurity oxides.

Two Ca doped CGO compositions were prepared, following the method described in chapter 9, and compared to the standard CGO powders. The compositions analysed were: $Ce_{0.9}Gd_{0.1}O_{2-X}$, $Ce_{0.9}Gd_{0.09}Ca_{0.01}O_{2-X}$, $Ce_{0.8}Gd_{0.2}O_{2-X}$ and $Ce_{0.8}Gd_{0.19}Ca_{0.01}O_{2-X}$.

Fig.14.1 shows an impedance spectrum for these compositions measured at 250°C. The impedance spectrum shows that although the bulk resistance of the Ca doped samples has increased a little, the grain boundary resistance has decreased considerably. The bulk and grain boundary resistances in the Ca doped CGO samples are also similar in magnitude over the temperature range used in these measurements.

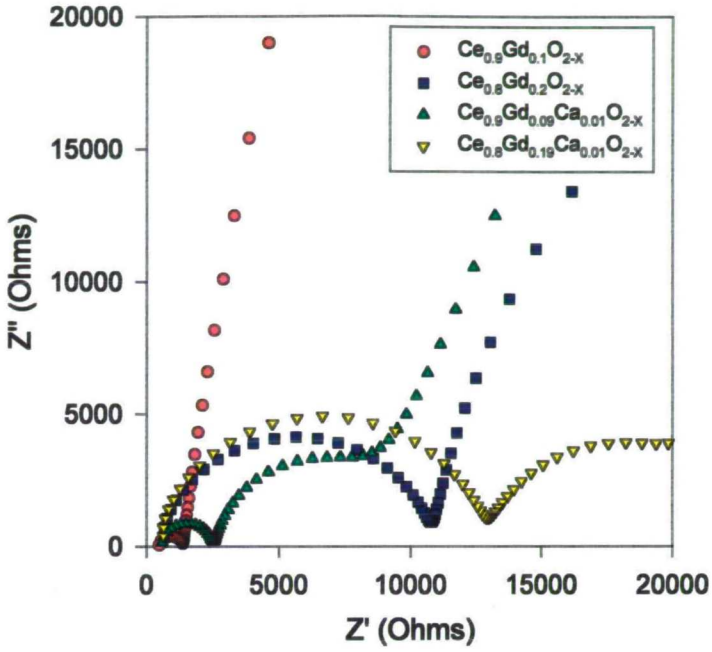


Fig.14.1. Impedance spectrum comparing the Ca doped CGO samples to the standard CGO compositions at 250°C.

From the impedance spectra, the Arrhenius plots for the bulk and grain boundary conductivities can be constructed. Fig.14.2 shows these Arrhenius plots, which compare the conductivities of the Ca doped and undoped CGO materials. While the bulk conductivity has been slightly decreased for the Ca doped samples, there is a significant increase in the grain boundary conductivity for these samples. The largest improvement is obtained for the Ce-9%Gd-1%Ca sample, where an increase of over two orders of magnitude is measured compared to the Ce-10%Gd sample. It must be remembered, that the grain size of this particular sample was shown in chapter 11, to be almost twice the size of the other CGO samples. However, after performing calculations similar to that used in chapter 12, to obtain the true grain boundary conductivity, it is found that the grain boundary conductivity is still around two orders of magnitude higher than that of the standard Ce-10%Gd sample.

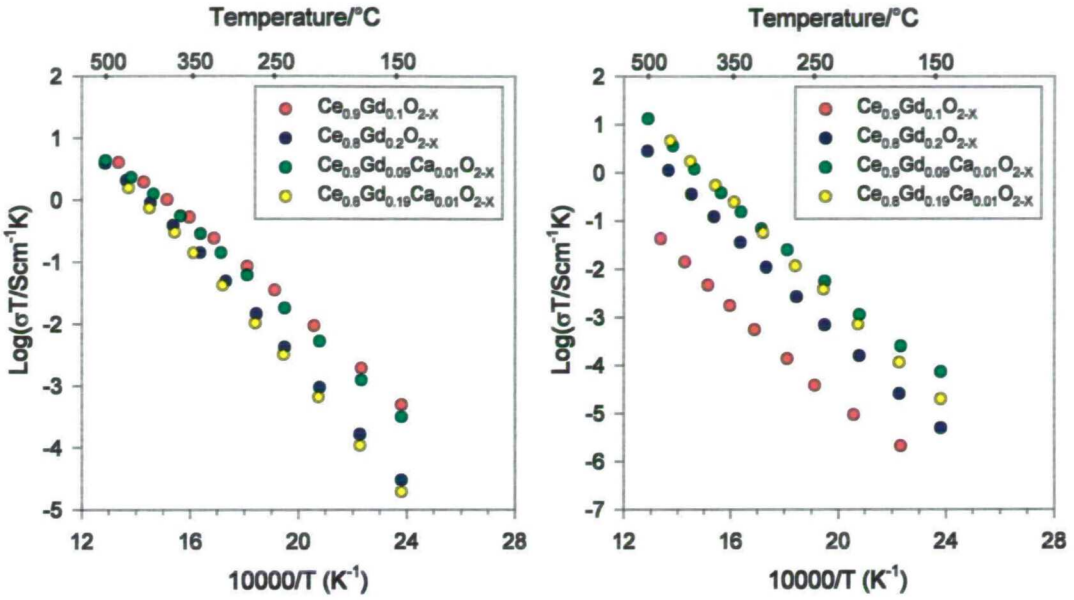


Fig.14.2. Arrhenius plots of conductivity comparing Ca doped and undoped CGO. (A) is the bulk conductivity and (B) is the grain boundary conductivity.

Combining the bulk and grain boundary conductivities to obtain the total conductivity (Fig.14.3), it is clear that the Ce-9%Gd-1%Ca sample has the highest conductivity, closely followed by the Ce-19%Gd-1%Ca sample. The improvement in the Ce-19%Gd-1%Ca sample over the Ce-20%Gd sample is not so great because the grain boundary conductivity also increases with Gd concentration (as shown in chapter 12).

The LEIS data shown in chapter 12, suggests that there is considerable segregation of Ca to high energy surfaces and so the earlier assumption of the formation of a calcium rich phase appears probable. The LEIS data also revealed segregation of Na and K. The TEM data in chapter 13 showed that dopant segregation to grain boundaries occurred and thus the formation of a relatively high conducting Gd-Ca-O phase is possible and may additionally contain some Na or K. The low concentrations of Si detected at the grain boundaries using both LEIS and TEM analysis, suggests that silica is only partly responsible for the high grain boundary resistances observed in the standard CGO samples.

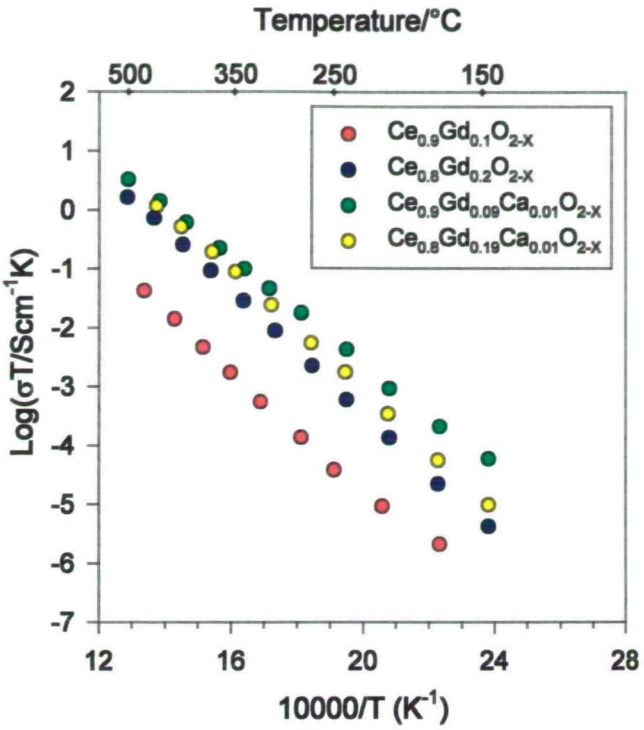


Fig.14.3. Arrhenius plot for the total conductivity of Ca doped and undoped CGO.

The addition of a small quantity of calcia to improve the grain boundary conductivity in CGO, may be of importance industrially because it would allow the use of cheaper, lower purity starting precursors. The Ca additions also permit the use of the low Gd concentration materials, which display the higher bulk conductivities. Chapter 13 showed that it was difficult to improve upon the bulk conductivities of CGO and thus increasing the grain boundary conductivity becomes more important.

Similar to chapter 13, the total conductivity of these samples was measured by d.c. conductivity in air, to ensure that the bulk and grain boundary components were fitted correctly. The d.c. conductivity also permits the conductivity of these materials to be observed at higher temperatures. Fig.14.4 shows the d.c. and a.c. conductivity of Ca doped and undoped CGO. The curvature observed in both slopes around 400°C is produced by the crossover from grain boundary dominated behaviour at the lower temperatures, to bulk dominated behaviour at the higher temperatures. This is further confirmed by the gradient of the high temperature data approaching that measured for the bulk. It is clear that there is excellent agreement between the a.c. and d.c. data, which indicates that the impedance data has been fitted correctly.

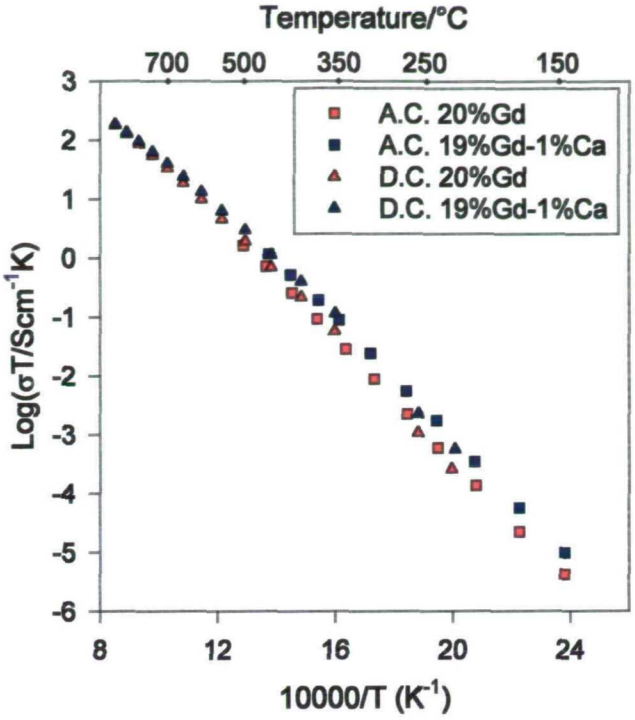


Fig.14.4. Comparison of the total conductivity data obtained in air from a.c. and d.c. techniques, for Ca doped and undoped CGO.

Chapters 12, 13 and 14 have shown that by selecting the correct dopant type and concentration it is possible to optimise the total conductivity in ceria. It is interesting to now compare the total conductivities of the best materials from each chapter, to help decide which doping scheme is the best. Fig.14.5 shows the Arrhenius plot for the total conductivity of the best conducting materials.

The highest conductivity is obtained by the Ce-3%Sm-3%Y sample, which is only slightly higher than the Ca doped CGO sample (Ce-9%Gd-1%Ca). The high Gd doped CGO sample has a significantly lower total conductivity. In all three samples, the grain boundary conductivity becomes greater than the bulk conductivity above 350°C. Therefore, at higher temperatures the bulk conductivity dominates. The bulk conductivity was shown in chapter 12, to reach a maximum between 6-10mol% dopant and thus the higher total conductivity measured for the two lower dopant concentration samples in Fig.14.5 (6 and 10mol%), confirms the dominance of the bulk conductivity. From these results it is suggested that in electrolyte applications, it is desirable to try and improve the grain boundary conductivities for the highest bulk conducting

compositions because these materials ultimately produce the highest total conductivities, especially at low temperatures.

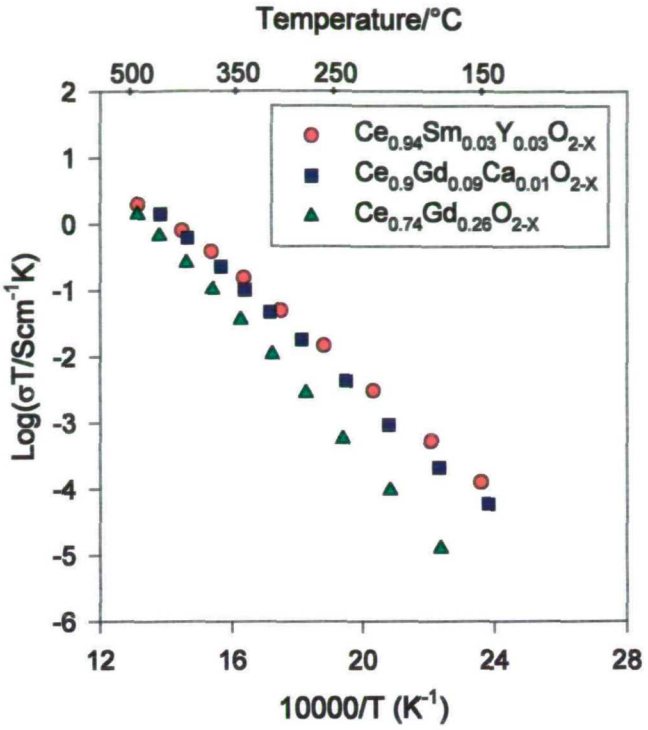


Fig.14.5. Comparison of the total conductivities for the best conductors in each material group studied.

14.3. Electron Trapping Using Variable Valent Dopants

Attention in this section is now focused on the behaviour of ceria electrolytes in reducing conditions and the introduction of electronic carriers. Firstly, the conductivity of a standard CGO composition is measured and compared to that of a Ca doped CGO sample. These measurements are then used as a reference level with which to gauge the improvements of new materials. Secondly, the effects of adding multiple valent dopants is explored as a technique for locally trapping electrons at dopant sites. Section 6.13 explains the theory behind this technique in more detail. Initially, the electronic conductivity is measured in air, before analysing the conductivity in reducing conditions.

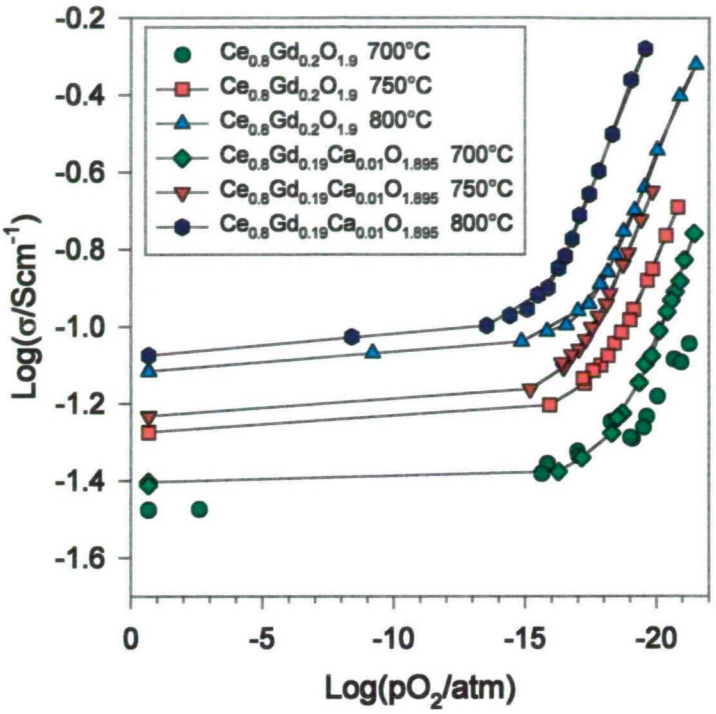


Fig.14.6. Electrical Behaviour of Ca doped and undoped CGO in reducing conditions at three different temperatures.

Fig.14.6 shows the variation in d.c. conductivity as a function of P_{O_2} for Ca doped and undoped CGO, at three temperatures: 700, 750 and 800°C. The electrolytic domain decreases as the temperature is increased because the formation of electrons is thermally activated. It is interesting to note that the Ca doped samples have a slightly smaller electrolytic domain at all temperatures, compared to the standard CGO sample. The gradient of each graph in reducing atmospheres ($>10^{-15}$atm), where the electronic conductivity dominates, was found to be between -1/3 and -1/4. This is in agreement with the predicted gradient of -1/4 calculated in the theory section of chapter 5.

Assuming the ionic conductivity remains constant in Fig.14.6, the value of the conductivity measured at high P_{O_2} can be used as the ionic conductivity. By subtracting this value from the total conductivity, a value for the electronic conductivity can be calculated. Performing this calculation at a fixed P_{O_2} value for each temperature, it is possible to construct an Arrhenius plot for the electronic conductivity. Fig.14.7 shows the Arrhenius plot for both compositions studied in Fig.14.6. The gradient of each curve represents the activation enthalpy for the reduction of ceria, i.e. the activation enthalpy for electronic conduction.

Fig.14.7 displays the calculated activation enthalpies and shows that the Ca doped CGO material displays a higher activation enthalpy. It can be seen that below 700°C, the Ca doped material will exhibit a greater resistance to reduction compared to the standard CGO. This is a significant result because the Ca doped material has already been shown to display higher ionic conductivities at 500°C and thus an increased electrolytic domain at this temperature would make this material very attractive for SOFC applications. For comparison, the value of activation enthalpy for the electronic conductivity obtained by Maricle [1], for Ce-17%Gd-3%Pr was 2.18eV.

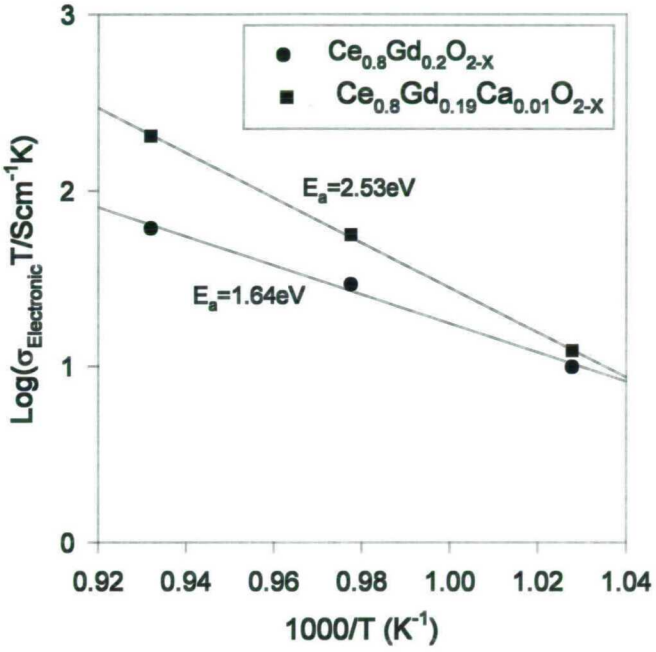


Fig.14.7. Arrhenius graph of the electronic conductivity for both Ce-20%Gd and a Ca doped CGO.

Several multi-valent elements have been considered as dopants, which may act as electron trapping sites in CGO including, Mn, Pr and Fe. It was found that Mn doped samples could not be sintered to a sufficient density for electrical analysis [2] and thus only Pr and Fe doped CGO (supplied by ECN and Rhône-Poulenc respectively) were studied further. Fig.14.8 shows an Arrhenius plot of the bulk and grain boundary conductivities for an Fe and Pr doped CGO, compared to a Ca doped CGO. At 500°C there is very little difference between the conductivities of the three materials. This result suggests that the small addition of a second dopant, has again increased the grain boundary conductivity compared to a standard CGO composition and further supports

the idea, introduced earlier in this chapter, that the second dopant forms a relatively good ionically conducting phase at the grain boundary.

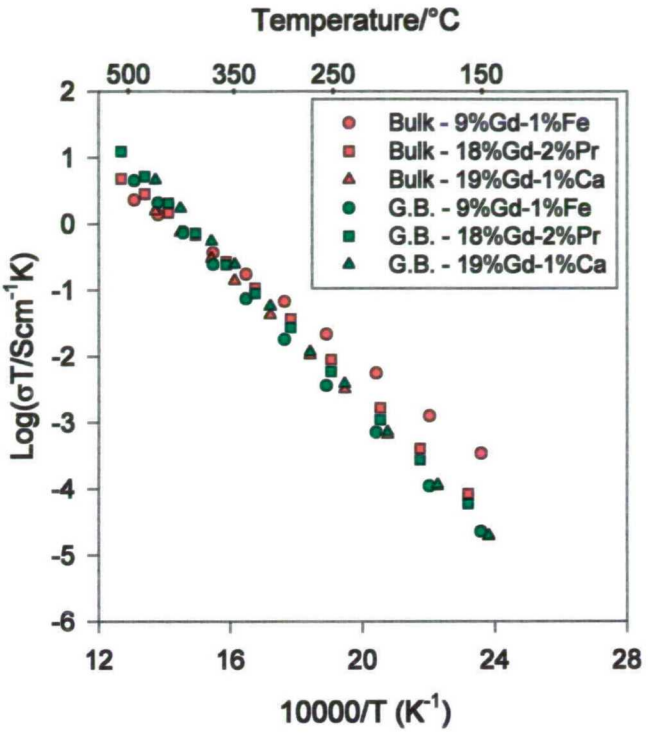


Fig.14.8. Arrhenius graph showing the bulk and grain boundary conductivities for a number of codoped CGO samples.

The results of Rudkin [3] at Imperial College have previously shown that the Pr doped CGO has had no significant effect on the width of the electrolytic domain to the standard CGO. Fig.14.9 shows the variation of conductivity with P_{O_2} at 700°C, for the Fe doped CGO compared to the reference samples measured earlier. Again, it is clear that there is no marked improvement in the width of the electrolytic domain.

The P(-) value for these three materials has been calculated using the method described in chapter 13 and are compared in Fig.14.10. It can be seen that the codoped samples produce no improvement in the P(-) value (10^{-19}atm for Ce-9%Gd-1%Fe and 5×10^{-19}atm for Ce-19%Gd-1%Ca) over that of the standard CGO (10^{-20}atm). These results suggest that it is not possible to reduce the electronic conductivity for CGO in reducing conditions, by creating local sites to trap the electrons. However, these dopants have produced some interesting improvements in the grain boundary conductivities in air, which need to be explored further.

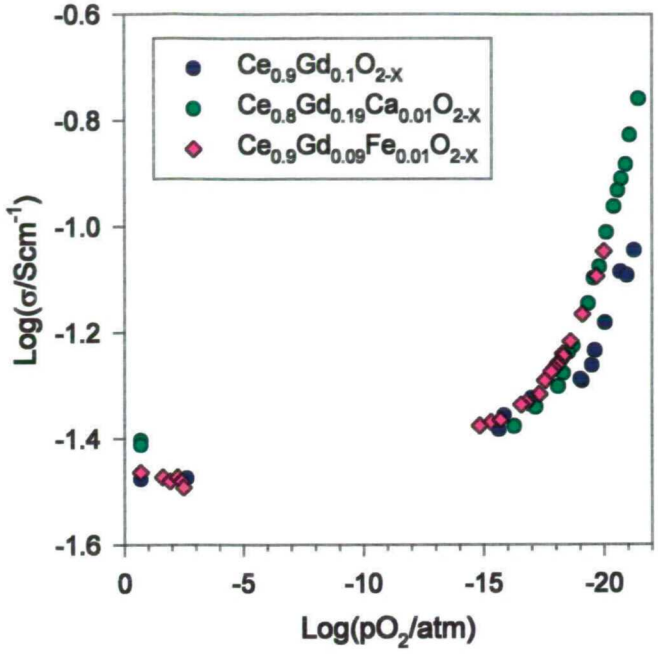


Fig.14.9. Comparison of the total conductivity of several doped ceria samples in reducing conditions at 700°C.

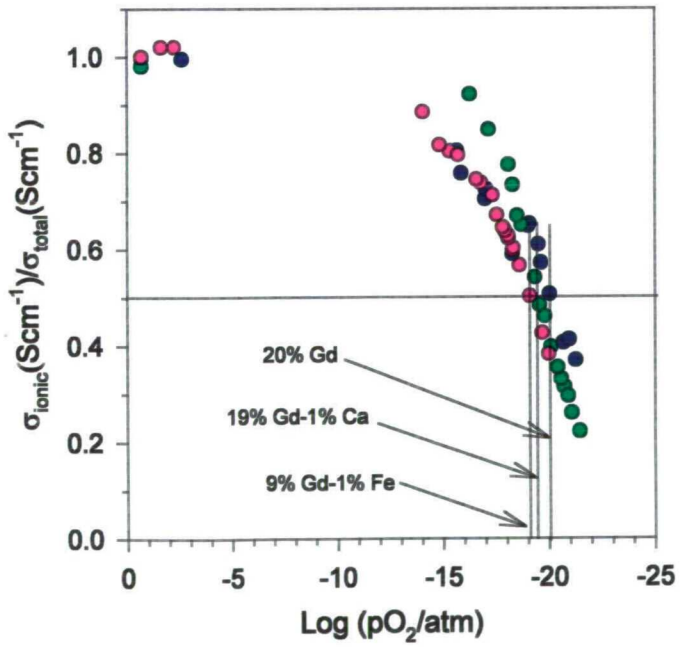


Fig.14.10. Graph showing the P(-) values calculated at 700°C, for the samples analysed in Fig.14.9.

14.4. Effect of Strontium Gallate Additions

Chapter 8 discussed the possible benefits of adding strontium gallate, either in its glassy or crystalline form to CGO. This section explores the areas in which it is thought that the strontium gallate additions may be beneficial, i.e. reduction of the sintering temperature, increased grain boundary ionic conductivity and decreased electronic conductivity in reducing atmospheres.

14.4.1. Preparation

The strontium gallate glasses were prepared, by first, adding the appropriate quantities of the precursors, $Sr(NO_3)_2$ and Ga_2O_3 to form $Sr_2Ga_2O_5$. The mixture was initially heated to 500°C, to permit the nitrate to decompose. The temperature was then increased to 1350°C to obtain a melt. The melt was then quenched by pouring onto a hot plate, to avoid explosive shattering.

The ceramic form of strontium gallate was prepared using a similar route, except the mixture was only heated to 1210°C for 5hrs and then furnace cooled. The XRD pattern for the ceramic strontium gallate powder showed that the required composition ($Sr_2Ga_2O_5$) had disproportionated into a predominantly $Sr_3Ga_4O_9$ phase, as found by Feng [4].

14.4.2. Conductivity Measurements

Impedance analyses was then performed on both forms of strontium gallate (SGO) to obtain values for their conductivity. A piece of the strontium gallate glass was shaped into a square section and platinum electrodes applied and dried under a UV lamp. The strontium gallate crystalline powder was pressed into a pellet and sintered at 1210°C for 12hrs. It was found that pellets sintered at 1230°C and above, melted, which suggests that the eutectic temperature measured by Kobzareva [5] may be too high. Platinum electrodes were then applied and baked on at 950°C for ½hour. Fig.14.11 shows the Arrhenius conductivity graph for both the ceramic and glass strontium

gallates, compared to a standard Ce-10%Gd (the boron doped strontium gallate sample is explained below).

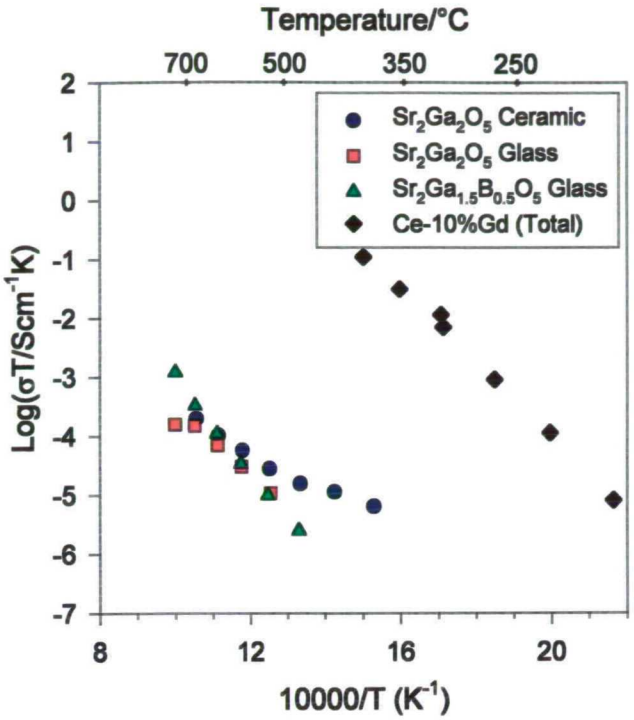


Fig.14.11. Arrhenius graph of the conductivity of glassy and crystalline strontium gallate. The total conductivity of Ce-10%Gd is also shown for comparison.

The conductivity of both the glass and ceramic strontium gallate (SGO) were much lower than the total conductivity of a Rhône-Poulenc Ce-10%Gd. This was expected because glasses are known to be poor oxygen ion conductors (see chapter 8) and the ceramic strontium gallate had disproportionated from the desired brownmillerite phase. To stabilise the brownmillerite phase, which is thought to have a reasonable oxygen ion conductivity, it is necessary to force the gallium ion into octahedral sites in the lattice. It was suggested that this could be achieved by the correct doping [6] and initially boron was selected. The boron ion is smaller than the gallium ion and will therefore prefer the tetrahedral sites and force the gallium ion into the octahedral sites. In addition, B_2O_3 is a common fluxing agent in glasses and may lower the melting point of the glass.

Boron oxide was thus added to SGO to prepare three different glass compositions: $Sr_2Ga_{1.8}B_{0.2}O_5$, $Sr_2Ga_{1.5}B_{0.5}O_5$ and $SrGaB_{0.5}O_{3.25}$. Only the first two compositions

formed glasses and so these were investigated further. Fig.14.11 shows the conductivity of a boron doped SGO glass. Again the conductivity of this glass is low compared to the reference CGO. The conductivity of the ceramic form will be discussed later. Attempts to make an SGO glass with other dopants has been performed by Bailly [7], using Sc and Zr-Mg and Wistance [8], using B-Y and B-Zr. In all cases it was not possible to produce a glass.

To determine the stability of these glasses, it was necessary to measure the glass transition temperature, T_g. This analysis was performed by Mr.E.Bailly, using DTA (explained in chapter 10), on SGO and boron doped SGO. The glass transition temperature for all glasses was found around 860°C. It was also found that the melting points were lower than that reported by Kobzareva [5], ranging from 1180°C for the boron doped SGO, to 1240°C for SGO. This agrees with the observation made earlier, that ceramic samples melted above 1230°C. The longer term stability of these glasses was tested by placing a piece of each glass into a furnace at a temperature of 700°C. After 161hrs at this temperature all samples showed areas of devitrification, which suggests the operation temperature for these glasses must be kept below 700°C.

The low conductivities of the glass and ceramic SGO samples does not exclude these materials as additives to CGO because the advantages of reducing the electronic conductivity with these additions and lowering the sintering temperature, would be acceptable, even if there was a slight decrease in the ionic conductivity. To assess the behaviour of the three SGO additions when added to CGO, a standard Ce-10%Gd powder from Rhône-Poulenc was mixed with 3mol% additions of the ceramic and glass SGO. The glass SGO was first ground to a fine powder before addition. The powders were mixed in a shear mixer for several hours, before uniaxial pressing to form pellets. No isostatic pressing was performed. Three sintering conditions were employed, as shown in Table 14.1.

For all three sintering conditions the density of the pellets was <95% of the theoretical density. The ceramic SGO addition to CGO achieved the highest density for the samples slow cooled from 1200°C (93%), while the SGO glass addition achieved the highest density for the other two sintering conditions (90% for the slow cool from

1300°C and 89% for the quenched samples). It was therefore decided to electrically test two SGO doped CGO samples: a ceramic SGO addition which had been slow cooled and a SGO glass addition which had been quenched. Platinum electrodes were applied to the samples and baked on at 500°C for ½hour. Fig.14.12 shows the Arrhenius conductivity plot for the total conductivities of each sample compared to an undoped CGO.

Composition	Type of Cooling after sintering at 1200°C for 6hrs	Type of Cooling after sintering at 1300°C for 6hrs	Type of Cooling after sintering at 1300°C for 6hrs
CGO + SGO (ceramic)	Furnace Cooled	Furnace Cooled	Quench in air
CGO + SGO (glass)	Furnace Cooled	Furnace Cooled	Quench in air
CGO + $Sr_2Ga_{1.8}B_{0.2}O_5$ (glass)	Furnace Cooled	Furnace Cooled	Quench in air
CGO + $Sr_2Ga_{1.5}B_{0.5}O_5$ (glass)	Furnace Cooled	Furnace Cooled	Quench in air

Table 14.1. Sintering and cooling characteristics for the production of SGO doped CGO pellets.

Fig.14.12 shows that above 350°C, the total conductivity of the ceramic and glass additions to CGO, results in a decrease in the conductivity compared to the standard CGO. The bulk conductivity of all samples is very similar and the decrease in total conductivity is entirely related to a decrease in the grain boundary conductivities. It is thought that the mechanical preparation of these samples may be responsible for the low densities and low conductivities measured. If the powders were inhomogeneous, this would result in liquid phase sintering in discrete areas of the sample, while leaving other areas with a low density. The lower density areas could then contribute to the higher resistances measured. It is also possible that the strontium gallate phase itself is responsible for the increased resistance, having seen earlier that this has a high resistance. Below 350°C, the furnace cooled CGO with ceramic SGO powder additions, displayed a higher total conductivity. Again, this result could be explained by considering the grain boundary conductivity.

To prepare more homogeneous samples, SGO was prepared by a wet chemical route and the resulting powder atomised onto the CGO powder. This technique is described in chapter 9. Two pellets were then sintered, one furnace cooled from 1300°C/6hrs and the second quenched from 1300°C/6hrs. Both pellets displayed densities >90%. The total electrical conductivity of these pellets are shown in Fig.14.12.

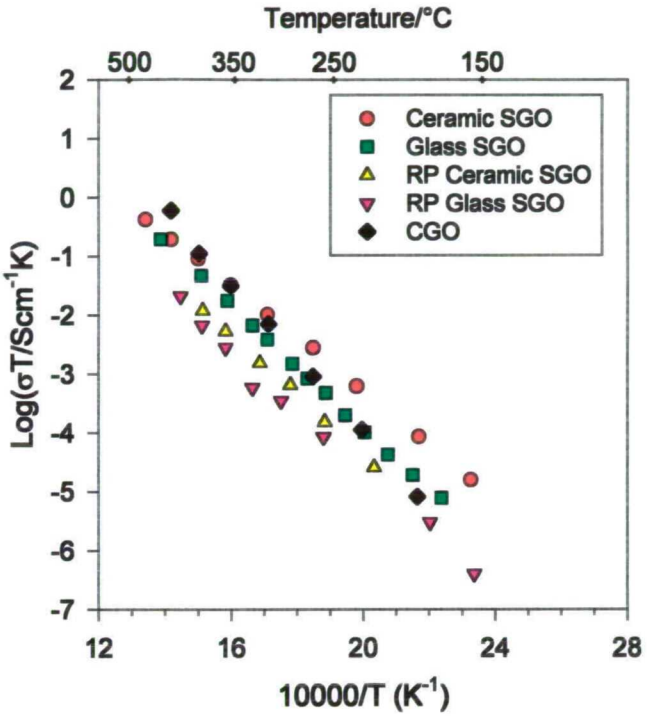


Fig.14.12. Arrhenius graph of the total conductivity of SGO doped CGO pellets, made by mechanical mixing and powder atomisation (RP samples), compared to an undoped CGO.

From Fig.14.12 it appears that for both the mechanically mixed and atomised powders, the quenched samples display the lowest conductivities. It is also clear, that despite having a higher homogeneity and a higher density, the powder atomised samples have a lower conductivity compared to the mechanically mixed pellets. An explanation for this fact is that the low conductivity SGO completely covers the grain boundary in the atomised powders but only partially covers the boundaries in the mechanically mixed pellets. The grain boundary conductivity in the latter pellets would therefore be closer to that of an undoped CGO.

The most important criterion of these additions to CGO, is their ability to reduce the conductivity of electrons, by creating electron blocking layers at the grain boundary. Therefore, the d.c. conductivity of these materials in reducing conditions must be assessed. Two bar samples were prepared, as described in chapter 10, for d.c. analysis: a glass SGO addition to CGO and the powder atomised SGO onto CGO. Both samples were sintered at 1300°C/6hrs before quenching to room temperature. Fig.14.13 shows the d.c. conductivity graph measured at 700°C for these two samples compared to a reference sample measured earlier in this chapter.

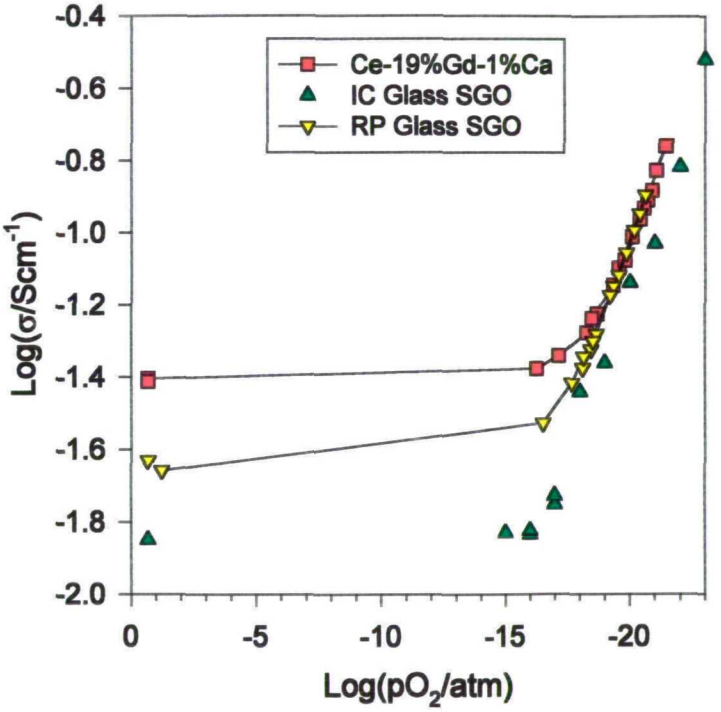


Fig.14.13. D.C. conductivity in reducing H_2/CO_2 conditions for CGO with SGO additions, measured at 700°C. IC powder is mechanically mixed and RP powder has been atomised onto CGO.

Fig.14.13 shows that there is no significant increase in the width of the electrolytic domain and in fact, the P(-) has moved to higher P_{O2}. Surprisingly, the atomised powder sample now displays a higher ionic conductivity compared to the mechanically mixed sample. The higher ionic conductivity has slightly increased the electrolytic domain but it is still less than that for the standard CGO samples measured earlier. The gradient of the two curves at the lower P_{O2} values is approximately -1/5, which is

close to the expected -1/4. These results indicate that the presence of strontium gallate, if at the grain boundaries, does not block the migration of electrons under reducing conditions.

14.5. Conclusions

The Ca doped CGO samples show improved ionic conductivity and reduced electronic conductivity at 500°C and remain promising materials for the electrolyte in SOFC stacks. These results also suggest that variable valence doping does not increase the width of the electrolytic domain, as suggested previously. Finally, the addition of strontium gallate has not shown the same effect as that found in zirconia but further experiments are required to understand the behaviour of this addition in CGO.

References

1. D.L. Maricle, T.E. Swarr and S. Karavolis. Solid State Ionics. **52**, (1992), 173.
2. R.Rudkin. Private Communications.
3. R.Rudkin. Unpublished data.
4. M.Feng and J.B.Goodenough. J.Am.Ceram.Soc. **77**, 7, (1994), 1954.
5. V.P.Kobzareva, L.M.Kovba, L.M.Lopato, L.N.Lykova and A.V.Shevchenko. Russian J.Inorganic Chem. **21**, 6, (1976), 903.
6. C.A.J.Fisher. Ph.D. Thesis. University of Oxford, 1996.
7. E.Bailly and J.M.Ralph. Unpublished data.
8. W.Wistance and J.M.Ralph. Unpublished data.

Section 4

Conclusions

And

Future Work

Conclusions

The performance of doped ceria electrolytes for operation in solid oxide fuel cells has been discussed. The high temperatures required for present SOFC devices necessitates the use of expensive materials to construct a complete system. The review of the literature revealed that ceria based electrolytes show the most promise for low temperature operation (500°C), which would lead to a substantial reduction in the cost of an SOFC system. This thesis has concentrated on both optimising the ionic conductivity of doped ceria, and reducing the electronic conductivity in low P_{O_2} atmospheres.

A number of techniques have been used to study both the bulk material and grain boundaries including, a.c. impedance spectroscopy, d.c. conductivity, transmission electron microscopy, secondary ion mass spectrometry and low energy ion scattering.

Gadolinia is the most common used dopant in ceria because it produces the highest ionic conductivity. It has been found in this work, that the highest total conductivity is achieved at a doping level of 26mol% Gd, which is higher than the Gd concentrations normally used. The total conductivity is dominated by the grain boundary contribution at temperatures <500°C, especially for Gd concentrations below 20mol%. However, the grain boundary conductivity increased for higher Gd concentrations, reaching a maximum at 26mol% Gd. TEM and LEIS measurements have indicated the presence of a crystalline phase at the grain boundaries consisting of a complex Gd-Ca-Na-K oxide structure. The grain boundary conductivity is thought to be determined by the thickness of this oxide phase. It is interesting that the high Gd concentration ceria samples produce the highest total conductivity, because data discussed in chapter 6 showed that the electrolytic domain is widened at higher dopant concentrations. Further discussions in appendix A, also show that high Gd concentrations produce the most mechanically stable electrolytes. It therefore appears beneficial to construct SOFC electrolytes with Gd concentrations >20mol%Gd, despite the slight reduction in the bulk conductivity.

Chapter 13 explored the possibility of optimising the bulk conductivity by reducing the global lattice strain to zero. The reduction in strain was achieved by using rare earth doping pairs, with a smaller and a larger ion compared to that of Gd. The Sm-Y system was most successful in reducing the lattice strain but no improvement in the bulk conductivity was measured. From these results it was concluded that reducing the local lattice strains, through defect trapping energies, a higher good bulk conductivity is achieved. Gadolinium achieves the lowest local lattice strains and thus it does not appear possible to improve on this, however, Ce-3%Sm-3%Y shows promise for use at temperatures above 500°C.

The grain boundary conductivity was again found to be important in these materials. For Ce-3%Sm-3%Y, the grain boundary conductivity was an order of magnitude higher than a CGO sample with a similar Gd concentration. Impedance and TEM results suggested the formation of a relatively good oxygen ion conducting phase containing the dopant, Ca and Si ions. This sample displayed the highest total conductivity of all the samples studied in this thesis. Unfortunately, this material displayed poorer characteristics in reducing conditions, which will limit the temperature of operation of such electrolyte materials to ~500°C.

The final chapter in this thesis concentrated on the electronic conductivity in doped ceria. It was discovered that small additions of Ca to CGO dramatically improved the grain boundary conductivity, especially for the low Gd concentration sample. The electronic conductivity in this material below 700°C, was also shown to be lower compared to CGO. Ca-codoped CGO therefore looks a promising material for future electrolyte applications at low temperatures (<700°C). The addition of variable valent dopants to act as electron trapping sites, in reducing conditions, did not appear to be successful. The addition of strontium gallate to decrease the sintering temperature (by forming a liquid phase) and to lower the electronic conductivity (by creating a grain boundary electron blocking layer), was also not successful. However, these were the first experiments of their kind performed on CGO, and there is a large scope with which to continue research into electron blocking layers.

Suggestions for Future Work

This work provides many avenues for further research into ceria electrolytes but there are four particular areas where further experiments could prove fruitful. The first of these areas is the testing of the heavily doped CGO materials (>20mol% Gd) in reducing conditions, to assess the affect on the P(-) value. If these experiments prove successful, then longer term experiments operating under working SOFC conditions would release information about the mechanical stability, which is expected to be better in these heavily doped samples.

The ionic conductivity in the Sm-Y doped ceria system needs further consideration, to understand the properties at the grain boundary which lead to the significantly higher conductivity compared to CGO. Electrolytes based on Ce-Sm-Y oxide are more likely to be considered in air separation membranes, where less reducing conditions will be experienced.

It is necessary to conduct experiments on Ca doped CGO in reducing conditions at lower temperatures (500°C). If there is a significant improvement in the P(-) value, then this material has the potential to replace YSZ electrolytes and overcome one problem in the production of low temperature SOFC systems. Experiments with other codopants may further improve on the electrical properties.

Finally, the addition of electron blocking phases in CGO may be the ultimate answer to lowering the electronic conductivity in reducing conditions. It appears that strontium gallate has not initially been successful but further experiments with different dopants are necessary. The search for alternative low melting point ceramics, which exhibit reasonable oxygen ion conductivities, is currently underway at Imperial College.

Appendix A

A.1. Mechanical and Dielectric Breakdown Relationship

The mechanical properties of ceria electrolytes have received very little attention, considering the large stresses that can be imposed on this ceramic under the operating conditions of an SOFC. Besides having an adequate strength and toughness to withstand the stresses of construction in building a fuel cell stack, there are a number of operational stresses which need to be considered.

Firstly, the thermal mismatch between the different materials in the stack induces stresses during thermal cycling of the SOFC. Chapter 6 showed that ceria electrolytes have a higher thermal expansion coefficient than zirconia electrolytes, which enables a closer matching to electrode materials. The lower operating temperatures of a ceria electrolyte based SOFC will also lower the thermal stresses experienced during thermal cycling, compared to a zirconia based electrolyte. Therefore, ceria electrolytes would perform better than zirconia under the thermal constraints of the SOFC.

Secondly, at the anode side of the electrolyte, a reducing atmosphere (10^{-19}atm) causes partial reduction of the cerium ion (Ce^{4+}-Ce^{3+}), introducing oxygen vacancies and localised electrons into the lattice for charge compensation (equation A.1).

$$2O_o^x \Leftrightarrow V_o^{\bullet\bullet} + 2e^{'} + O_{2(g)} \qquad (A.1)$$

The partial reduction increases both the lattice parameter and hence the overall dimensions of the electrolyte [1, 2]. At the cathode the oxygen partial pressure is around 0.2atm and therefore, the ceria electrolyte is situated in an oxygen pressure gradient. This gradient results in an increased strain across the thickness of the electrolyte, which can lead to fracture. This is perhaps the greatest mechanical problem associated with ceria electrolytes and until satisfactorily resolved, will prevent the use of ceria in SOFC designs.

Atkinson [3] has used calculations to show that the region of non-stoichiometry through a CGO electrolyte, is confined closer to the anode side, as more current is drawn from the cell. Another interesting finding is that the tensile stress is shown to decrease, as Gd concentration increases from 5-25%. Therefore, higher Gd concentrations would be preferable under SOFC conditions. The explanation for this may be related to the fact that higher Gd doping shifts the P(-) to lower values of P_{O_2} (see chapter 6). At these higher dopant concentrations ceria appears to have a greater resistance to reduction, resulting in the creation of fewer oxygen vacancies and thus a lower electrolyte stress. Combined with the electrical measurements in chapter 12, which showed a higher ionic conductivity for high dopant levels, it would appear that a high dopant concentration is needed for the optimum ceria electrolyte. The calculations also indicate that the maximum 'safe' operating temperature for CGO in a $P_{O_2}=10^{-20}$atm is about 750°C.

The remainder of this appendix concentrates on the physical stresses applied to the electrolyte during their production and incorporation into the stack. For the scale-up in production required for commercialisation, the mechanical properties become even more important. There have been very few studies concerning the mechanical behaviour of doped ceria electrolytes. This is partly a result of the large quantity of material needed and partly due to the difficulty in performing meaningful tests on ceramics.

Shemilt [4], using an indentation fracture technique, calculated the fracture toughness, K_c, of samaria doped ceria to be insensitive when the doping level was between 10-20mol% $SmO_{1.5}$. The fracture surfaces, examined by SEM, revealed predominantly transgranular fracture, which is typical of cubic systems [5]. Table A.1 shows a comparison of literature values for some mechanical properties in YSZ and doped ceria electrolytes.

It is clear, that ceria electrolyte fracture toughnesses are at the lower end, compared to those of YSZ. It also appears, that the dopant composition has relatively little effect on K_c. Table A.1 shows that the measured strength is much lower than the calculated strength, which uses the measured fracture toughness values. This implies, that large

extrinsic defects, introduced during preparation of these materials, are responsible for failure. The difficulties in performing reliable mechanical experiments, has necessitated the search for a more appropriate testing technique.

Composition	Fracture Toughness, K_c (MPa $m^{1/2}$)	Fracture Strength, σ (MPa)
$Ce_{0.9/0.8}Sm_{0.1/0.2}O_X$	2.4±0.3 [4]	720 (calculated) [4]
$Ce_{0.8}Gd_{0.2}O_X$	2.1-2.5 [6]	140 (measured) [6]
YSZ	1.5-4.2 [7]	150-200 [8]

Table A.1. Comparison of mechanical properties between YSZ and ceria electrolytes.

Ceramic materials are inherently brittle and will fail catastrophically, when subjected to sufficiently large tensile forces. In most cases, the flaws which lead to failure are surface defects, which propagate under the applied stress. In each ceramic specimen there will be a distribution of flaw sizes, flaw orientations and locations, with respect to the applied stress. It is this flaw distribution that determines the strength of a ceramic and it is therefore necessary, to use a statistical distribution function to describe the strength variation. The most widely used function is that of Weibull [9], who defines the survival probability, P, of a specimen of volume, V by:

$$P = 1 - \exp\left[-\left(\frac{V}{V_0}\right)\left(\frac{\sigma}{\sigma_0}\right)^m\right] \qquad (A.2)$$

where σ is the fracture stress, V_0 is the unit volume and σ_0 and m are constants. The constant, m, is known as the *Weibull modulus* and characterises the width of the fracture stress distribution, i.e. The larger the value of m, the smaller the variation in the measured fracture stress. For most engineering ceramics, m is in the range of 5-10.

When analysing mechanical breakdown strengths, Weibull statistics use the "weakest link hypothesis", i.e. the largest flaw causes failure. To obtain statistically significant values, many test pieces are required. Mechanical test samples are relatively large in size and must be accurately shaped. This generally produces large quantities of expensive waste material.

Dielectric breakdown has also been shown to follow the weakest link theory and dielectric strengths are usually estimated by means of Weibull statistics. The microstructure is expected to play a similar role in both mechanical and dielectric strength distributions and so an analogy between the two is likely. It would then be possible to evaluate the reliability of mechanical strength data, using dielectric strength tests. Dielectric strength measurements require only small areas for electrodes, need many fewer specimens and can be performed in an automated process, however, measuring high voltage breakdown across an insulating surface is not a simple process. Normally, a large scatter in the breakdown voltages occurs, at a particular spacing, due to variable factors, such as the surface roughness (both the electrodes and the insulator), statistical breakdown distribution, power supply characteristics, atmospheric conditions and the actual technique employed for testing. Generally, the breakdown voltage is assumed to follow a Gaussian distribution [10].

Yamashita [11] has adapted the Weibull equation for dielectric analysis, according to equation A.3.

$$P = 1 - \exp\left[-V\left(\frac{E_b - E_u}{E_o}\right)^m\right] \qquad (A.3)$$

where, V is the volume subject to dielectric stress, E_b the dielectric strength, E_u is the threshold field and generally set to zero and E_o is a scaling parameter. For a series of test specimens with a maximum dielectric strength, E_n, the survival probability is normally calculated using equation A.4, for the following set of breakdown values:

$$E_1 < E_2 < E_3 < \ldots\ldots E_i \ldots\ldots < E_n$$

$$P_i = \frac{i}{n+1} \qquad (A.4)$$

Rearranging equation A.3 and taking logarithms gives equation A.5

$$\ln\ln\left(\frac{1}{1-P}\right) = \ln\left(\frac{V}{E_o^m}\right) + m\ln E_b \qquad (A.5)$$

A graph of lnln(1/(1-P)) verses $\ln E_b$, allows m to be calculated from the gradient.

Yamashita [11] was the first to propose this concept, using $BaTiO_3$ ceramics, and found similar Weibull moduli for both mechanical and electrical types of failure. Further experiments on $BaTiO_3$ thick films [12] and MgO [13], both at room and elevated temperature, have shown high correlations between the dielectric and mechanical strength distributions.

The similarity in mechanical and dielectric distributions, strongly suggests that breakdown initiates and propagates along the same flaws. Surface flaws, grain boundaries, pores, dislocations and voids are all common stress concentrating defects in ceramics. Beauchamp [14] studied MgO and found dielectric breakdown to occur at the grain boundaries and often at triple points.

Silver electrodes applied to the surfaces, for the production of dielectric samples, will penetrated to the bottom of the sample roughness. The electric field in the vicinity of these electrode tips, is inversely proportional to the radius of curvature at the tip, which is determined by the surface flaw shape. Consequently, the sharpest surface flaws would lead to dielectric breakdown. This is analogous to mechanical breakdown. Kishimoto [15] showed that surface roughness played a critical role in the distribution of both dielectric and mechanical strength in TiO_2 ceramics. Smoother surfaces demonstrated higher average dielectric strength and higher Weibull moduli. Mechanical and dielectric strength distributions, with similar roughness, showed close agreement on Weibull plots.

Beauchamp [14] showed the dielectric strength to decrease, as both the porosity and grain size increased. This suggests, that breakdown is most likely to initiate and propagate in the vicinity of the largest grains in a sample. In MgO, breakdown was shown to propagate along the grain boundaries, after initiation at an unknown source.

It is often observed that as the sample thickness increases, the breakdown voltage decreases. This can be explained, by the increased probability of creating a breakdown pathway in a thicker sample.

Nakamura [16], in a recent study of gypsum, suggested that large pores present in both mechanical and dielectric breakdown samples, were responsible for the initiation of failure. In these experiments, SEM analysis showed the inner surfaces of the breakdown path to have melted, due to the Joule heat generated during failure. Atmospheric discharge was observed as the sudden breakdown occurred, suggesting breakdown originated at a gas filled pore.

There are three common dielectric breakdown mechanisms: Intrinsic, thermal and avalanche [13]. Intrinsic breakdown is electronic in nature, is very fast and occurs at low temperatures. The breakdown strength is independent of the sample and electrode geometries and the mode of the applied electric field. Thermal breakdown occurs, whenever the Joule heat generated in the sample cannot be extracted fast enough by conduction and convection. As a consequence the sample temperature rises until permanent damage occurs. Thermal breakdown often displays a circular melted track between the two electrodes. Avalanche breakdown occurs by the rapid breakdown through a region of gradually accumulated electrons.

Experimentally, a time lag is always observed between voltage application and breakdown. The time, t_s, which elapses between the application of a potential difference $\geq V_b$ (the breakdown voltage) and the appearance of a suitably placed electron, is called the statistical time lag. Once an electron has appeared, an avalanche ionisation process causes breakdown in time, t_f, known as the formative lag time. The total time (or spark) lag, t, is thus given by,

$$t = t_s + t_f \qquad \text{(A.6)}$$

The statistical time lag depends on ionisation between the electrodes, at the time the voltage reaches the breakdown value. In most cases, the formative time is short (nanoseconds), in comparison to the statistical time lag and can be neglected.

A.2. Experimental

Standard CGO powder (10% $GdO_{1.5}$) supplied by Rhône-Poulenc, was pressed uniaxially in a 25mm diameter die, before isostatic pressing at 300MPa. The samples were sintered at 1550°C for 2 hours, ensuring all samples had densities >95% of the theoretical. Both faces of each pellet were then ground with 1200 grit SiC paper to produce a uniform roughness. Silver electrodes (8mm diameter) were then screen printed onto both sides of each pellet. The electrodes were located in the centres of each pellet and were small enough to prevent any edge-field concentration effects, such as corona discharge [14]. All samples were immersed in silicone oil, to prevent surface discharge, before testing. A d.c. voltage was then applied to each sample and increased at the rate of ~$300Vs^{-1}$, using a SEFELEC PRF high voltage supply. The breakdown field at which the current abruptly increased (after t_s), was regarded as the dielectric strength and was measured automatically. All measurements were performed at room temperature.

A.3. Results and Discussion

Figure A.1 shows the graph of dielectric breakdown voltage, verses the thickness of the test sample. It is clear, that the breakdown voltage does not increase linearly with the sample thickness. The thicker samples breakdown more easily compared to the thinner samples, which is in agreement with the statistical approach, that there is a greater probability of a larger critical flaw existing in thicker samples. Inspection of the surfaces of each sample immediately after breakdown, revealed a small charred marking on both electrodes, indicating that the breakdown had occurred through the sample and not across the surface. The charring also indicates a thermal breakdown process, as discussed previously. At present, it has not been possible to determine the propagation route of the current through the sample, because the re-oxidation of the electrodes conceals the location of the surface charring.

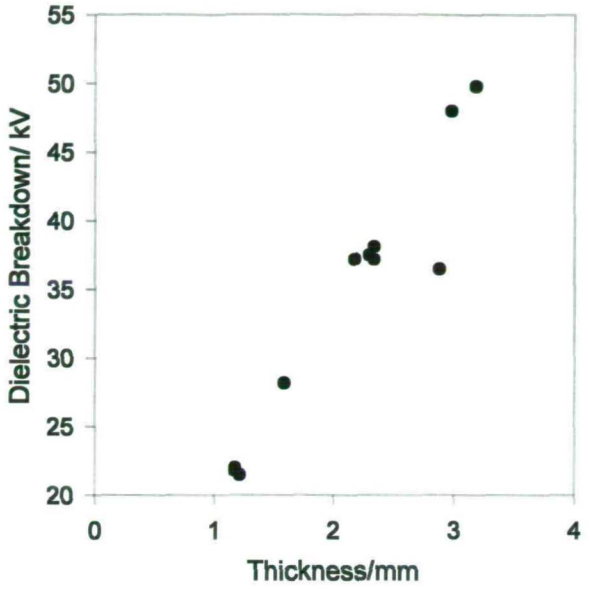


Fig.A.1. Dielectric breakdown characteristics of $Ce_{0.9}Gd_{0.1}O_{2-X}$ as a function of thickness.

The breakdown fields measured in this study are considerably higher than those reported for TiO_2 and $BaTiO_3$ but much less than those of MgO. Using the data in Fig.A.1 and applying equation A.5, a Weibull plot was created for CGO and can be seen in Fig.A.2. The graph shows some scatter at the lower breakdown fields but a fitted straight line gives a value of m = 9.01. This value is inside the range that is typical for most engineering ceramics.

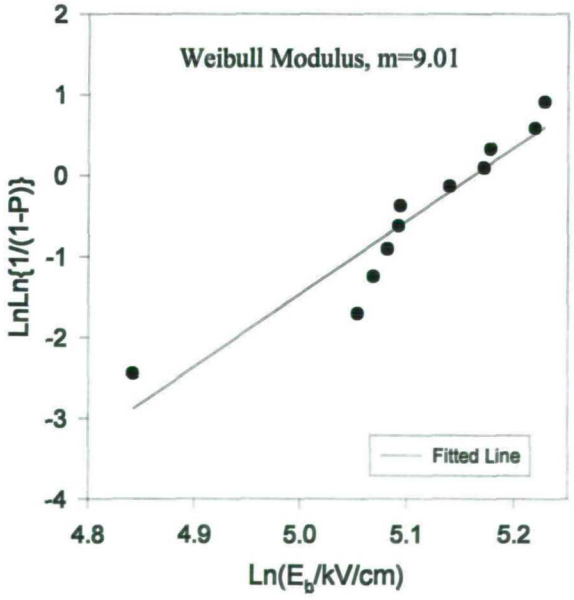


Fig.A.2. Weibull plot of dielectric strength for $Ce_{0.9}Gd_{0.1}O_{2-X}$.

It will now be interesting to see, what value researchers acquire for the Weibull modulus of CGO, when analysing its mechanical strength. If the value of m is similar and the shape of the Weibull plots are the same, then this technique may be used to assess the mechanical reliability of ceria electrolytes and reduce the amount of waste test material.

References

1. G.Brauer and K.A.Gingerich. J.Inorg.Nucl.Chem. **16**, (1960), 87.
2. J.R.Sims and N.Blumenthal. High Temp.Sci. **8**, (1976), 99.
3. A.Atkinson. Solid State Ionics. **95**, (1997), 249.
4. J.E.Shermilt, H.M.Williams, M.J.Edirisinghe, J.R.G.Evans and B.Ralph. Scripta Materialia. **36**, 8, (1997), 929.
5. J.E.Shermilt. Private Communications.
6. N.M.Sammes and Y.Zhang. Proc. of the 2nd European SOFC Forum. Ed. B.Thorstensen. (1996), 697.
7. I.Abraham and G.Gritzner. J.Euro.Ceram.Soc. **16**, (1996), 71.
8. M.Sumi, K.Mori, N.Uchida and K.Uematsu. Proc. of the 14th Risø International Symposium on Materials Science. Eds. F.W.Poulsen, J.J.Bentzen, T.Jacobsen, E.Skou and M.J.L.Østedård. (1993), 431.
9. W.Weibull. J.Appl.Mech. **18**, 3, (1951), 293.
10. E.W.Gray and D.J.Harrington. J.Appl.Phys. **53**, 1, (1982), 237.
11. K.Yamashita, K.Koumoto, H.Yanagida. Comm.Am.Ceram.Soc. (1984), C-31.
12. A.Kishimoto, K.Koumoto and H.Yanagida. J.Mater.Sci. **24**, (1989), 698.
13. H.Murata, S.Chul Choi, K.Kuomoto, H.Yanagida. J.Mater.Sci. **20**, (1985), 4507.
14. E.K.Beauchamp. J.Am.Ceram.Soc. **54**, 10, (1971), 484.
15. A.Kishimoto, K.Koumoto and H.Yanagida. J.Am.Ceram.Soc. **72, 8**, (1989), 1373.
16. Y.Nakamura, M.Suzuki, N.Motohira, A.Kishimoto and H.Yanagida. J.Mater.Sci. **32**, (1997), 115.

Appendix B

The following calculations show the derivation of the impedance of a parallel RC circuit and why this is represented by a semi-circle in the complex plane.

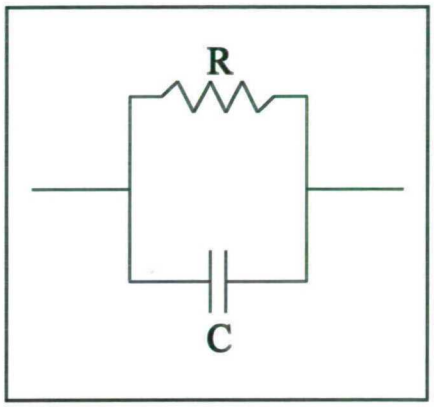


Fig.B.1. A parallel RC circuit.

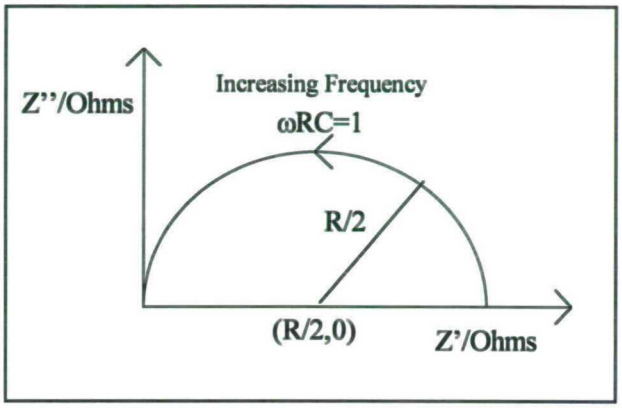


Fig.B.2. Corresponding impedance semi-circle.

The current through the resistor is given by I=V/R. The current through the capacitor is given by the differential of charge, Q with respect to time, t (Q=CV), therefore, I=C(δV/δt). The total current is therefore given by,

$$I = \frac{V}{R} + C\frac{\partial V}{\partial t} \qquad (B.1)$$

where C is the capacitance and t, time. The capacitance is related to the relative permittivity of the material by,

$$C = \frac{\varepsilon_0 \varepsilon_R A}{\ell} \qquad (B.2)$$

where ε_0 is the permittivity of free space, ε_R is the relative permittivity of the dielectric, A is the cross sectional area of the material and ℓ is the thickness of the material. If a sinusoidal voltage is applied according to equation B.3,

$$V = V_0 \exp\{j\omega t\} \qquad (B.3)$$

where V_0 is the amplitude of the voltage, then the resulting current is given by,

$$I = \frac{V}{R} + j\omega CV \qquad (B.4)$$

which can be rearranged to give,

$$I = V\left(\frac{1}{R} + j\omega C\right) \qquad (B.5)$$

The impedance of a sample was shown in chapter12 to be given by Z=V/I, therefore, using equation B.5, the impedance can be expressed as,

$$Z = \frac{V}{V\left(\frac{1}{R} + j\omega C\right)} \qquad (B.6)$$

Rearranging this equation gives the commonly quoted expression for the impedance of a parallel RC circuit,

$$\frac{1}{Z} = \frac{1}{R} + j\omega C \qquad (B.7)$$

This equation is now shown to be the equation of a circle as follows: Rearranging for Z gives,

$$Z = \frac{1}{1/R + j\omega C} \qquad (B.8)$$

Multiplying top and bottom by $1/R - j\omega C$

$$Z = \frac{1/R - j\omega C}{1/R^2 + \omega^2 C^2} \qquad (B.9)$$

Complex number theory states that $|Z| = Z' - jZ''$, therefore,

$$Z' = \frac{1/R}{1/R^2 + \omega^2 C^2} \tag{B.10}$$

And,

$$Z'' = \frac{\omega C}{1/R^2 + \omega^2 C^2} \tag{B.11}$$

Rearranging (B.10) gives:

$$\omega^2 C^2 = \frac{1}{RZ'} - \frac{1}{R^2} \tag{B.12}$$

Thus,

$$\omega C = \sqrt{\left(\frac{1}{RZ'} - \frac{1}{R^2}\right)} \tag{B.13}$$

Substituting (B.12) and (B.13) into (B.11) gives,

$$Z''\left[\frac{1}{R^2} + \frac{1}{RZ'} - \frac{1}{R^2}\right] = \sqrt{\left(\frac{1}{RZ'} - \frac{1}{R^2}\right)} \tag{B.14}$$

Squaring both sides,

$$\left[\frac{Z''}{RZ'}\right]^2 = \frac{1}{RZ'} - \frac{1}{R^2} \tag{B.15}$$

Eliminating and simplifying gives,

$$(Z')^2 - RZ' + (Z'')^2 = 0 \tag{B.16}$$

Adding $R^2/4$ to both sides gives,

$$(Z')^2 - RZ' + R^2/4 + (Z'')^2 = R^2/4 \qquad \text{(B.17)}$$

Finally, this rearranges to give,

$$(Z' - R/2)^2 + (Z'')^2 = (R/2)^2 \qquad \text{(B.18)}$$

This is the equation of a circle of radius R/2 and whose centre is located at (R/2,0). If ω,R,C>1 this will result in a semi-circle above the x-axis.

"The Answer to the Great Question Of.....Life, the Universe and Everything.....Is.....Forty-Two."

Douglas Adams (1952-)

BIBL. LONDIN. UNIV.